Fermi National Accelerator Laboratory

FN-447
0103.000
(SSC-106)

Shielding Calculations for Multi-TeV Hadron Colliders

A. Van Ginneken and P. Yurista
Fermi National Accelerator Laboratory
P.O. Box 500, Batavia, IL 60510 USA

and

C. Yamaguchi
KEK
Oho-machi, Tsukuba-gun, 305 Japan

January 1987

Operated by Universities Research Association Inc. under contract with the United States Department of Energy

SHIELDING CALCULATIONS

FOR

MULTI-TeV HADRON COLLIDERS

A. Van Ginneken and P. Yurista
Fermilab, Batavia, IL, 60510, USA

and

C. Yamaguchi
KEK, Oho-machi, Tsukuba-gun, 305 Japan

January 1987

TABLE OF CONTENTS

Entries in tables refer to both figure number and page number. Since there is exactly one page to each figure, referencing is made easier by re-numbering the pages of section VI to match page and figure number. To distinguish from text, page numbers of this section are preceded by a letter F. A blank table entry means the corresponding graph is not included.

A. HADRONS. FIXED TARGET

Star Densities

	C			cct/sl*				Al			Fe			Pb		
E,TeV	CP*	∫dr	∫dz	CP	∫dr	∫dz	DE	CP	∫dr	∫dz	CP	∫dr	∫dz	CP	∫dr	∫dz
5	1			6			11	14			19			24		
10	2	4	5	7	9	10	12	15	17	18	20	22	23	25	27	28
20	3			8			13	16			21			26		

*cct means concrete; sl means soil
*CP denotes contour plots (of star density), ∫dr and ∫dz refer to radial and longitudinal integrals, DE denotes contour plots of dose equivalent

Stars outside Block

	Fe			cct/sl	
E,TeV	CP	r=∞	z=∞	r=∞	z=∞
5					
10		30	31	32	33
20	29				

Energy Density

E, TeV	C			cct/sl			Al			Fe			Pb		
	CP	∫dr	∫dz	CP	∫dr	∫dz	CP	∫dr	∫dz	CP	∫dr	∫dz	CP	∫dr	∫dz
5	34			39			44			49			54		
10	35	37	38	40	42	43	45	47	48	50	52	53	55	57	58
20	36			41			46			51			56		

Catastrophic Beam Loss. Hadron Dose

E, TeV	continuous dipole*							beam pipe*	
	inside		middle		outside			side	
	CP	∫dr	CP	∫dr	CP	∫dr	∫dz	C-P	∫dr	∫dz
5	59		62		65			69		
10		61		64		67	68		71	72
20	60		63		66			70		

*in a tunnel

Stars in Air

E, TeV	cont. dipole	bmpipe stsect
	∫dr	∫dr
5		
10	74	75
20		

B. MUONS. FIXED TARGET

Muon Beam in Soil

E, TeV	z, rest	x, rest	z, xSP*	ρ_E, CP¶	ρ_E vsz
.01	76	84	88	92	96
.03	77				
.1	78	85	89	93	97
.3	79				
1.	80	86	90	94	98
3.	81				
10.	82	87	91	95	99
20.	83				

*Scatter plot of z,x where μ comes to rest
¶Contour plot of energy density

Catastrophic Beam Loss. Muon Dose

Hadron Cascade in ∞ soil

E, TeV	CP	∫dr	∫dz
5	100		
10	101	103	104
20	102		

Loss on Beampipe in a tunnel

E, TeV	CP	∫dr
5	105	
10	106	108
20	107	

Continuous Dipole. Beam Frame

	beam on inside									beam on outside					beam in middle			
E,TeV	inside			up & down			outside			inside			outside		inside			out
	CP	∫dr	∫dz	CP	∫dr	∫dz	CP	∫dr	∫dz	CP	∫dr	∫dz	∫dr	∫dz	CP	∫dr	∫dz	CP
5	109						117			122					128			
10	110	112	113		115	116	118	120	121		124	125	126	127		130	131	
20	111			114			119			123					129			132

Continuous Dipole. Magnet Frame

	bm inside			bm outside		
E,TeV	inside			inside		
	CP	∫dr	∫dz	CP	∫dr	∫dz
5	133			138		
10	134	136	137		140	141
20	135			139		

C. COLLIDING BEAMS. HADRONS

Collision Hall Geometry

	side wall			back wall		
E,TeV	CP	∫dr	∫dz	CP	∫dr	∫dz
5	143			147		
10		145	146		149	150
20	144			148		

Beam Pipe in Soil

E, TeV	CP	∫dr	∫dz
5	151		
10		153	154
20	152		

D. COLLIDING BEAMS. MUONS

Downstream Penetration

	wall at						all
E, TeV	20m		100m		250m		
	CP	∫dr	CP	∫dr	CP	∫dr	∫dz
5	155	158	161	164	167	170	173
10	156	159	162	165	168	171	174
20	157	160	163	166	169	172	175

Collision Hall Geometry

	sw*	bw+
E, TeV	CP	CP
5	176	
10		
20	177	178

*side wall
+back wall

I. INTRODUCTION

The present volume is most easily described as an extension of an earlier similar effort.[1] The extension is mainly to higher energies but it also includes colliding beam simulations as well as muon production and transport. There is also a larger variety of geometries presented. But the purpose remains the same: to provide a collection of graphs which may serve as a rough guide in shielding applications. Detailed designs seldom resemble the idealized cases analyzed here and deserve specific computation with particular attention to any suspected weak spots. The graphs included here are intended to go no further than to form a useful starting point in design work. Such an approach is already quite effective at 1 TeV and below and will become even more so at higher energies where shielding costs are even larger.

The choice of standard energies (5, 10 and 20 TeV) reflects the range of collider energies presently contemplated and allows for modest extrapolation outside this range. For fixed target results up to 1 TeV refs. 1 and 2 may be consulted. As in refs. 1 and 2, all results in this volume (except those pertaining to "muon beams") use the Monte Carlo code CASIM.[3] Where π° induced electromagnetic showers are included as, e.g., in muon production or in energy deposition, they are simulated with the AEGIS[4] code. Predictions of CASIM (plus AEGIS where applicable) for target heating, induced radioactivity and absorbed dose in the sub-TeV regime agree quite well with experiment.[5] Likewise CASIM results compare well with a set of absorbed dose measurements taken outside thick shields for a variety of beam loss and shielding geometries.[6] The full extension of CASIM into the multi-TeV domain requires considerable modifications to both particle production and particle transport models. This extension is presently only partly completed.

Particle production in CASIM for the fixed target (particle-nucleus) case is still described by the Hagedorn-Ranft model[7] plus a high p_T component and a low energy nucleon component.[8] This model compares well with experiment in the sub-TeV range.[9] No such comparisons exist for the extended (>1 TeV) model but at least no grossly unphysical features seem to appear. Some trends are worth noting: (1) the average fast charged particle multiplicity increases too slowly with energy, e.g., for copper it rises from 13 at 1 TeV to about 17 at 40 TeV. From CERN Collider results a larger multiplicity is to be expected; (2) the normalization of the Hagedorn-Ranft production cross sections becomes somewhat worrisome at the higher energies. In CASIM leading particle spectra are normalized to a total of exactly two such particles and pion spectra are normalized to enforce overall energy conservation. Both factors stay within 10% of unity in the 3 to 1000 GeV range. However the leading particle normalization factor climbs to 1.17 at 40 TeV while for pions it falls to 0.46 (using again copper as an example).

This does not mean that the typical shielding calculation is invalidated by these defects. Such calculations usually sum over many generations and the mechanism of energy conservation (built into the model) ensures some self-correction for reasonably small deviations from reality. For example, by underestimating its multiplicity, a Monte-Carlo interaction at 40 TeV necessarily produces particles with higher average energy, which in turn produce more particles in the next generation than would be the case if the correct multiplicity were predicted. It should also be emphasized that these deficiencies of the model are limited to the highest energies and hence affect only the first few generations. In fact, predictions of CASIM on star densities and broad beam energy deposition in the TeV domain agree well[10] with results of other codes which employ production models of more recent vintage. Also, while an improved particle production model is clearly desirable, some care must be taken in its formulation to assure agreement with experiment at the highest available energies while maintaining the predictive power of CASIM in the sub-TeV domain. This might be best undertaken when more detailed results of the CERN Collider and Fermilab Tevatron are available.

Hadron production by colliding beams is described by an empirical model based mostly on Fermilab data, along with some CERN Collider results and constrained by conservation laws. This model is outlined in Sec. II. Prompt muon production is described by an empirical formula[11] which expresses muons as a fraction of pions produced as a function of Feynman-x. This formula is based on much lower energy work and is used here mainly out of convenience. Nonetheless, the formula does feature a slow increase in muon multiplicity with incident energy as is expected from increased charm and bottom (plus perhaps top) meson production though it is not attempted to quantitatively justify this particular rate of increase.

Particle transport in the multi-TeV regime differs significantly from that at lower energies due to the increasing importance of bremsstrahlung and direct pair production as a source of energy loss and angular diffusion. The basic approach and implementation into CASIM is described elsewhere.[12] Results presented here involving muon transport are obtained with the updated code. Predictions of this code are in excellent agreement with data of Kopp et al.[13] on the energy distribution of a 120 GeV muon beam transmitted through a 9.3m thick iron target. Hadron dose and star density calculations are performed with a simple extension of the old code which treats energy loss due to bremsstrahlung and pair production on an averaged basis and neglects the associated angular diffusion. This is justified for this type of calculation since only the most energetic particles are affected by this and since production angles will tend to be much larger than the deflection incurred over one interaction length. Energy deposition at large radii is calculated in similar fashion.

By contrast, energy deposition calculations over radial distances of the order of typical beam sizes anticipated at the colliders (as low as 50 μm) must include an accurate description of these new sources of angular diffusion. The reason is that for such small beams the radial dependence of the energy density varies rapidly over distances

comparable to the beam size. This has important applications in the design of beam dumps and the problem of radiation induced quenching in superconducting magnets. Calculations of this type are also more likely to be affected by the details of the particle production model. Therefore they are not included in the present volume.

The basic CASIM code is reasonably well documented[3] and the recent update to the (muon) transport part is described elsewhere.[12] Below, in Section II, the particle model used to simulate colliding beam interactions is described. Section III deals with presentation and interpretation of results, while the results themselves are briefly reviewed in IV. Section V contains some information on the codes used in preparing this volume.

II. PARTICLE PRODUCTION IN COLLIDING BEAMS

The particle production model used in the simulation of colliding beams is a simple parametrization based on extrapolation of lower energy experimental results. As is the case for the Hagedorn-Ranft model used in the fixed target part, leading particles, i.e., final state particles which may be identified with the incident particles, are distinguished from particles newly created in the collision. For the present purpose leading particles are always protons or neutrons. Elastically scattered (colliding) protons will almost always either remain within the beam or else leave the beam aperture at large distances from the interaction region and are therefore ignored. The more energetic leading particles will typically also remain in the beam pipe for a considerable distance. Hence leading particle production need not be treated in utmost detail. (Large angle elastics and leading particles along with other produced particles must be removed by some collimation scheme so as to protect the downstream superconducting magnets. This type of problem is not considered here. It is also possible that such a collimator, particularly one intercepting a large fraction of these particles near the interaction region, may require shielding for personnel or environmental protection. This is strongly dependent on the detailed design of the interaction region and therefore likewise omitted here.)

A. Leading Particles

Leading particles are divided into a diffractive and non-diffractive component. Goulianos[14] uses the parametrization

$$d\sigma/dx_R = .01A/(1-x_R) + A(1-x_R) \qquad 0.9 \leq x_R \leq x_R^{max} \qquad (1)$$

where the first term is the diffractive part. To conform to the treatment of the produced particles (see below) the radial scaling variable, x_R,

the particle's energy in the center of mass expressed as a fraction of its maximum kinematically allowed value, replaces the more usual Feynman x used by Goulianos. For the present work these should be completely interchangeable. From the coherence condition[14] the diffractive part must vanish around $x_R \approx 0.9$. It is therefore assumed that

$$d\sigma/dx_R = B(1-x_R) = 2A(1-x_R) \qquad x_R^{min} \leq x_R \leq 0.9 \qquad (2)$$

where the second equality follows from continuity at $x_R=0.9$. The value of A follows from normalizing eqs. (1) and (2) to unity. The behavior of $d\sigma/dx_R$ when x_R approaches its kinematic limit is not well described by eq. (1). Note that x_R can be expressed as

$$x_R=(s-M_X^2+M_p^2)/s \qquad (3)$$

where s is the square of the total energy in the center of mass and M_X is the invariant mass recoiling against the leading proton. The data[15] at low M_X (high x_R) show that $d\sigma/dx_R$ starts at zero at $M_X^{min}=M_p+M_\pi$ and (on average) increases relatively rapidly through a series of resonances in M_X, to a maximum whereupon it the declines in accordance with eq. (1). For our present purpose the complicated behavior of $d\sigma/dx_R$ near threshold is simulated by assuming that it remains constant between

$$x_R^o = 1-0.6/s \qquad (4)$$

(corresponding to M_X=1.22 GeV) and x_R^{max} (where $M_X=M_X^{min}$). Below x_R^o eq. (1) is assumed to hold.

The p_T dependence of the leading particle cross section is assumed to be of the type

$$d\sigma/dp_T^2 \propto \exp(-bp_T^2) \qquad (5).$$

For the non-diffractive part b is set to 5 $(GeV/c)^{-2}$. For the diffractive part $b=2b_{el}$,[14] where b_{el} pertains to elastic scattering near the forward direction and is taken from the parametrization of Block and Cahn.[16] It is assumed that diffractive protons do not undergo charge exchange but that non-diffractive protons convert into neutrons with a probability of one half. This is in rough accord with data of Engler et al.[17]

Upon multiplying eqs. (1) and (2) by x_R and integrating over the entire x_R range one obtains the leading particle center of mass inelasticity, i.e., the fraction of the total energy carried off by leading particles. This equals about 0.43 with little variation over the 5 to 20 TeV colliding beam energies explored here.

B. Pions and Kaons

As in CASIM, the leading particles' energy is subtracted from the total energy and the remainder is shared among the produced particles. Not every particle species is represented in the simulated collisions. In CASIM the produced particles are simply the three types of pions. For the colliding beams, partly because the cross section formulae are much simpler, kaons are included as well. In either scheme other particles can always be added without having to recast the entire model.

The invariant cross section for π and K production is assumed to be

$$Ed^3\sigma/dp^3 = A(1-x_R)^n[(m-2)(m-1)1.3^{m-2}/2(p_T+1.3)^m] \qquad (6)$$

where A and n depend on particle type: $A(\pi^*)\simeq 1$ and $A(K^*)=A(\pi^*)/9$, and $n(\pi^+)=3.5$, $n(\pi^-)=4.2$, $n(K^+)=2.8$, $n(K^-)=5.2$. Since small angle particle production has not yet been studied in detail at the CERN Collider these parameters are taken (somewhat loosely) from Fermilab data of A. Brenner et al.[18] and J. R. Johnson et al.[19] and with the $A(\pi^*)$ fixed by energy conservation. The p_T parametrization is based on the work of Arnison et al.[20] with the value of m based on extrapolation of CERN ISR and Collider data. For the present work m=6.5 for $\eta<2$ and m=9.0 for $\eta>7$ (η being the center of mass rapidity) and m is taken to vary linearly in between. The usual rule of taking the $\pi^\circ(K^\circ)$ production cross section to be one half the sum of the charged $\pi(K)$ cross sections is followed.

This simple model predicts a charged particle inelasticity of about 0.77 and a rms p_T is about 0.67 GeV/c both with little variation

over the range of $\sqrt{s}$ from 10 to 40 TeV. The charged particle multiplicity varies from 43.9 to 48.3 over this range. This is likely to be an underestimate.

Eq. (6) as well as its counterparts for leading particles, eqs. (1) and (2), permit relatively simple Monte Carlo selection schemes to be implemented, whether selecting proportional to the multiplicity or to the inelasticity.

III. INTERPRETATION OF RESULTS

A. Dose and Star Densities.

A frequently used procedure (followed, e.g., in Ref. 1) is to present star densities above some predetermined cut-off. The standard cut-off is 0.3 GeV/c.[21] (Above this value cross sections vary only slowly with energy and this permits a number of shortcuts in the program which could not be maintained at lower momenta. The precise value of the cut-off is somewhat arbitrary but considerable convenience is derived by adhering to the 0.3 GeV/c standard.) These star densities may then be converted to dose assuming the presence of an equilibrium momentum spectrum of the participating hadrons. Such an equilibrium spectrum (with a spectrum shape insensitive to location) prevails only at sufficiently large depths and radii. At lower values of r and z a conversion factor based on an equilibrium spectrum would underestimate the dose. In these cases one must use a location dependent conversion factor.[1]

This procedure is included in a number of experimental tests[6] of CASIM and yields quite satisfactory results. It is however limited to shields composed of soil and concrete for which the equilibrium spectrum shape is reasonably well established. For shields composed of iron or heavier elements application of a similar procedure[1,22] requires great caution. Because of large fluctuations in neutron cross sections as a function of energy for these elements and because of the absence of hydrogen it requires deeper penetration to establish an equilibrium spectrum. Furthermore while an equilibrium spectrum, e.g., in soil, may be expected to be reasonably robust with respect to small changes in (soil) composition this is not necessarily so for the heavier shields. Perhaps most importantly the empirical basis of the procedure, which is quite well established for soil and concrete, is lacking.

The rule adopted here is to present results in terms of dose equivalent (rem) for soil and concrete and in terms of star densities for all other materials. The dose is calculated by applying a star-to-dose conversion factor, which depends on particle type and on momentum, within the Monte-Carlo. For low energy neutrons this factor is identical to the one of Ref. 1 thereby guaranteeing agreement with the above mentioned procedure in regions where low energy neutrons predominate. Closer to the incident beam there are additionally significant contributions due to π° initiated showers and due to charged particles. For comparison, the results for a solid concrete (soil) cylinder are presented both ways.

The limitation of reliable dose calculations to soil or concrete is in practice not a severe one. Almost all accelerator shielding relies on an outer layer of soil or concrete for neutron attenuation. A rule of thumb is that about 1m of concrete (radially) is required to establish an equilibrium spectrum.

Hadron production (mostly low energy neutrons) by electromagnetic cascades is not included in any of the calculations. Compared to direct production this seems quite inefficient, but the fractional energy spent on electromagnetic showers (~67% at 20 TeV in iron) increases monotonically with energy and this guarantees that eventually this mechanism will become significant.

Expressing dose-equivalent in rem (in lieu of sievert) may, regrettably, inconvenience some but it offers at least some continuity with ref. 1. Since rem is still widely used and the conversion is trivial, there need be no further apology. More serious is a likely future revision of quality factors, particularly if the calculated dose-equivalent has more than one significant component which could undergo dissimilar revisions. Fortunately, in most applications a dominant component (usually either muons or low energy neutrons) may be readily identified and a revised dose-equivalent can then be evaluated.

Ref. 1, among many other sources, contains some hints and recipes on converting calculated results of the type presented here into more immediately useful numbers. For convenience some often encountered conversion factors are reproduced here with the caveat that these are not universally agreed upon.

In concrete and in regions where the cascade is sufficiently developed the beam-on dose rate may be estimated from the star density:

one [star/cm^3] corresponds to 350 hadrons/cm^2
or $1.5\ 10^{-6}$ rad
or $9.0\ 10^{-6}$ rem.

In iron and in regions where the cascade is sufficiently developed star density may be converted into exposure rate resulting from induced radioactivity. For the "worst case" of infinite irradiation time, zero cooling time and on contact:[23]

one [star/(cm^3•sec)] corresponds to $3\ 10^{-6}$ rad/hr.

To protect against ground water activation, the criterion is a limiting concentration of radioactivity in drinking water. It is the practice at Fermilab to translate this into a limiting number of stars per incident proton produced in uncontrolled soil. This, in turn, dictates size and shape of beamdumps. There is no unique conversion factor from radioactivity concentration to stars per incident proton. This depends on the expected beam intensity as well as the (usually poorly known) transport of the radioactivity produced around the dump to the water source. Based on very conservative arguments a typical Fermilab beamdump admits 0.015 stars/incident proton in uncontrolled soil. In contrast to the conversion factors above this number is only meant as an illustration and is not for direct use in design calculations.

B. Scaling.

For homogeneous shields of roughly the same atomic composition simple scaling rules[24] may be applied to adjust for different densities. Since the basic parameters (interaction length, stopping power, particle production characteristics, etc.) vary only slowly with atomic mass these scaling rules have a rather wide range of application particularly where rough answers suffice. In the present study these rules are applied over a very narrow range viz., to inter-relate calculations for wet soil, dry soil and concrete. Given their similar composition the scaling should be nearly exact. For convenient access it appears useful to repeat here some formulae of Ref. 24 upon which the scaling (illustrated in a large number of the graphs) is based.

Star densities scale as:

$$S_w(\rho_c \vec{r}_c/\rho_w) = S_c(\vec{r}_c)(\rho_w/\rho_c)^3 \qquad (7)$$

where $\vec{r}$ is the position vector within the shield and ρ is the density. The subscripts identify different materials, e.g., c for concrete and w for wet soil with assumed densities ρ_c=2.4 g/cm^3 and ρ_w=2.24 g/cm^3. In eq. (7) it is assumed that S_c is explicitly calculated and that S_w is derived by scaling, i.e.,

$$S_w(1.071\vec{r}_c) = 0.813 \cdot S_c(\vec{r}_c) \qquad (8).$$

For star density results presented in the form of contour plots the above equations show how both r and z axes must be recalibrated as well how as the contours are to be relabelled.

Dose scales as

$$D_w(\rho_c \vec{r}_c/\rho_w) = D_c(\vec{r}_c)(\rho_w/\rho_c)^2 \qquad (9),$$

i.e. with the axes to be recalibrated as for star densities but with the contours relabelled differently. Star densities integrated over radius

$$I(z) = \int_0^\infty S(\vec{r})2\pi r dr \qquad (10)$$

obey the scaling rule

$$I_w(\rho_c z_c/\rho_w) = I_c(z_c)\rho_w/\rho_c) \qquad (11).$$

Note that in all cases presented here (unlike eq. (11)) the upper limit is actually some finite radius (problem boundary). Use of the scaling law requires that the problem radius be large.

The integrals of star density over depth (z) shown in the graphs refer to

$$I(r) = 2\pi r \int_0^Z S(\vec{r})dz \qquad (12).$$

I(r) follows the same scaling law as I(z), shown in eq. (11) and with the same caveat about the upper limit of integration. The factor $2\pi r$ in eq. (12), while somewhat unconventional, facilitates subsequent integration of I(r) over r.

For heterogeneous shields scaling laws are obviously less applicable. Yet one may identify instances where these laws may be used though generally to a lesser degree of approximation. The case of a beam striking a target in an otherwise empty tunnel provides a suitable illustration. For example, one may seek to apply scaling for different tunnel wall materials while keeping everything else identical. If the tunnel wall surface is thought of as a source of particles at constant r but widely distributed in z then it is clear that scaling does not apply in the z-direction. However the integral over all z can still be scaled provided radial distances are measured from the tunnel wall:

$$I_w(\rho_c r_c/\rho_w - r_o) = (\rho_w/\rho_c)I_c(r_c - r_o) \qquad (13).$$

For a cave, scaling may be applied for the integral over r in the z-direction provided the dominant contribution enters through the back wall rather than through the tunnel wall. Certain problems, though in principle heterogeneous, will yield reasonably approximate answers when treated as homogeneous for scaling purposes, e.g., the more energetic muons emanating from a multi-TeV proton beam loss in a magnet inside a tunnel may traverse several km of soil before stopping and little accuracy will likely be lost by scaling on the basis of the homogeneous soil case.

IV. RESULTS

A convenient tabulation of all results appears in the Table of Contents. For ease of reference the entries in this listing refer to the page number of the corresponding graph. Most of the graphs are readily interpreted but, where appropriate, some commentary is provided in this section. The results are divided into : (A) hadron dose and (B) muon dose from fixed target initial interactions, (C) hadron dose and (D) muon dose from colliding beam initial interactions, where "initial" indicates that effects of the cascades induced by these interactions are included.

A. Hadron Dose. Fixed Target.

Figs. 1-3 present contour plots of star density for 5 ,10 and 20 TeV protons incident on a solid (i.e., homogeneous) carbon cylinder. Fig. 4 shows radially integrated star densities as a function of depth (z) and fig. 5 longitudinally integrated star densities as a function of radius (r), also for carbon and for the same incident proton energies. Figs. 6-10 repeat this sequence of graphs for concrete and simultaneously, via the scaling of Sec. III, for soil. Figs. 11-13 are iso-dose plots for the concrete/soil case, obtained from the same calculations as the star densities but converted to dose-equivalent by a factor which depends on particle type and momentum. Figs. 14-28 show star density results for aluminum, iron and lead. For all cases the beam is parallel to the cylinder axis and has a Gaussian distribution independently in x and y with $\sigma_x=\sigma_y=1$ mm.

Figs. 29-33 deal with radioactivity induced in soil outside thick targets. Fig. 29 plots contours of equal total star production in soil outside an iron block by 20 TeV protons incident on axis. Forward and backward directions are shown separately. Note that these results

pertain to a block, not a cylinder as for the star densities, with x(=y) indicating the half width of the block. As can be seen in fig. 29 all iso-star contours quickly assume their asymptotic form parallel to the x and z axes. This is expected since little can be gained by adding to the sides when escape is predominantly from the back and vice versa. Since not much information is contained in the "corners" of the contours, the rest of the plots, figs. 30-33, show only the location of the asymptotes as a function of x or z. Thus fig. 30 exhibits the total number of stars produced outside an infinitely wide, semi-infinitely long iron block, i.e., the block has finite length in either the positive or negative z-direction. Fig. 31 plots the total number of stars produced outside of an infinitely long iron target which is likewise infinitely wide for either $z>0$ or $z<0$ but has finite width in the other half-space. Figs. 32 and 33 are the corresponding graphs for concrete/soil. Results for $z<0$ are less well established and conservative interpretation is advised. These figures may be useful as starting values in, e.g., optimizing the outer dimensions of a beam dump. Although the star density contours contain essentially the same information, the results presented in figs. 29-33 are more convenient to use as well as expected to be more accurate, especially at large x or z. This is a result of a different Monte-Carlo strategy employed: (1) in computing the number of stars in soil due to escapees the "score" associated with each such escapee is the average total number in stars, a number not subject to fluctuation, and (2) collision length biasing is introduced to ensure that types and spectra of the escapees are sufficiently sampled. This strategy can be adapted to inhomogeneous targets as well as to more complex geometries.

Figs. 34-58 show energy density contour plots along with radially and longitudinally integrated energy densities for the same standard cases as shown for the star densities. These results emphatically exclude the region close to the beam trajectory where more care must be taken in evaluating the energy deposition.

Calculations of the hadron dose resulting from catastrophic beam loss appear in figs. 59-72. Calculations of a more specialized nature such as these are more useful, by virtue of a more realistic geometry, but at the same time less useful since they are influenced by design changes and since some simplification in modelling beam loss, accelerator geometry and magnetic fields is inevitable. Two geometries are included here: (i) a continuous, circularly curved dipole represented by a "C5" magnet and (ii) a 1 mm thick beampipe in a straight section, each enclosed in a 1.2 m radius (respectively curved and straight) tunnel. Beampipe, magnet and tunnel are assumed to be concentric. The composition of the tunnel wall is assumed to be wet soil. Because the main objective is to determine the wall thickness needed for protection from catastrophic beam loss, the star density is evaluated in the tunnel wall only.

Design drawings of the cross-section of the dipole along with a sketch of its representation in the program are shown in fig. 73. An ideal magnetic field is assumed present in the gap. In all cases of this study the central field is taken to be 6.0 Tesla. This means that for a continuous dipole case (the only type considered here when a field is present) the ring radius is adjusted for different beam momenta. Outside the gap the field is obtained by interpolation from arrays of its x and y components specified on a rectangular grid with 0.25 inch spacings covering the magnet cross-section.[25] Also for the dipole case three beam loss modes are presented: (i) beam loss on inside of the beampipe, i.e., towards the center of the ring, (ii) beam loss on outside and (iii) middle. The latter may be thought of as resulting, e.g. from beam-gas interaction. In each mode the beam is assumed to interact precisely at z=0 and with its direction tangential to the curving magnet. For inside and outside beam loss the beam is of infinitesimal extent in the horizontal direction and has a Gaussian spread of 0.01 cm vertically. For beam loss in the middle the beam is assumed to be (uncorrelated) bi-Gaussian with $\sigma_x=\sigma_y=0.01$ cm.

To obtain the azimuthal dependence of the star density the 0 to π range (the problem is symmetric about the midplane) is divided

into three bins: 0 to $\pi/4$, $\pi/4$ to $3\pi/4$, and $3\pi/4$ to π. Not unexpectedly the azimuthal dependence is small enough to be ignored since the dose in the tunnel wall is neutron dominated. The z axis for all cases is the distance along the central orbit of the accelerator. Results for 10 TeV are not shown since these are easily obtained by interpolation from the 5 and 20 TeV graphs. The interesting second bump appearing for the case of inside beam loss is due to particles crossing the aperture which is geometrically favored in this case. The location of the peak is roughly where the tangent to the inside of the beampipe at the interaction point meets the beampipe once again on the outside, which is where neutral secondaries are expected to land.

Figs. 74 and 75 show the linear star density in the air of the tunnel, which surrounds respectively a magnet and a bare beampipe, as a function of distance from the point of interaction. This serves as an estimate of air activation resulting from beam loss. For the beampipe case the dose calculated in the backward direction is not shown since it is both very small and very uncertain.

B. Muon Dose. Fixed Target.

The first set of figures survey some results on muon penetration in soil. For all cases a mono-energetic, parallel muon beam of infinitesimal extent is incident on a homogeneous soil target of infinite extent. The incident energies range from 10 GeV to 20 TeV. Figs.76-83 show the distribution in z where the muons come to rest as well as the rms spread of the muon beam as it penetrates into the soil. These graphs illustrate strikingly the qualitative changes occurring with increasing energy in the slowing down process of the muons. At the lower energies where collision losses are still dominant the distribution is well described by a range plus a straggling tail ($\sigma/\langle z\rangle$=0.070 at 10 GeV). At the higher energies where pair production, bremsstrahlung and nuclear inelastic scattering are more important the distribution resembles a broad Gaussian ($\sigma/\langle z\rangle$=0.29 at 20 TeV). Figs. 84-87 display the x distribution

of muons coming to rest. Figs. 88-91 are scatter plots showing the density of stopped muons as a function of radius and depth. Figs. 92-95 are contour plots of the energy deposition density as a function of r and z. For small r and z these results are not well resolved. Figs. 96-99 display the linear energy density as a function of z along with a breakdown of muon energy deposition mechanisms.

Figs. 100-104 pertain to muons generated by the hadron cascade when a mono-energetic hadron beam enters a homogeneous soil target. While this has few immediate applications it may be of interest as a limiting case, since the presence of any voids will generally increase the muon flux. Also, without geometric or other complications, it may serve as a test case, e.g., in comparison with other calculations.

More practical fixed target muon problems are addressed in figs. 105-141. Muon dose from catastrophic beam loss on a beampipe is shown in figs. 105-108. The geometry is the same as for the hadron case but, because of the deep penetration by the muons, the tunnel length must now be made explicit and is chosen to extend 1 km beyond the interaction point. This is of the order of the length of a straight section contemplated for the SSC.[26]

The remaining figures in this set deal with muon dose from catastrophic loss in a continuous dipole. Again the geometry and magnetic field description are identical to the hadron case. The presence of a magnetic field along with the large distances involved and the curved geometry introduce some ambiguity in the choice of reference frame to analyze this problem. There are two obvious choices: (i) a "beam frame" in which the z axis is tangential to the accelerator and (ii) a "magnet frame" where z is replaced by s, the distance along the central orbit. Analyzing the same calculation separately in each frame is not necessarily an optimal procedure but it should produce an overview of the problem from which more detailed calculations can then depart.

The beam loss mode is idealized as in the hadron dose calculations with the same distinction of losses on the inside, outside and middle of the beampipe. In contrast to the hadron case the muon dose rates show a marked azimuthal dependence. An exhaustive treatment is not attempted, but figs. 109-141 present an overview as well as (hopefully) the more interesting cases. Note also that results for beam frame and magnet frame overlap to some extent at small z or s. Magnet frame results are given only for the azimuthal quadrant to the inside of the ring since (i) muon dose in the outside quadrant is better analyzed in the beam frame and (ii) muons can travel large distances by "channelling", i.e., being repeatedly reflected between magnet aperture and return field. From the latter viewpoint positive muons are somewhat more interesting than negatives by virtue of (i) having the proper guide field orientation in the aperture where there is no energy loss and (ii) being produced in somewhat larger numbers by proton induced cascades, particularly the more energetic muons. Since positives reflect off the inside of the magnet they are expected to leave the tunnel in that direction.

Longitudinally integrated energy density plots in the beam frame have some contribution at radii less than the tunnel radius which is omitted in the figures for lack of simple interpretation, on account of the curved geometry, and because this region is easier to analyze in the magnet frame. This also applies just outside the tunnel wall.

C. Colliding Beams. Hadron Dose.

The idealized geometry of a collision hall used in the present calculations is shown in Fig. 142. Dimensions are roughly those given in ref. 26. A 1 mm thick beampipe runs through the center of the hall. The protons are assumed to collide at the origin and produce secondaries according to the model of Sec. II. These particles in turn interact with nuclei in the beampipe and walls according to the extended Hagedorn-Ranft model. In addition to the usual azimuthal symmetry there is also reflection symmetry about the vertical center line. This is exploited in the calculations and also in the presentation of the results, which cover only half of the interaction region. This must be borne in mind when integrating results over the entire region.

Results are given separately for the side wall and for the back wall of the cylindrical hall in figs. 143-150. This geometry provides a "worst case" since the hall will typically house some apparatus, e.g., a large detector, which provides significant shielding. Figs. 151-154 show results for another extreme: a beampipe surrounded completely by soil. These results plus some interpolation and extrapolation could provide a useful starting point for a more realistic calculation.

D. Colliding Beams. Muon Dose.

Muon dose calculations from colliding beams sources are primarily concerned with the deeply penetrating muons travelling along the collision axis. The relevant geometry is that of the accelerator near the interaction regions and it strongly influences the relative importance of decay versus prompt muons, since this is largely determined by the distance traversed through voids by π and K produced in the collision. A realistic calculation would trace the produced particles through a reasonable idealization of the accelerator components and thus compute for each particle of the sample its appropriate decay probability into a muon, as well as keep track of scattering and any magnetic bending of both produced particle and resulting muon. Such an undertaking is probably warranted when the design of the machine is sufficiently frozen. Here a much cruder approach is taken: the interaction is assumed to take place in a void at a fixed distance from a semi-infinite homogeneous soil shield in which the muon energy deposition is analyzed. The distance to the soil shield is taken to be respectively 20 m, 100 m and 250 m. The 20 m and 100 m represent the distance to the beginning and end of the strongly focussing quadrupoles near the interaction region where some of the produced π and K are expected to leave the aperture. The 250 m corresponds roughly to the distance at which the two beams re-enter their separate apertures.[26] The main objective here is not to make quantitative predictions for the SSC but rather to explore the question of prompt versus decay muons for a reasonable range of decay lengths. Figs. 155-175 show results for the penetrating muons. The radially integrated plots also contain a breakdown on the muon production mechanisms.

The final set of graphs pertain to muon dose in the vicinity of the collision hall. The particle production model indicates that, in an average event, a large number of soft hadrons are emitted. Accompanying these hadrons one expects some muons of comparable energies to be present, resulting both from prompt and decay mechanisms. The different character of hadron and muon absorption poses the question as to which component determines the shield thickness. It appears that for the side walls (figs. 176 and 177) the muon dose already becomes comparable to the hadron dose at around 2m of soil for the region nearest to the colliding beams. At the far end of the hall this equi-dose thickness is about 4m. For the back wall (fig. 178) the hadron dose dominates completely. The collision hall geometry is the same as used to calculate hadron dose. To obtain meaningful results in reasonable execution times the selection of hadrons and prompt muons in the colliding beams must be heavily biased towards those with large p_T.

In the light of these results and of the uncertainty of the production model, especially for muons, the side wall calculation might be worth repeating with different sets of assumptions as a check on sensitivity of this result to the model. Another uncertainty about this problem is geometrical: to find a reasonably simple geometry which approximates a "worst case" from the muon shielding point of view. It has been ascertained by separate calculations (not explicitly included here) that the removal of the 1mm beampipe changes the results very little, i.e., the beampipe's effect as an absorber of muons roughly compensates for its effect as a source of new muons. This is not clear a priori, and it is also not clear that this will continue to hold as the beampipe's thickness is increased, e.g., to simulate the presence of other apparatus.

V. PROGRAMS

As mentioned in the Introduction the basic program used in this work is CASIM supplemented by AEGIS for electromagnetic showers, by the empirical particle production model for colliding beams and by muon production and transport. To generate the various results CASIM was cast into several different versions. The differences between any two such versions not only reflect the presence (or absence) of colliding beam or muon beam simulations but also include different geometries, presence of magnetic fields as well as binning, normalization and printing of the results. This modus operandi, vis-a-vis the obvious alternative of combining everything into one program with multiple options, is the result of both necessity and convenience. A single program alternative would easily exceed the ~100 Kword limit at the CYBERs of the Fermilab Computer Department where most of the development and debugging was done. Actual running took place almost exclusively on the FPS of the Accelerator Division where storage is more than sufficient but where turn-around for short debugging runs might create a problem.

Any of the various versions is available by contacting one of the Fermilab authors. The programs are all in FORTRAN V and are tested on both CYBER and (VAX equivalent) FPS computers. Most need one or more extra files (e.g., range-energy tables) as well as a data file. The codes are not necessarily "user friendly" but all carry an introductory description specifying where the major changes from the standard CASIM occur and which files are referred to by the program. All such files as well as sample data files are likewise available. This work, especially the graphs, may serve as a "menu" of what is available as a suitable starting point for further exploration.

CASIM VERSIONS FOR SSC SHIELDING STUDIES

A. Fixed Target. Hadron Dose

CAS2. Standard CASIM. Computes star densities, rem dose and (at large radii only) energy deposition.

CSX7. Catastrophic beam loss in continuous dipole placed in a (curved) tunnel or of beampipe in straight section.

CAIR. Star density in air of tunnel for catastrophic beam loss in continuous dipole or beampipe in straight section.

B. Fixed Target. Muon Dose

MUP3. Muon beam in infinite, homogeneous soil. Requires histogramming package, e.g., KIOWA or HBOOK.

CMUN. Muons from catastrophic beam loss in continuous dipole.

CMSS. Muons from catastrophic beam loss in straight section.

C. Colliding Beams. Hadron Dose

IRHS. Collision hall geometry. Calculates star density or rem dose in side wall or back wall.

D. Colliding Beams. Muon Dose

IRMS. Colliding beams in void. Variation of decay space is simulated by moveable wall. Includes contribution of hadron cascades in soil.

NIRM. High p_T muons in collision hall geometry.

Communications about bugs, improvements, new or unusual applications, etc., with reference to the above codes will always be greatly appreciated.

ACKNOWLEDGMENTS

Our thanks to Igor Baishev, Don Cossairt and Manfred Hofert for helpful comments on the manuscript, to Graciela Finstrom for her care concerning the presentation of the graphs and to Angela Gonzales for the cover design.

REFERENCES

1. A. Van Ginneken and M. Awschalom, "High Energy Interactions in Large Targets", Fermilab, Batavia, IL. (1975).

2. J. D. Cossairt, "A Collection of CASIM Calculations", Fermilab TM-1140 (1982).

3. A. Van Ginneken, "CASIM. Program to Simulate Hadronic Cascades in Bulk Matter", Fermilab FN-272 (1975).

4. A. Van Ginneken, "AEGIS. A Program to Calculate the Average Behavior of Electromagnetic Showers", Fermilab FN-309 (1978).

5. M. Awschalom et al., Nucl. Inst. Meth. 131, 235 (1975); M. Awschalom et al., Nucl. Inst. Meth. 138, 521 (1976).

6. J. D. Cossairt et al., Nucl. Inst. Meth. 197, 465 (1982); J. D. Cossairt et al., Nucl. Inst. Meth. A238, 504 (1985).

7. R. Hagedorn, Suppl. Nuovo Cim., 3, 147 (1965); R. Hagedorn and J. Ranft, Suppl. Nuovo Cim., 6, 169 (1968); J. Ranft, "Secondary Particle Spectra According to the Thermodynamical Model. A Fit to Data Measured in p-Nucleus Collisions", TUL-36, Karl Marx Univ., Leipzig, DDR (1970).

8. J. Ranft and J. T. Routti, "Hadron Cascade Calculations of Angular Distributions of Secondary Particle Fluxes from External Targets and Description of the Program FLUKU", CERN-II-RA/72-8 (1972).

9. H. Grote, R. Hagedorn and J. Ranft, "Atlas of Particle Spectra", CERN, Geneva, Switzerland (1970); A. Van Ginneken, "Comparison of Data on p-Nucleus Interactions with Hagedorn-Ranft Model Predictions", Fermilab FN-260 (1974).

10. N. V. Mokhov and J. D. Cossairt, Nucl. Inst. Meth. A244, 349 (1986).

11. J. Ritchie et al., Phys. Rev. Lett. 44, 230 (1980).

12. A. Van Ginneken, Nucl. Inst. Meth. A251, 21 (1986); see also S. Qian and A. Van Ginneken, "Characteristics of Inelastic Interactions of High Energy Hadrons with Atomic Electrons", Fermilab-Pub-86/145 (1986), to be publ. in Nucl. Inst. Meth.

13. R. Kopp et al., Z. Phys. C - Particles and Fields 28, 171 (1985). We thank C. N. Brown for bringing this work to our attention and for a related discussion.

14. K. Goulianos, Phys. Repts 101, 169 (1983).

15. Y. Akimov et al., Phys. Rev. D14, 3148 (1976).

16. M. M. Block and R. N. Cahn, Rev. Mod. Phys. 57, 563 (1985).

17. J. Engler et al., Nucl. Phys. B84, 70 (1975).

18. A. E. Brenner et al., Phys. Rev. D26, 1497 (1982).

19. J. R. Johnson et al., Phys. Rev. D17, 1292 (1978).

20. G. Arnison et al., Phys. Lett. 118B, 167 (1982).

21. The 0.3 GeV/c standard goes back at least as far J. Ranft, Nucl. Inst. Meth. 48, 133 (1967) whence it probably originated.

22. P. J. Gollon, "Dosimetry and Shielding Factors Relevant to the Design of Iron Beam Dumps", Fermilab TM-664 (1976).

23. I. S. Baishev et al.,"Calculation of Residual Gamma Radiation Dose Rate near High Energy Accelerators",IHEP Serpukhov, 86-76 (1986); K. Tesch and H.Dinter, Radiat. Prot. Dosim. 15, 89 (1986). The conversion factor stated in the text is a rough average over the results of these two references. The older value of $9\ 10^{-8}$ from ref. 1 pertains to the case where the dosimeter is buried in the iron.

24. A. Van Ginneken, "Stretching Shielding Calculations", Fermilab TM-883 (1979).

25. We thank S. Snowdon and L. Oleksiuk for providing the field map.

26. "Report of the Reference Design Study Group on the Superconducting Super Collider", May 8, 1984.

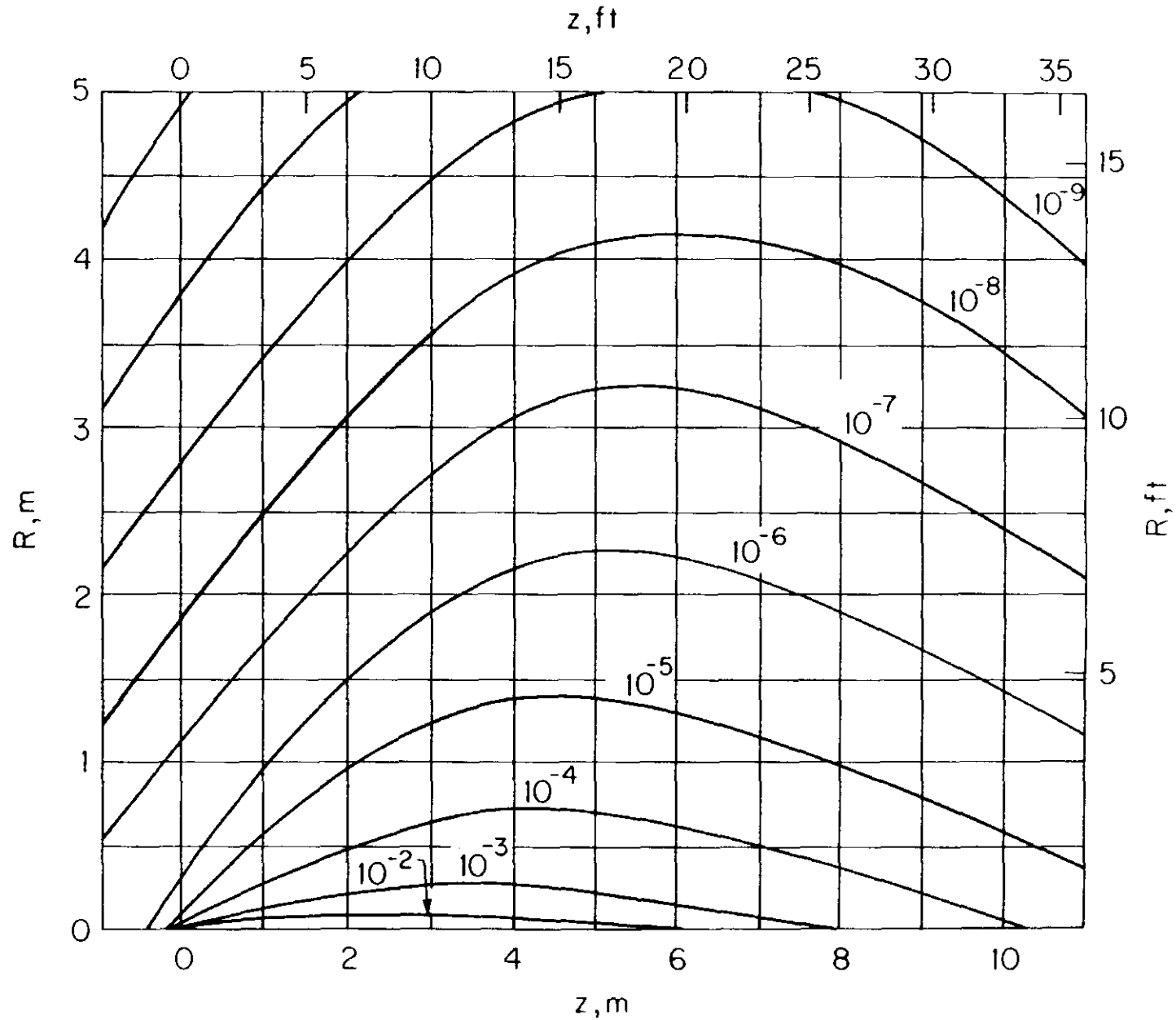

Fig. 1. Contours of equal star density (in stars/cm^3•incident proton) for 5 TeV protons incident on solid carbon cylinder. The beam has a bi-Gaussian spatial distribution with $\sigma_x=\sigma_y=0.1$cm and is parallel to and centered on the cylinder axis. The beam starts interacting at zero depth. The calculation has a cut-off momentum of 0.3 GeV/c. Some contours may be omitted for clarity or due to statistical uncertainty.

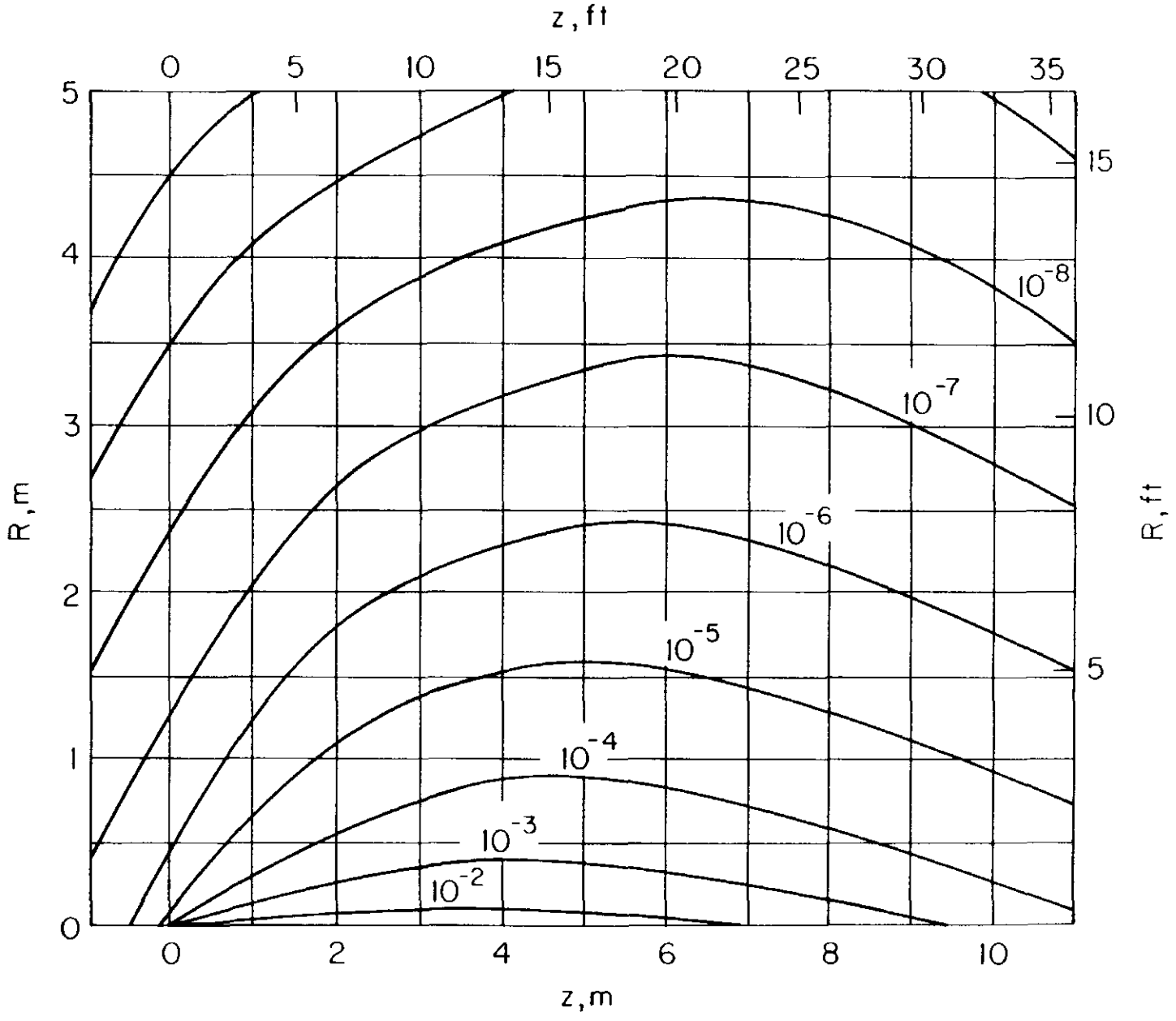

Fig. 2. Contours of equal star density (in stars/cm^3•incident proton) for 10 TeV protons incident on solid carbon cylinder. The beam has a bi-Gaussian spatial distribution with $\sigma_x = \sigma_y = 0.1$cm and is parallel to and centered on the cylinder axis. The beam starts interacting at zero depth. The calculation has a cut-off momentum of 0.3 GeV/c. Some contours may be omitted for clarity or due to statistical uncertainty.

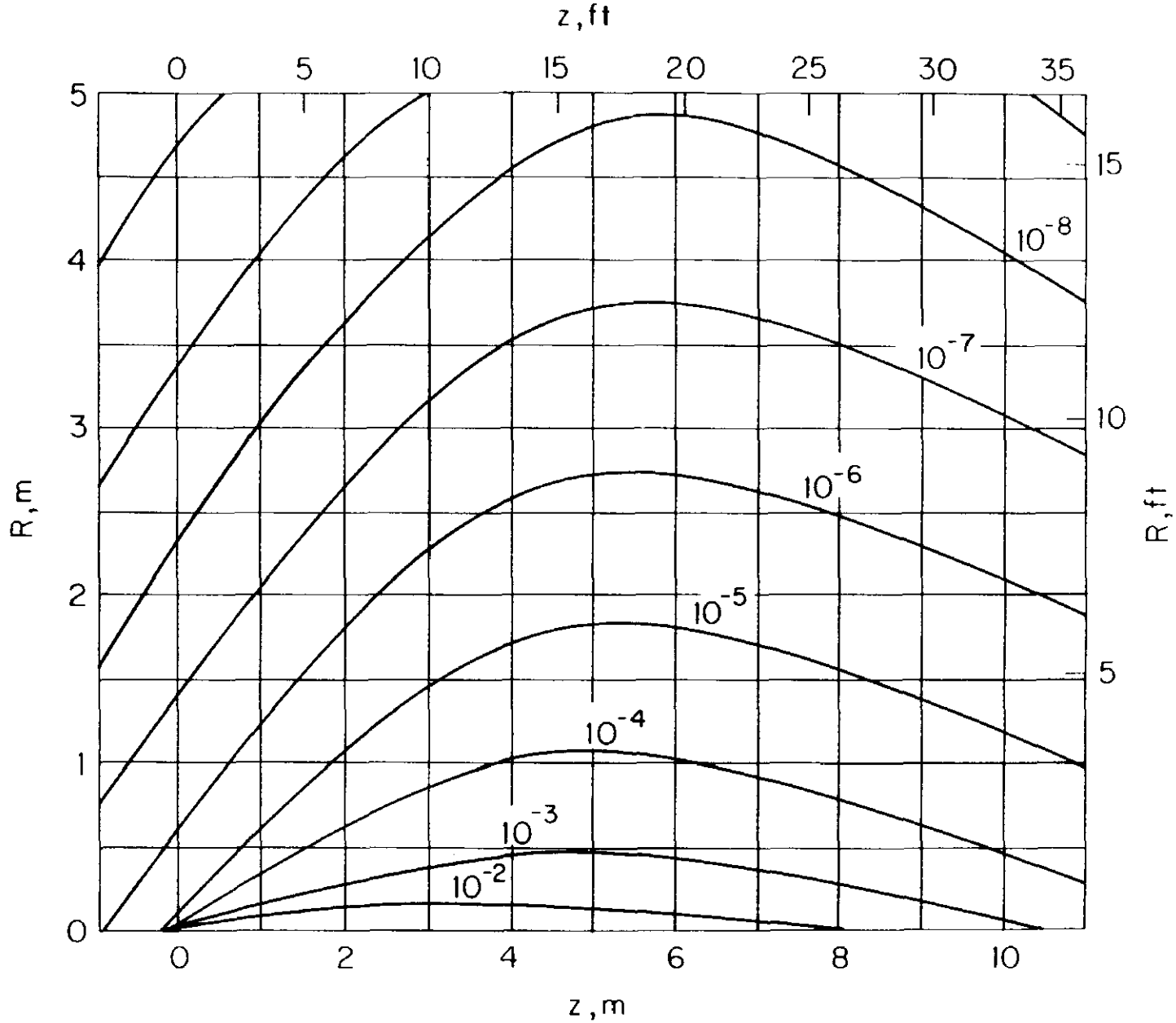

Fig. 3. Contours of equal star density (in stars/cm^3•incident proton) for 20 TeV protons incident on solid carbon cylinder. The beam has a bi-Gaussian spatial distribution with $\sigma_x=\sigma_y=0.1$cm and is parallel to and centered on the cylinder axis. The beam starts interacting at zero depth. The calculation has a cut-off momentum of 0.3 GeV/c. Some contours may be omitted for clarity or due to statistical uncertainty.

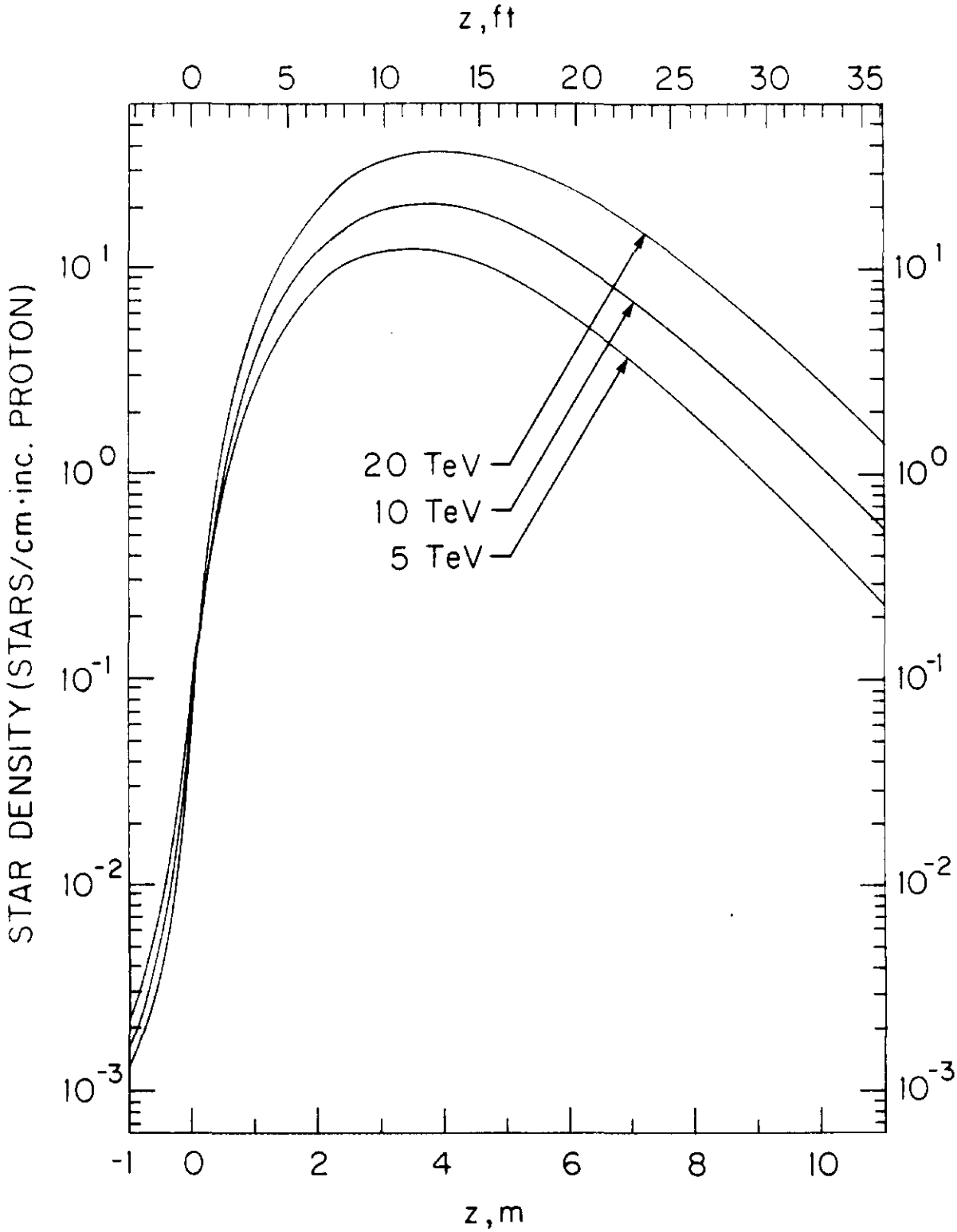

Fig. 4. Radially integrated star density (in stars/cm•incident proton) for 5, 10 and 20 TeV protons incident on 12m long solid carbon cylinder. The calculation has a cut-off momentum of 0.3 GeV/c. The protons begin interacting at zero depth.

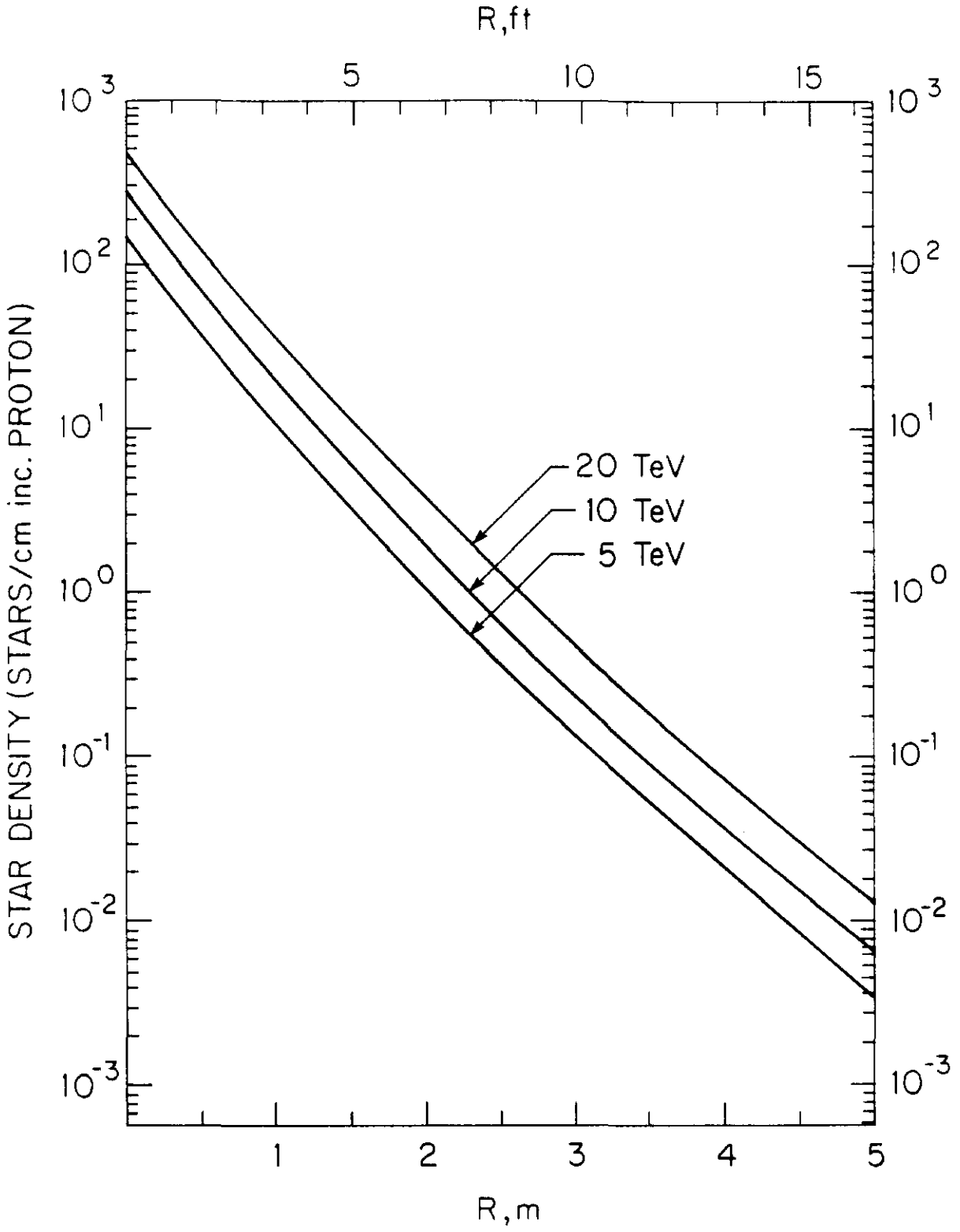

Fig. 5. Longitudinally integrated star density (in stars/cm•incident proton) for 5, 10 and 20 TeV protons incident on 5.0m radius solid carbon cylinder. The calculation has a cut-off momentum of 0.3 GeV/c.

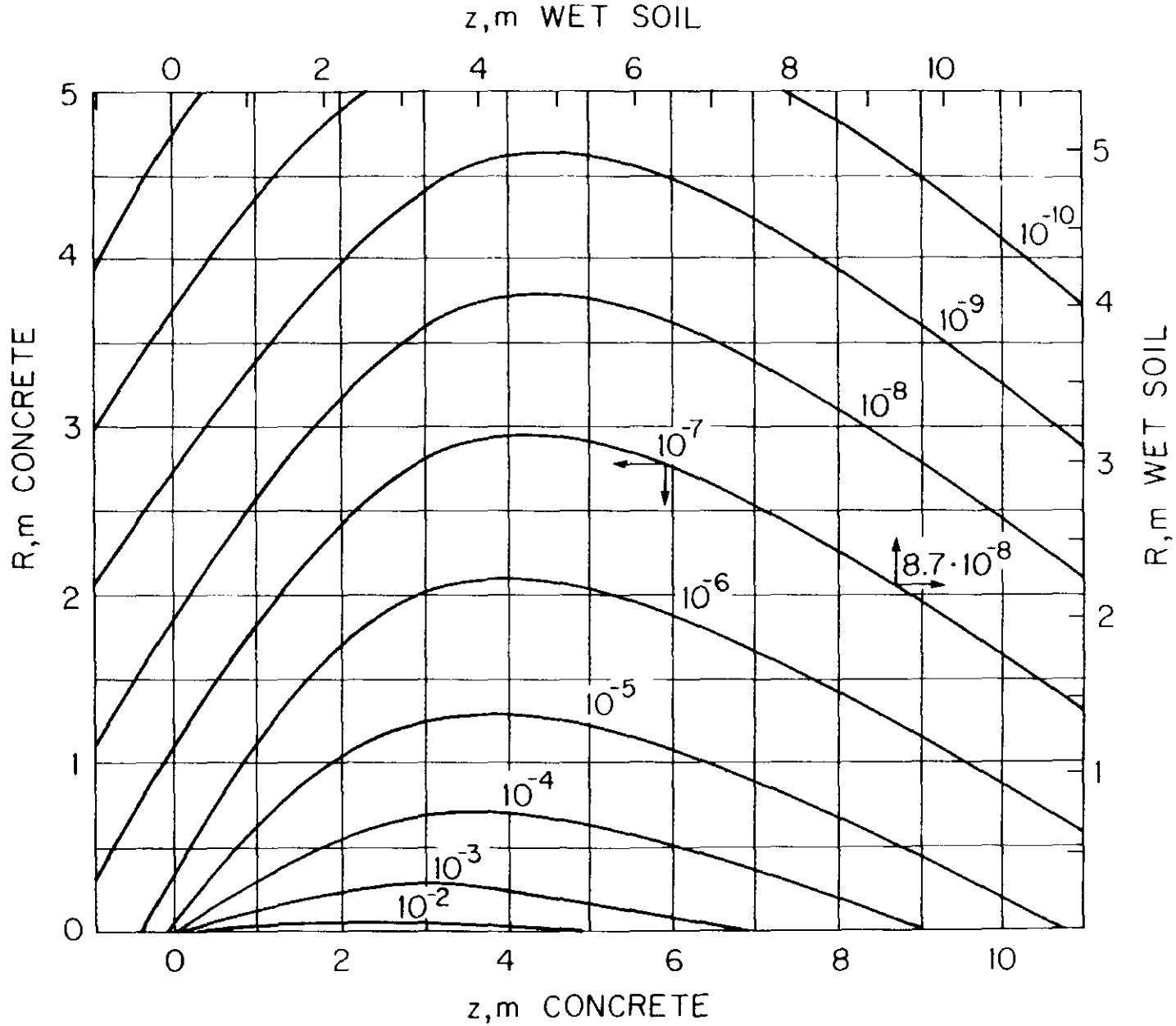

Fig. 6. Contours of equal star density (in stars/cm^3•incident proton) for 5 TeV protons incident on solid concrete/soil cylinder. The beam has a bi-Gaussian spatial distribution with $\sigma_x = \sigma_y = 0.1$cm and is parallel to and centered on the cylinder axis. The beam starts interacting at zero depth. The calculation has a cut-off momentum of 0.3 GeV/c. Contours for concrete (left & bottom axes) are integral powers of ten. Contours for (wet) soil (right & top axes) must be scaled down by 0.81 as shown for one example. Some contours may be omitted for clarity or due to statistical uncertainty.

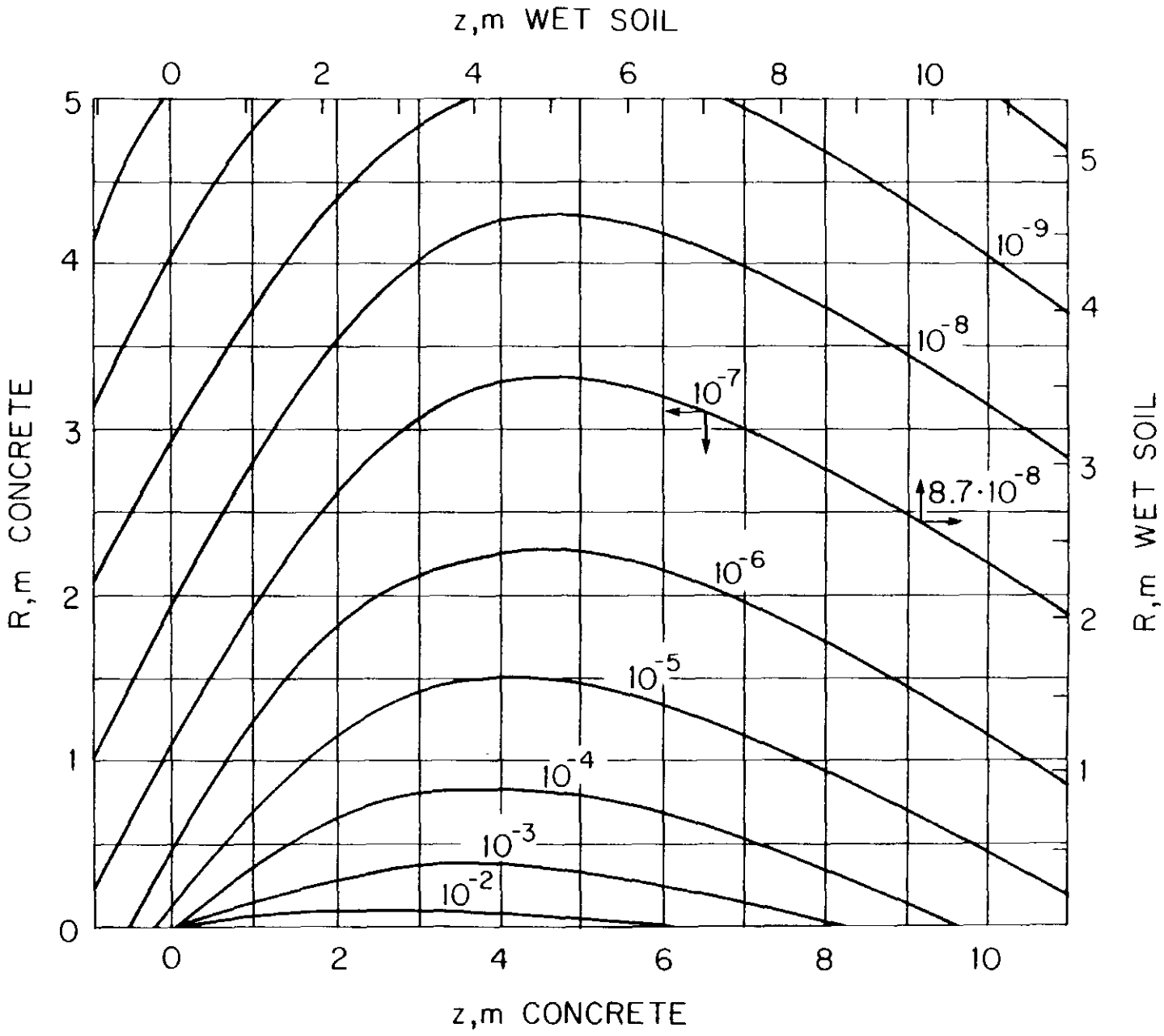

Fig. 7. Contours of equal star density (in stars/cm^3•incident proton) for 10 TeV protons incident on solid concrete/soil cylinder. The beam has a bi-Gaussian spatial distribution with $\sigma_x = \sigma_y = 0.1$cm and is parallel to and centered on the cylinder axis. The beam starts interacting at zero depth. The calculation has a cut-off momentum of 0.3 GeV/c. Contours for concrete (left & bottom axes) are integral powers of ten. Contours for (wet) soil (right & top axes) must be scaled down by 0.81 as shown for one example. Some contours may be omitted for clarity or due to statistical uncertainty.

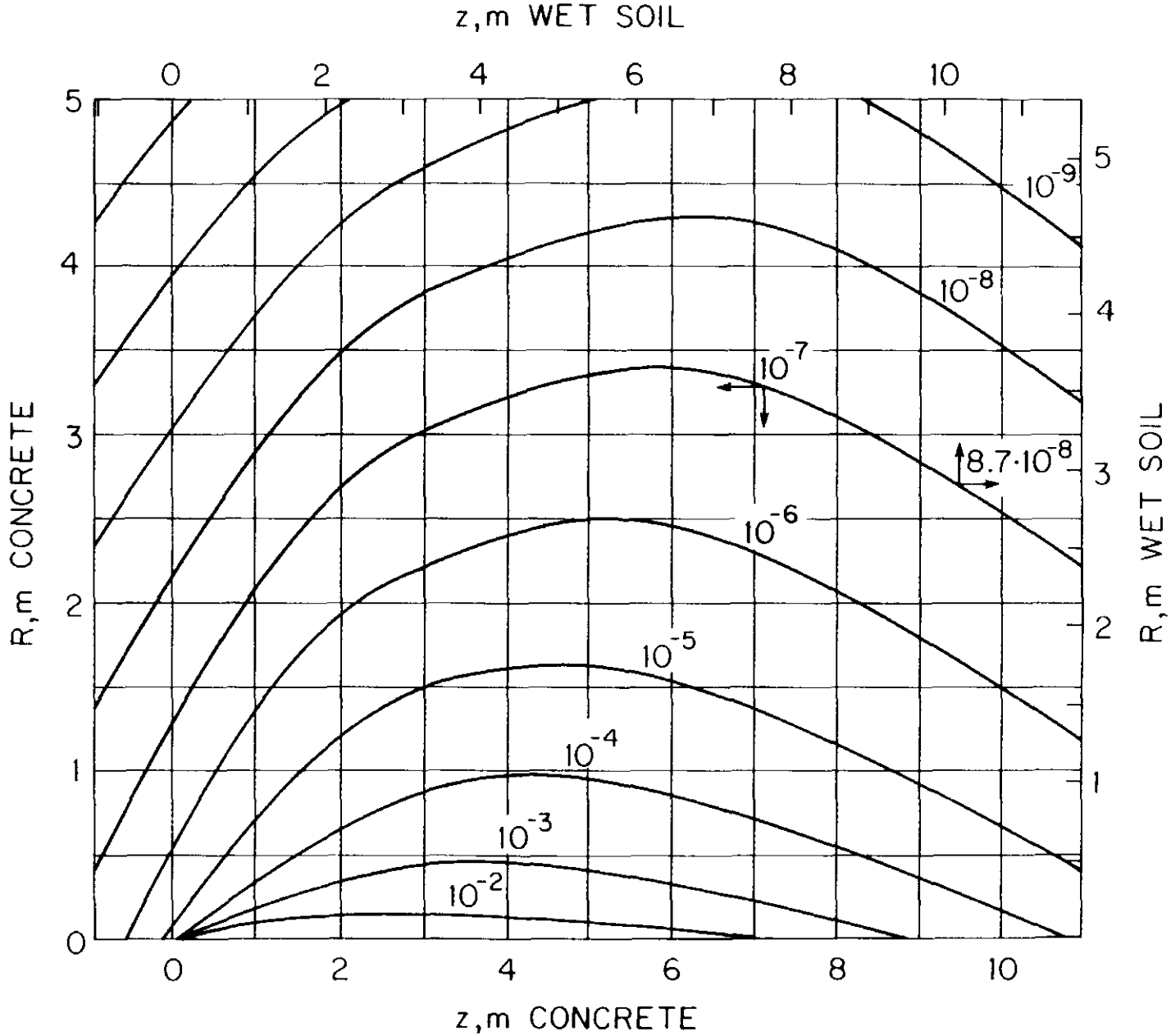

Fig. 8. Contours of equal star density (in stars/cm^3•incident proton) for 20 TeV protons incident on solid concrete/soil cylinder. The beam has a bi-Gaussian spatial distribution with $\sigma_x = \sigma_y = 0.1$cm and is parallel to and centered on the cylinder axis. The beam starts interacting at zero depth. The calculation has a cut-off momentum of 0.3 GeV/c. Contours for concrete (left & bottom axes) are integral powers of ten. Contours for (wet) soil (right & top axes) must be scaled down by 0.81 as shown for one example. Some contours may be omitted for clarity or due to statistical uncertainty.

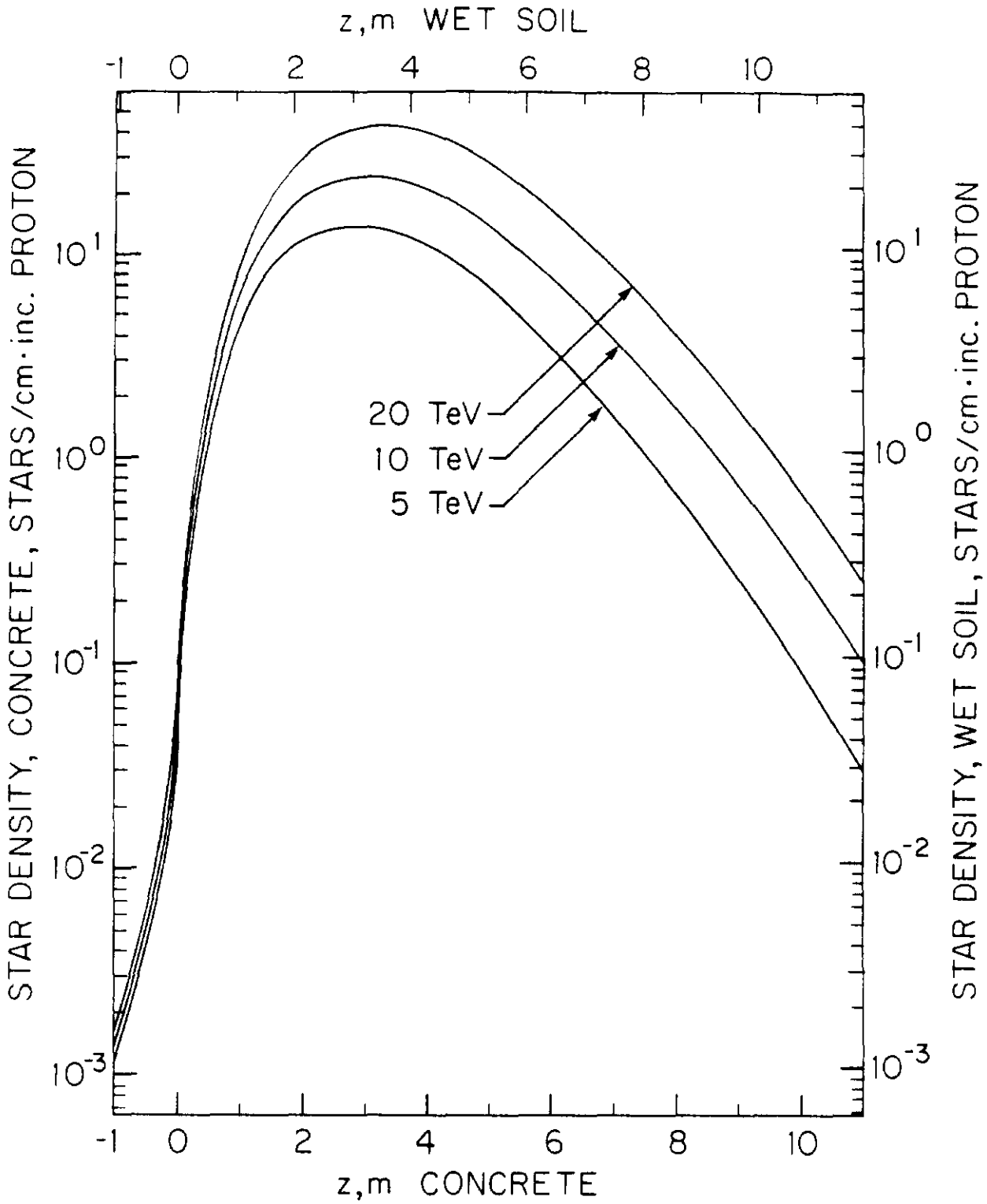

Fig. 9. Radially integrated star density (in stars/cm•incident proton) for 5, 10 and 20 TeV protons incident on 12m long solid concrete (left & bottom axes) or soil (right & bottom axes) cylinder. The calculation has a cut-off momentum of 0.3 GeV/c. The protons begin interacting at zero depth.

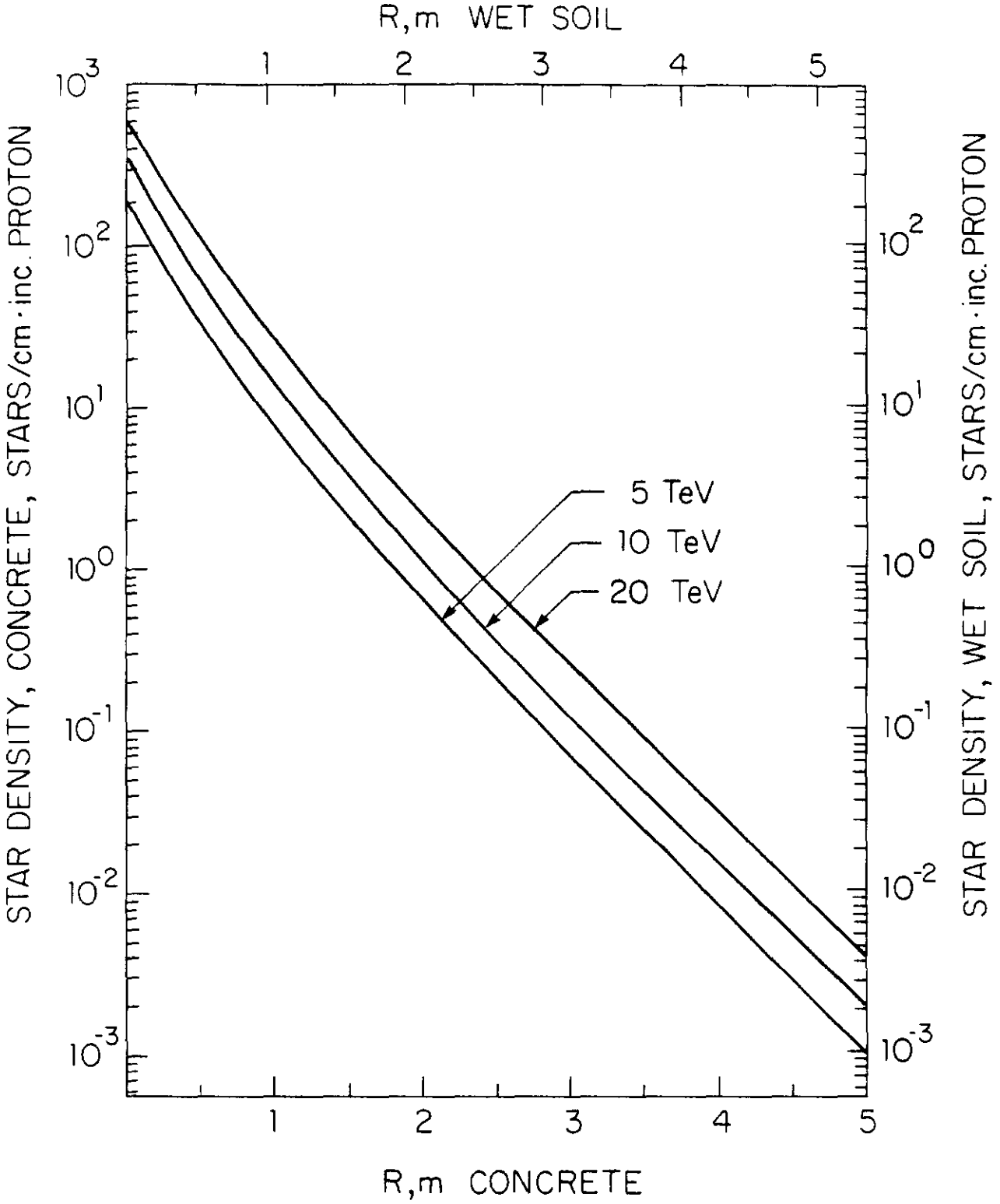

Fig. 10. Longitudinally integrated star density (in stars/cm•incident proton) for 5, 10 and 20 TeV protons incident on 5.0m radius solid concrete (left & bottom axes) or soil (right & bottom axes) cylinder. The calculation has a cut-off momentum of 0.3 GeV/c.

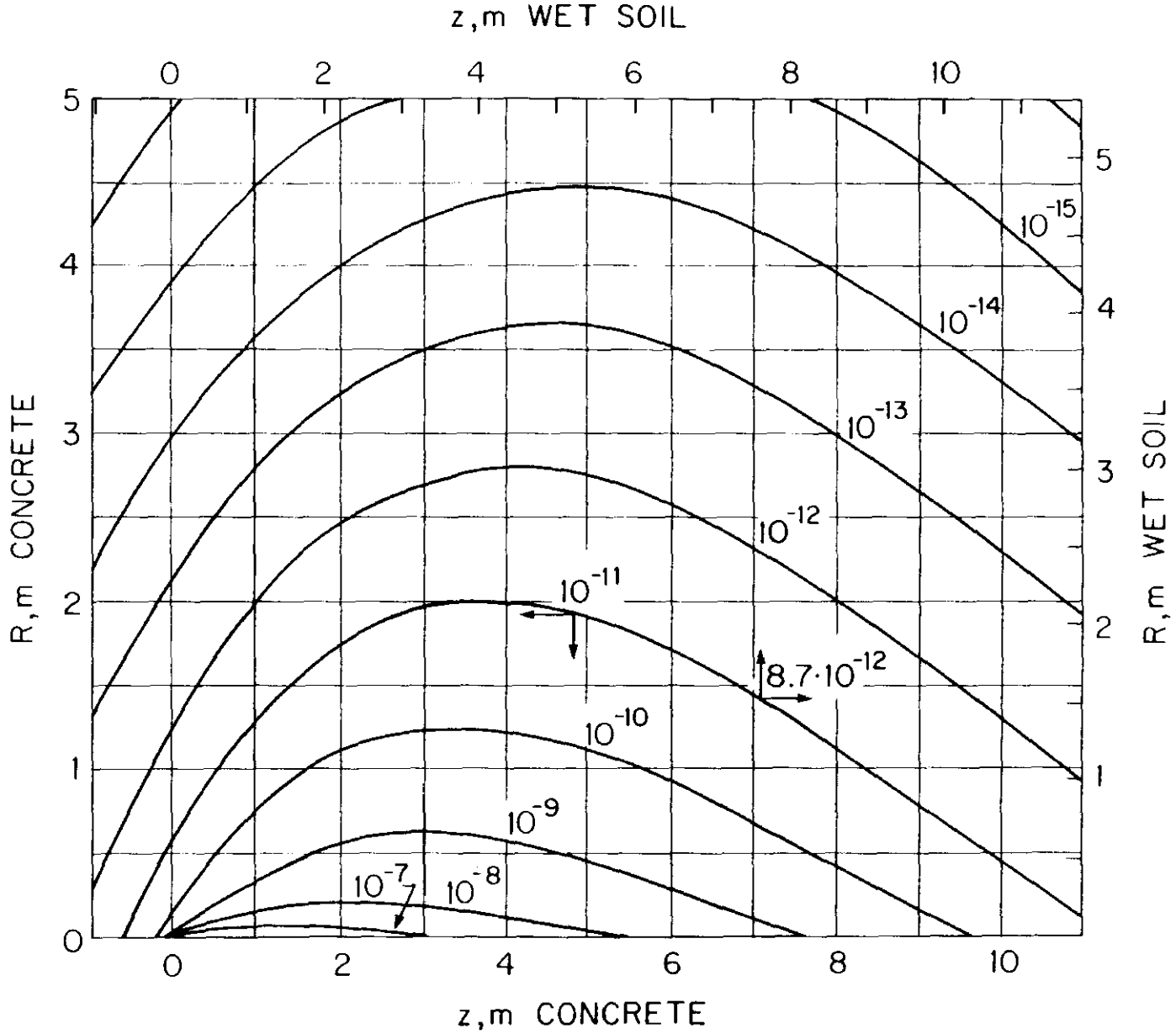

Fig. 11. Contours of equal dose equivalent (in rem/incident proton) for 5 TeV protons incident on solid concrete/soil cylinder. The beam has a bi-Gaussian spatial distribution with $\sigma_x = \sigma_y = 0.1$cm and is parallel to and centered on the cylinder axis. The beam starts interacting at zero depth. Contours for concrete (left & bottom axes) are integral powers of ten. Contours for (wet) soil (right & top axes) must be scaled down by 0.87 as shown for one example. Some contours may be omitted for clarity or due to statistical uncertainty.

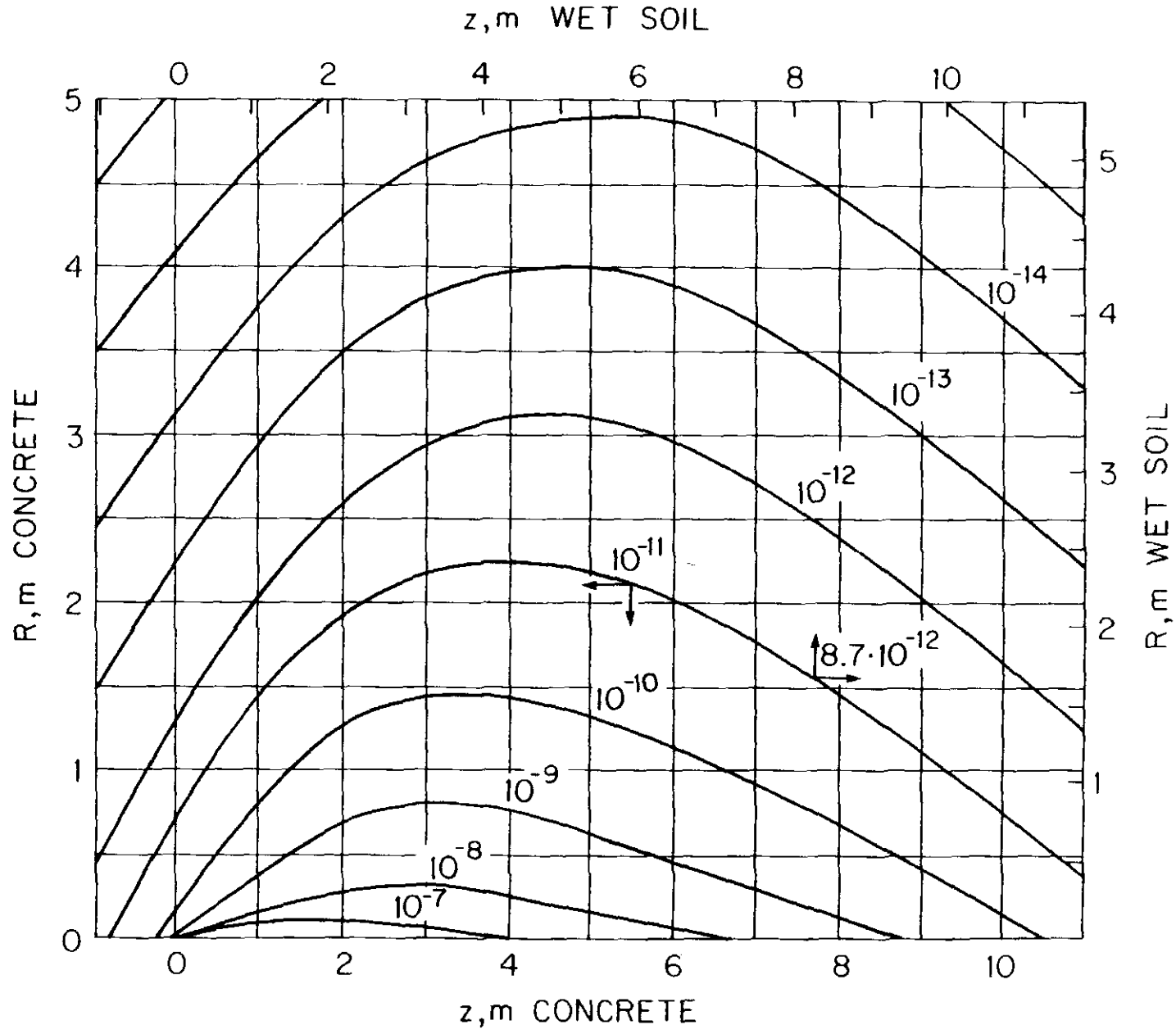

Fig. 12. Contours of equal dose equivalent (in rem/incident proton) for 10 TeV protons incident on solid concrete/soil cylinder. The beam has a bi-Gaussian spatial distribution with $\sigma_x = \sigma_y = 0.1$cm and is parallel to and centered on the cylinder axis. The beam starts interacting at zero depth. Contours for concrete (left & bottom axes) are integral powers of ten. Contours for (wet) soil (right & top axes) must be scaled down by 0.87 as shown for one example. Some contours may be omitted for clarity or due to statistical uncertainty.

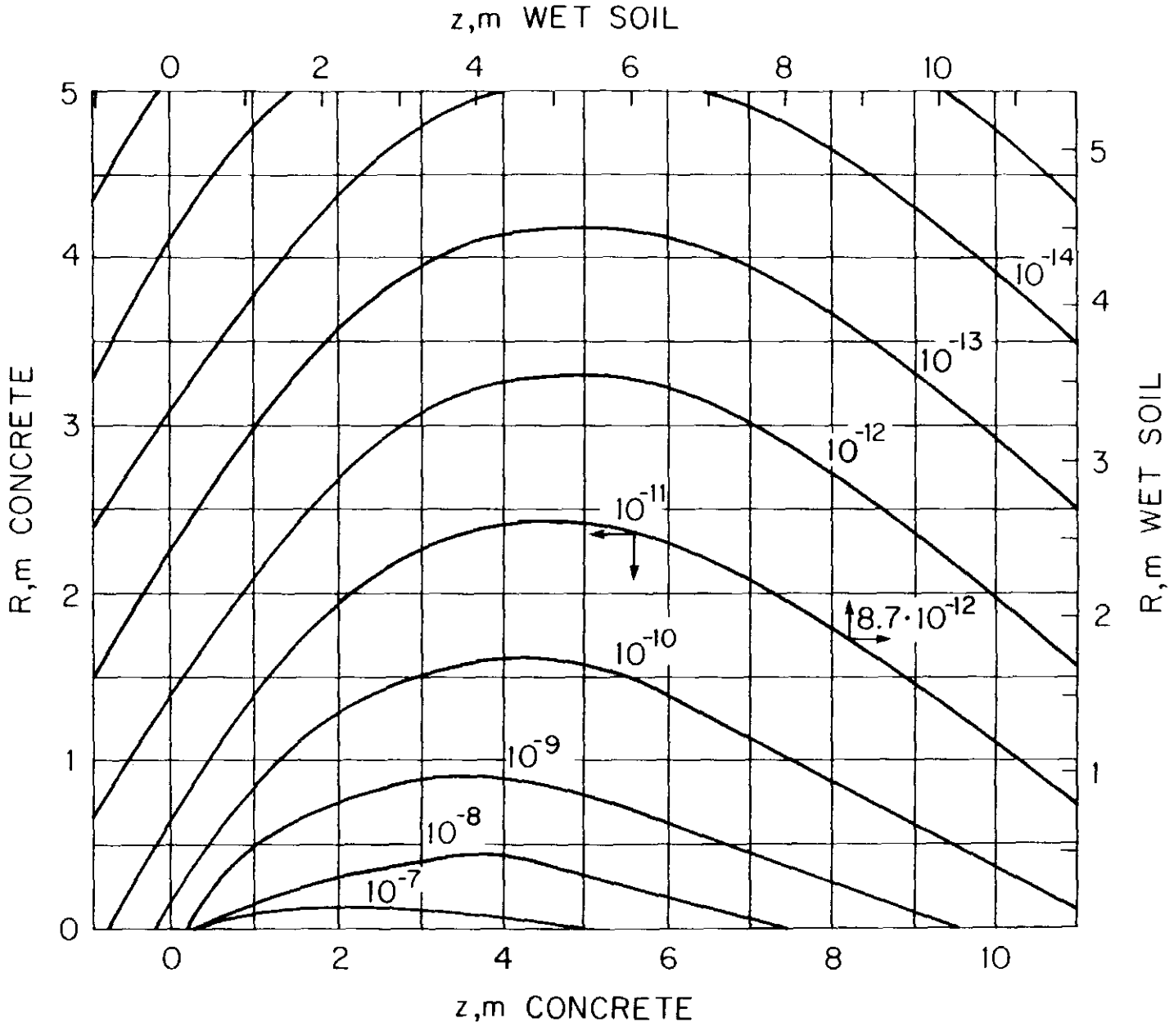

Fig. 13. Contours of equal dose equivalent (in rem/incident proton) for 20 TeV protons incident on solid concrete/soil cylinder. The beam has a bi-Gaussian spatial distribution with $\sigma_x = \sigma_y = 0.1$cm and is parallel to and centered on the cylinder axis. The beam starts interacting at zero depth. Contours for concrete (left & bottom axes) are integral powers of ten. Contours for (wet) soil (right & top axes) must be scaled down by 0.87 as shown for one example. Some contours may be omitted for clarity or due to statistical uncertainty.

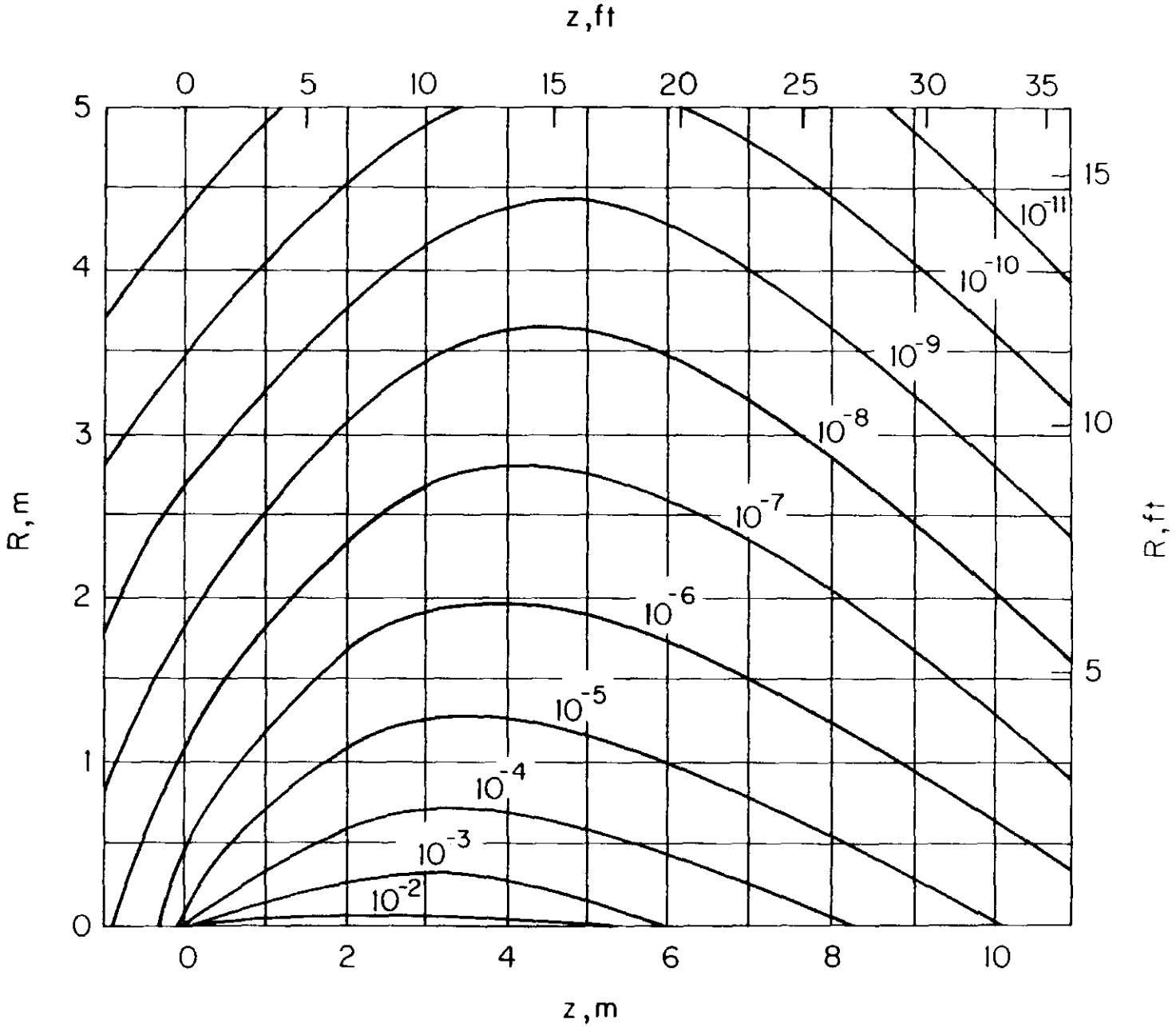

Fig. 14. Contours of equal star density (in stars/cm^3•incident proton) for 5 TeV protons incident on solid aluminum cylinder. The beam has a bi-Gaussian spatial distribution with $\sigma_x=\sigma_y=0.1$cm and is parallel to and centered on the cylinder axis. The beam starts interacting at zero depth. The calculation has a cut-off momentum of 0.3 GeV/c. Some contours may be omitted for clarity or due to statistical uncertainty.

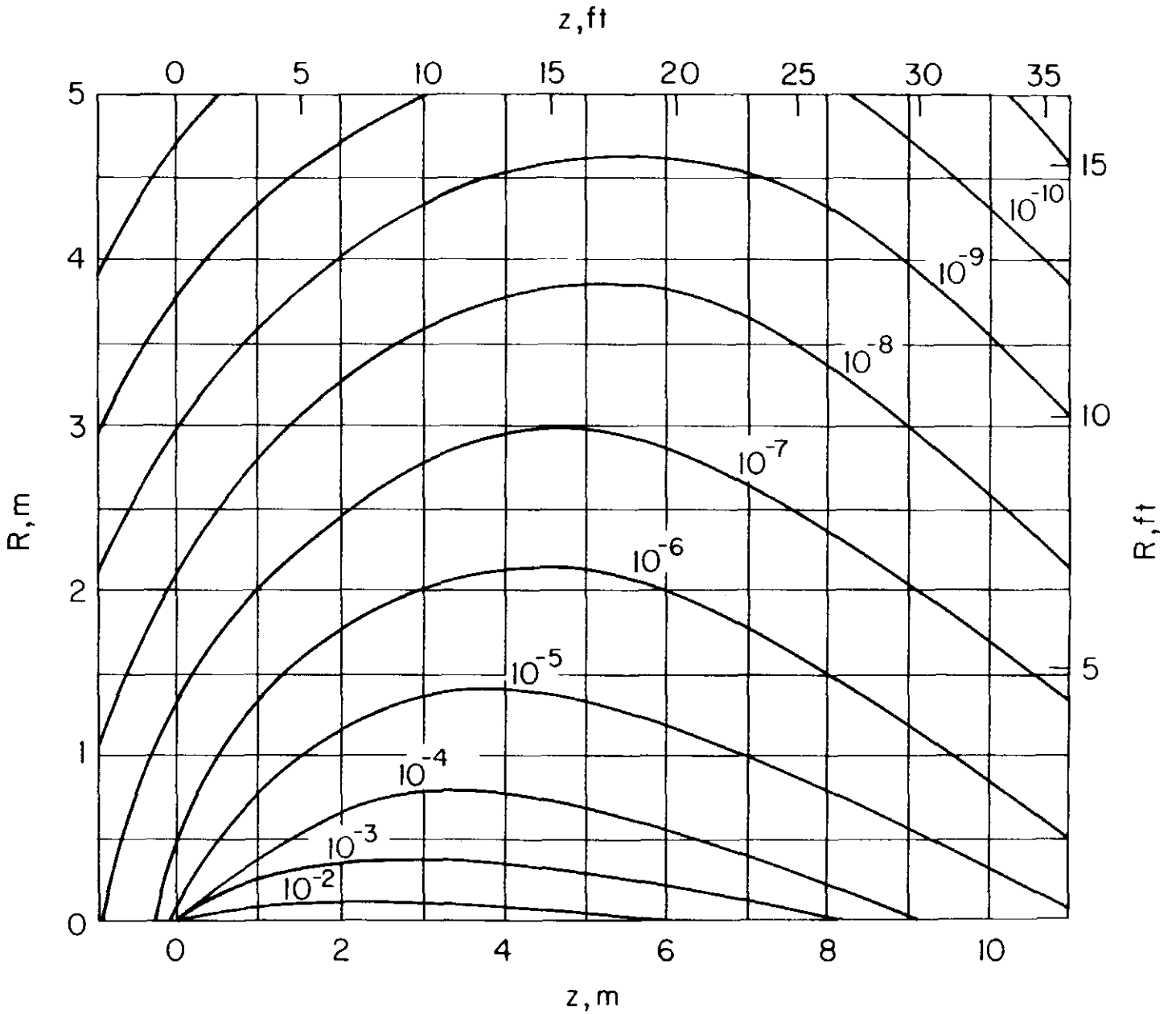

Fig. 15. Contours of equal star density (in stars/cm^3•incident proton) for 10 TeV protons incident on solid aluminum cylinder. The beam has a bi-Gaussian spatial distribution with $\sigma_x=\sigma_y=0.1$cm and is parallel to and centered on the cylinder axis. The beam starts interacting at zero depth. The calculation has a cut-off momentum of 0.3 GeV/c. Some contours may be omitted for clarity or due to statistical uncertainty.

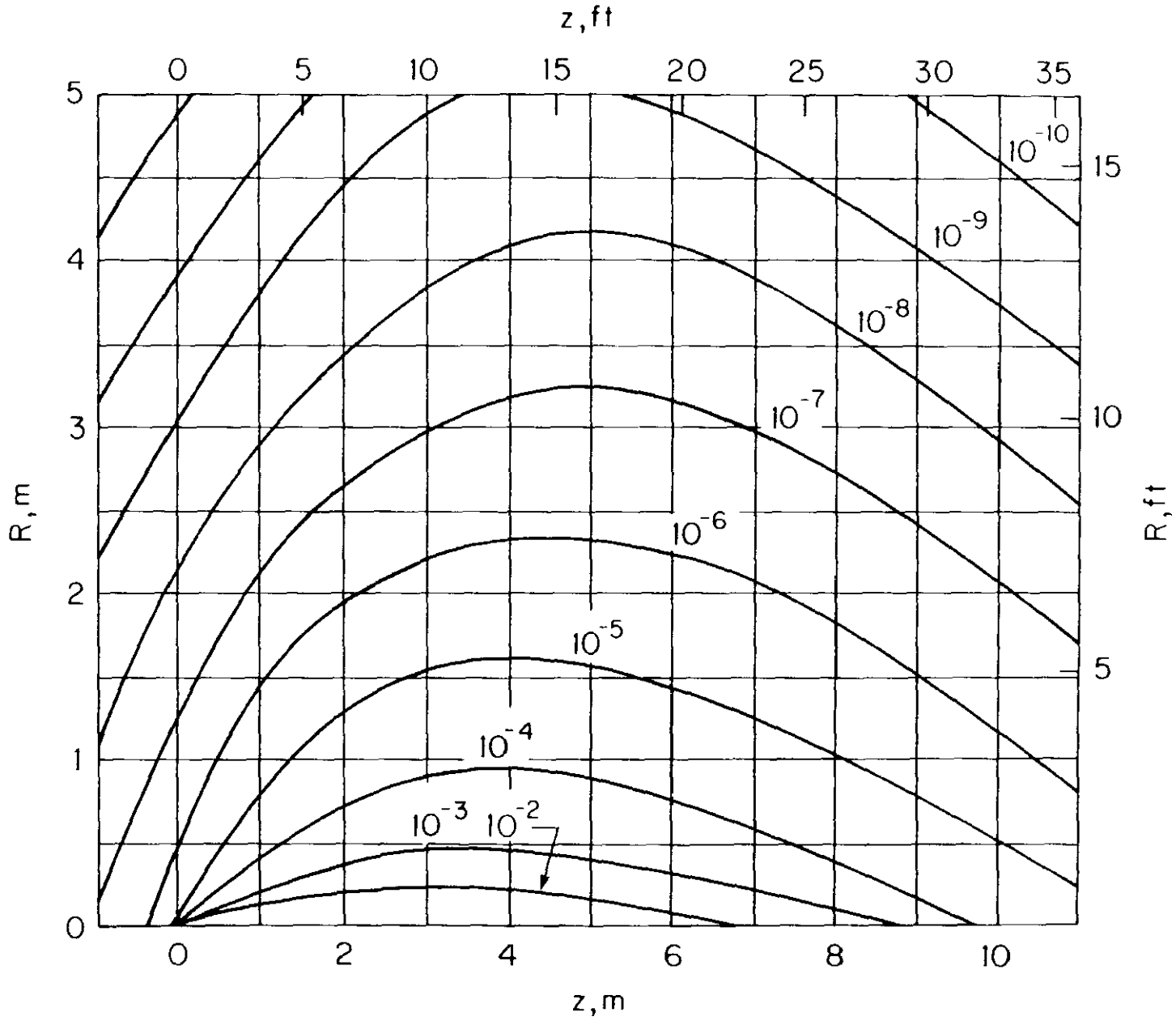

Fig. 16. Contours of equal star density (in stars/cm^3•incident proton) for 20 TeV protons incident on solid aluminum cylinder. The beam has a bi-Gaussian spatial distribution with $\sigma_x=\sigma_y=0.1$cm and is parallel to and centered on the cylinder axis. The beam starts interacting at zero depth. The calculation has a cut-off momentum of 0.3 GeV/c. Some contours may be omitted at high star density for clarity and at low star density due to statistical uncertainty.

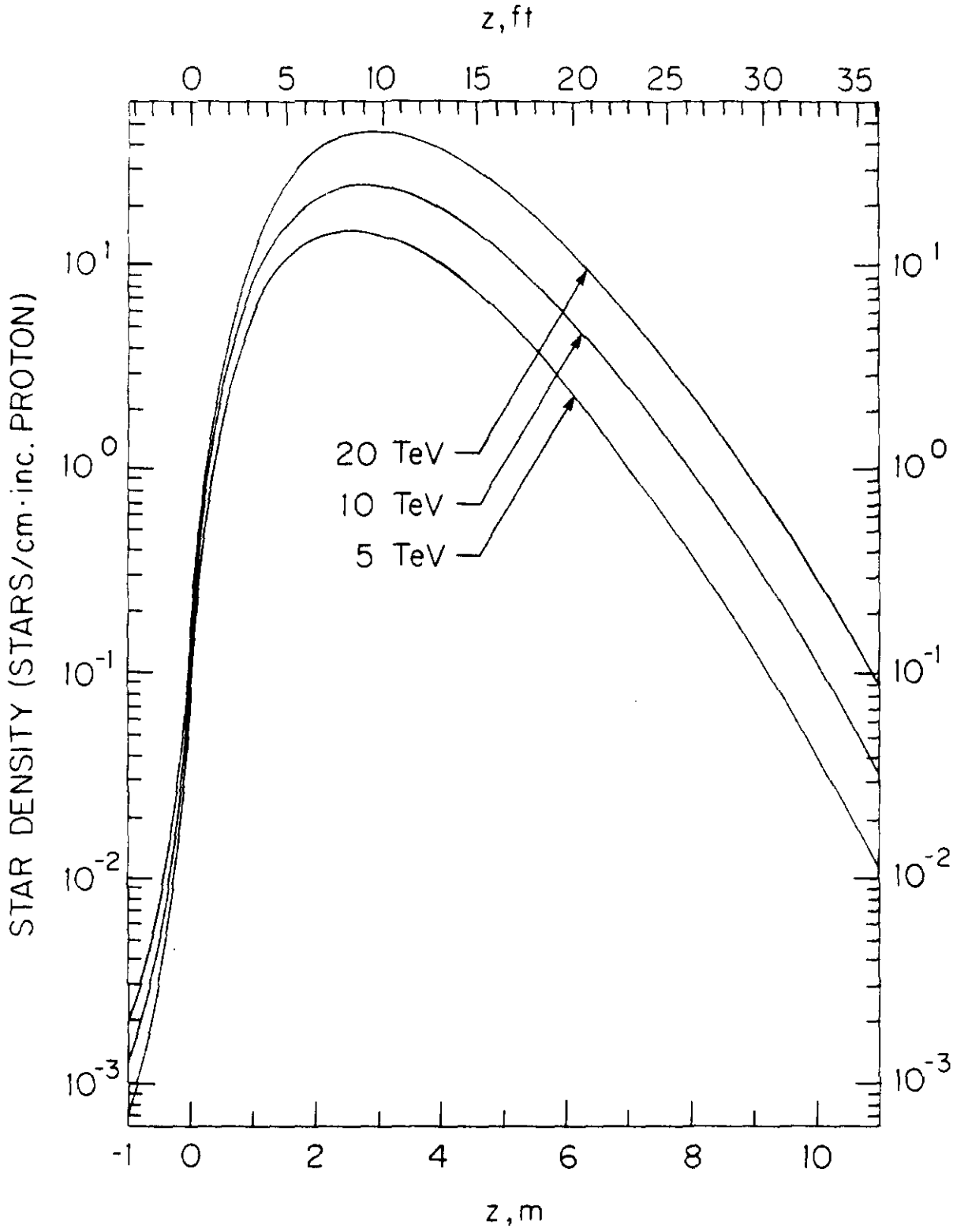

Fig. 17. Radially integrated star density (in stars/cm•incident proton) for 5, 10 and 20 TeV protons incident on 12m long solid aluminum cylinder. The calculation has a cut-off momentum of 0.3 GeV/c. The protons begin interacting at zero depth.

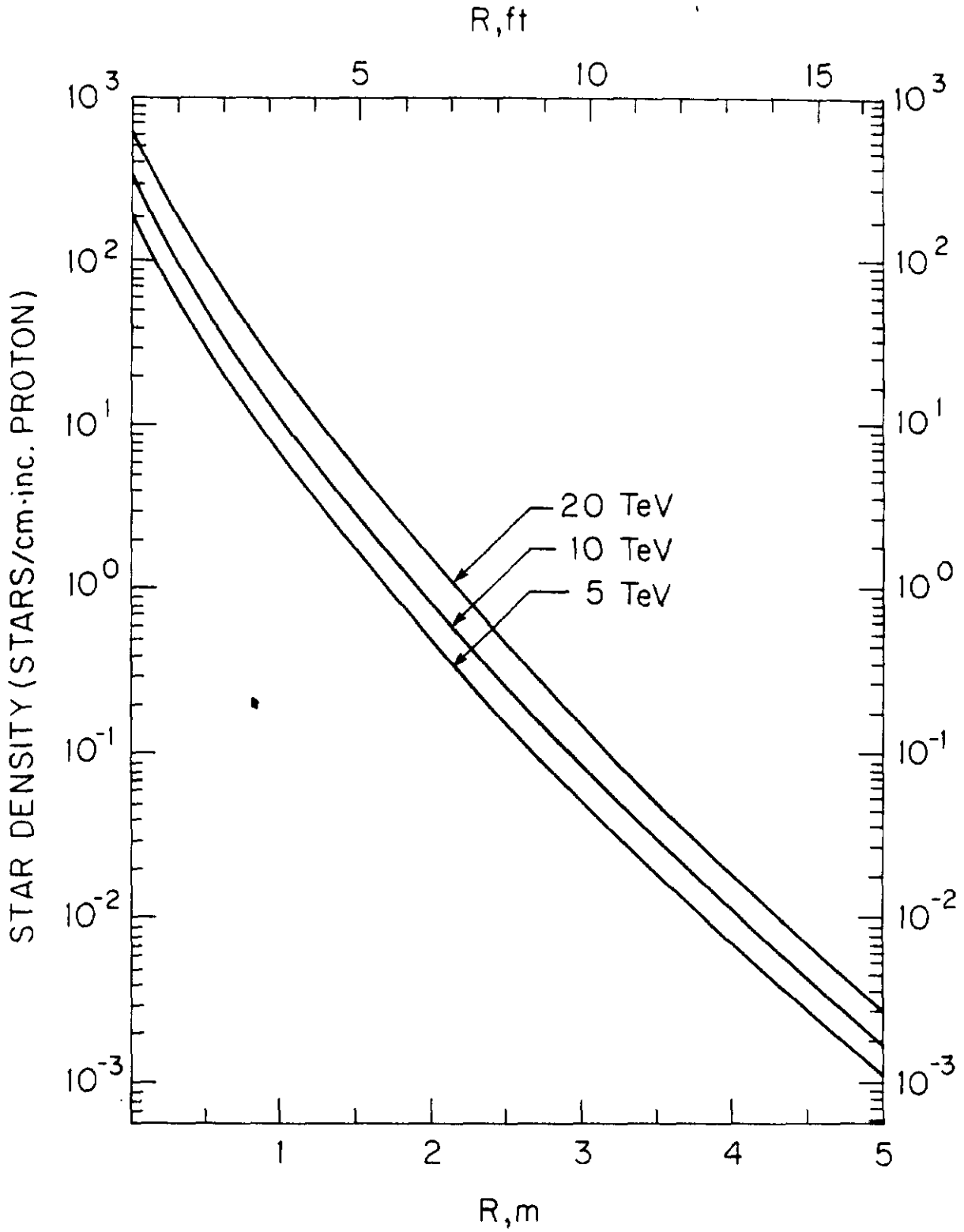

Fig. 18. Longitudinally integrated star density (in stars/cm•incident proton) for 5, 10 and 20 TeV protons incident on 5.0m radius solid aluminum cylinder. The calculation has a cut-off momentum of 0.3 GeV/c.

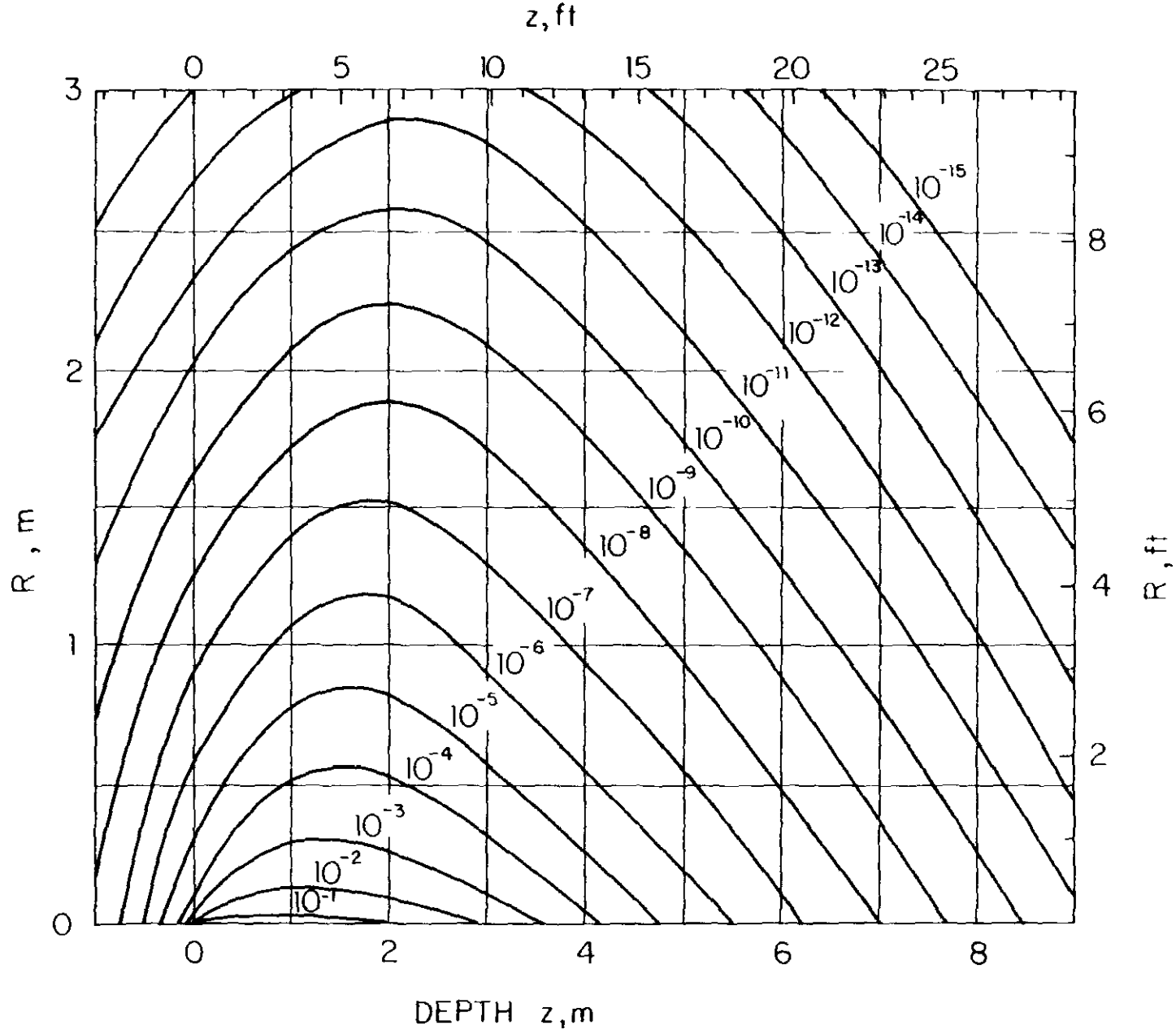

Fig. 19. Contours of equal star density (in stars/cm^3•incident proton) for 5 TeV protons incident on solid iron cylinder. The beam has a bi-Gaussian spatial distribution with $\sigma_x=\sigma_y=0.1$cm and is parallel to and centered on the cylinder axis. The beam starts interacting at zero depth. The calculation has a cut-off momentum of 0.3 GeV/c. Some contours may be omitted for clarity or due to statistical uncertainty.

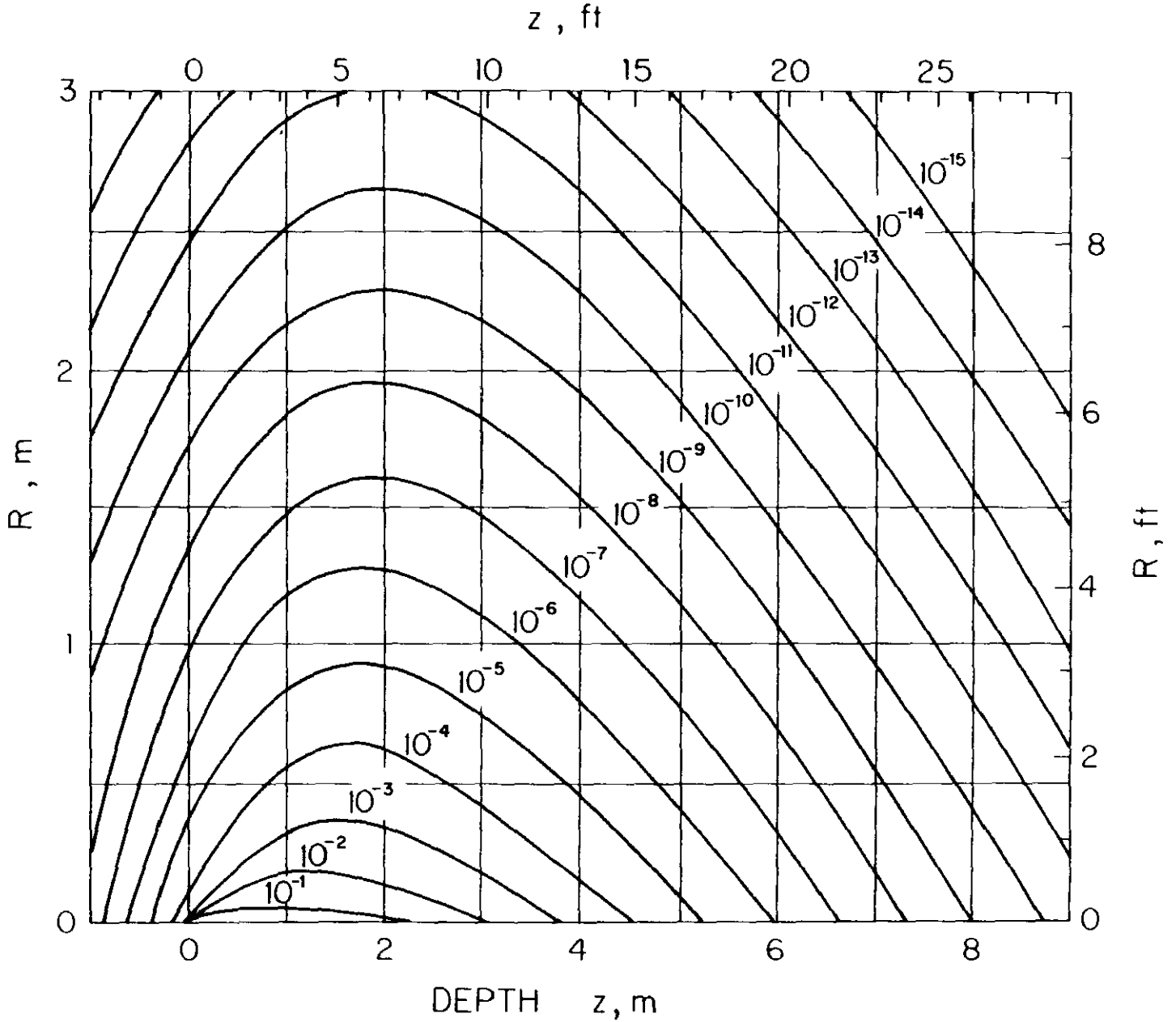

Fig. 20. Contours of equal star density (in stars/cm^3•incident proton) for 10 TeV protons incident on solid iron cylinder. The beam has a bi-Gaussian spatial distribution with $\sigma_x = \sigma_y = 0.1$cm and is parallel to and centered on the cylinder axis. The beam starts interacting at zero depth. The calculation has a cut-off momentum of 0.3 GeV/c. Some contours may be omitted for clarity or due to statistical uncertainty.

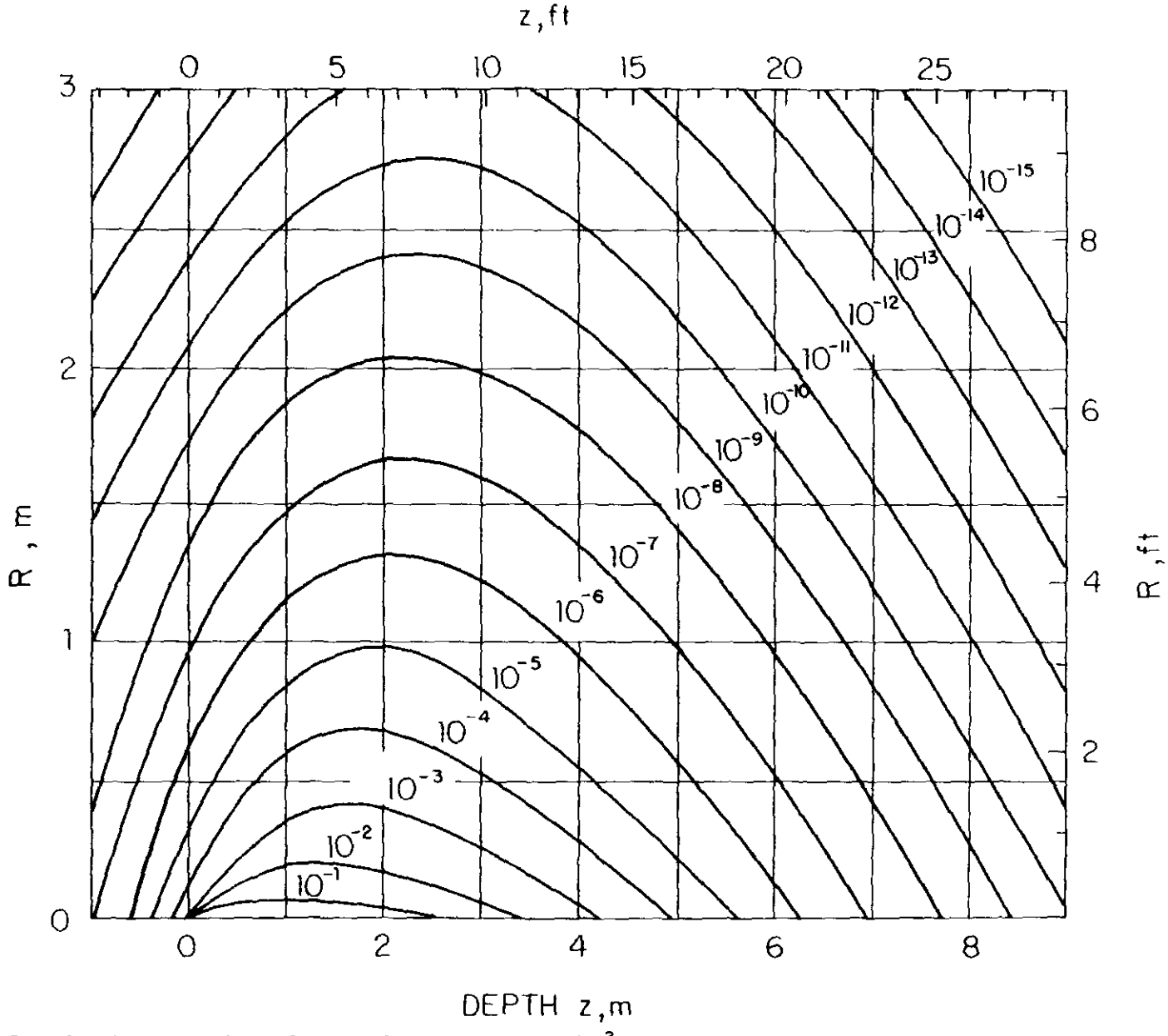

Fig. 21. Contours of equal star density (in stars/cm^3•incident proton) for 20 TeV protons incident on solid iron cylinder. The beam has a bi-Gaussian spatial distribution with $\sigma_x=\sigma_y=0.1$cm and is parallel to and centered on the cylinder axis. The beam starts interacting at zero depth. The calculation has a cut-off momentum of 0.3 GeV/c. Some contours may be omitted for clarity or due to statistical uncertainty.

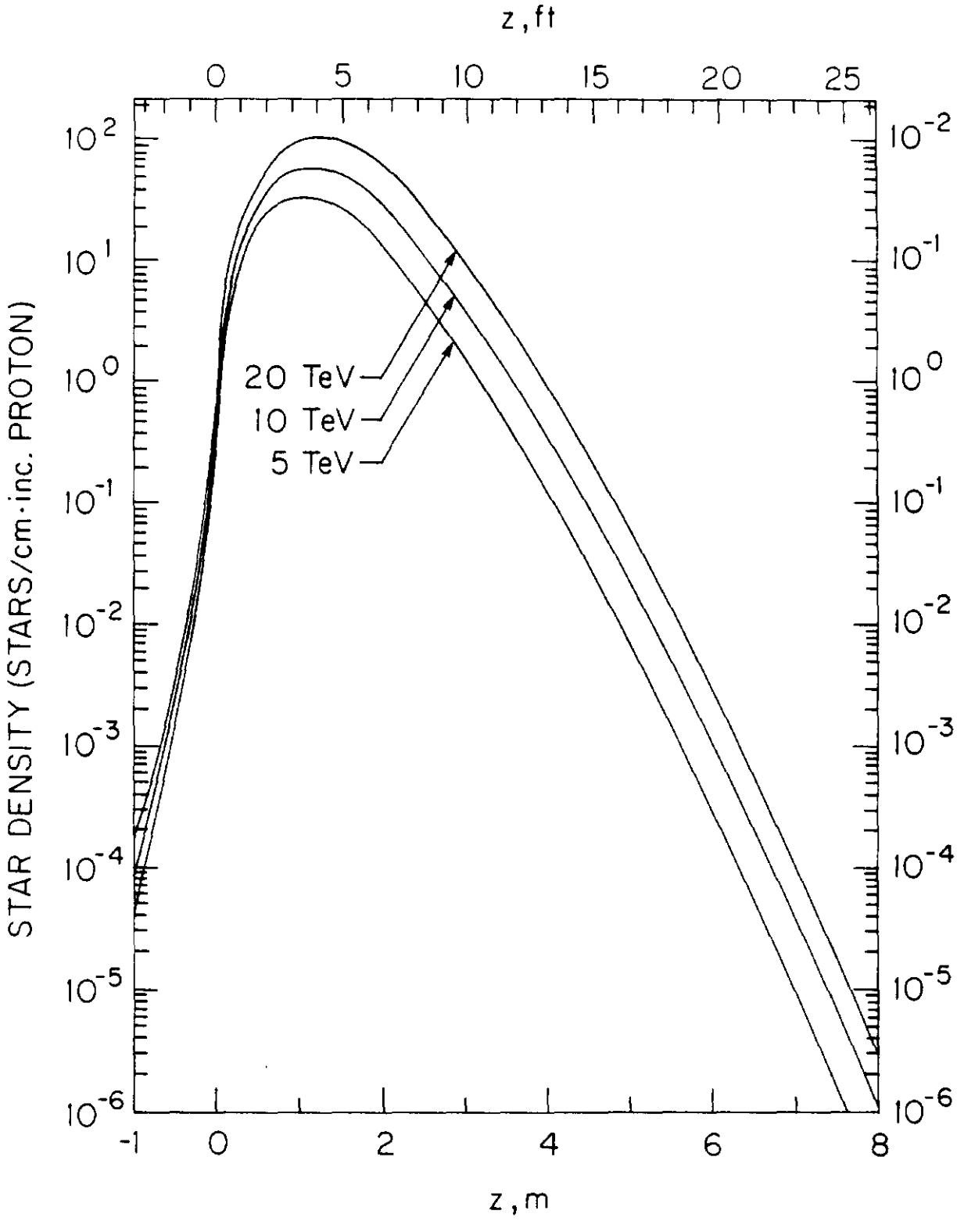

Fig. 22. Radially integrated star density (in stars/cm•incident proton) for 5, 10 and 20 TeV protons incident on 12m long solid iron cylinder. The calculation has a cut-off momentum of 0.3 GeV/c. The protons begin interacting at zero depth.

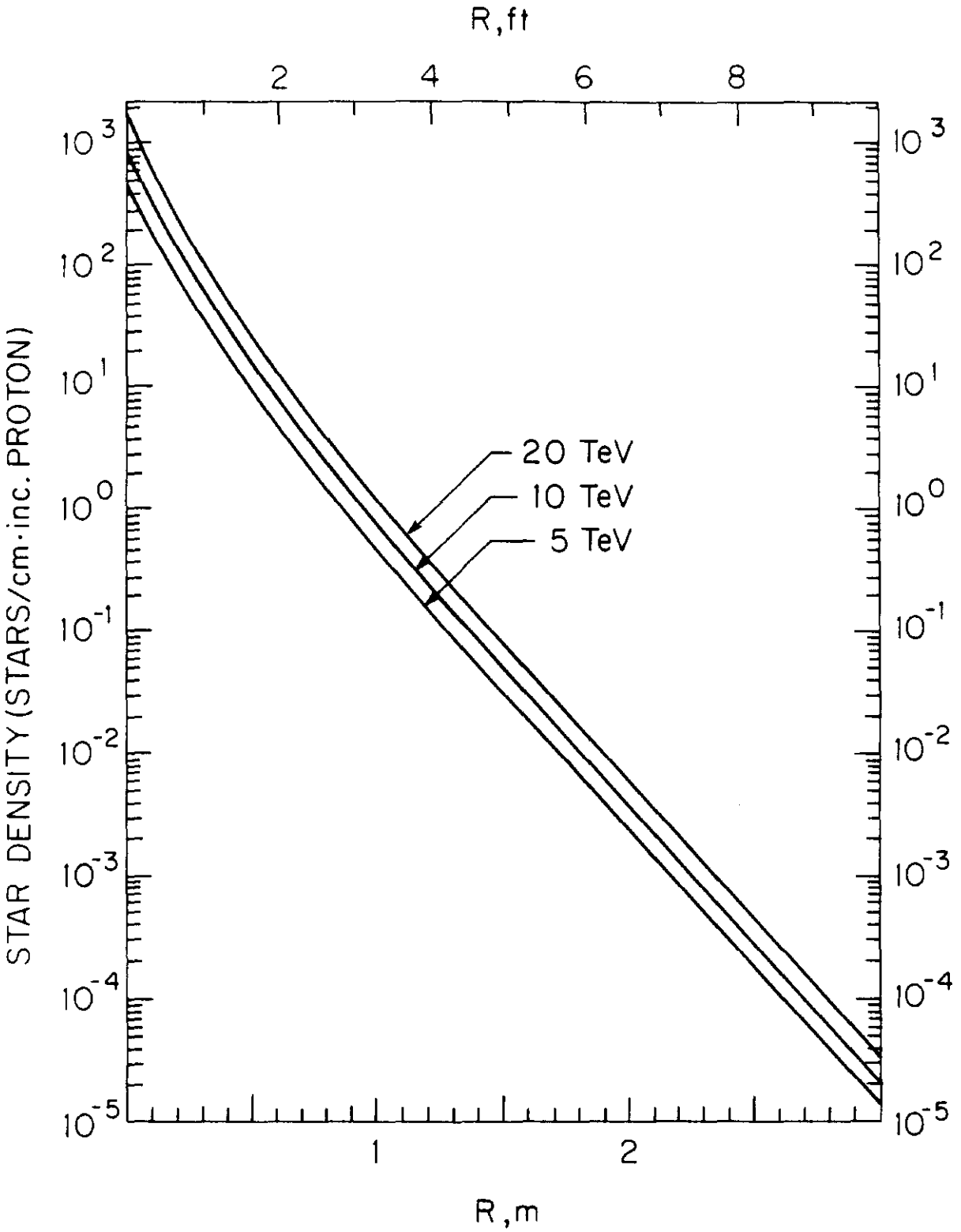

Fig. 23. Longitudinally integrated star density (in stars/cm•incident proton) for 5, 10 and 20 TeV protons incident on 5.0m radius solid iron cylinder. The calculation has a cut-off momentum of 0.3 GeV/c.

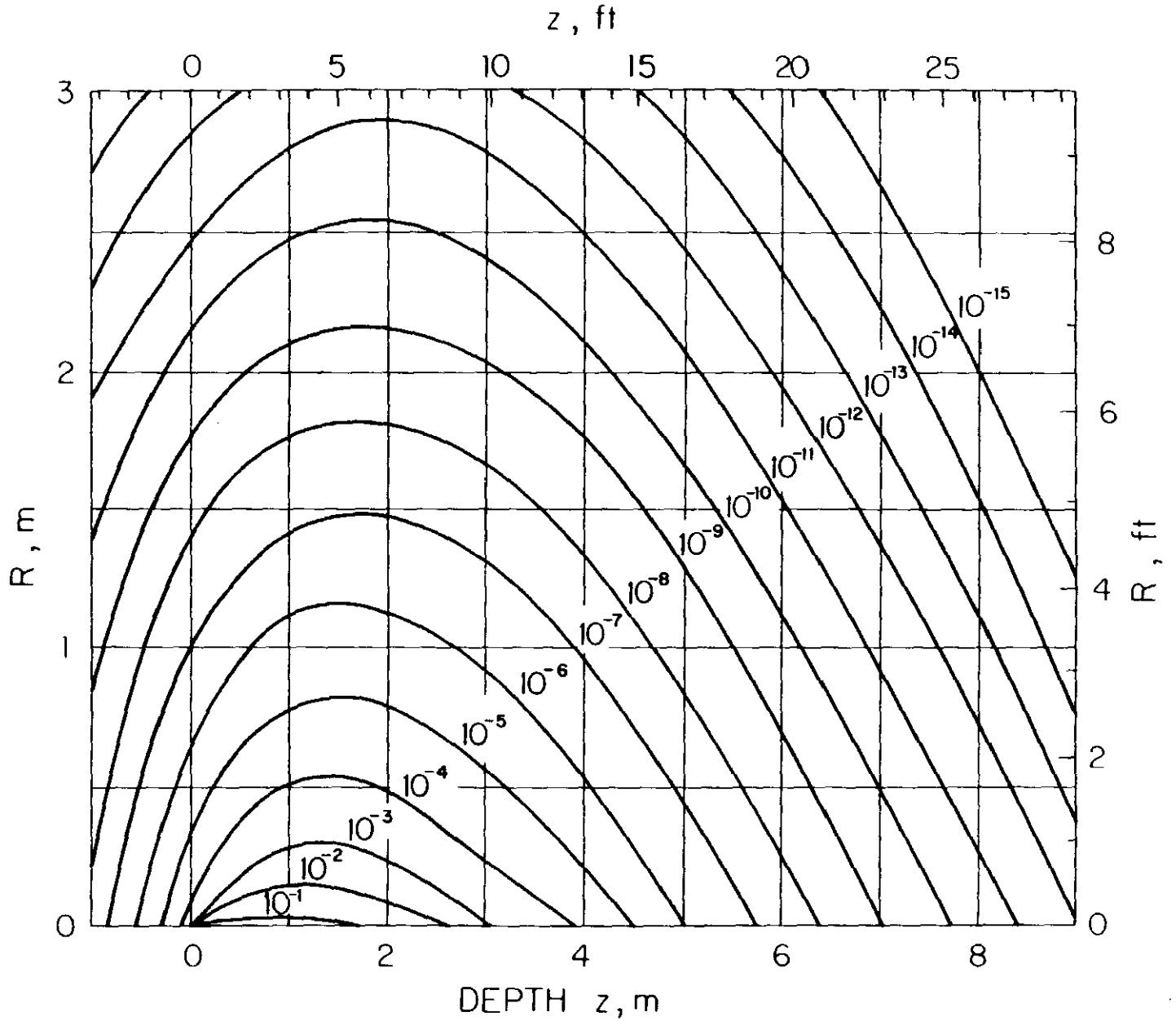

Fig. 24. Contours of equal star density (in stars/cm^3•incident proton) for 5 TeV protons incident on solid lead cylinder. The beam has a bi-Gaussian spatial distribution with $\sigma_x=\sigma_y=0.1$cm and is parallel to and centered on the cylinder axis. The beam starts interacting at zero depth. The calculation has a cut-off momentum of 0.3 GeV/c. Some contours may be omitted for clarity or due to statistical uncertainty.

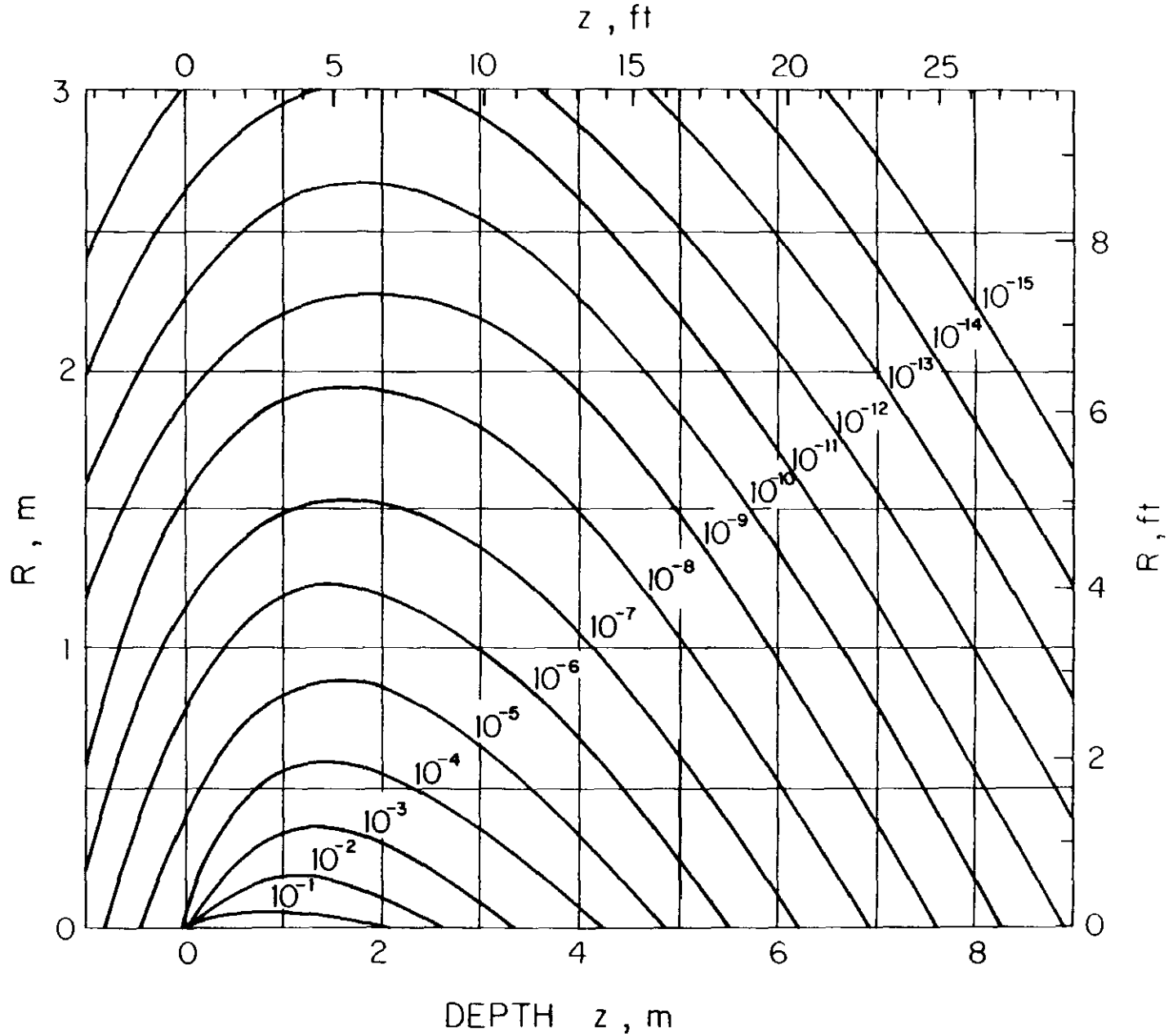

Fig. 25. Contours of equal star density (in stars/cm^3•incident proton) for 10 TeV protons incident on solid lead cylinder. The beam has a bi-Gaussian spatial distribution with $\sigma_x=\sigma_y=0.1$cm and is parallel to and centered on the cylinder axis. The beam starts interacting at zero depth. The calculation has a cut-off momentum of 0.3 GeV/c. Some contours may be omitted for clarity or due to statistical uncertainty.

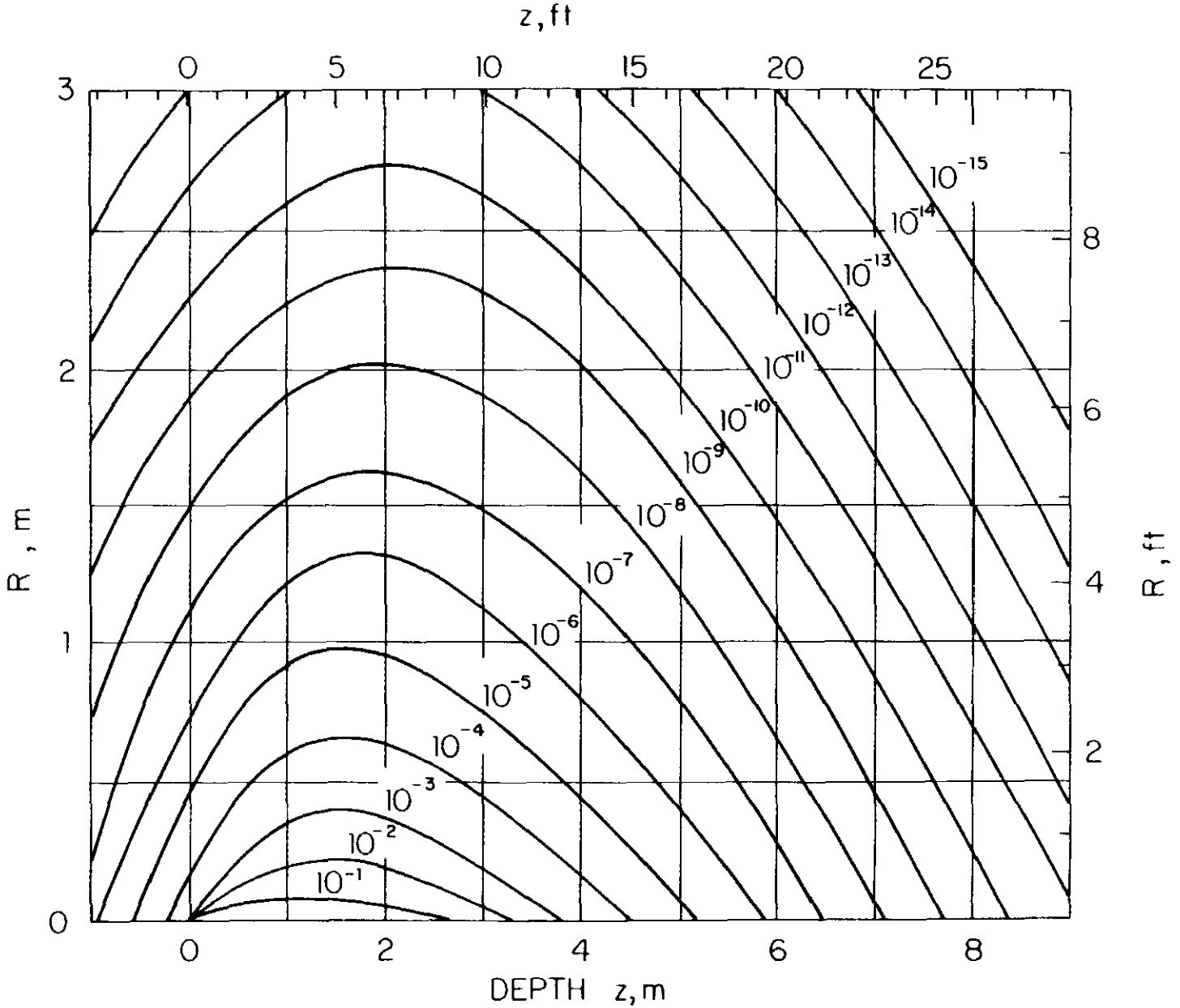

Fig. 26. Contours of equal star density (in stars/cm^3•incident proton) for 20 TeV protons incident on solid lead cylinder. The beam has a bi-Gaussian spatial distribution with $\sigma_x=\sigma_y=0.1$cm and is parallel to and centered on the cylinder axis. The beam starts interacting at zero depth. The calculation has a cut-off momentum of 0.3 GeV/c. Some contours may be omitted for clarity or due to statistical uncertainty.

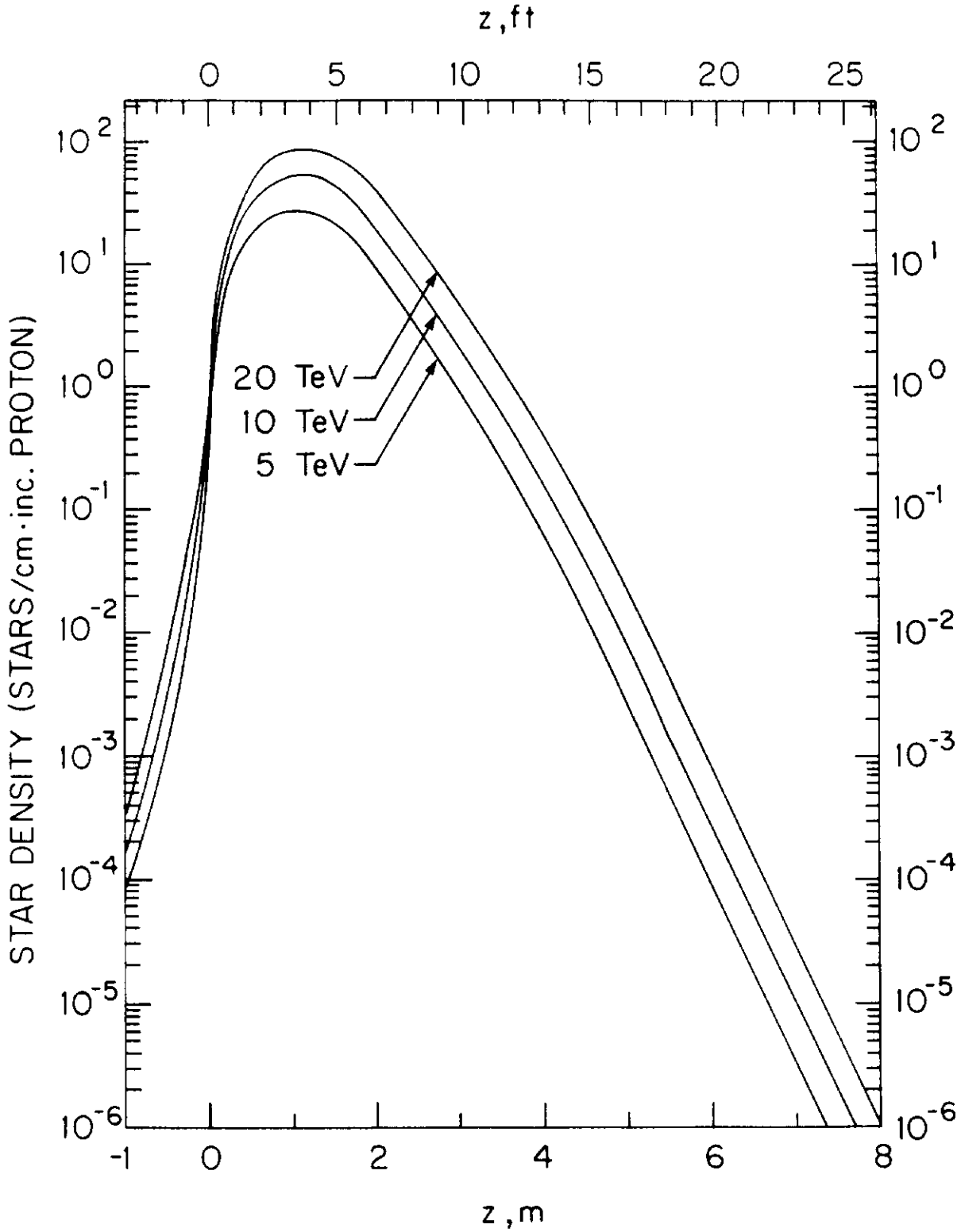

Fig. 27. Radially integrated star density (in stars/cm•incident proton) for 5, 10 and 20 TeV protons incident on 12m long solid lead cylinder. The calculation has a cut-off momentum of 0.3 GeV/c. The protons begin interacting at zero depth.

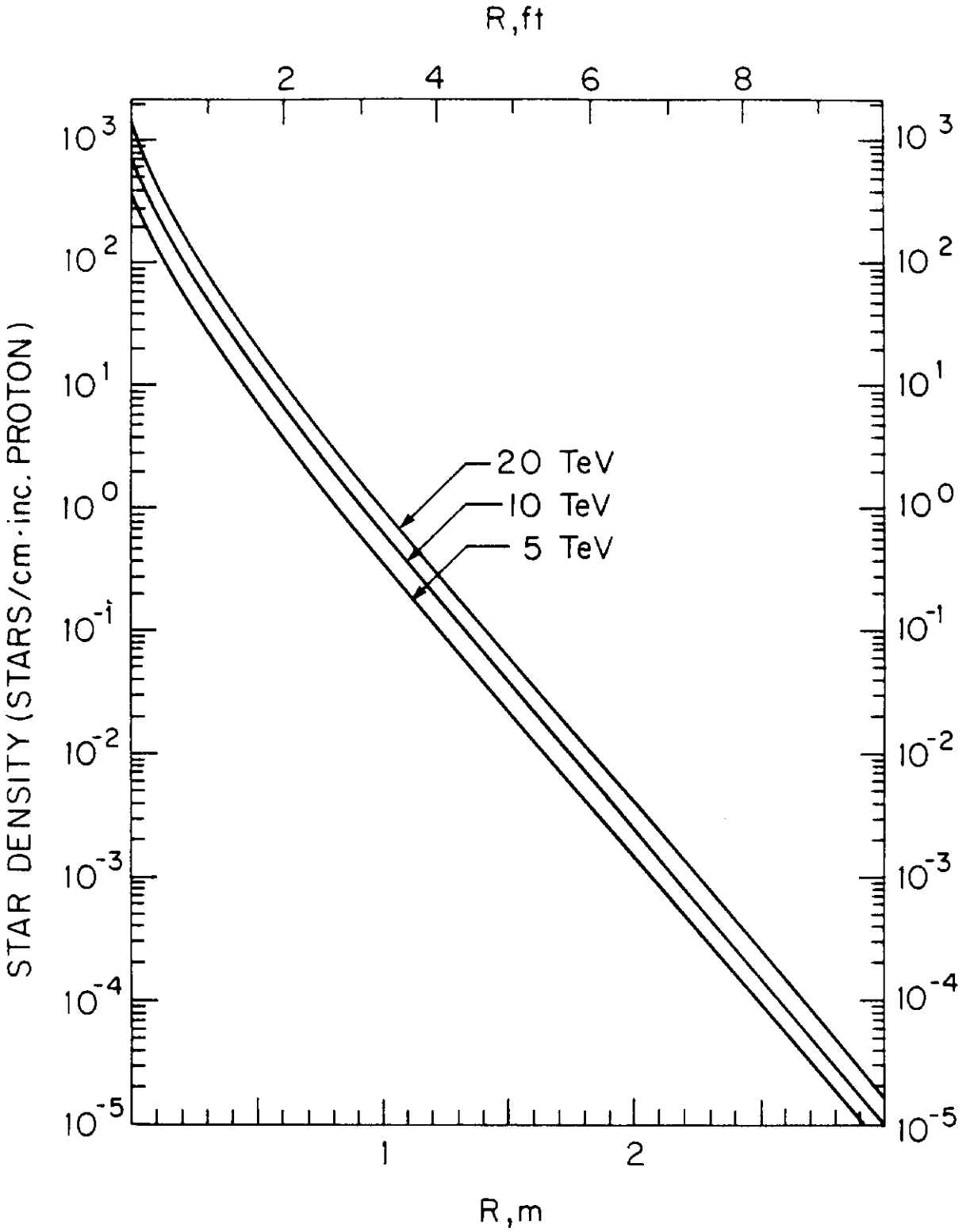

Fig. 28. Longitudinally integrated star density (in stars/cm•incident proton) for 5, 10 and 20 TeV protons incident on 5.0m radius solid lead cylinder. The calculation has a cut-off momentum of 0.3 GeV/c.

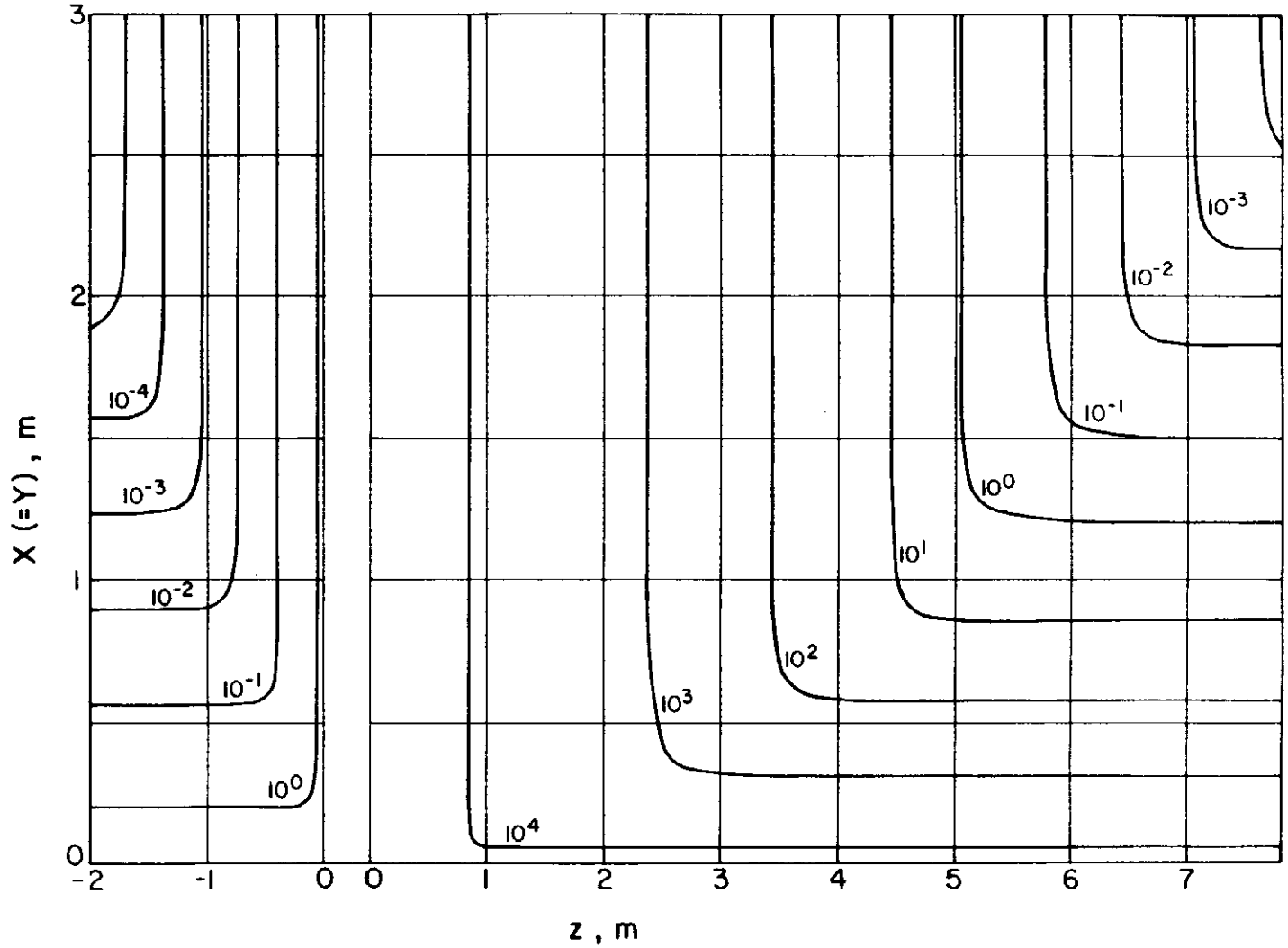

Fig. 29. Contours of equal total star production in (wet) soil (in stars/incident proton) outside solid iron block of dimensions 2x, 2y(=2x) and z in meter by 20 TeV protons. The beam has a bi-Gaussian spatial distribution with $\sigma_x = \sigma_y = 0.1$cm and is parallel to and centered on the axis of the block. The beam starts interacting at zero depth. The calculation has a cut-off momentum of 0.3 GeV/c.

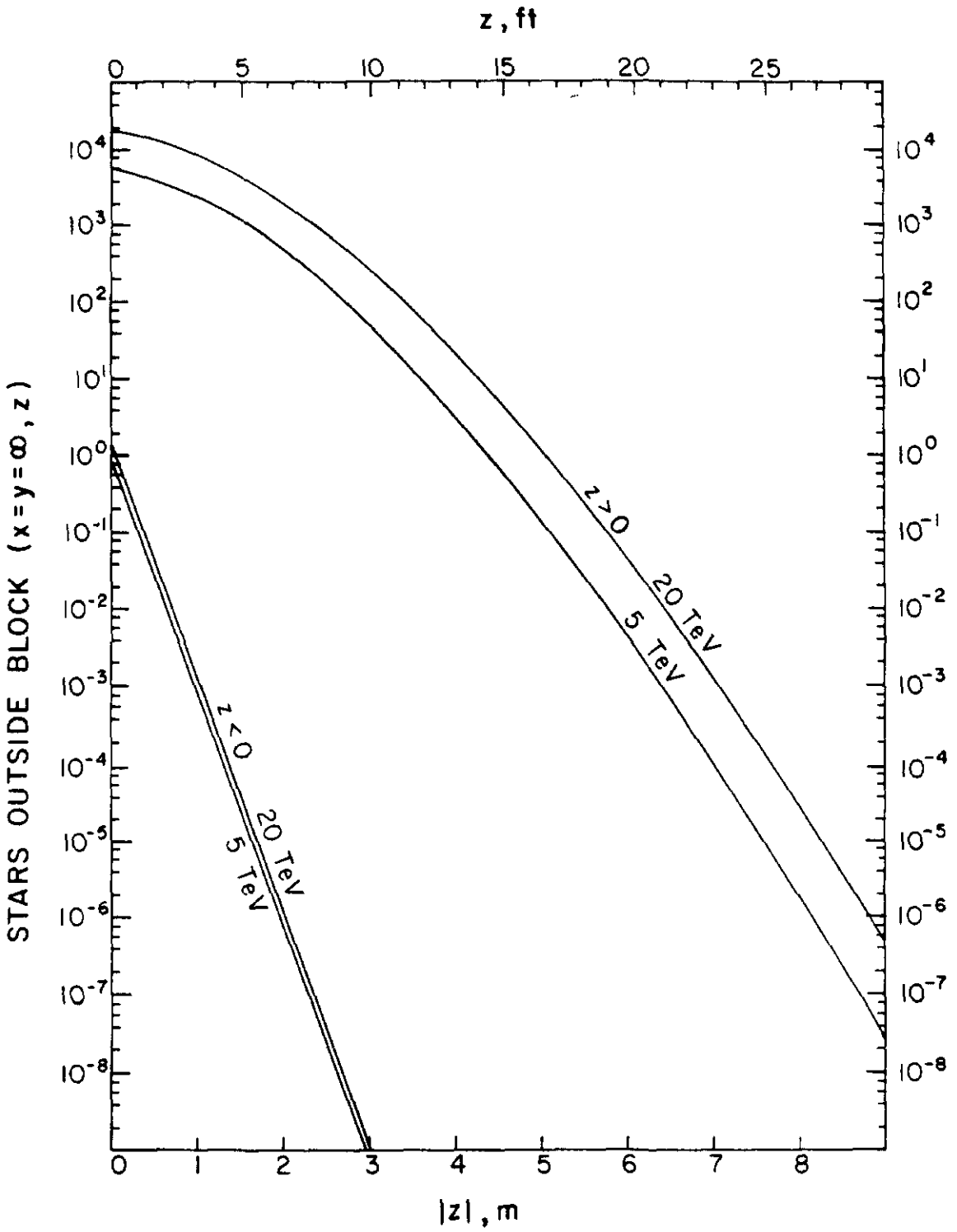

Fig. 30. Stars in soil (in stars/incident proton) outside infinitely wide solid iron block as a function of length of the block. The block has finite length either for z<0 or for z>0 and is infinitely long in the opposite direction. The calculation has a cut-off momentum of 0.3 GeV/c.

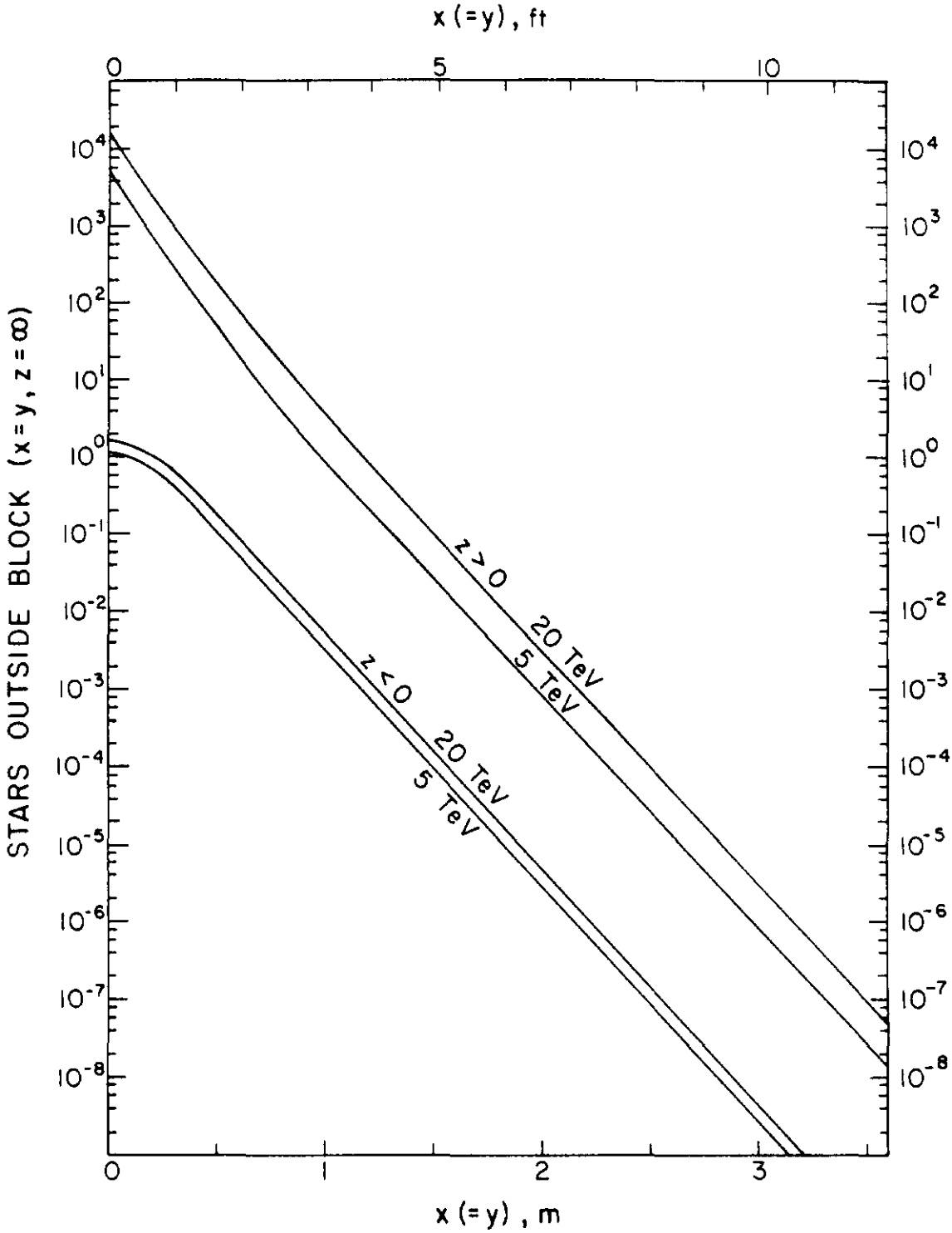

Fig. 31. Stars in soil (in stars/incident proton) outside infinitely long solid iron block as a function of length of the block. The block has finite width either for z<0 or for z>0 [x(=y) is the half width] and is infinitely wide in the other half-space. The calculation has a cut-off momentum of 0.3 GeV/c.

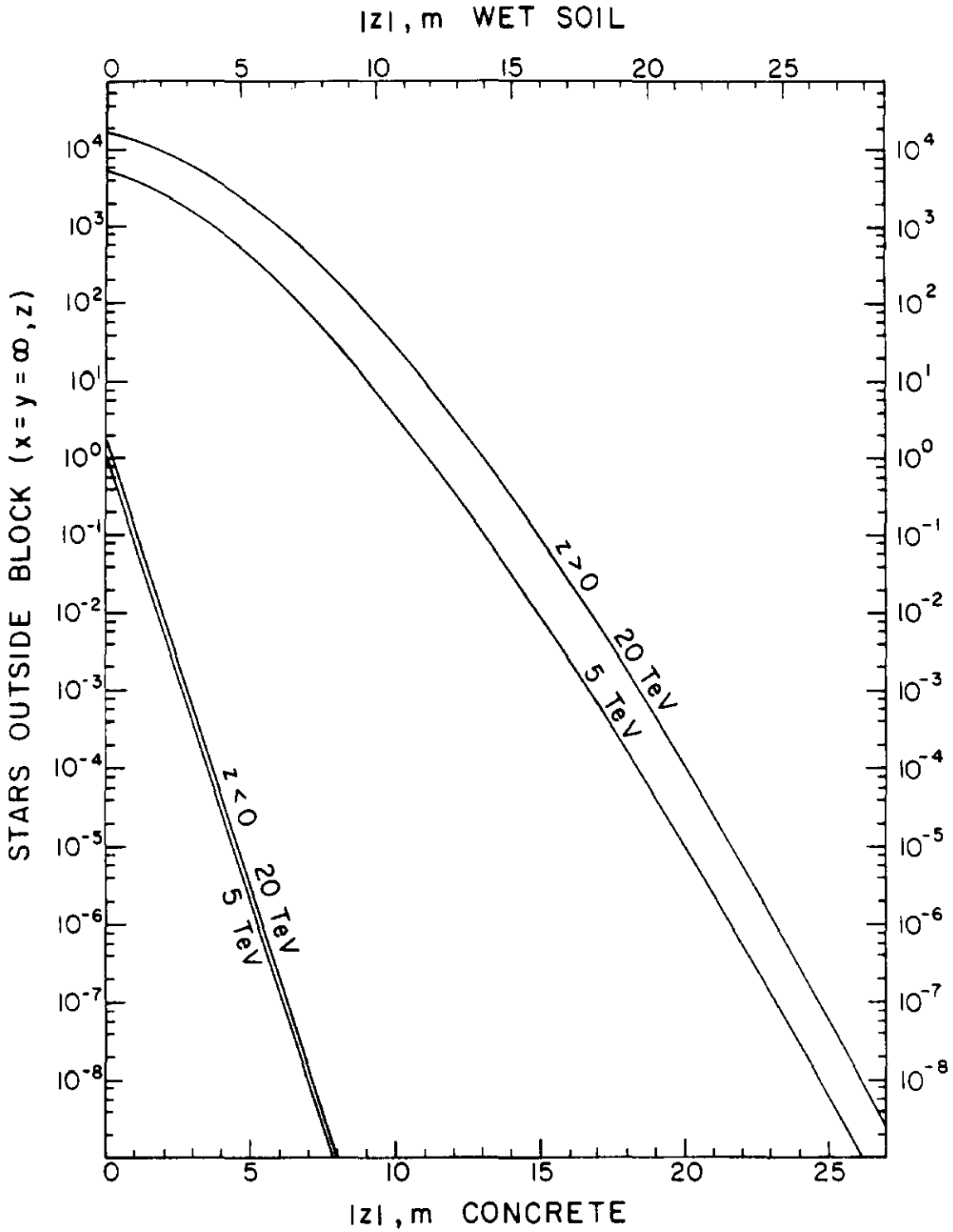

Fig. 32. Stars in soil (in stars/incident proton) outside infinitely wide solid concrete (bottom scale) or wet soil (top scale) block as a function of length of the block. The block has finite length either for $z<0$ or for $z>0$ and is infinitely long in the opposite direction. The calculation has a cut-off momentum of 0.3 GeV/c.

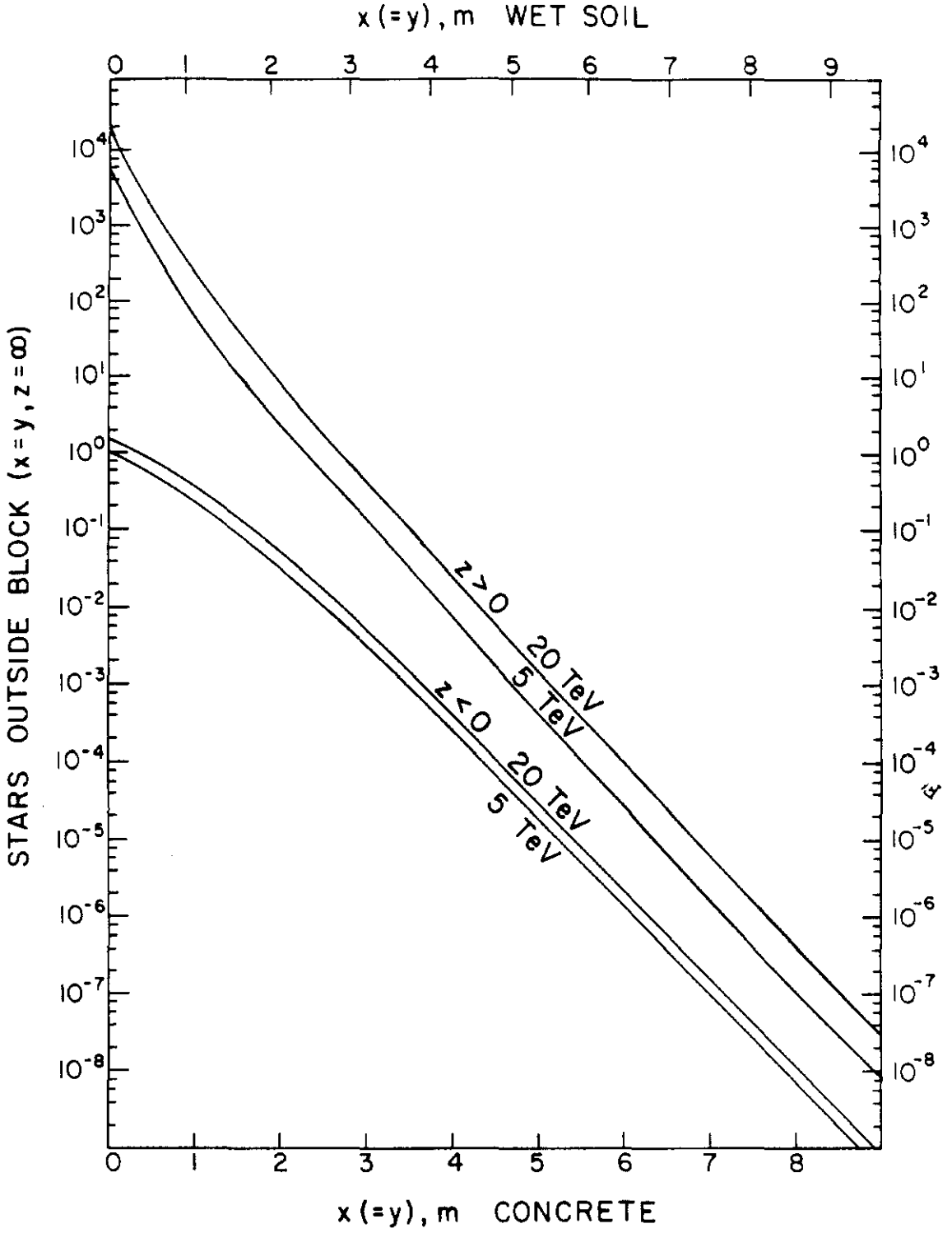

Fig. 33. Stars in soil (in stars/incident proton) outside infinitely long solid concrete (bottom scale) or wet soil (top scale) block as a function of length of the block. The block has finite width either for z<0 or for z>0 [x(=y) is the half width] and is infinitely wide in the other half-space. The calculation has a cut-off momentum of 0.3 GeV/c.

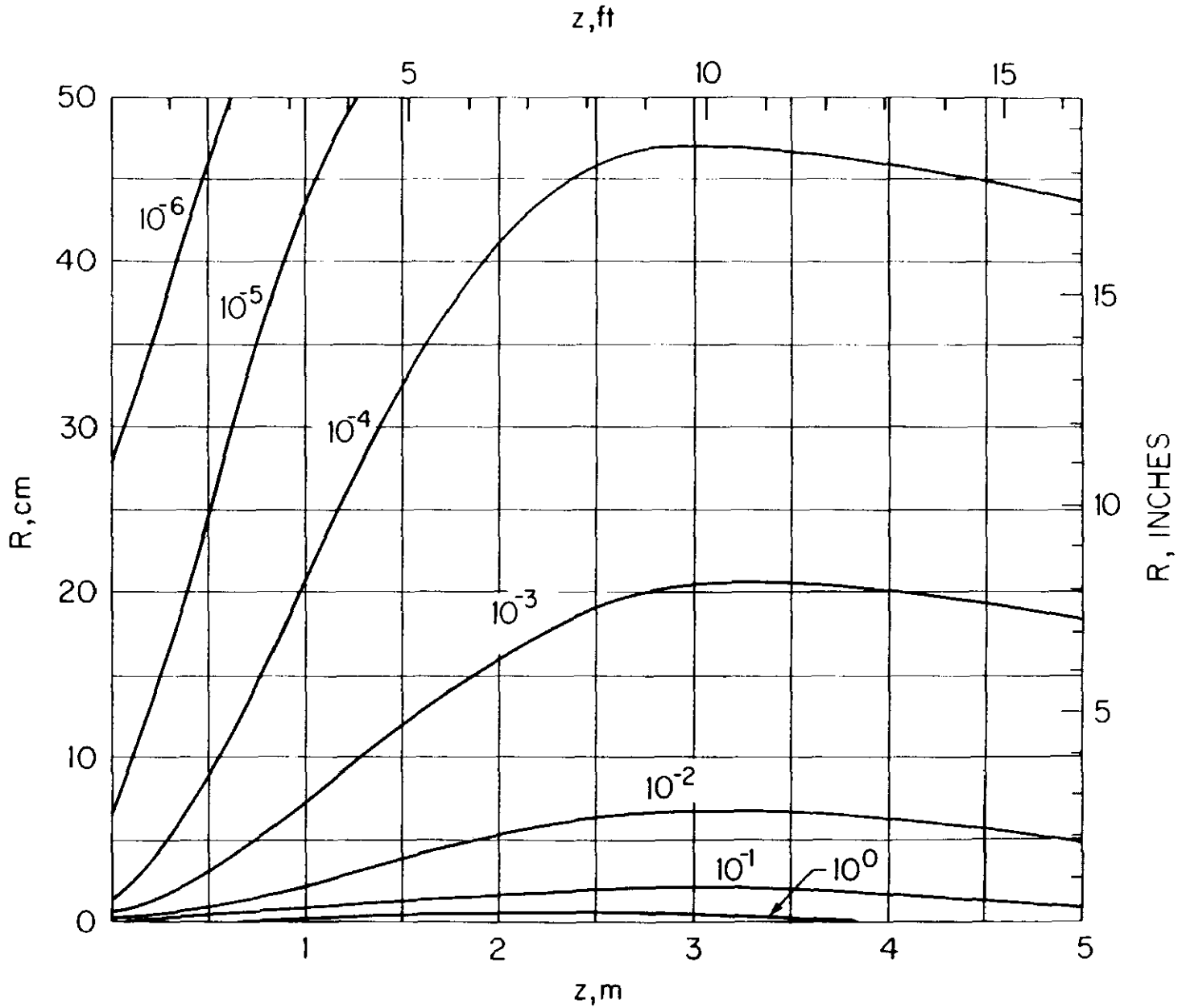

Fig. 34. Contours of equal energy density (in GeV/cm^3•incident proton) for 5 TeV protons incident on solid carbon cylinder. The beam has a bi-Gaussian spatial distribution with $\sigma_x = \sigma_y = 0.1$cm and is parallel to and centered on the cylinder axis. Some contours may be omitted for clarity or due to statistical uncertainty.

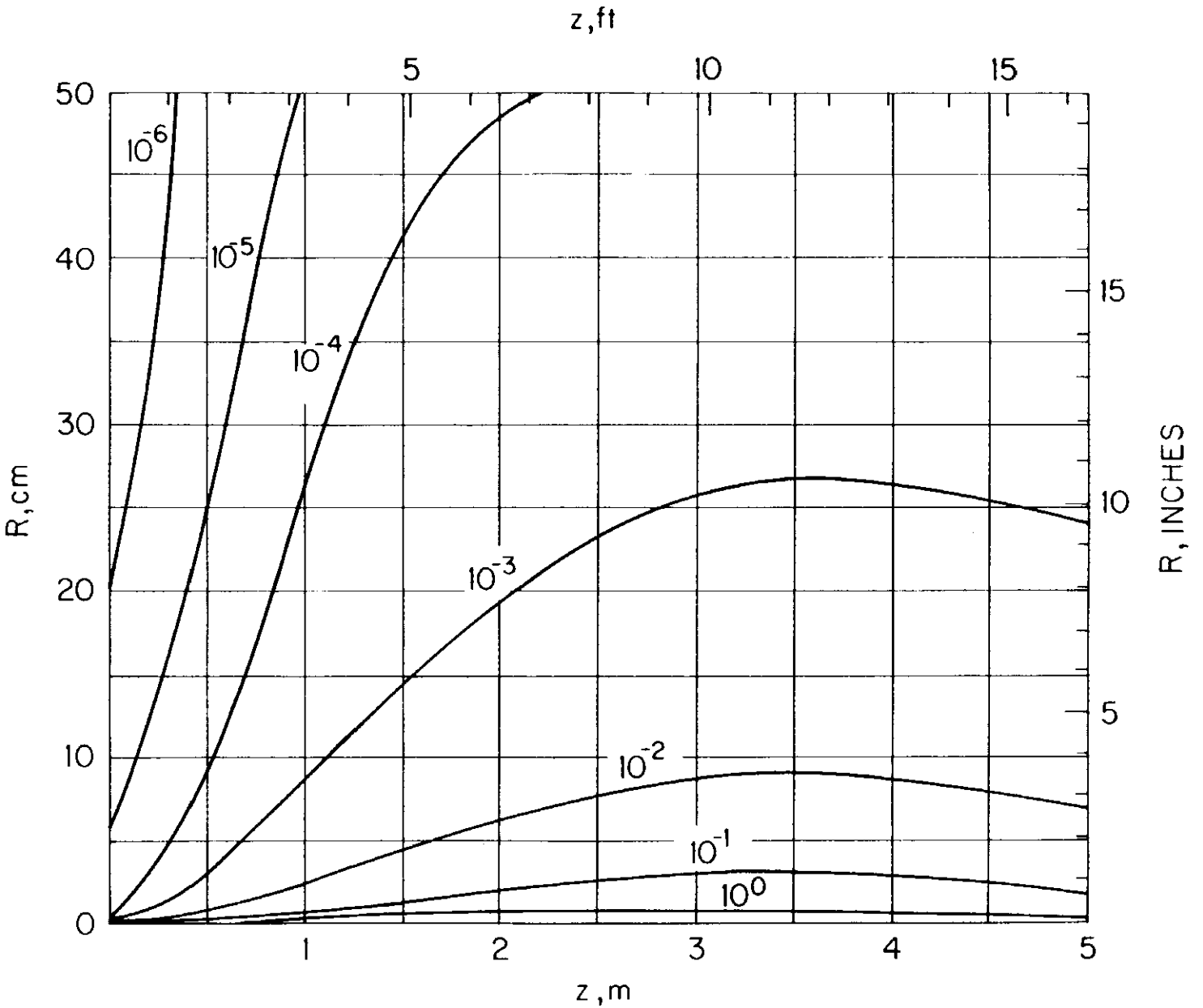

Fig. 35. Contours of equal energy density (in GeV/cm^3•incident proton) for 10 TeV protons incident on solid carbon cylinder. The beam has a bi-Gaussian spatial distribution with $\sigma_x=\sigma_y=0.1$cm and is parallel to and centered on the cylinder axis. Some contours may be omitted for clarity or due to statistical uncertainty.

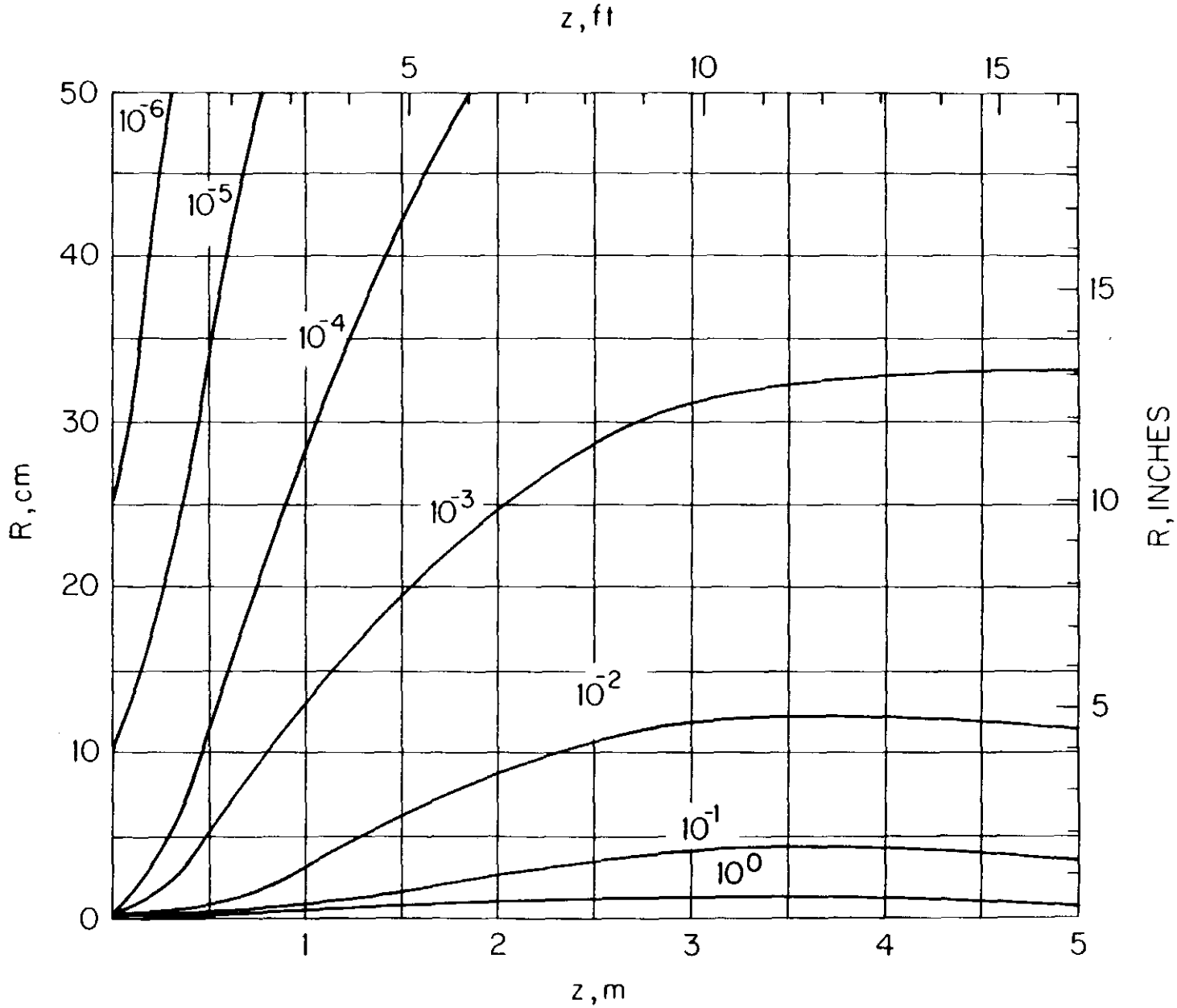

Fig. 36. Contours of equal energy density (in GeV/cm^3•incident proton) for 20 TeV protons incident on solid carbon cylinder. The beam has a bi-Gaussian spatial distribution with $\sigma_x = \sigma_y = 0.1$cm and is parallel to and centered on the cylinder axis. Some contours may be omitted for clarity or due to statistical uncertainty.

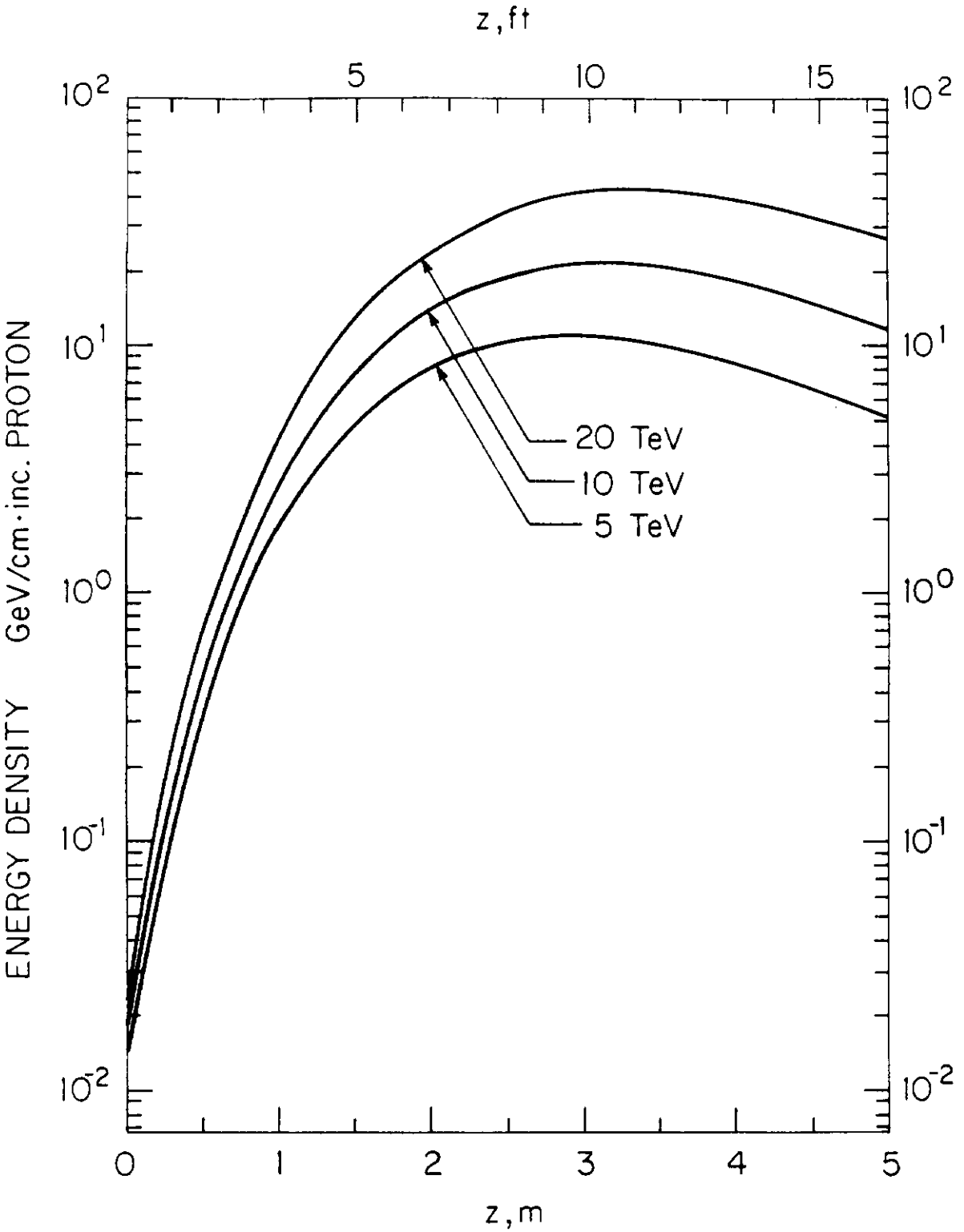

Fig. 37. Radially integrated energy density (in GeV/cm•incident proton) for 5, 10 and 20 TeV protons incident on 5m long solid carbon cylinder.

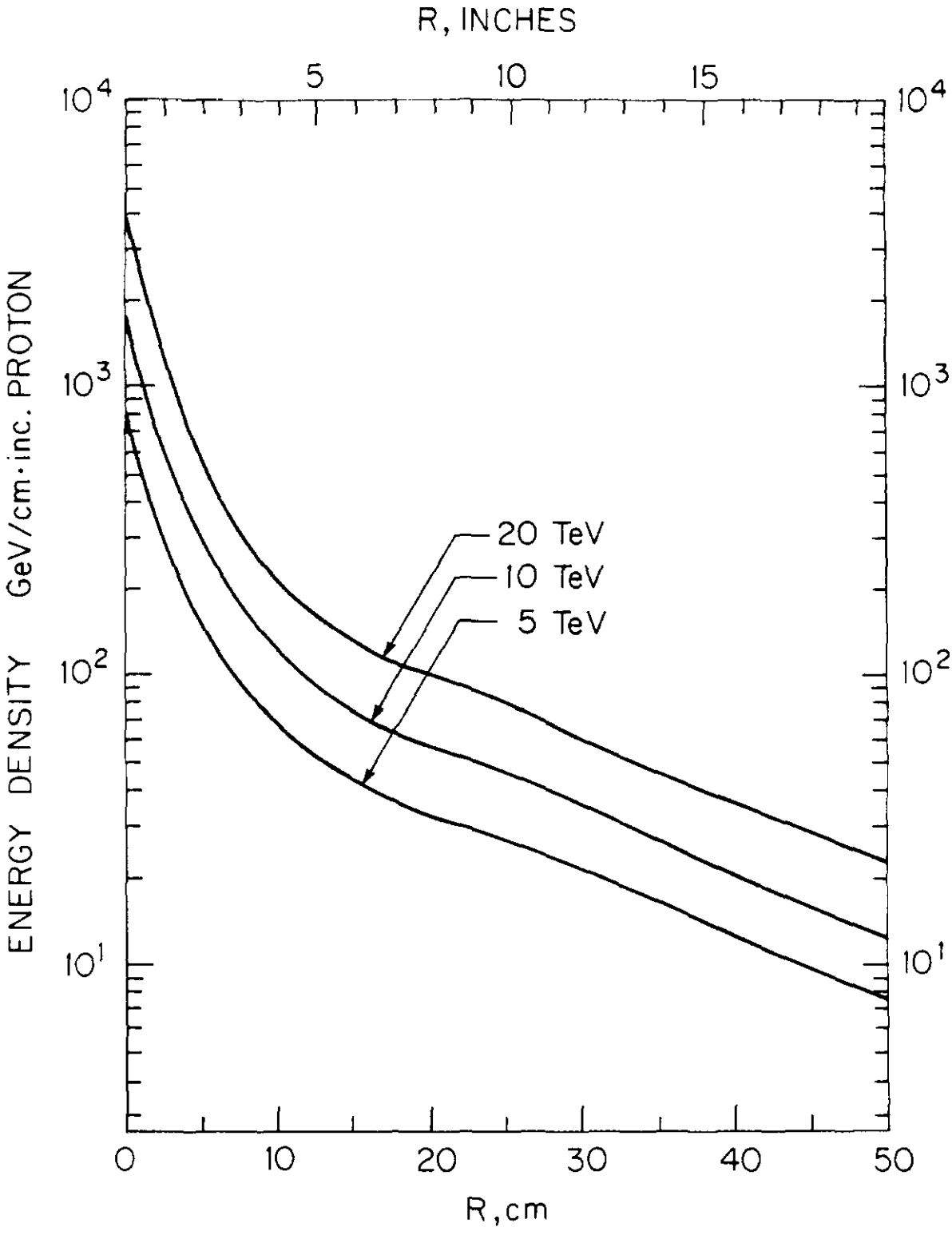

Fig. 38. Longitudinally integrated energy density (in GeV/cm•incident proton) for 5, 10 and 20 TeV protons incident on 0.5m radius solid carbon cylinder.

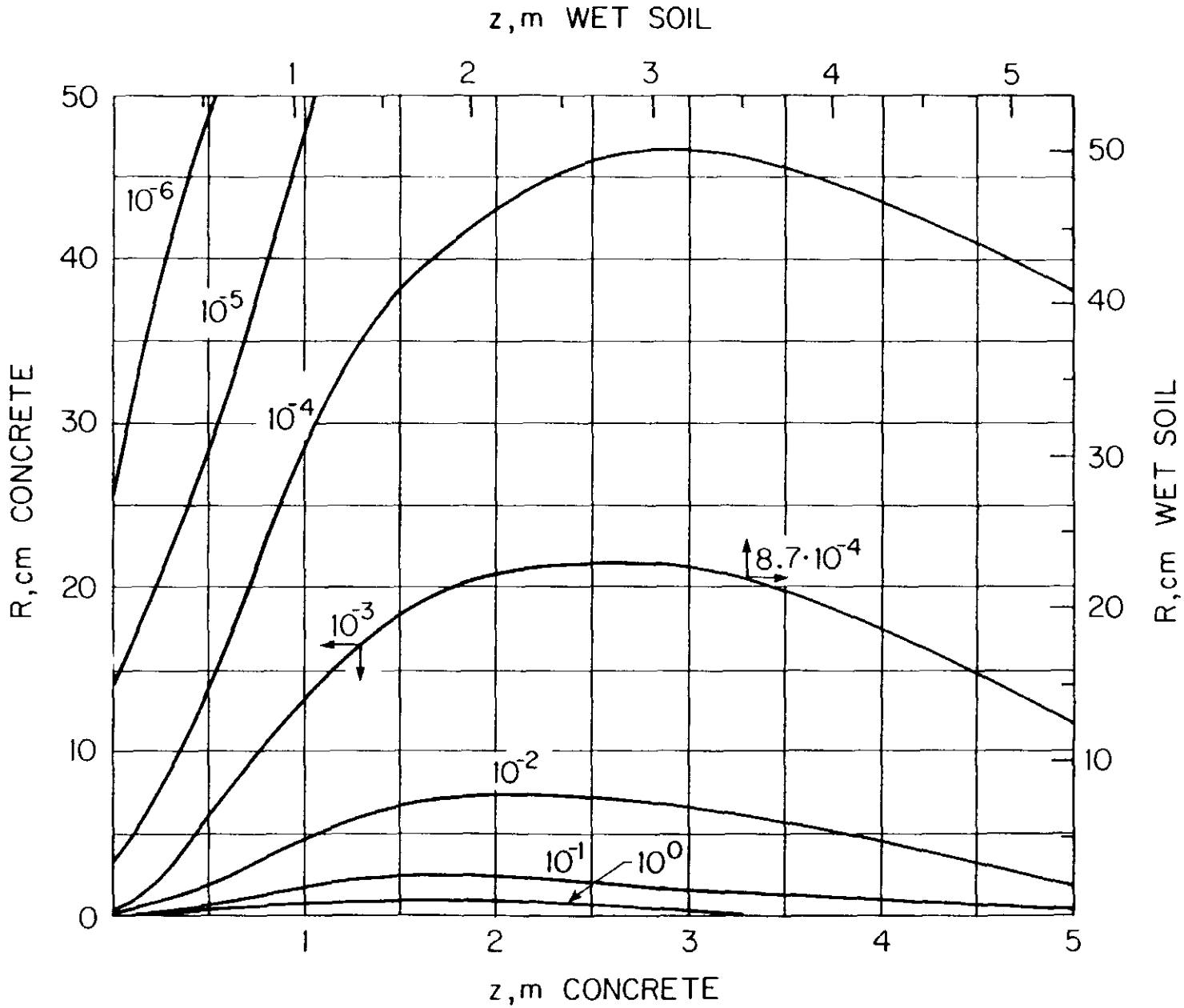

Fig. 39. Contours of equal energy density (in GeV/cm^3•incident proton) for 5 TeV protons incident on solid concrete/soil cylinder. The beam has a bi-Gaussian spatial distribution with $\sigma_x = \sigma_y = 0.1$cm and is parallel to and centered on the cylinder axis. Contours for concrete (left & bottom axes) are integral powers of ten. Contours for (wet) soil (right & top axes) must be scaled down by 0.81 as shown for one example. Some contours may be omitted for clarity or due to statistical uncertainty.

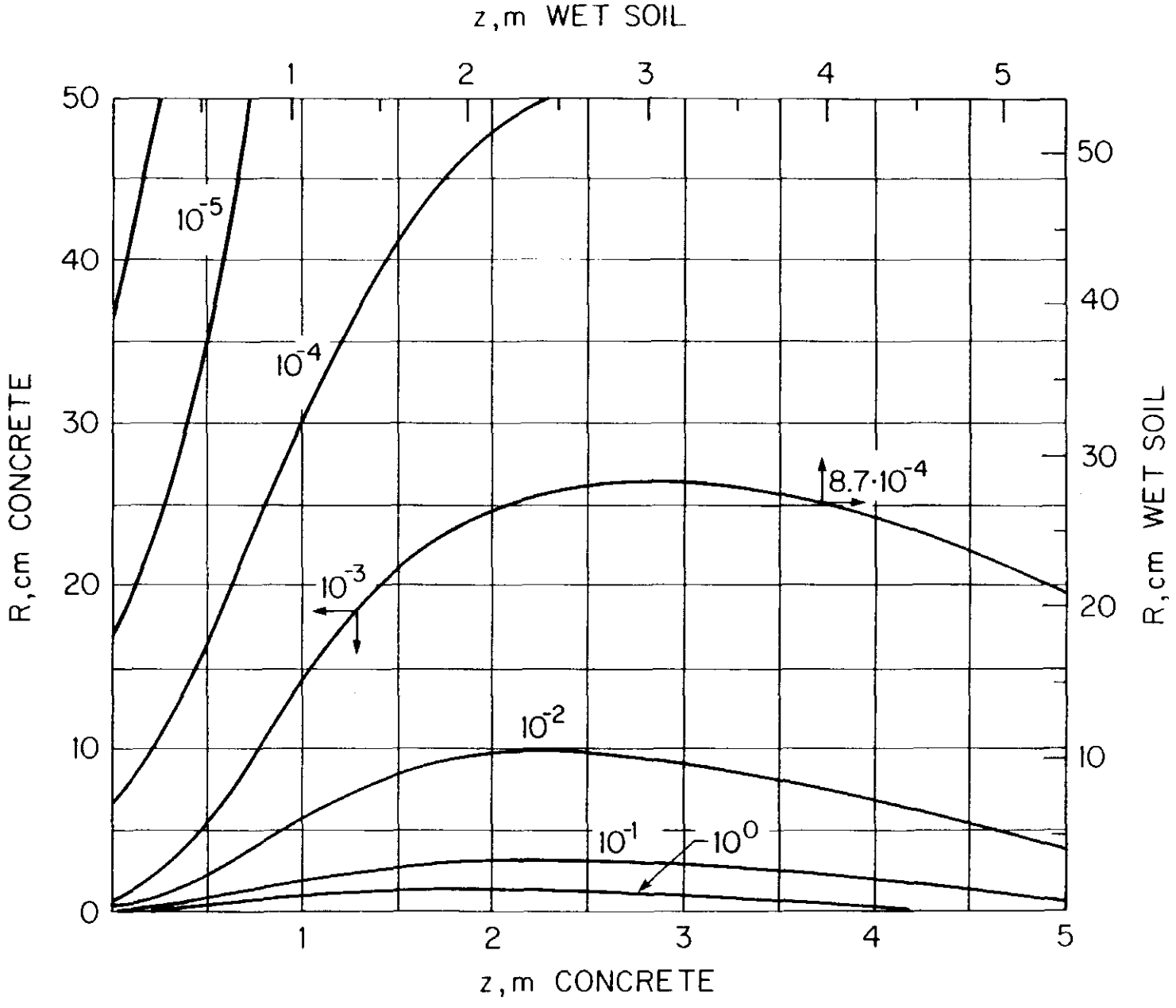

Fig. 40. Contours of equal energy density (in GeV/cm^3•incident proton) for 10 TeV protons incident on solid concrete/soil cylinder. The beam has a bi-Gaussian spatial distribution with $\sigma_x = \sigma_y = 0.1$cm and is parallel to and centered on the cylinder axis. Contours for concrete (left & bottom axes) are integral powers of ten. Contours for (wet) soil (right & top axes) must be scaled down by 0.81 as shown for one example. Some contours may be omitted for clarity or due to statistical uncertainty

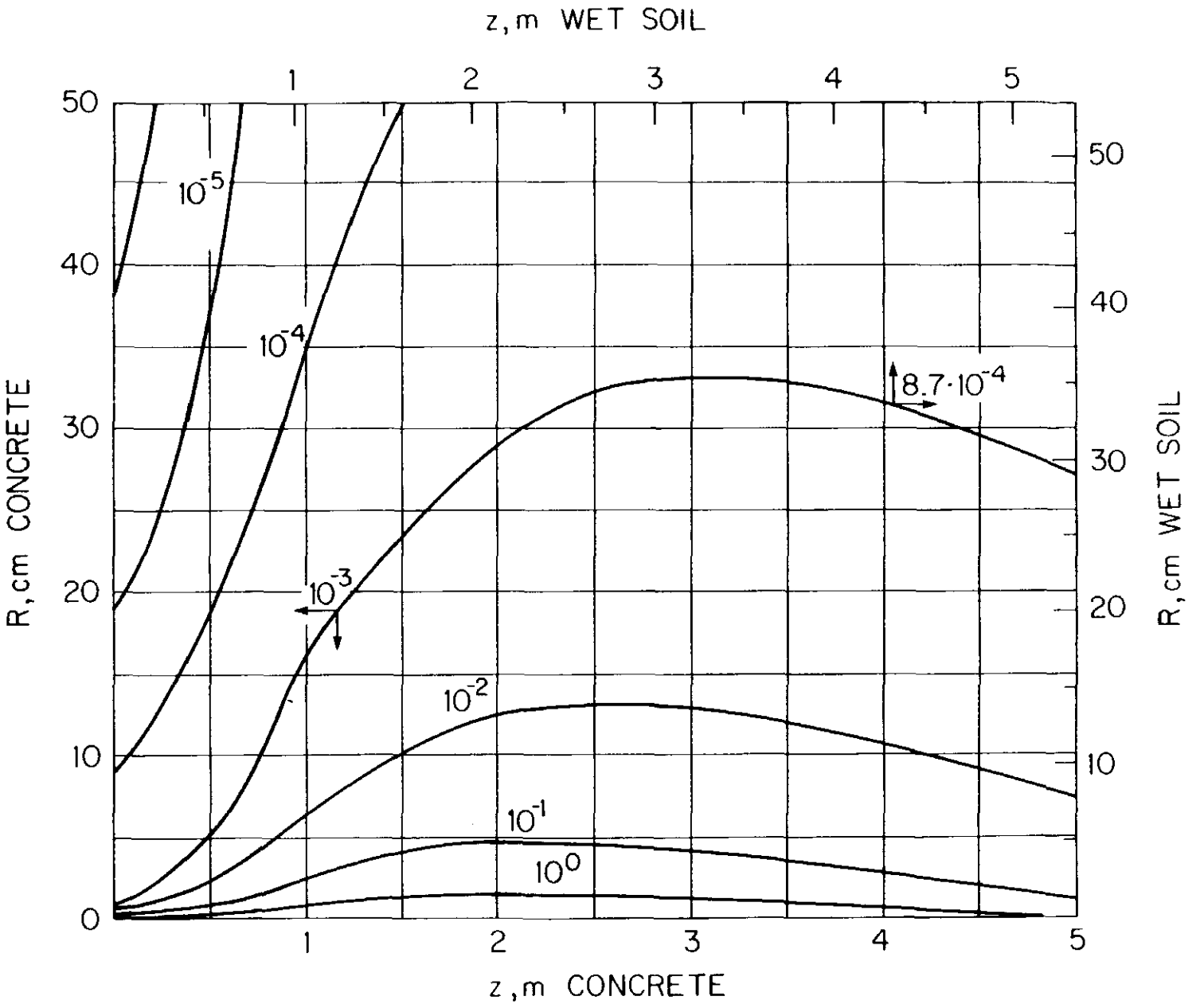

Fig. 41. Contours of equal energy density (in GeV/cm^3•incident proton) for 20 TeV protons incident on solid concrete/soil cylinder. The beam has a bi-Gaussian spatial distribution with $\sigma_x = \sigma_y = 0.1$cm and is parallel to and centered on the cylinder axis. Contours for concrete (left & bottom axes) are integral powers of ten. Contours for (wet) soil (right & top axes) must be scaled down by 0.81 as shown for one example. Some contours may be omitted for clarity or due to statistical uncertainty.

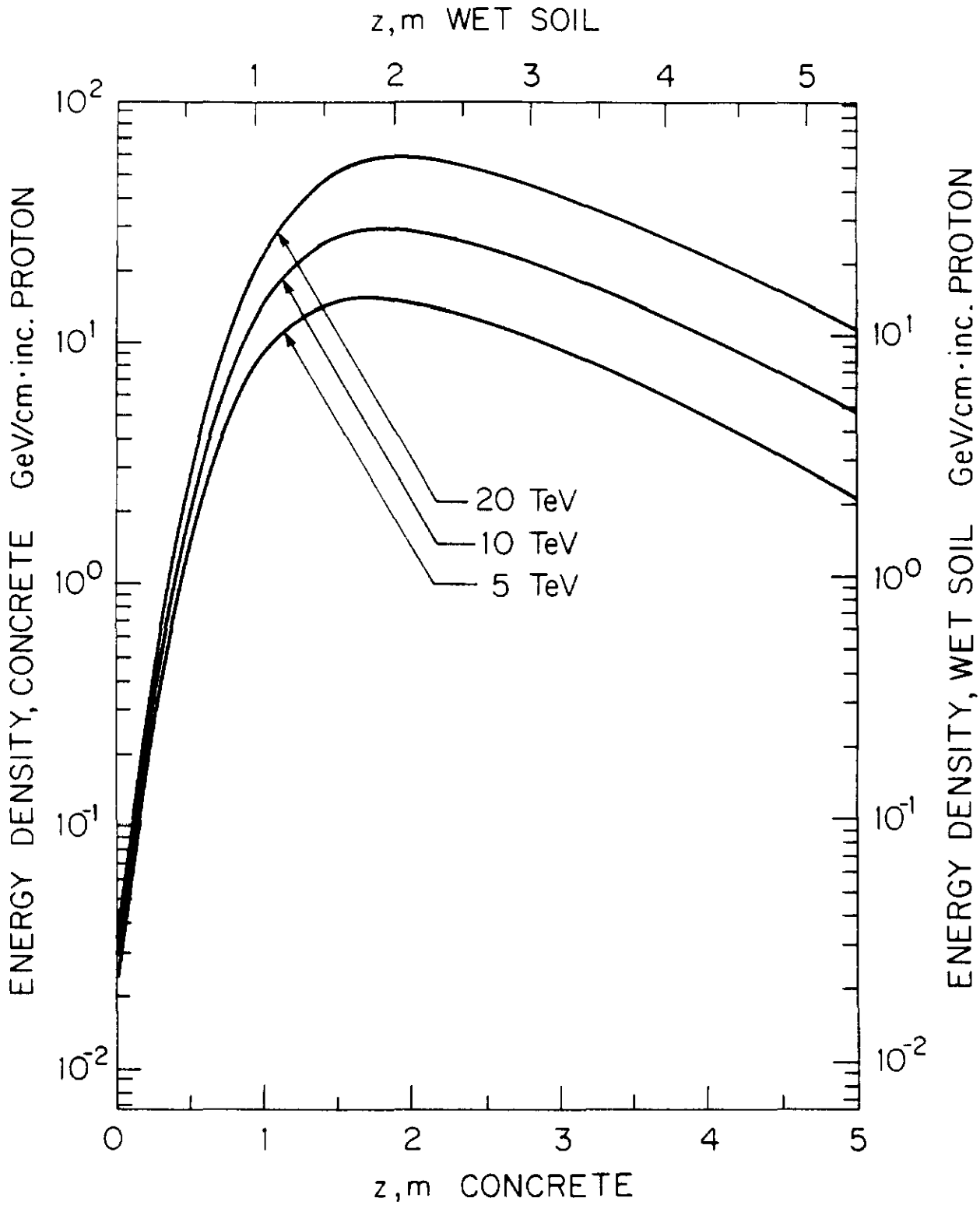

Fig. 42. Radially integrated energy density (in GeV/cm•incident proton) for 5, 10 and 20 TeV protons incident on a 5m long solid concrete (left & bottom axes) or soil (right & top axes) cylinder.

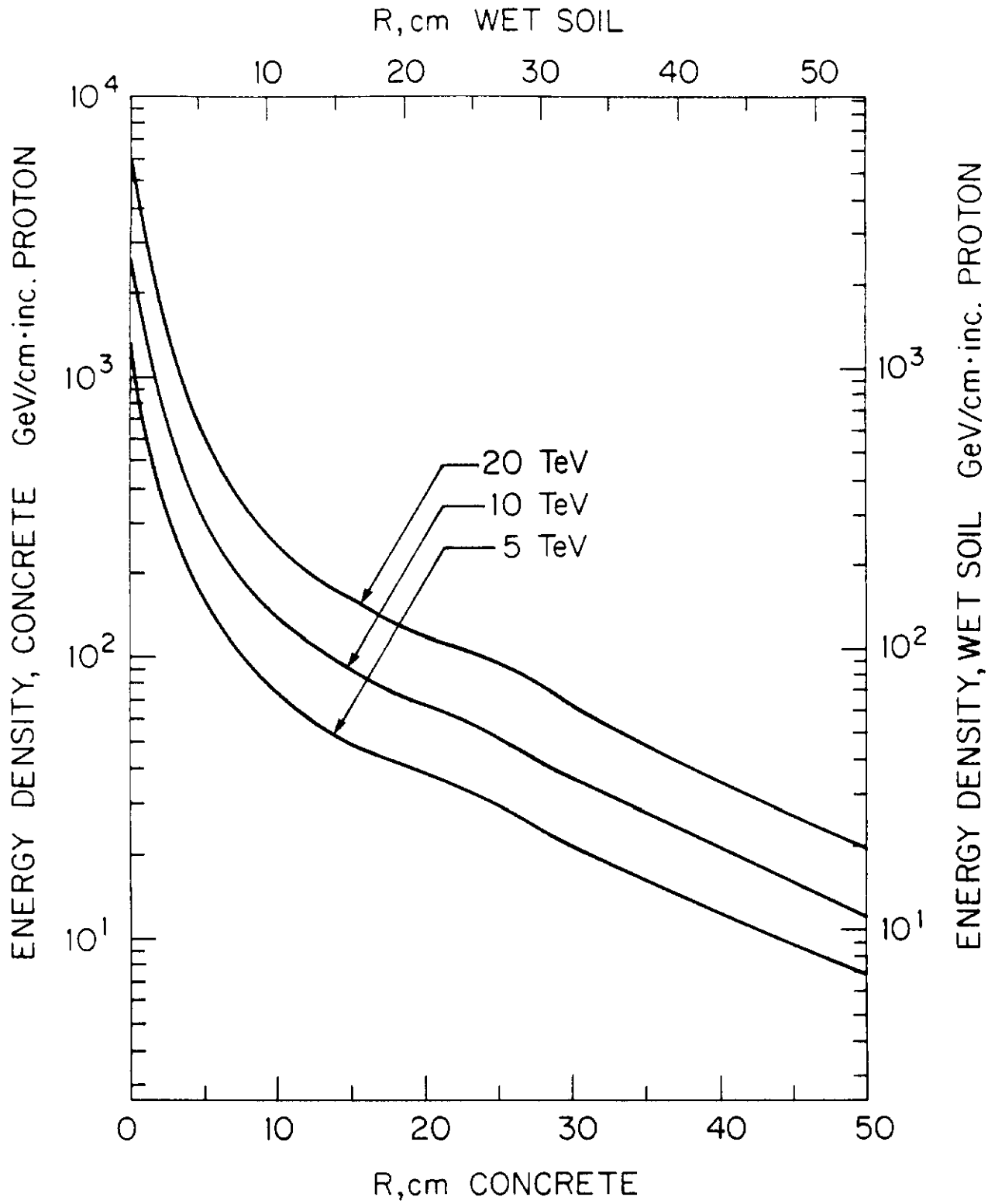

Fig. 43. Longitudinally integrated energy density (in GeV/cm•incident proton) for 5, 10 and 20 TeV protons incident on 0.5m radius solid concrete (left & bottom axes) or soil (right & top axes) cylinder.

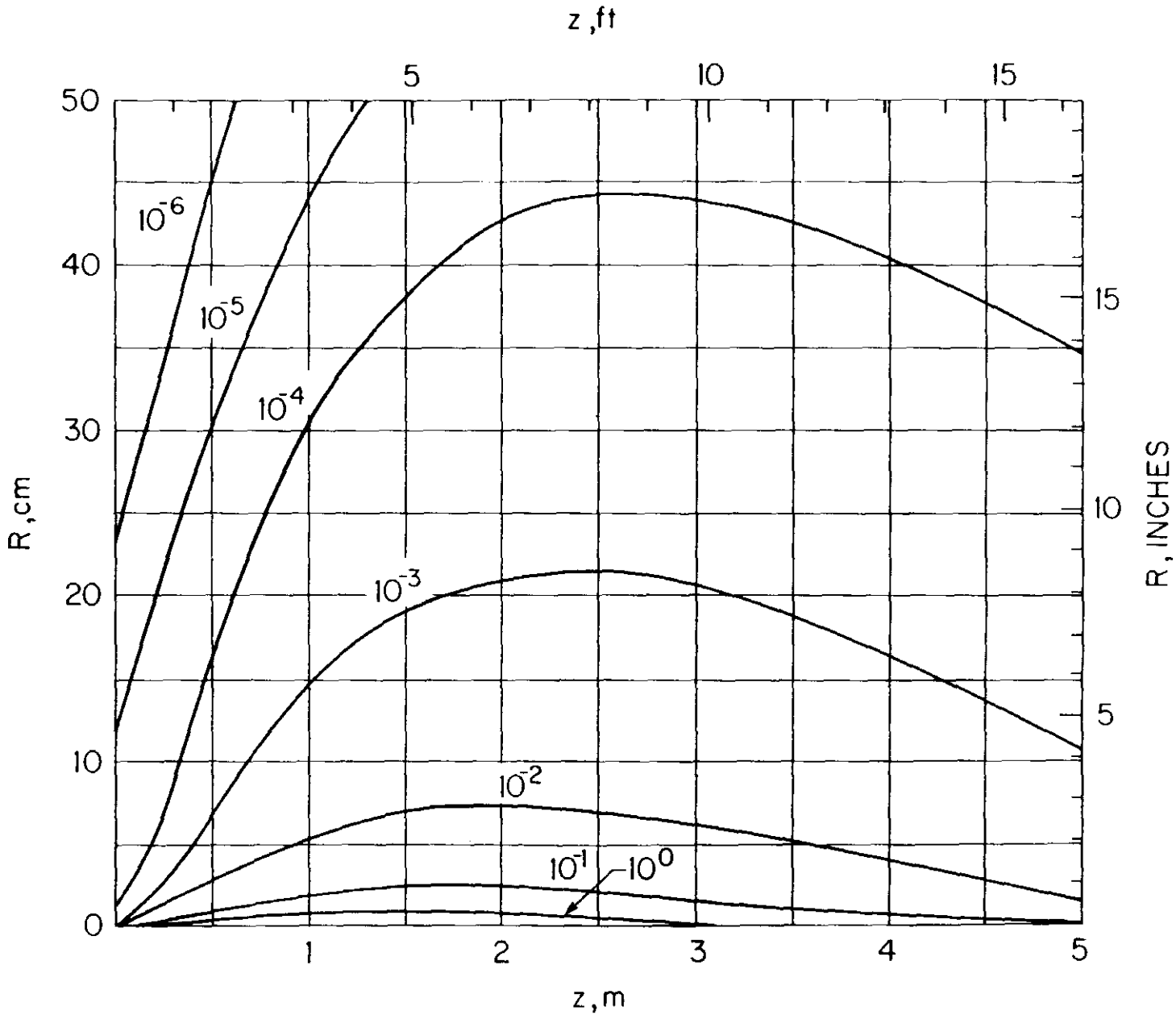

Fig. 44. Contours of equal energy density (in GeV/cm^3•incident proton) for 5 TeV protons incident on solid aluminum cylinder. The beam has a bi-Gaussian spatial distribution with $\sigma_x = \sigma_y = 0.1$cm and is parallel to and centered on the cylinder axis. Some contours may be omitted for clarity or due to statistical uncertainty.

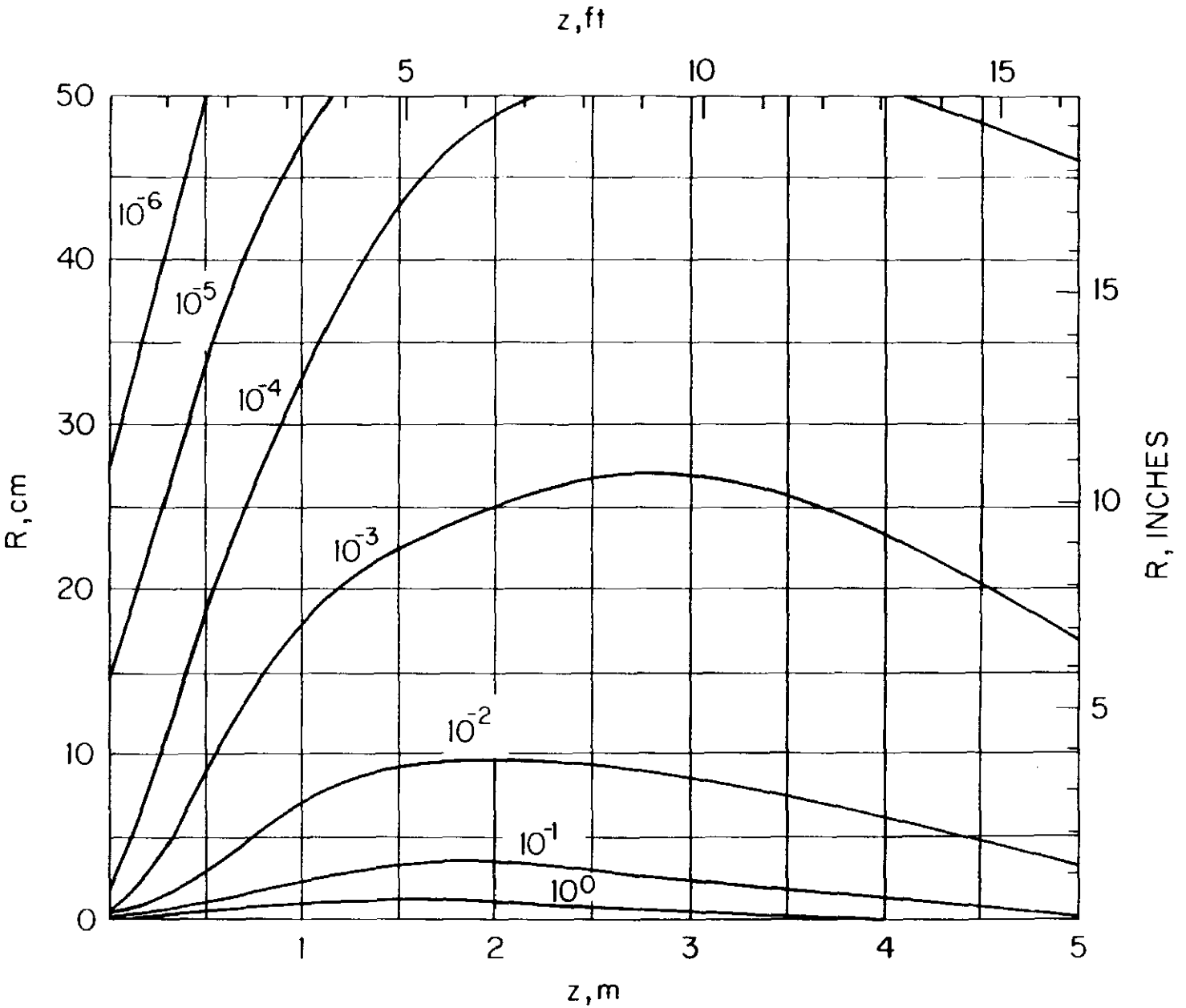

Fig. 45. Contours of equal energy density (in GeV/cm^3•incident proton) for 10 TeV protons incident on solid aluminum cylinder. The beam has a bi-Gaussian spatial distribution with $\sigma_x = \sigma_y = 0.1$cm and is parallel to and centered on the cylinder axis. Some contours may be omitted for clarity or due to statistical uncertainty.

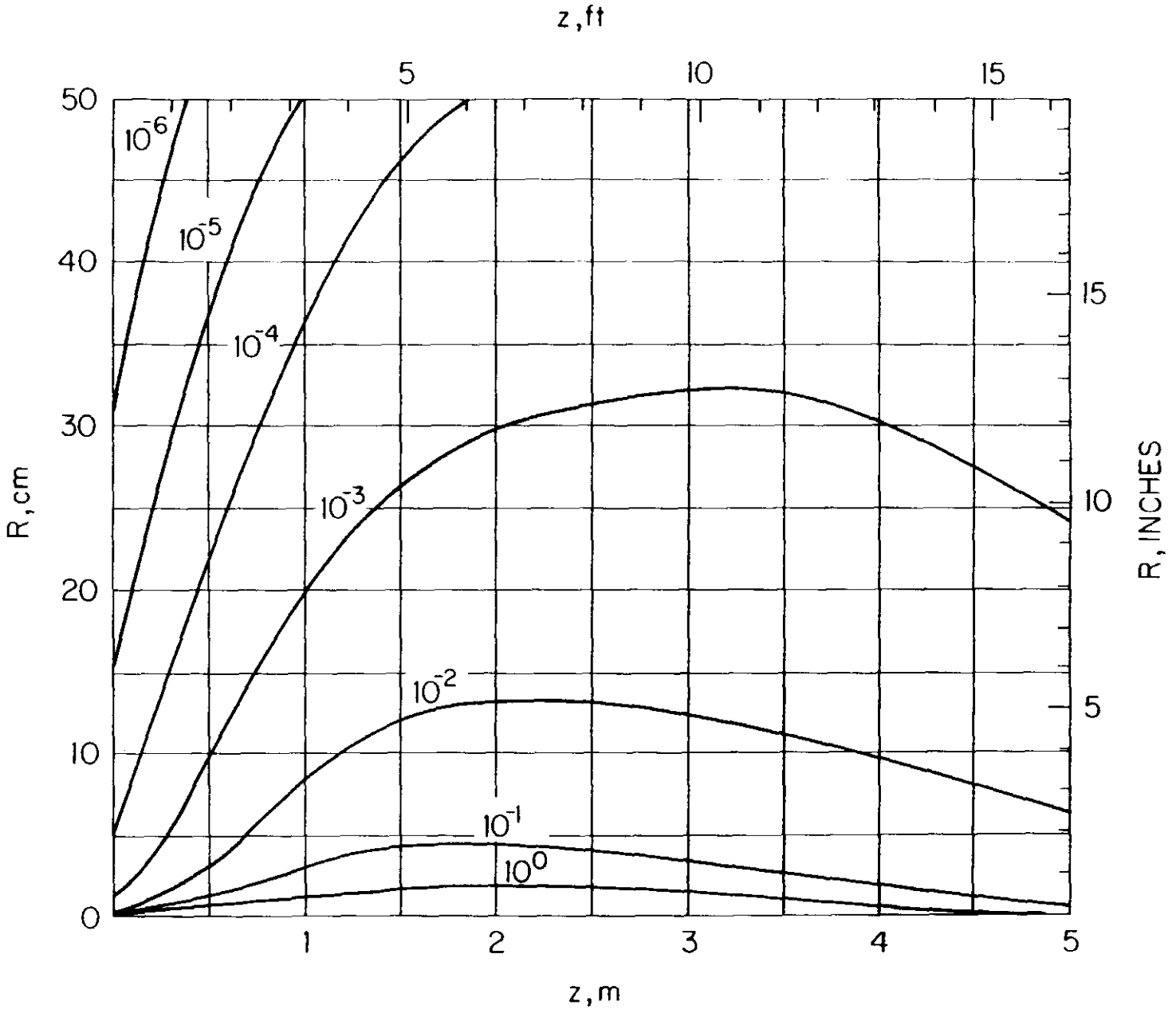

Fig. 46. Contours of equal energy density (in GeV/cm^3•incident proton) for 20 TeV protons incident on solid aluminum cylinder. The beam has a bi-Gaussian spatial distribution with $\sigma_x=\sigma_y=0.1$cm and is parallel to and centered on the cylinder axis. Some contours may be omitted for clarity or due to statistical uncertainty.

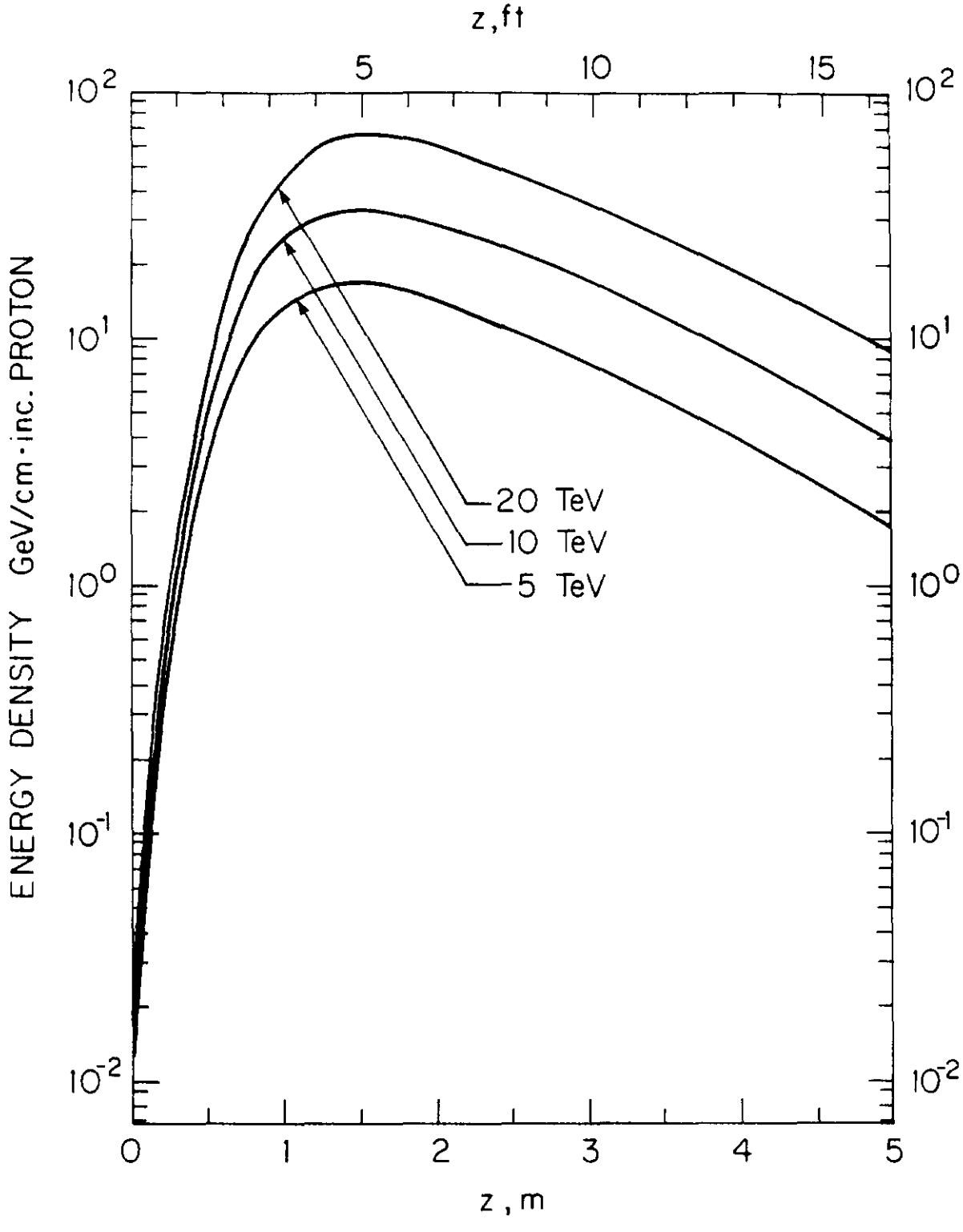

Fig. 47. Radially integrated energy density (in GeV/cm•incident proton) for 5, 10 and 20 TeV protons incident on 5m long solid aluminum cylinder.

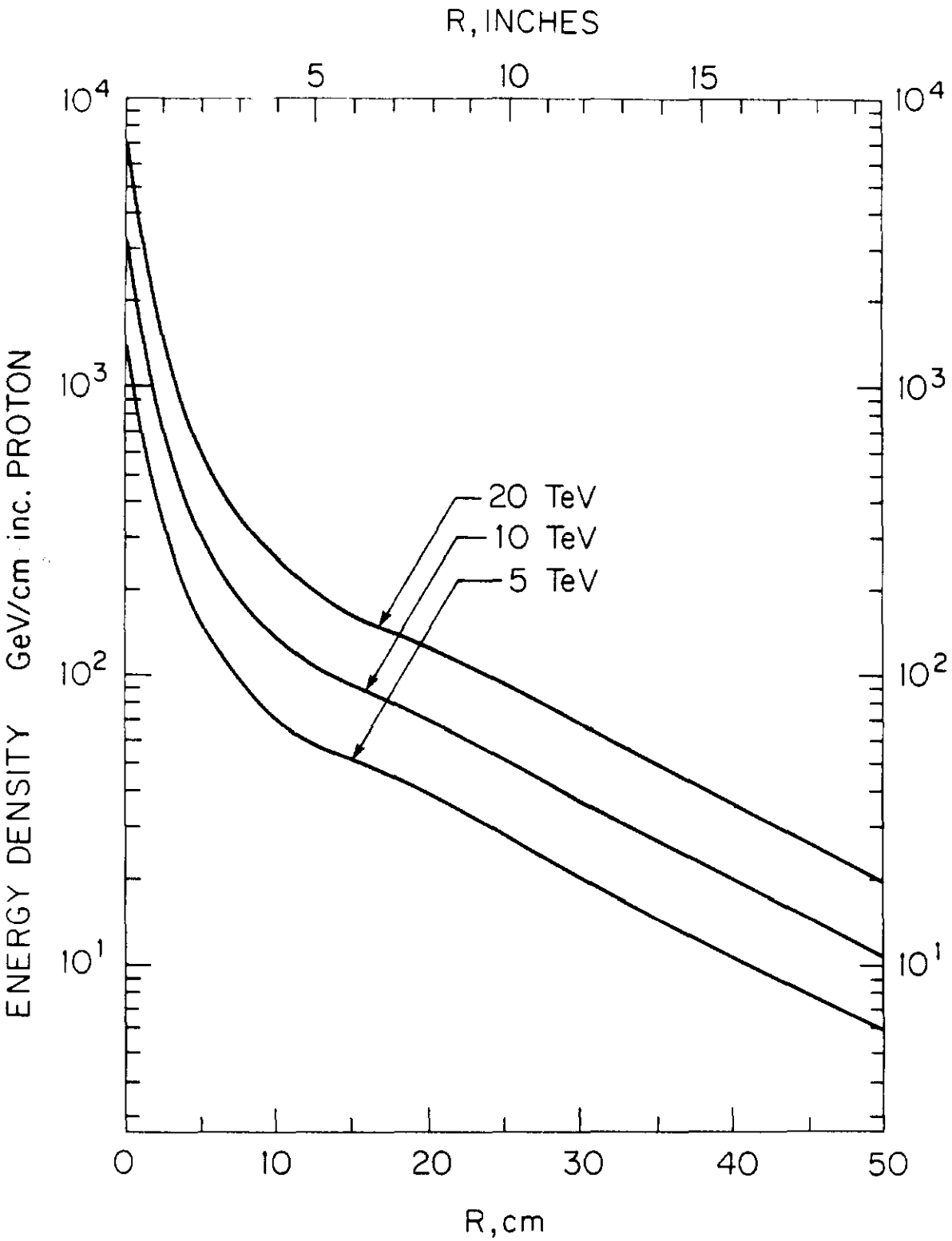

Fig. 48. Longitudinally integrated energy density (in GeV/cm•incident proton) for 5, 10 and 20 TeV protons incident on 0.5m radius solid aluminum cylinder.

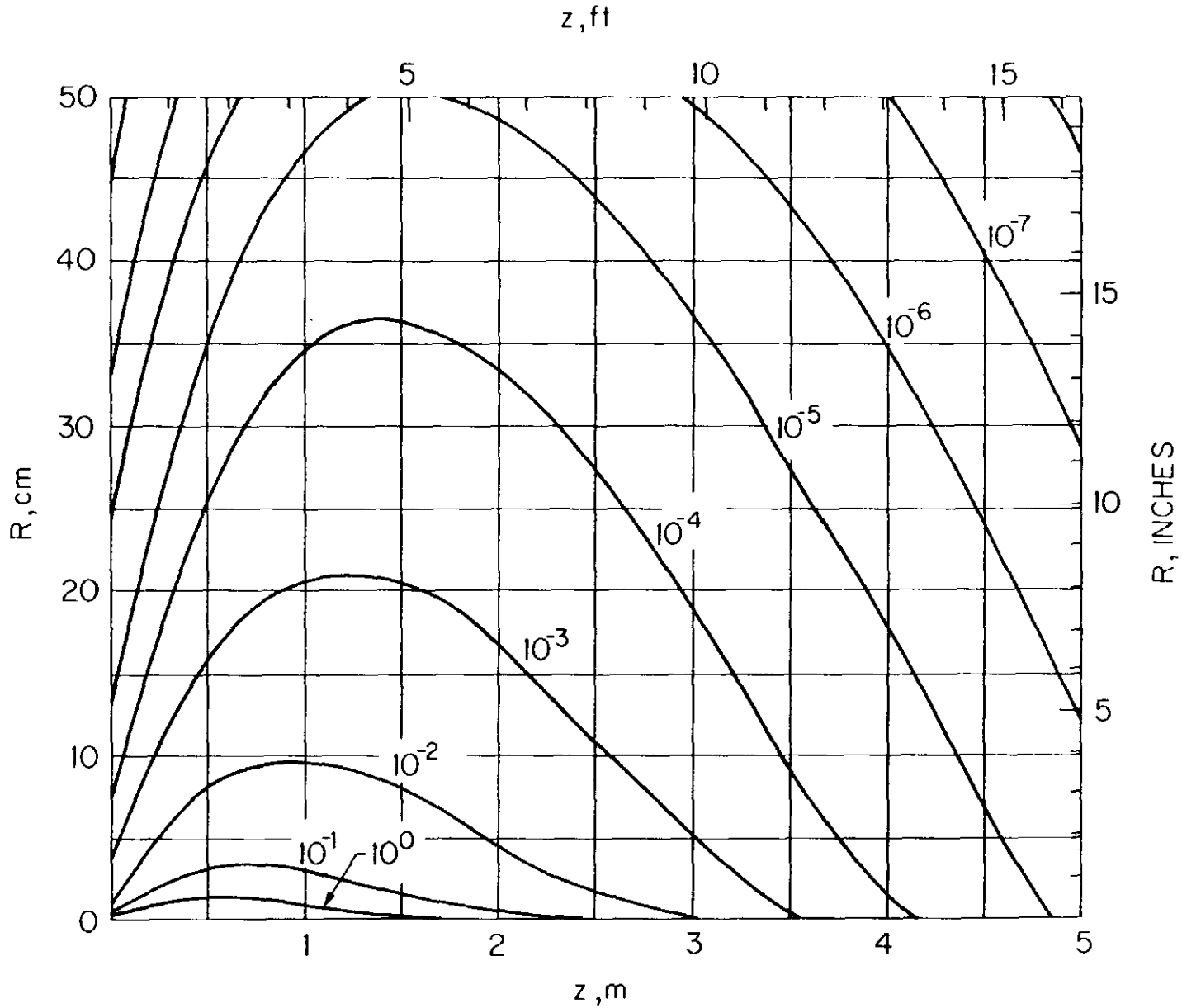

Fig. 49. Contours of equal energy density (in GeV/cm^3•incident proton) for 5 TeV protons incident on solid iron cylinder. The beam has a bi-Gaussian spatial distribution with $\sigma_x=\sigma_y=0.1$cm and is parallel to and centered on the cylinder axis. Some contours may be omitted for clarity or due to statistical uncertainty.

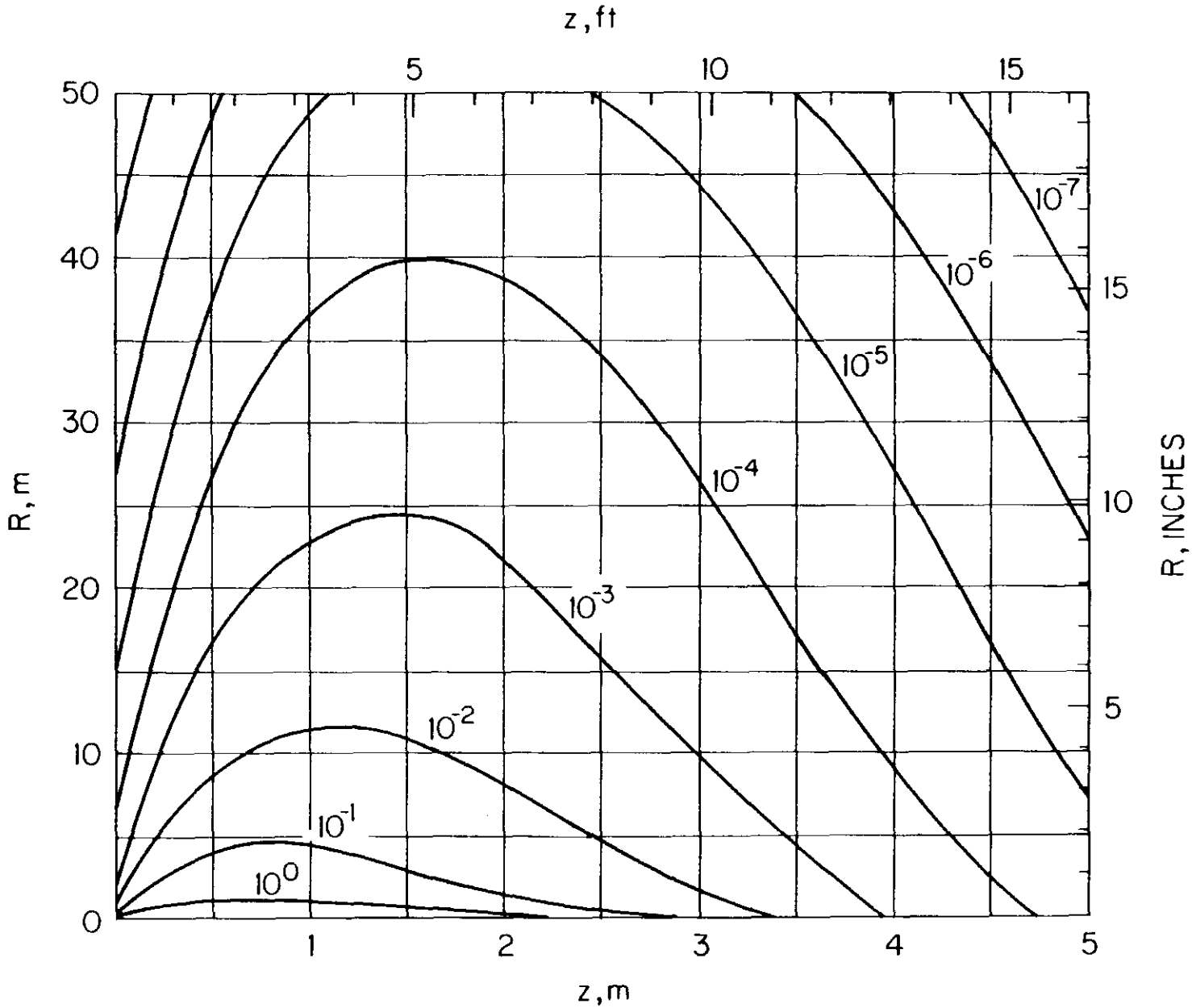

Fig. 50. Contours of equal energy density (in GeV/cm^3•incident proton) for 10 TeV protons incident on solid iron cylinder. The beam has a bi-Gaussian spatial distribution with $\sigma_x = \sigma_y = 0.1$cm and is parallel to and centered on the cylinder axis. Some contours may be omitted for clarity or due to statistical uncertainty.

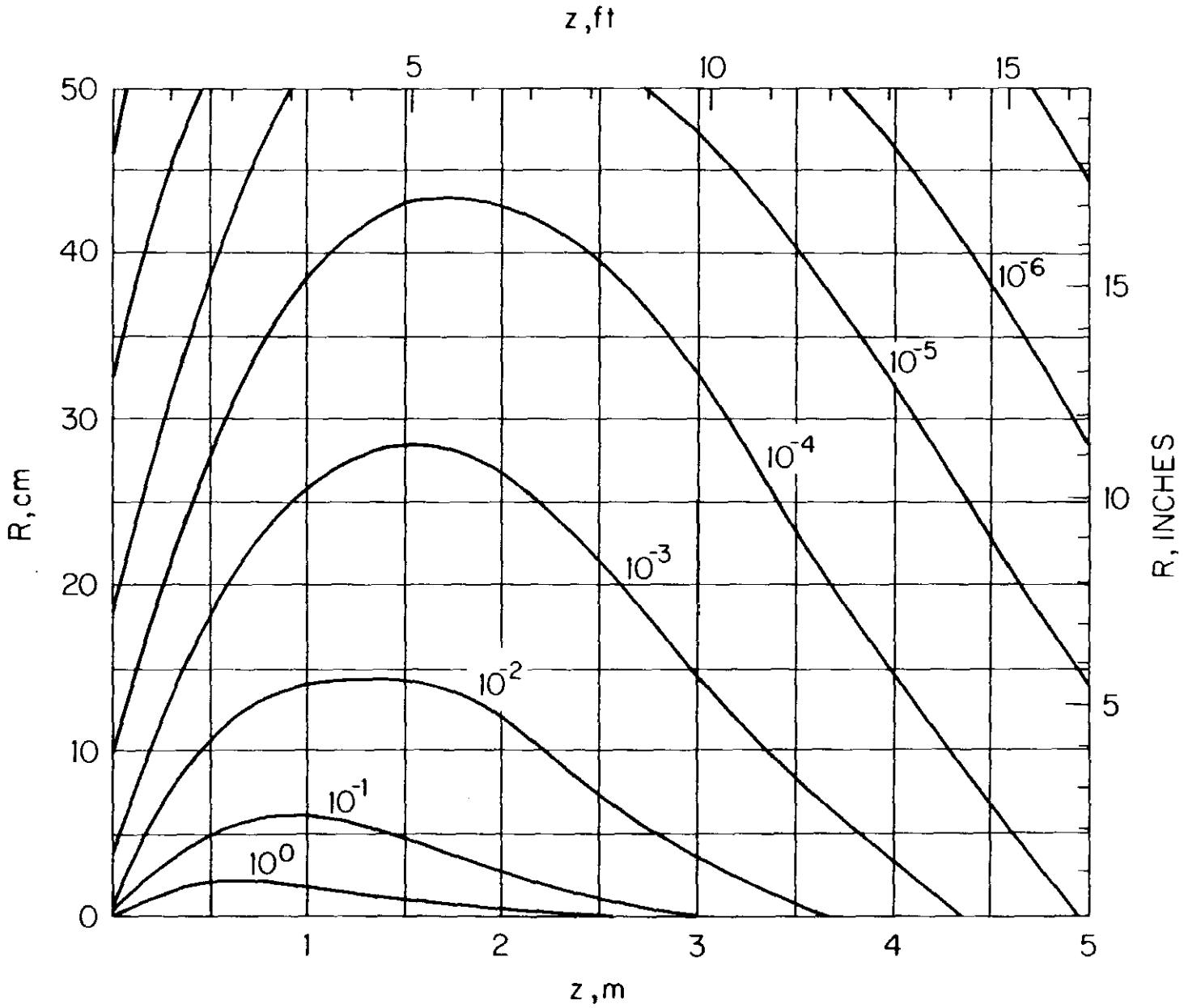

Fig. 51. Contours of equal energy density (in GeV/cm^3•incident proton) for 20 TeV protons incident on solid iron cylinder. The beam has a bi-Gaussian spatial distribution with $\sigma_x = \sigma_y = 0.1$cm and is parallel to and centered on the cylinder axis. Some contours may be omitted for clarity or due to statistical uncertainty.

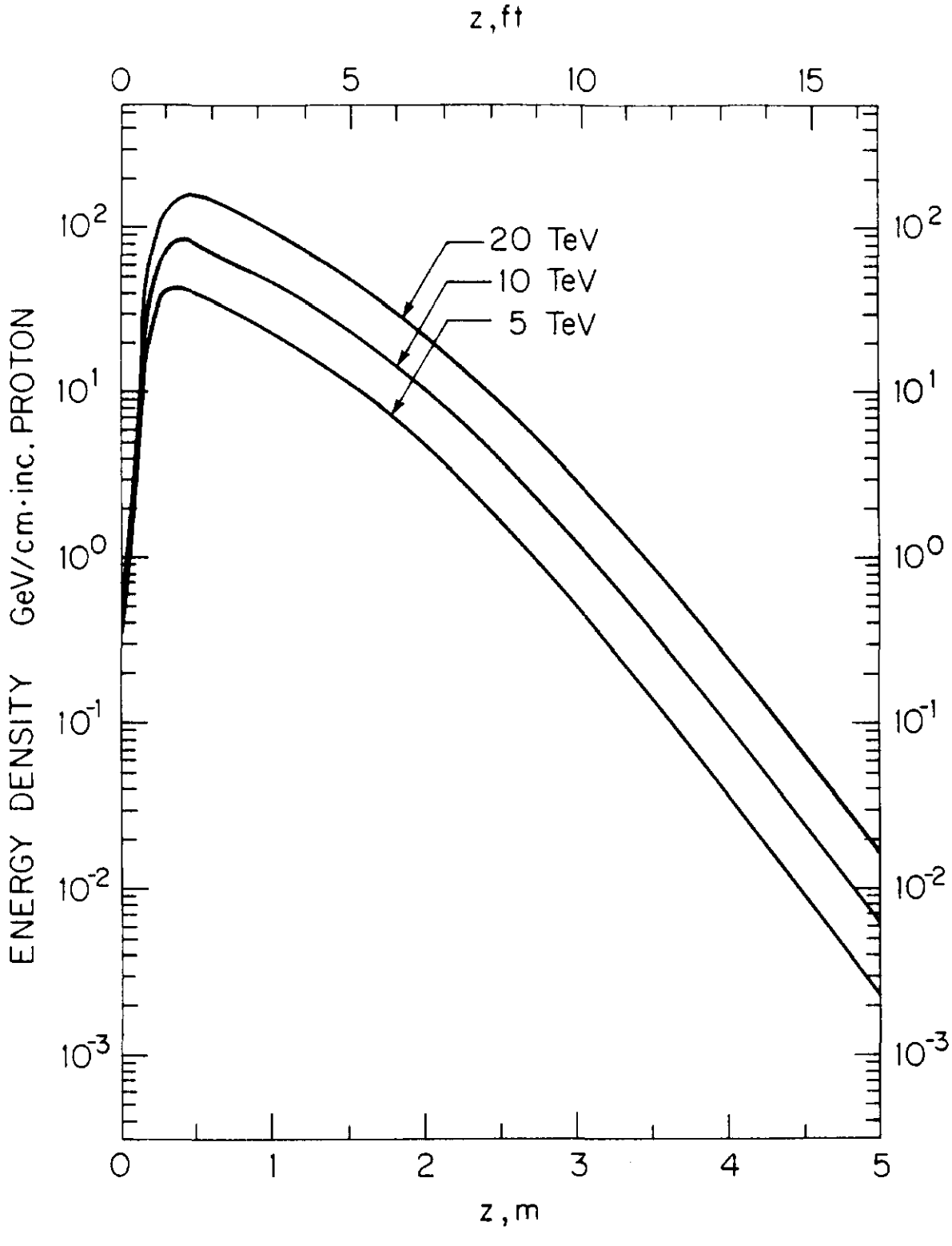

Fig. 52. Radially integrated energy density (in GeV/cm•incident proton) for 5, 10 and 20 TeV protons incident on 5m long solid iron cylinder.

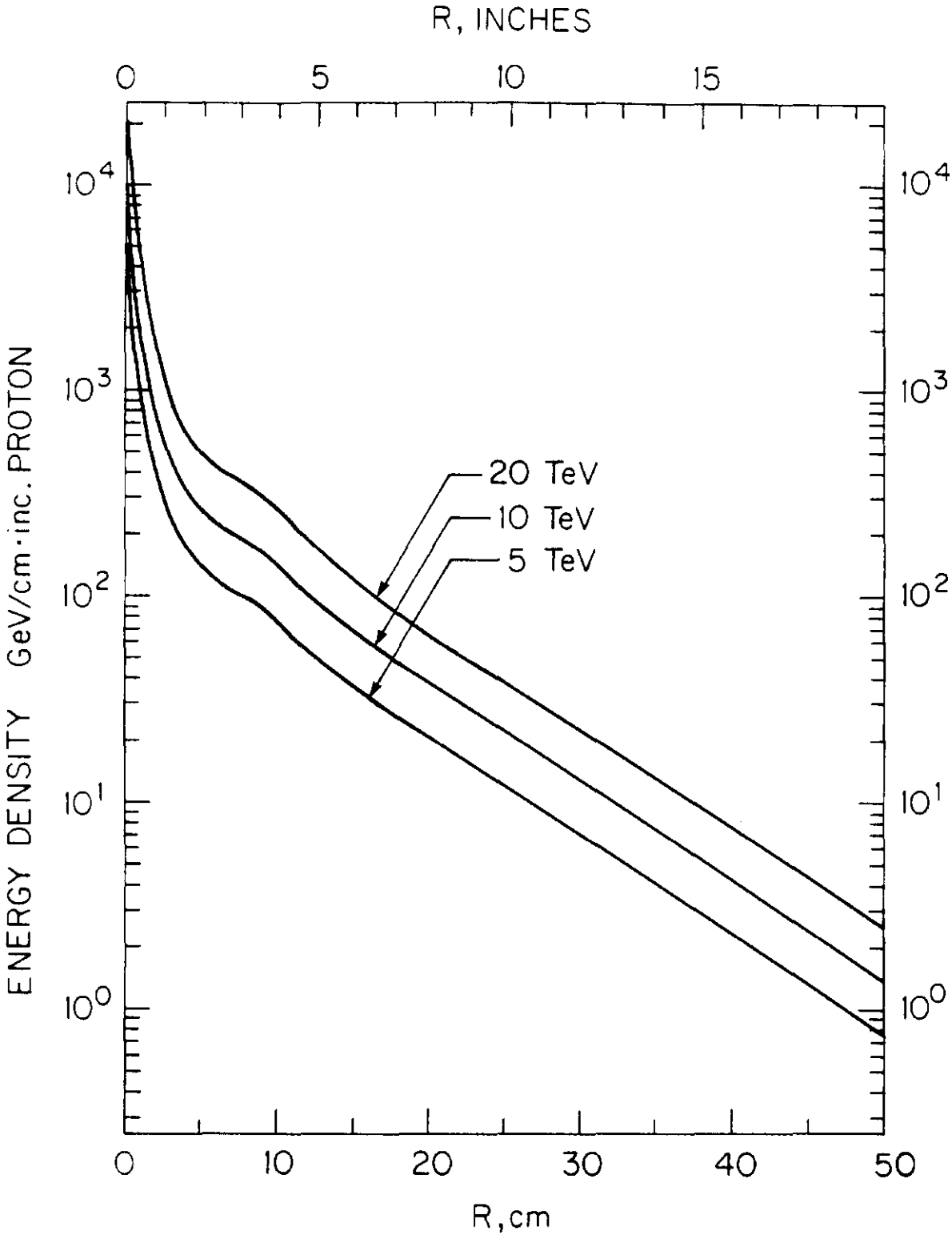

Fig. 53. Longitudinally integrated energy density (in GeV/cm•incident proton) for 5, 10 and 20 TeV protons incident on 0.5m radius solid iron cylinder.

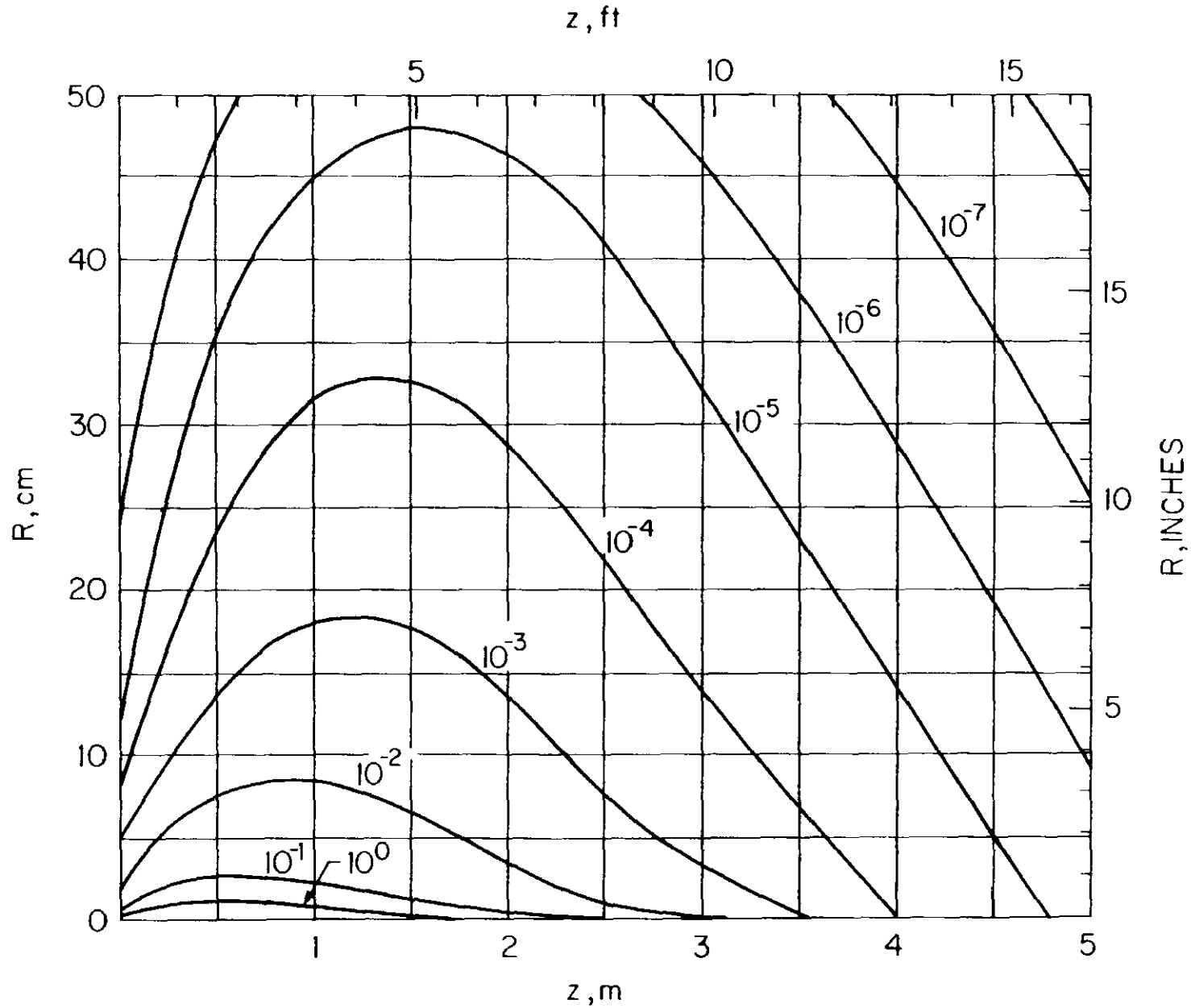

Fig. 54. Contours of equal energy density (in GeV/cm^3•incident proton) for 5 TeV protons incident on solid lead cylinder. The beam has a bi-Gaussian spatial distribution with $\sigma_x = \sigma_y = 0.1$cm and is parallel to and centered on the cylinder axis. Some contours may be omitted for clarity or due to statistical uncertainty.

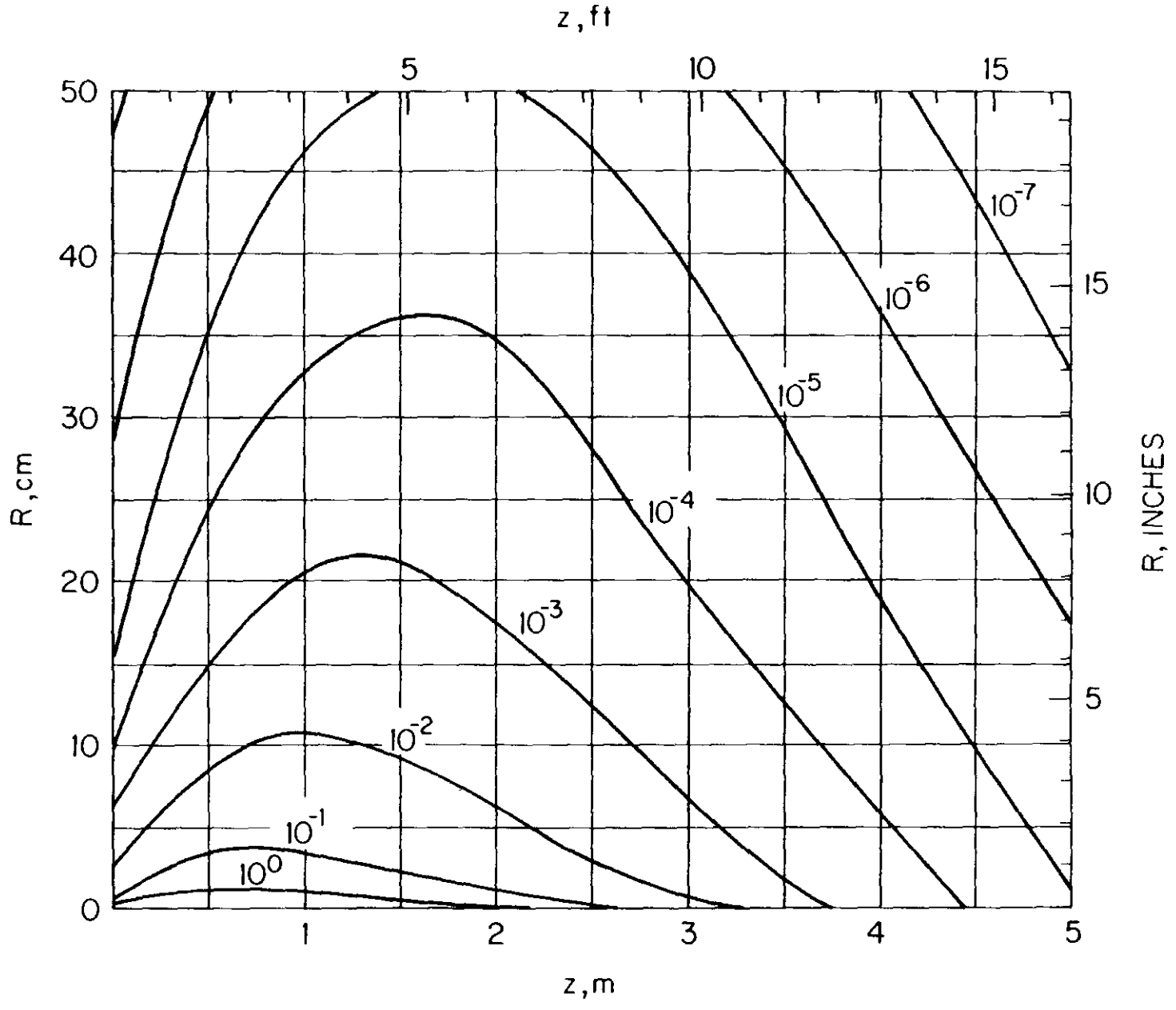

Fig. 55. Contours of equal energy density (in GeV/cm^3•incident proton) for 10 TeV protons incident on solid lead cylinder. The beam has a bi-Gaussian spatial distribution with $\sigma_x = \sigma_y = 0.1$cm and is parallel to and centered on the cylinder axis. Some contours may be omitted for clarity or due to statistical uncertainty.

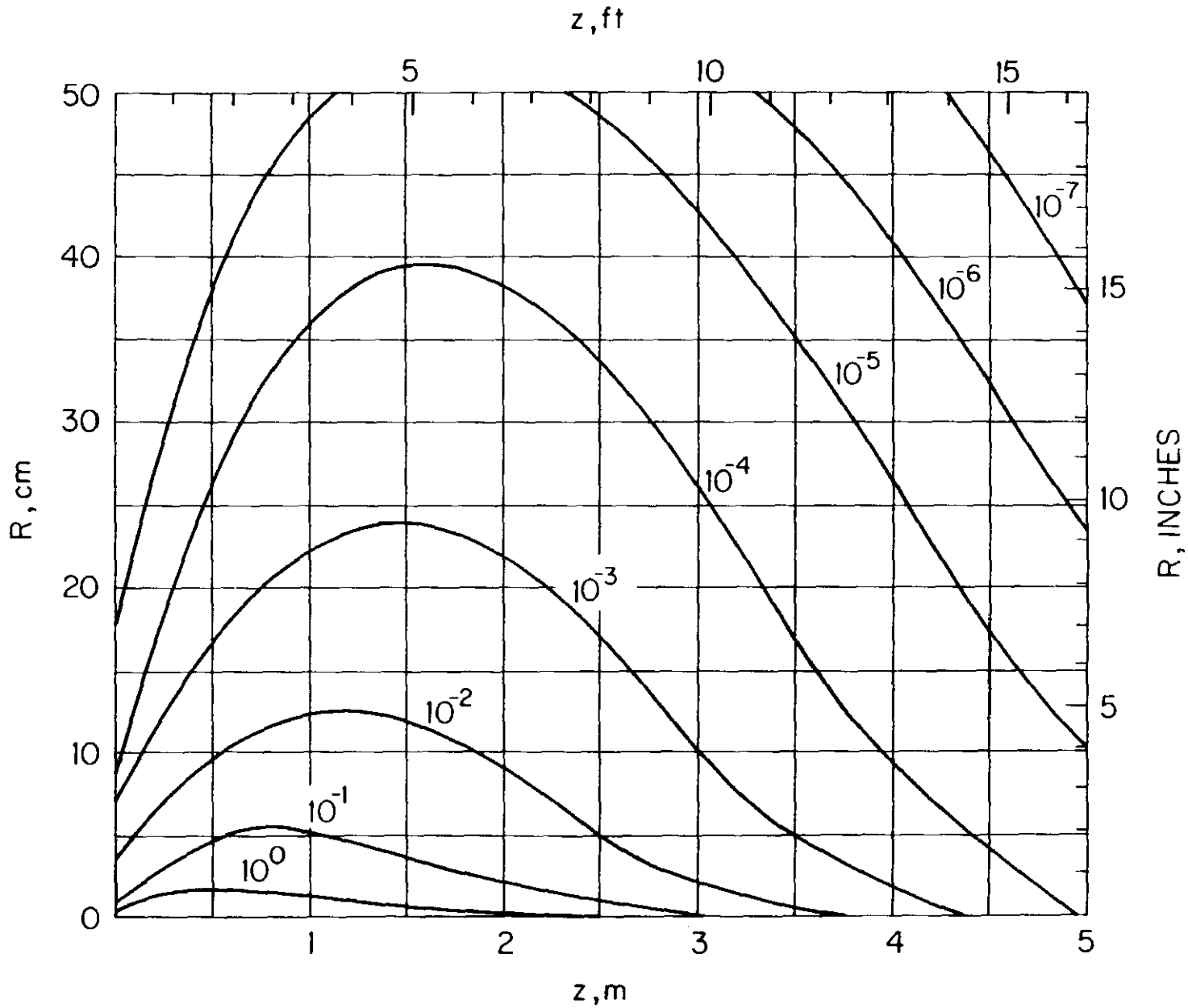

Fig. 56. Contours of equal energy density (in GeV/cm^3•incident proton) for 20 TeV protons incident on solid lead cylinder. The beam has a bi-Gaussian spatial distribution with $\sigma_x=\sigma_y=0.1$cm and is parallel to and centered on the cylinder axis. Some contours may be omitted for clarity or due to statistical uncertainty.

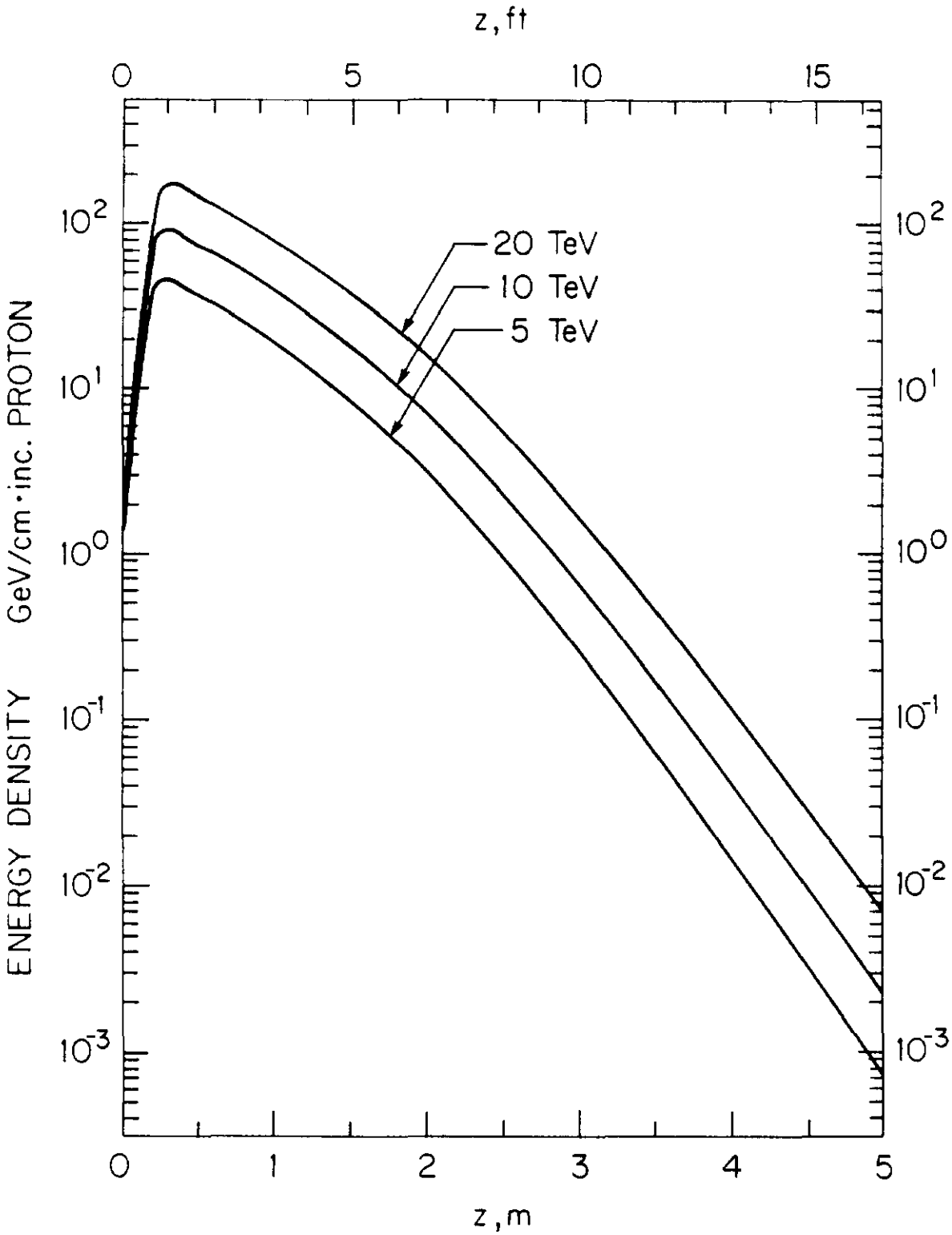

Fig. 57. Radially integrated energy density (in GeV/cm•incident proton) for 5, 10 and 20 TeV protons incident on 5m long solid lead cylinder.

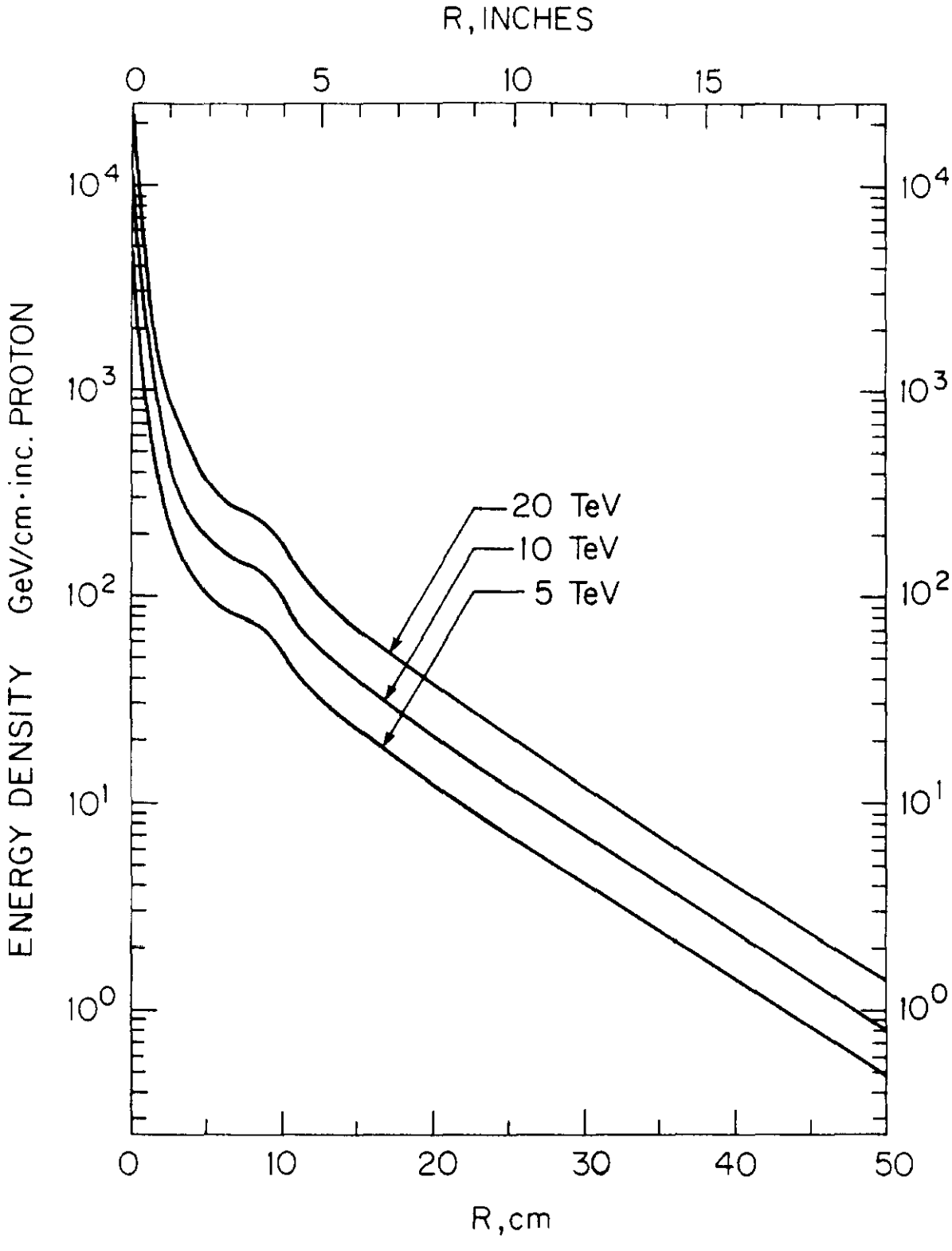

Fig. 58. Longitudinally integrated energy density (in GeV/cm•incident proton) for 5, 10 and 20 TeV protons incident on 0.5m radius solid lead cylinder.

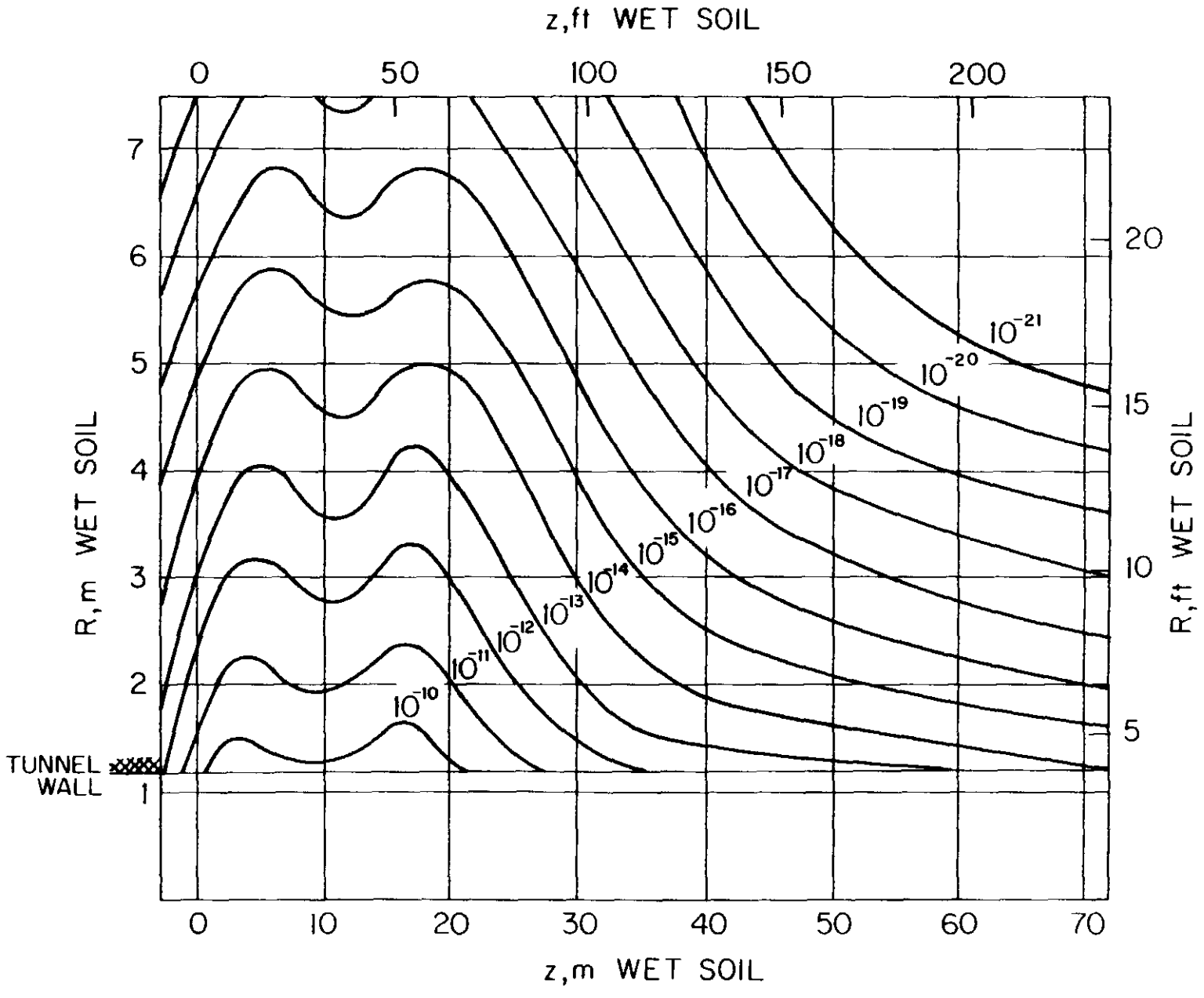

Fig. 59. Contours of equal dose equivalent (in rem/interacting proton) in soil around tunnel when 5 TeV protons are lost on the inside (with respect to the center of the ring) of the beampipe of a continuous dipole (see fig. 73). The protons interact at zero depth. Some contours may be omitted for clarity or due to statistical uncertainty.

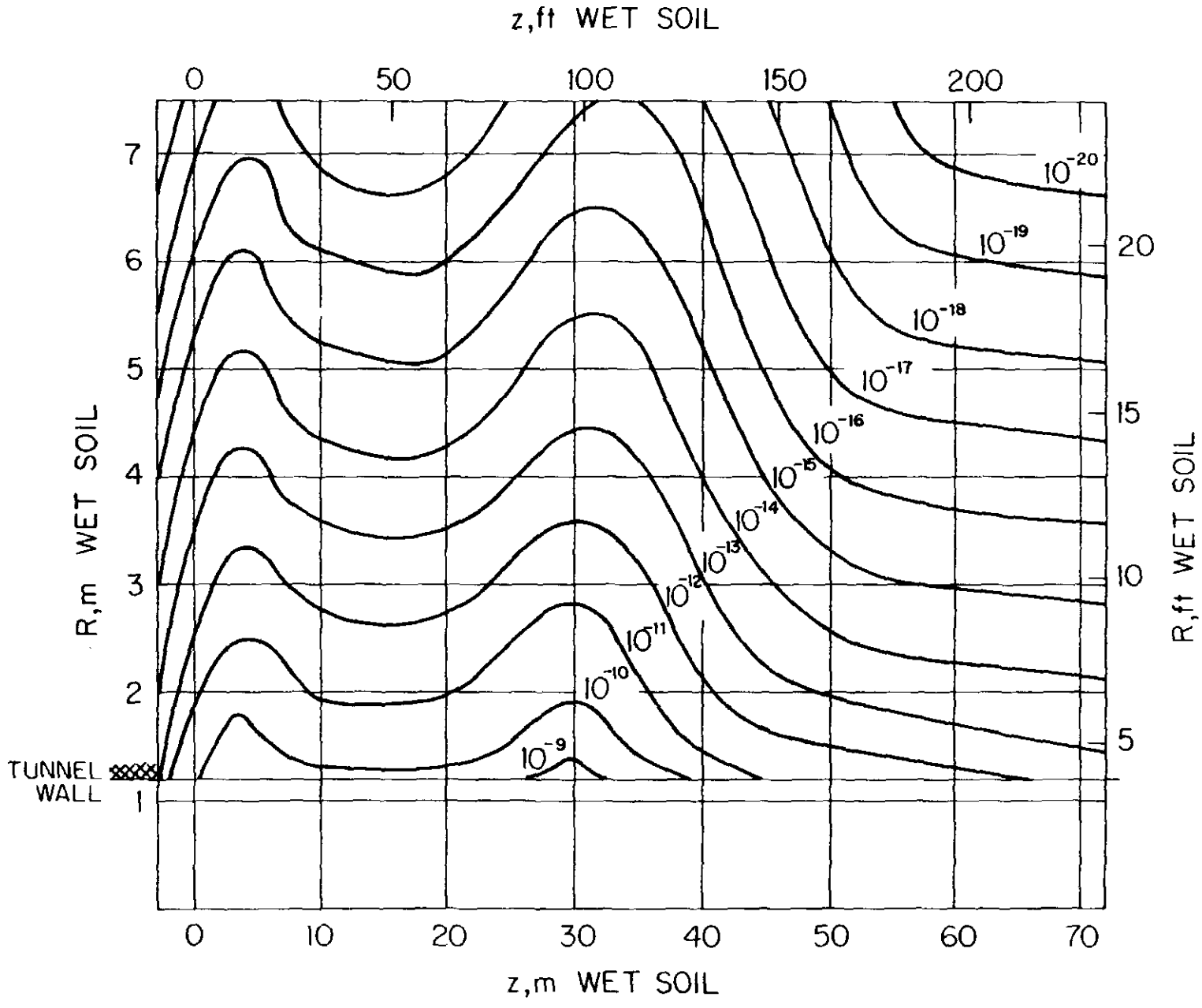

Fig. 60. Contours of equal dose equivalent (in rem/interacting proton) in soil around tunnel when 20 TeV protons are lost on the inside (with respect to the center of the ring) of the beampipe of a continuous dipole (see fig. 73). The protons interact at zero depth. Some contours may be omitted for clarity or due to statistical uncertainty.

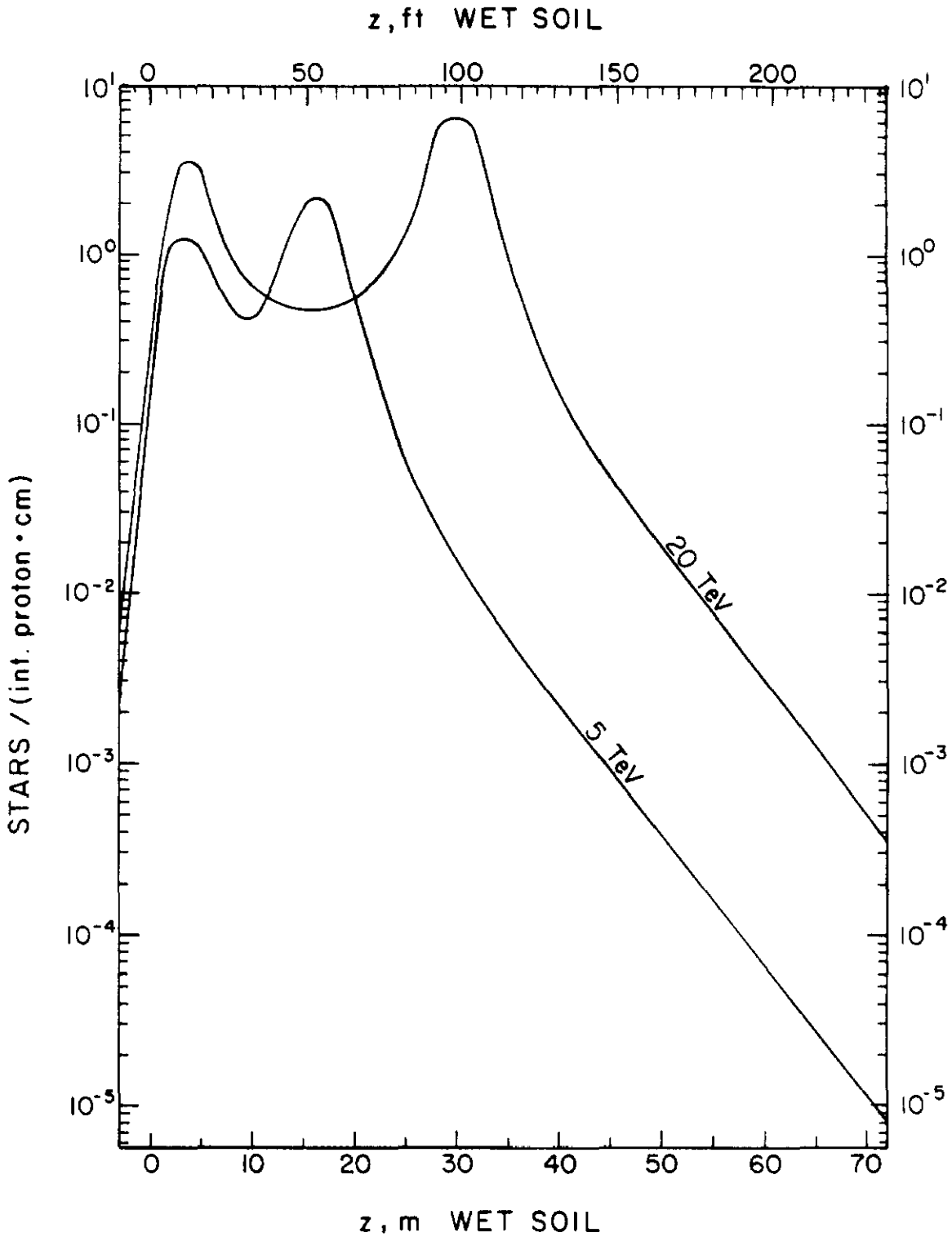

Fig. 61. Radially integrated star density (in stars/cm•interacting proton) in soil shield around a 1.2m radius tunnel for 5 and 20 TeV protons interacting on the inside (with respect to the ring) of the beampipe of a continuous dipole inside the tunnel. The protons interact at zero depth. The calculation has a cut-off momentum of 0.3 GeV/c.

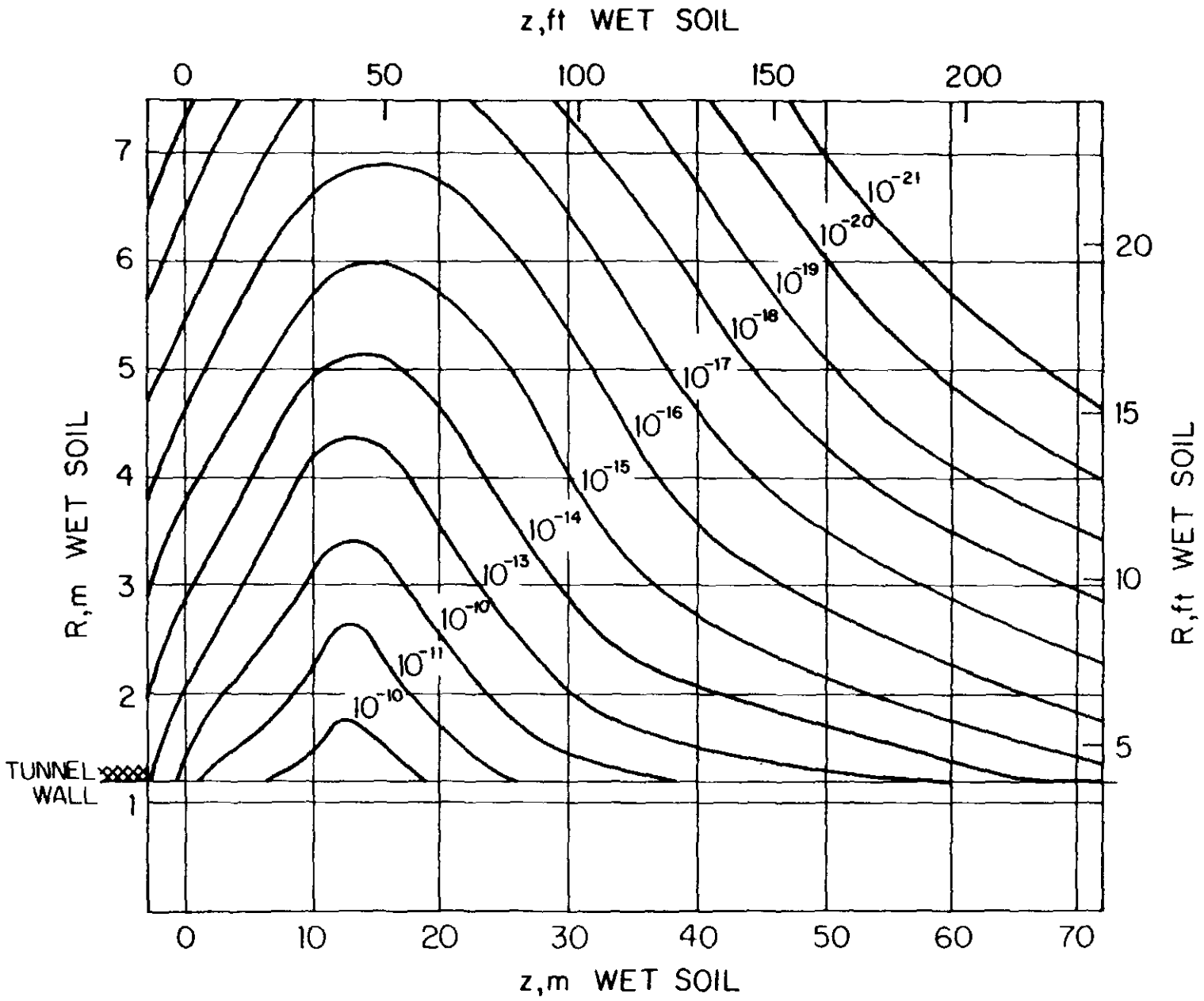

Fig. 62. Contours of equal dose equivalent (in rem/interacting proton) in soil around tunnel when 5 TeV protons are lost in the middle of the beampipe of a continuous dipole (see fig. 73). The protons interact at zero depth. Some contours may be omitted for clarity or due to statistical uncertainty.

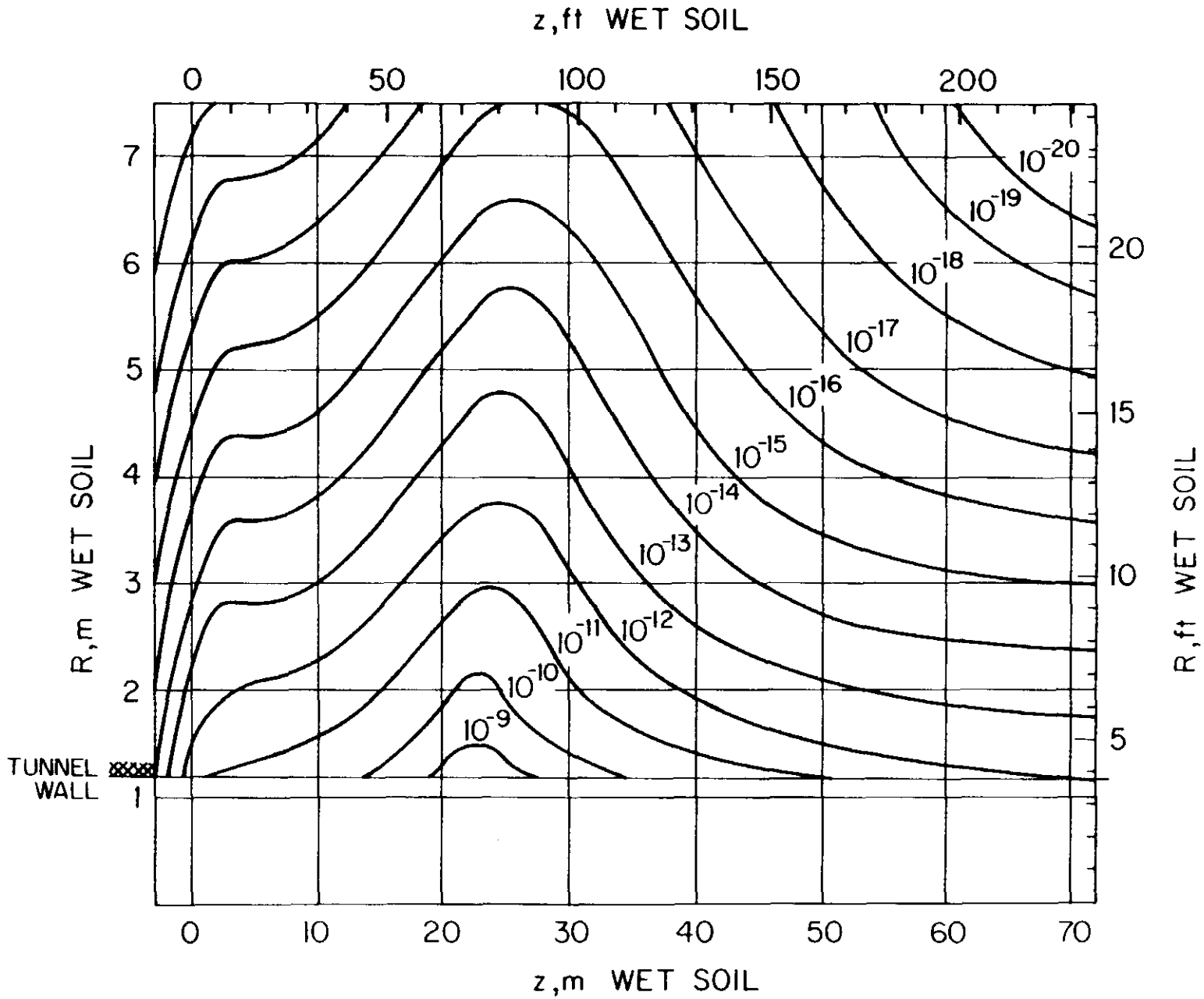

Fig. 63. Contours of equal dose equivalent (in rem/interacting proton) in soil around tunnel when 20 TeV protons are lost in the middle of the beampipe of a continuous dipole (see fig. 73). The protons interact at zero depth. Some contours may be omitted for clarity or due to statistical uncertainty.

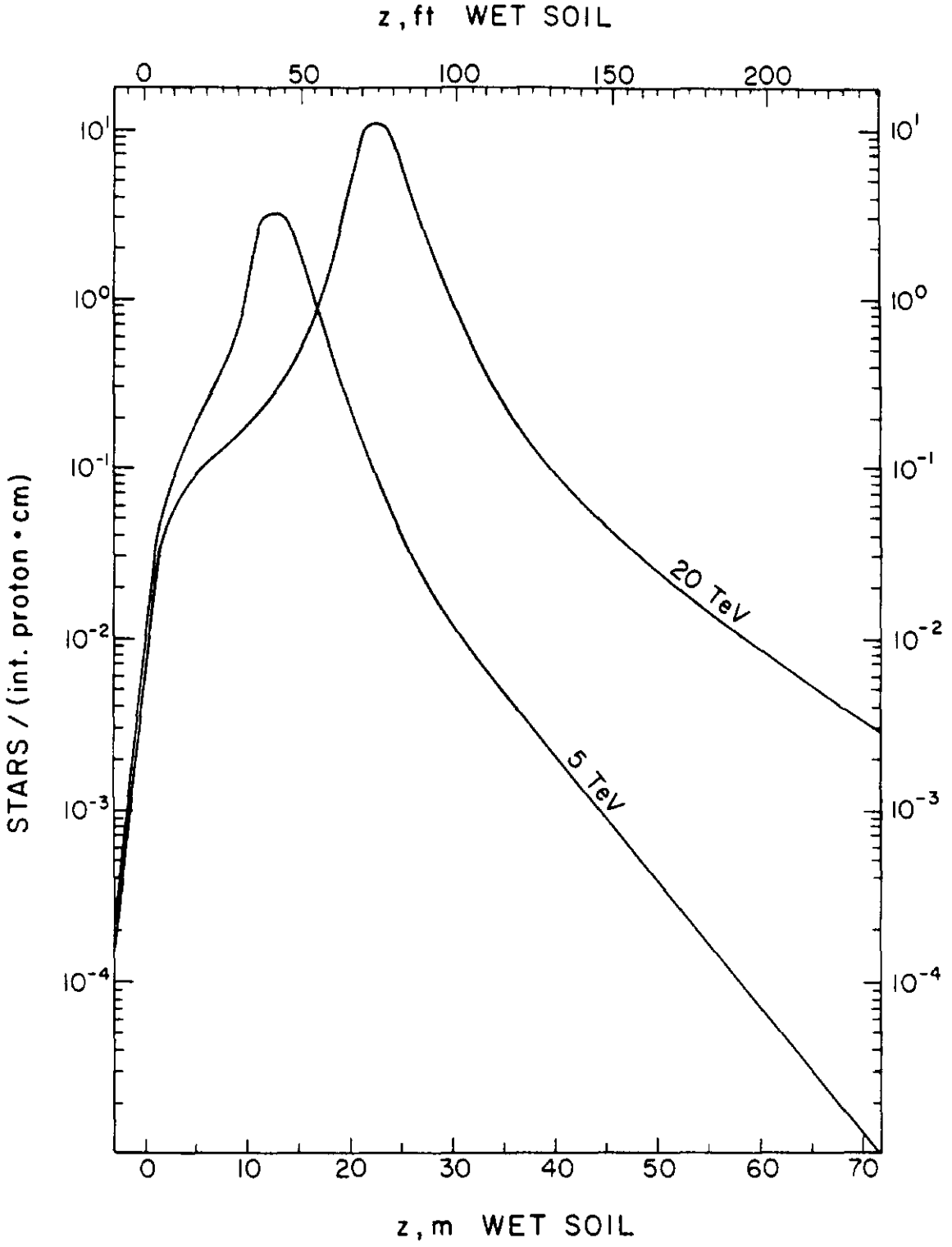

Fig. 64. Radially integrated star density (in stars/cm•interacting proton) in soil shield around a 1.2m radius tunnel for 5 and 20 TeV protons interacting in the middle of the beampipe of a continuous dipole inside the tunnel. The protons interact at zero depth. The calculation has a cut-off momentum of 0.3 GeV/c.

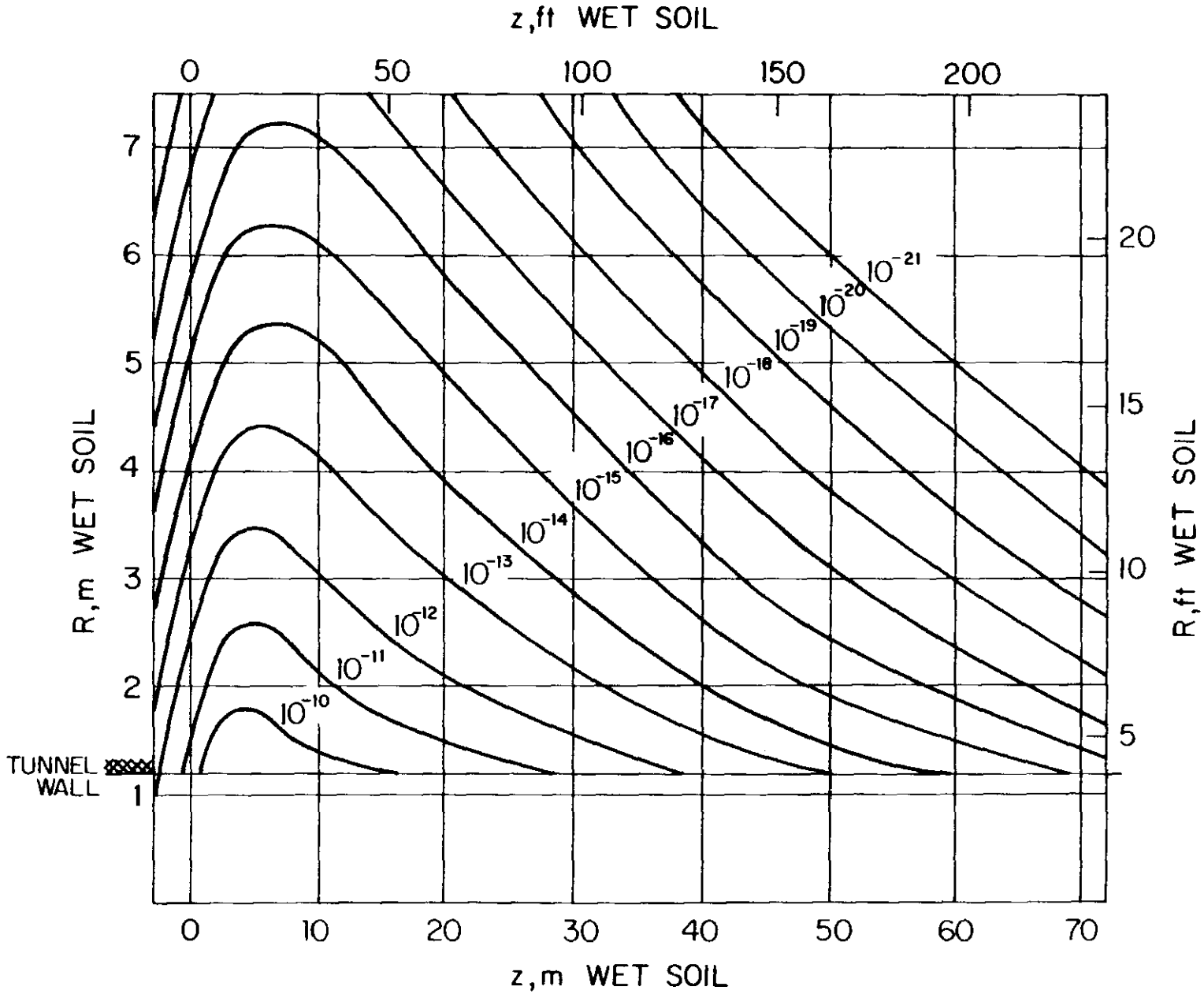

Fig. 65. Contours of equal dose equivalent (in rem/interacting proton) in soil around tunnel when 5 TeV protons are lost on the outside (with respect to the center of the ring) of the beampipe of a continuous dipole (see fig. 73). The protons interact at zero depth. Some contours may be omitted for clarity or due to statistical uncertainty.

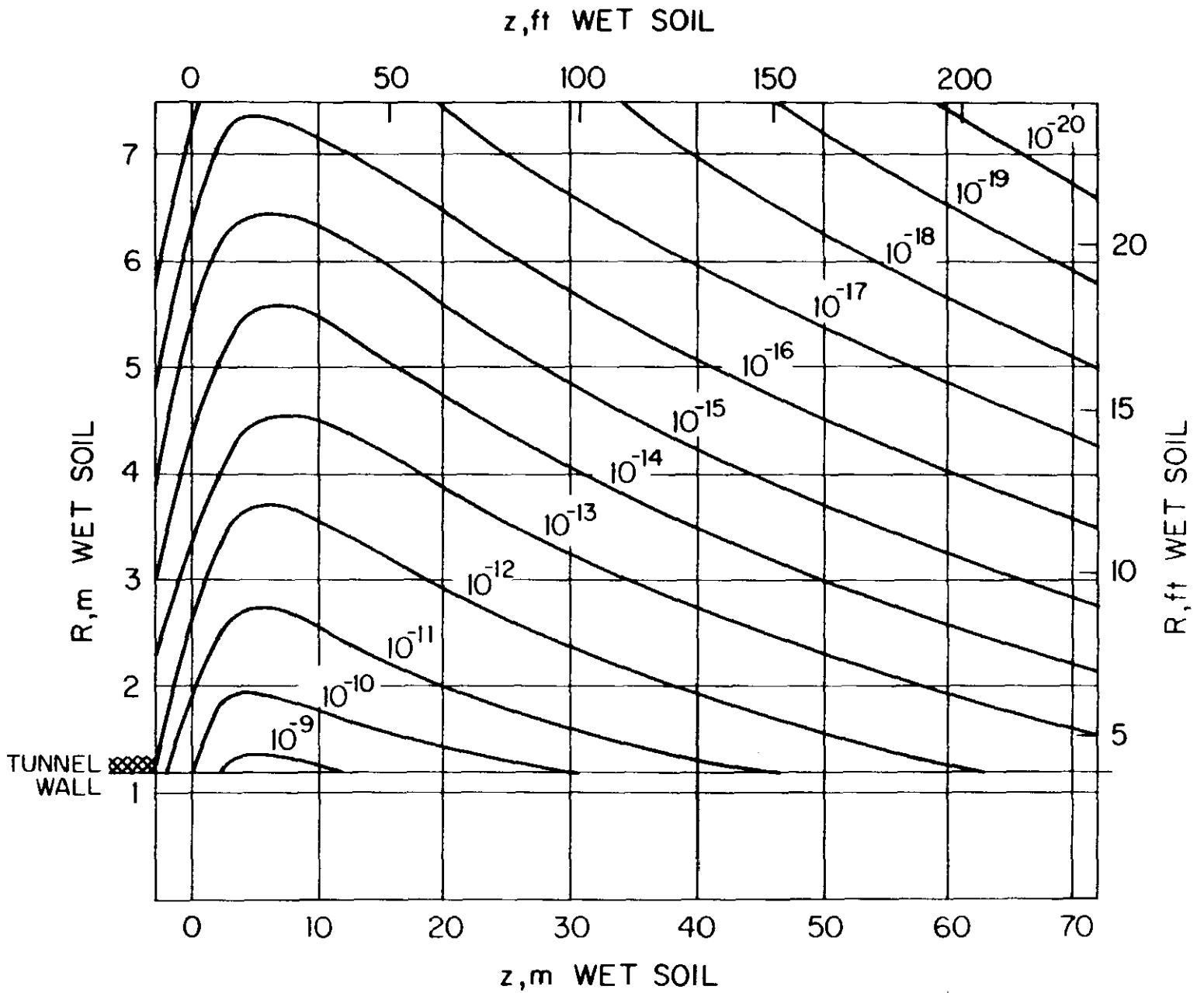

Fig. 66. Contours of equal dose equivalent (in rem/interacting proton) in soil around tunnel when 20 TeV protons are lost on the outside (with respect to the center of the ring) of the beampipe of a continuous dipole (see fig. 73). The protons interact at zero depth. Some contours may be omitted for clarity or due to statistical uncertainty.

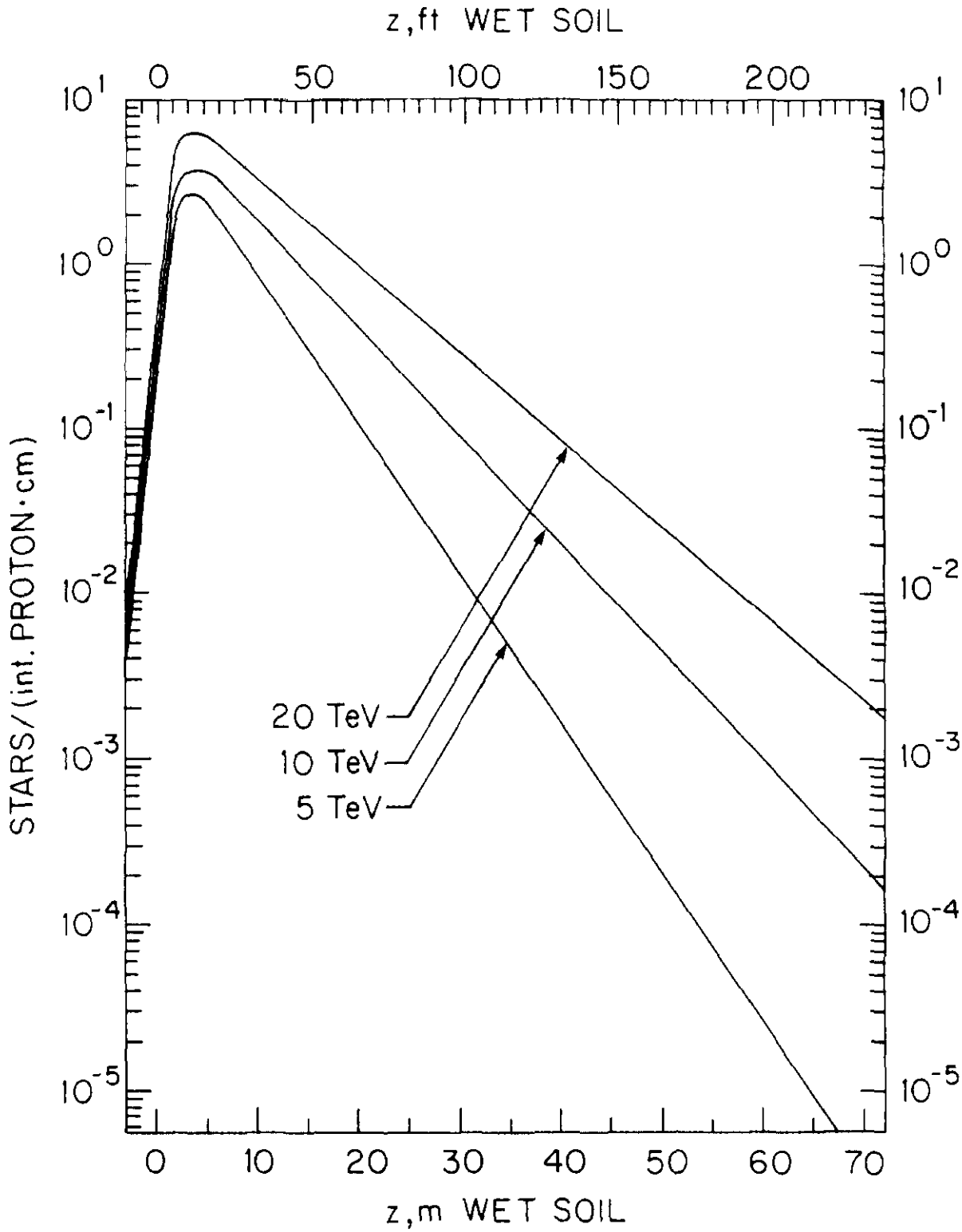

Fig. 67. Radially integrated star density (in stars/cm•interacting proton) in soil shield around a 1.2m radius tunnel for 5 and 20 TeV protons interacting on the outside (with respect to the ring) of the beampipe of a continuous dipole inside the tunnel. The protons interact at zero depth. The calculation has a cut-off momentum of 0.3 GeV/c.

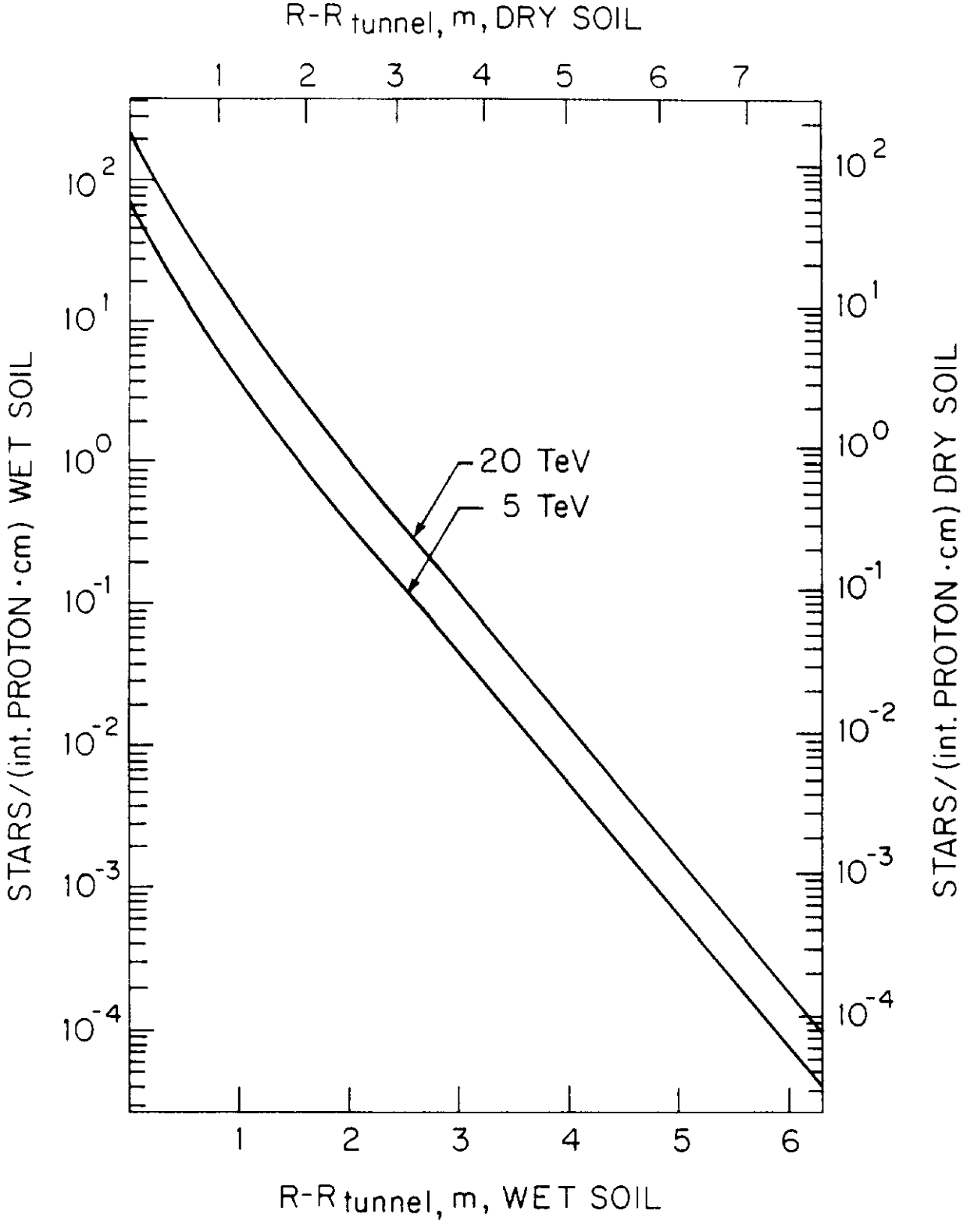

Fig. 68. Longitudinally integrated star density (in stars/cm•interacting proton) in soil shield around a 1.2m radius tunnel for 5 and 20 TeV protons interacting on the outside (with respect to the ring) of the beampipe of a continuous dipole inside the tunnel. For wet soil use left & bottom axes and for dry soil right & top axes. The calculation has a cut-off momentum of 0.3 GeV/c.

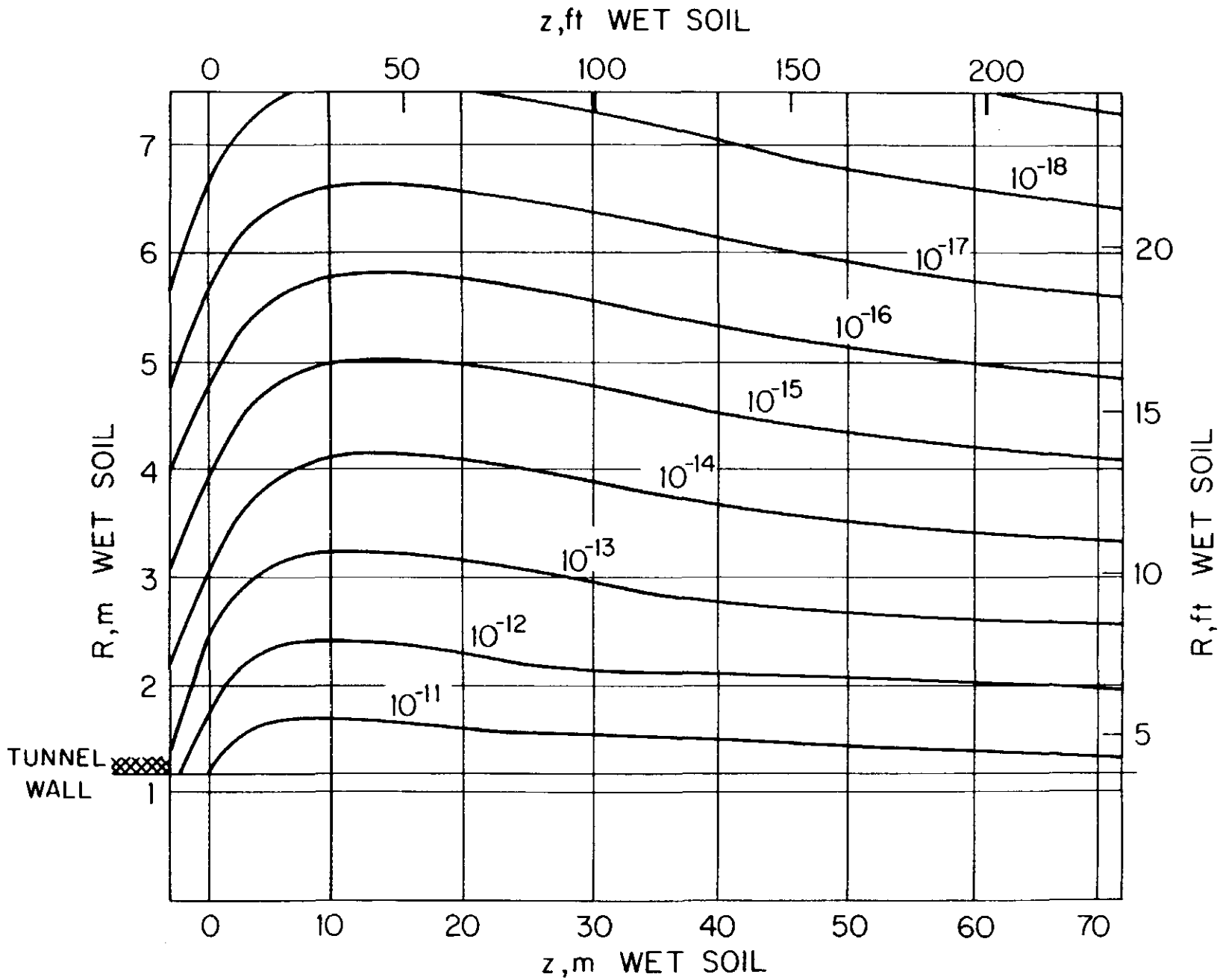

Fig. 69. Contours of equal dose equivalent (in rem/interacting proton) in soil around tunnel when 5 TeV protons are lost on the side of a bare beampipe. The protons interact at zero depth. Some contours may be omitted for clarity or due to statistical uncertainty.

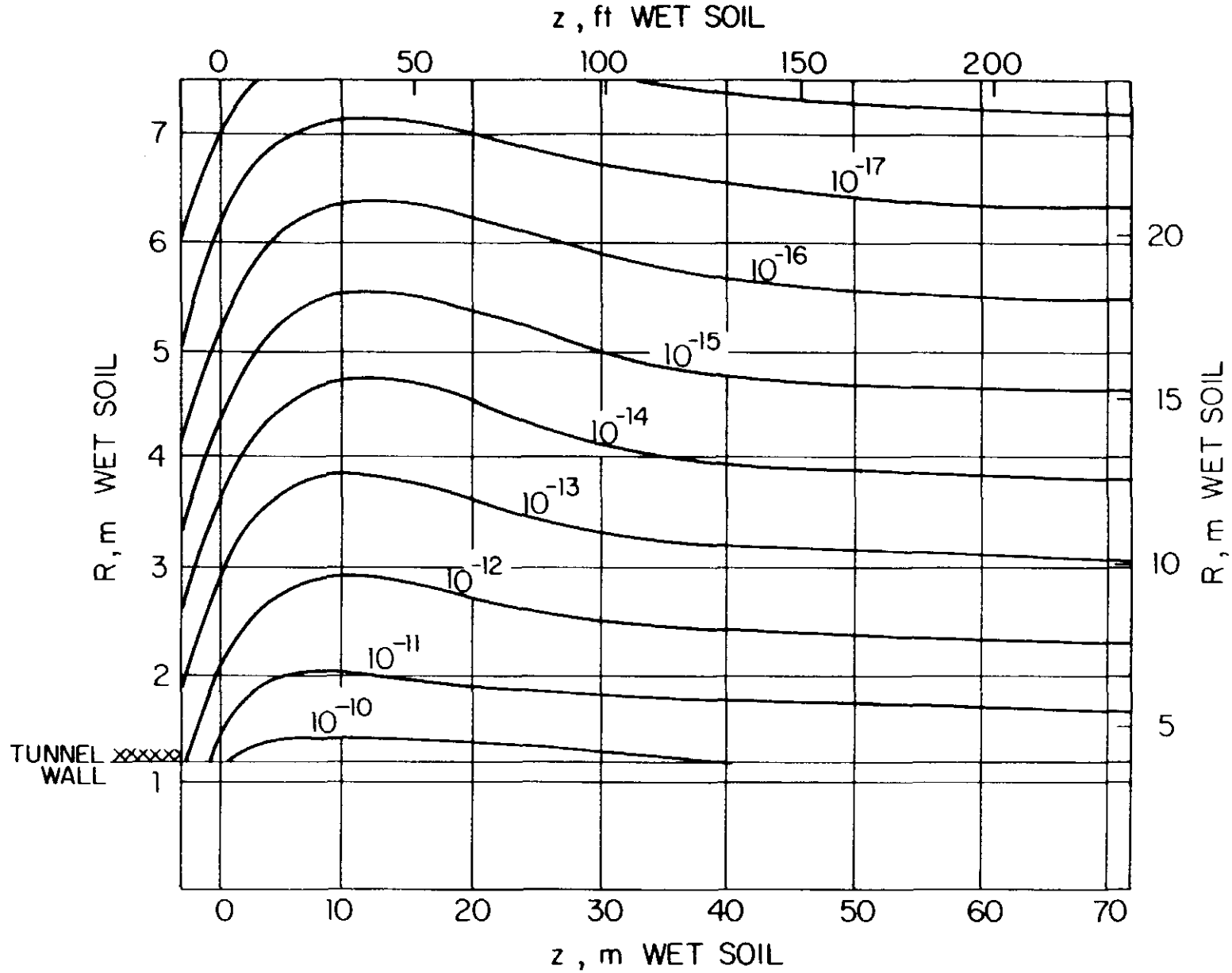

Fig. 70. Contours of equal dose equivalent (in rem/interacting proton) in soil around tunnel when 20 TeV protons are lost on the side of a bare beampipe. The protons interact at zero depth. Some contours may be omitted for clarity or due to statistical uncertainty.

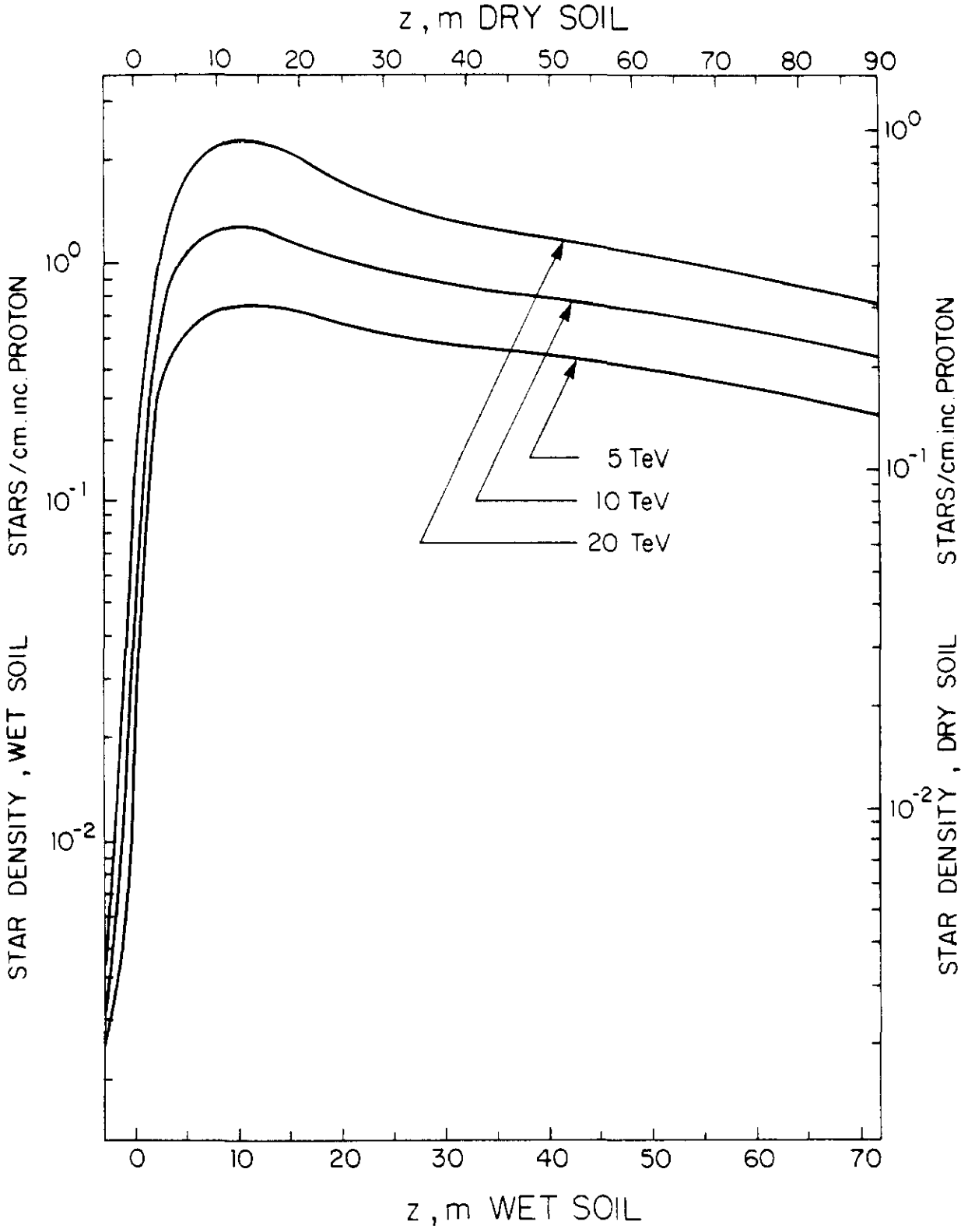

Fig. 71. Radially integrated star density (in stars/cm•interacting proton) in soil shield around a 1 .2m radius tunnel for 5 and 20 TeV protons interacting on the side of a bare beampipe inside the tunnel. The protons interact at zero depth. The calculation has a cut-off momentum of 0.3 GeV/c.

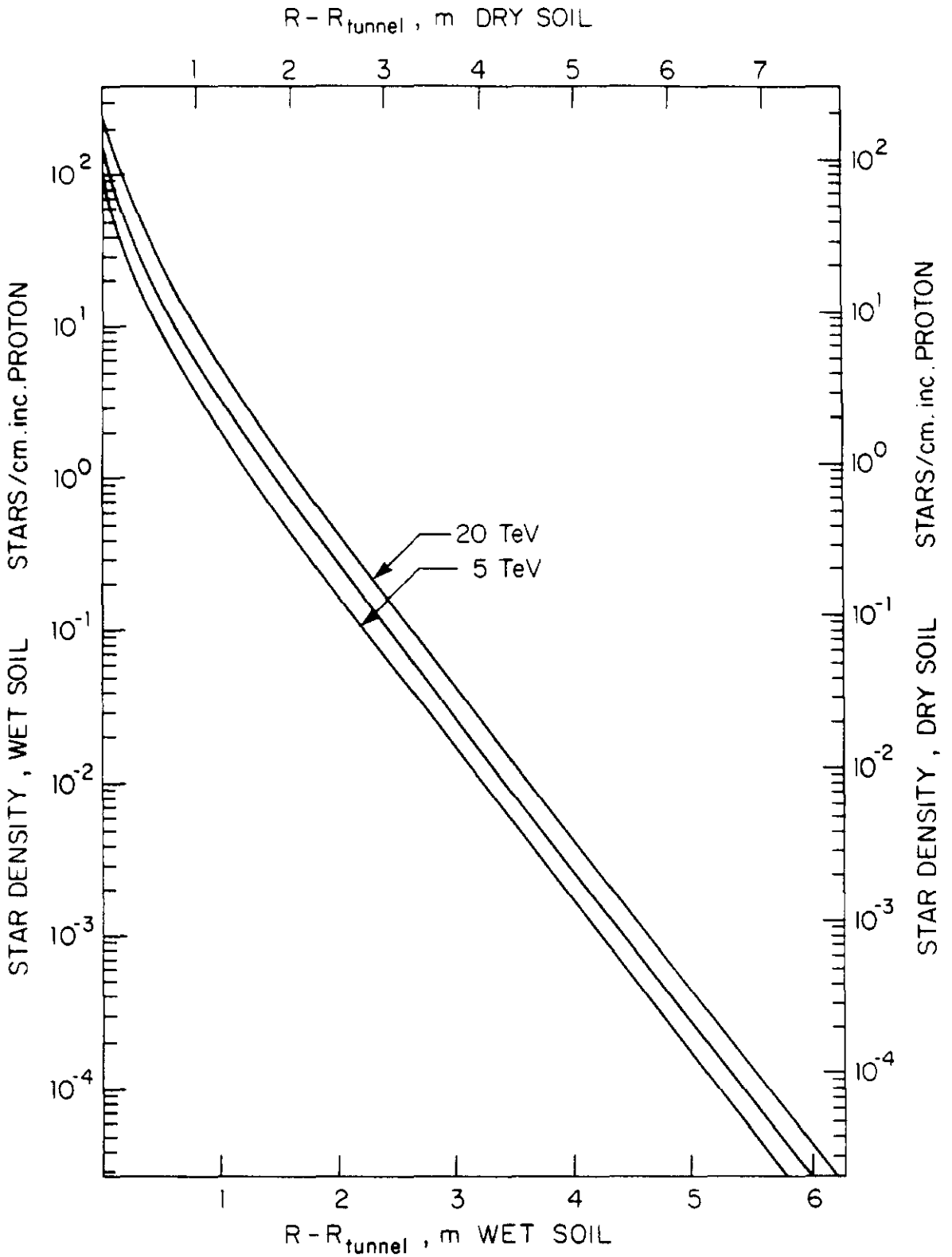

Fig. 72. Longitudinally integrated star density (in stars/cm•interacting proton) in soil shield around a 1.2m radius tunnel for 5 and 20 TeV protons interacting on the side of a bare beampipe inside the tunnel. For wet soil use left & bottom axes and for dry soil right & top axes. The calculation has a cut-off momentum of 0.3 GeV/c.

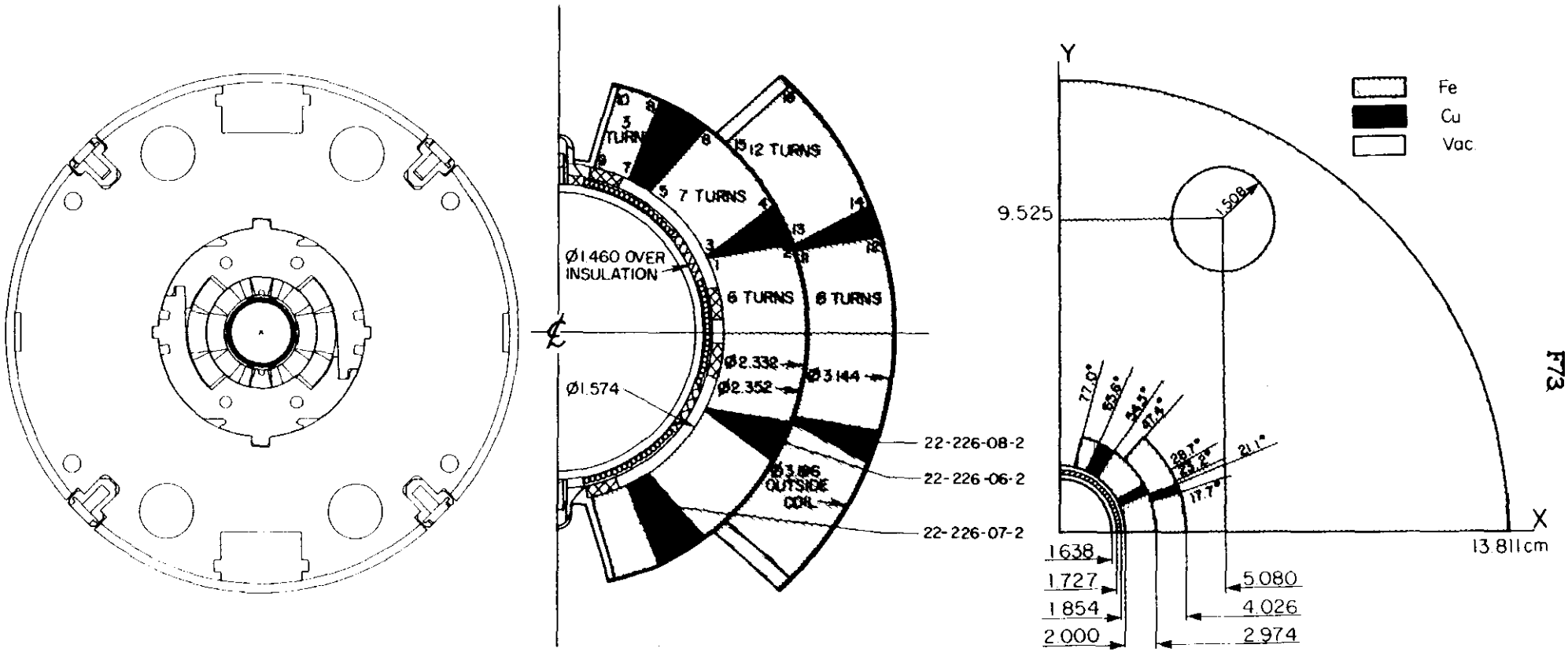

Fig. 73. Cross section of C5 magnet: engineering drawing (left), detail of coils (middle) and representation in program (right).

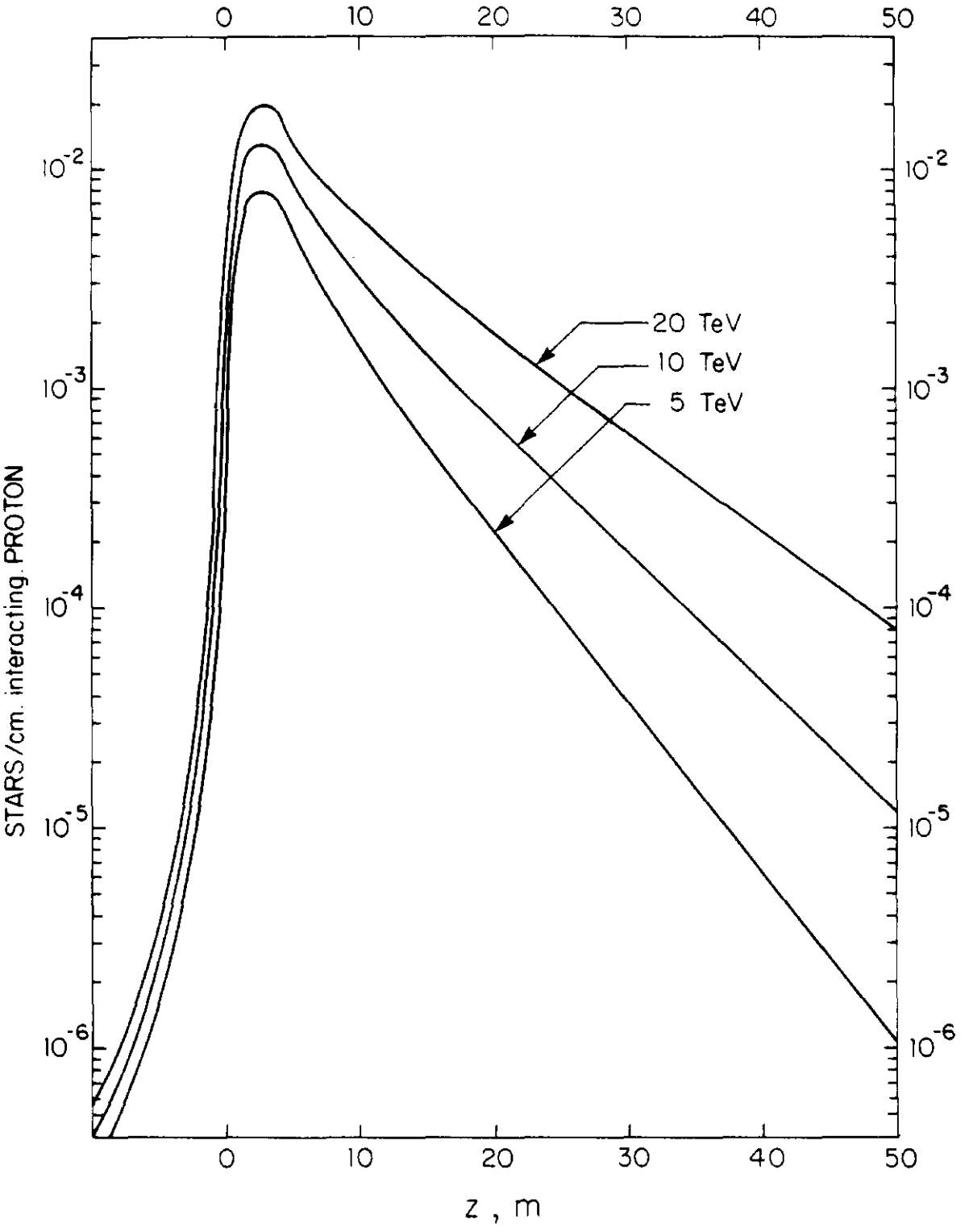

Fig. 74. Radially integrated star density (in stars/cm•interacting proton) in the air of 1.2m radius tunnel for 5, 10 and 20 TeV protons interacting in the middle of the beampipe of a continuous dipole in the tunnel. The protons interact at zero depth. The calculation has a cut-off momentum of 0.3 GeV/c.

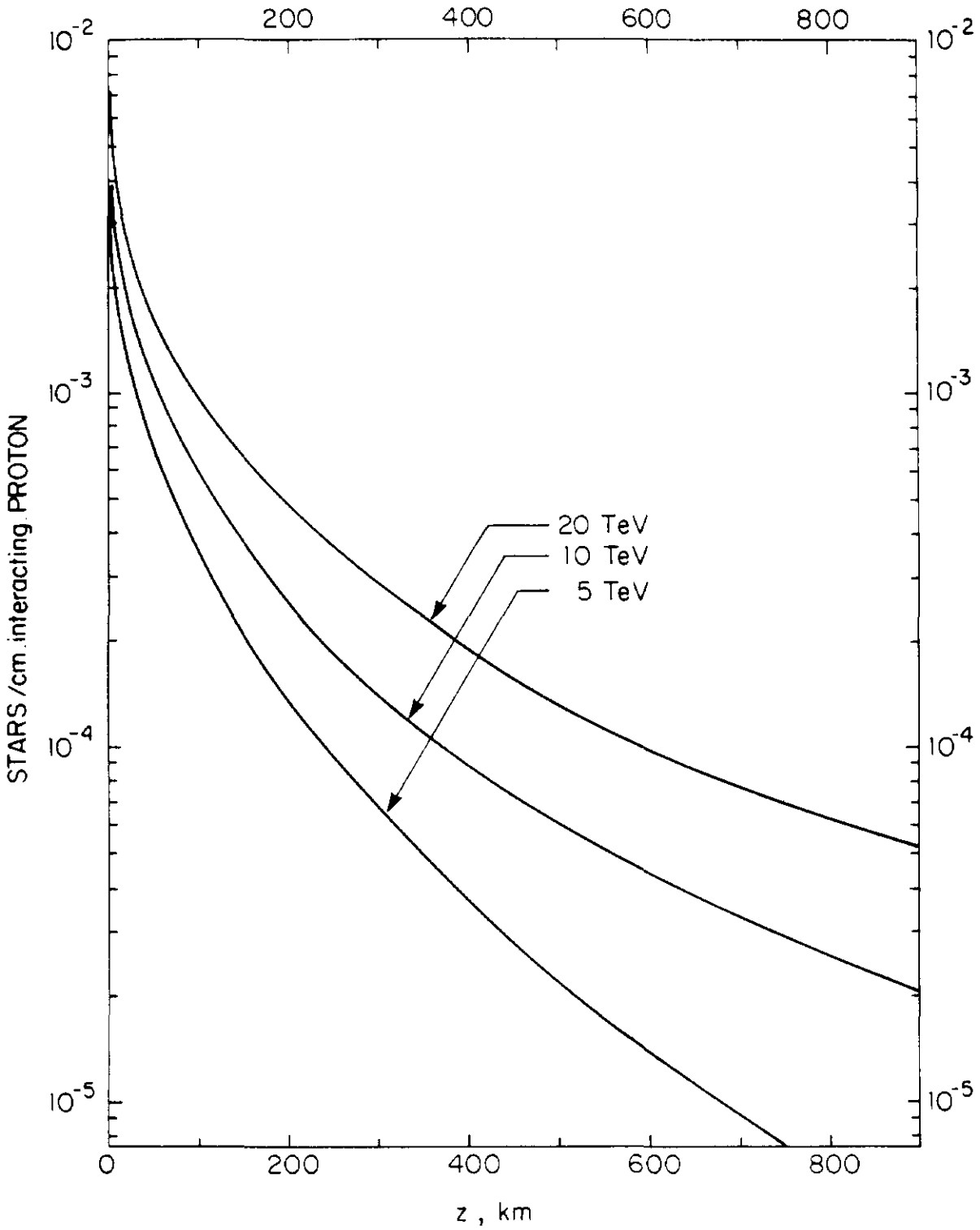

Fig. 75. Radially integrated star density (in stars/cm•interacting proton) in the air of 1.2m radius tunnel for 5, 10 and 20 TeV protons interacting on the side of a bare beampipe in the tunnel. The protons interact at zero depth. The calculation has a cut-off momentum of 0.3 GeV/c.

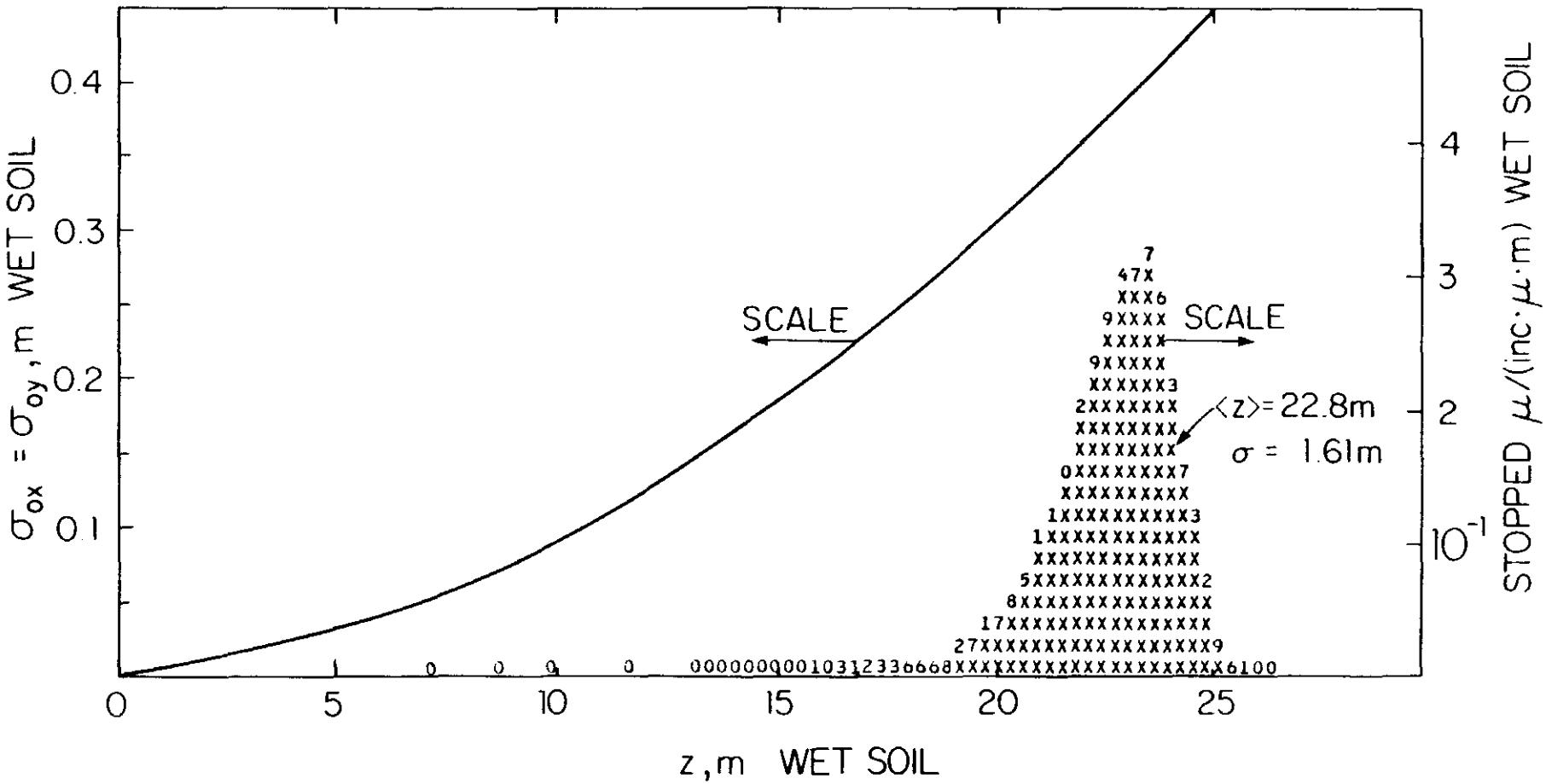

Fig. 76. Distribution in z of a pencil beam of 0.01 TeV muons stopped in soil (histogram, right scale, in m^{-1}). Projected rms spread of beam as a function of penetration (curve, left scale, in m).

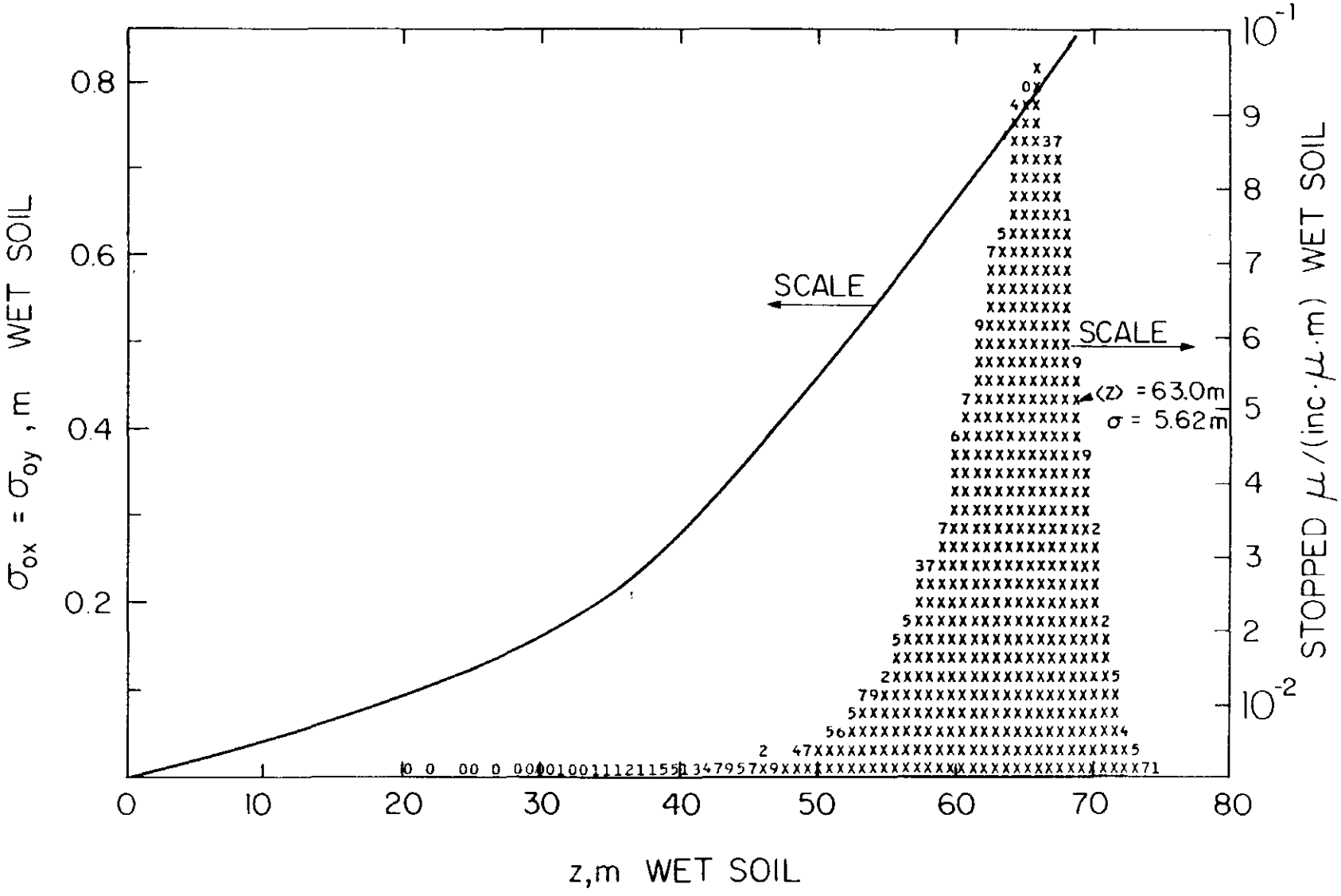

Fig. 77. Distribution in z of a pencil beam of 0.03 TeV muons stopped in soil (histogram, right scale, in m^{-1}). Projected rms spread of beam as a function of penetration (curve, left scale, in m).

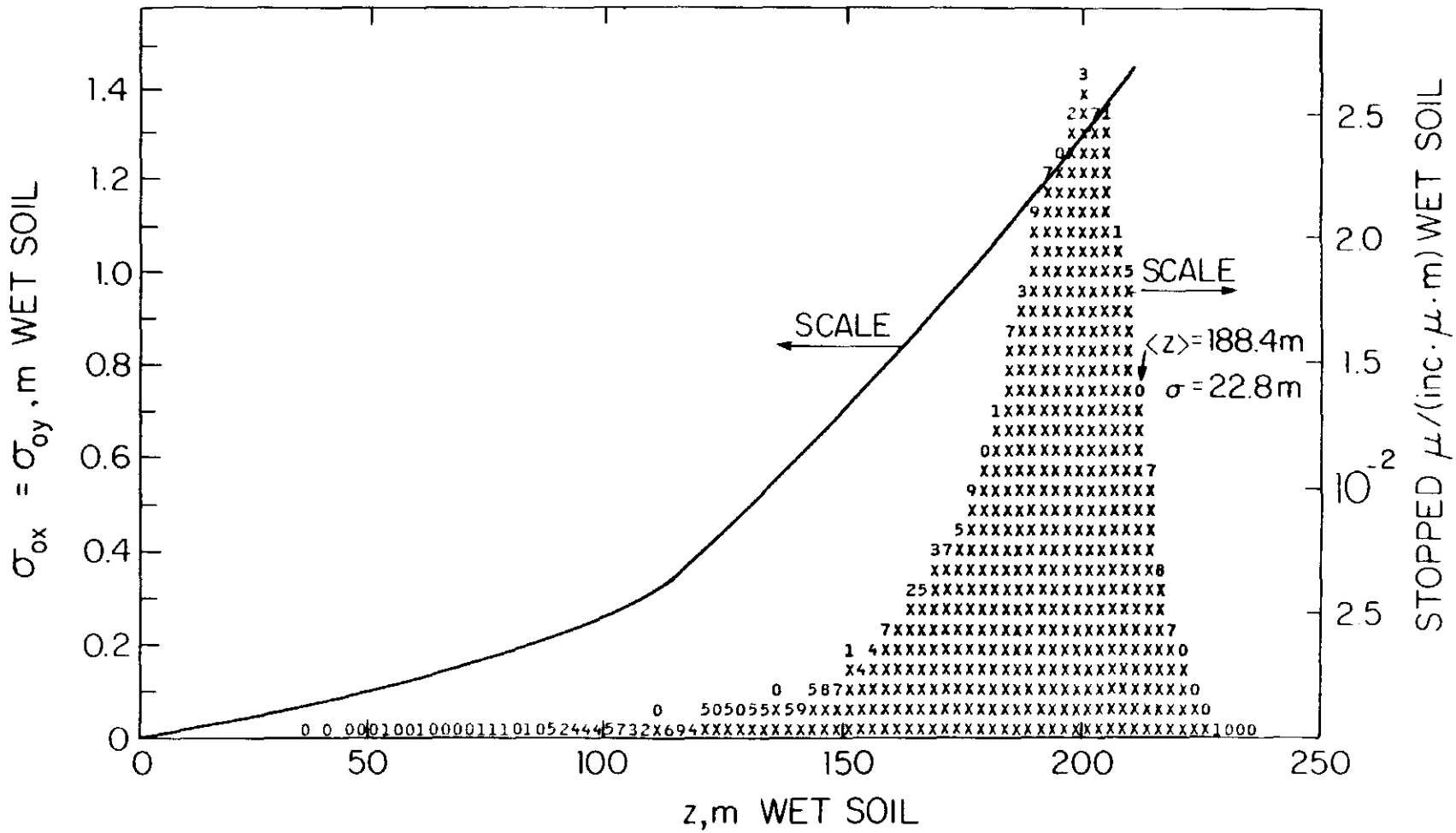

Fig. 78. Distribution in z of a pencil beam of 0.10 TeV muons stopped in soil (histogram, right scale, in m^{-1}). Projected rms spread of beam as a function of penetration (curve, left scale, in m).

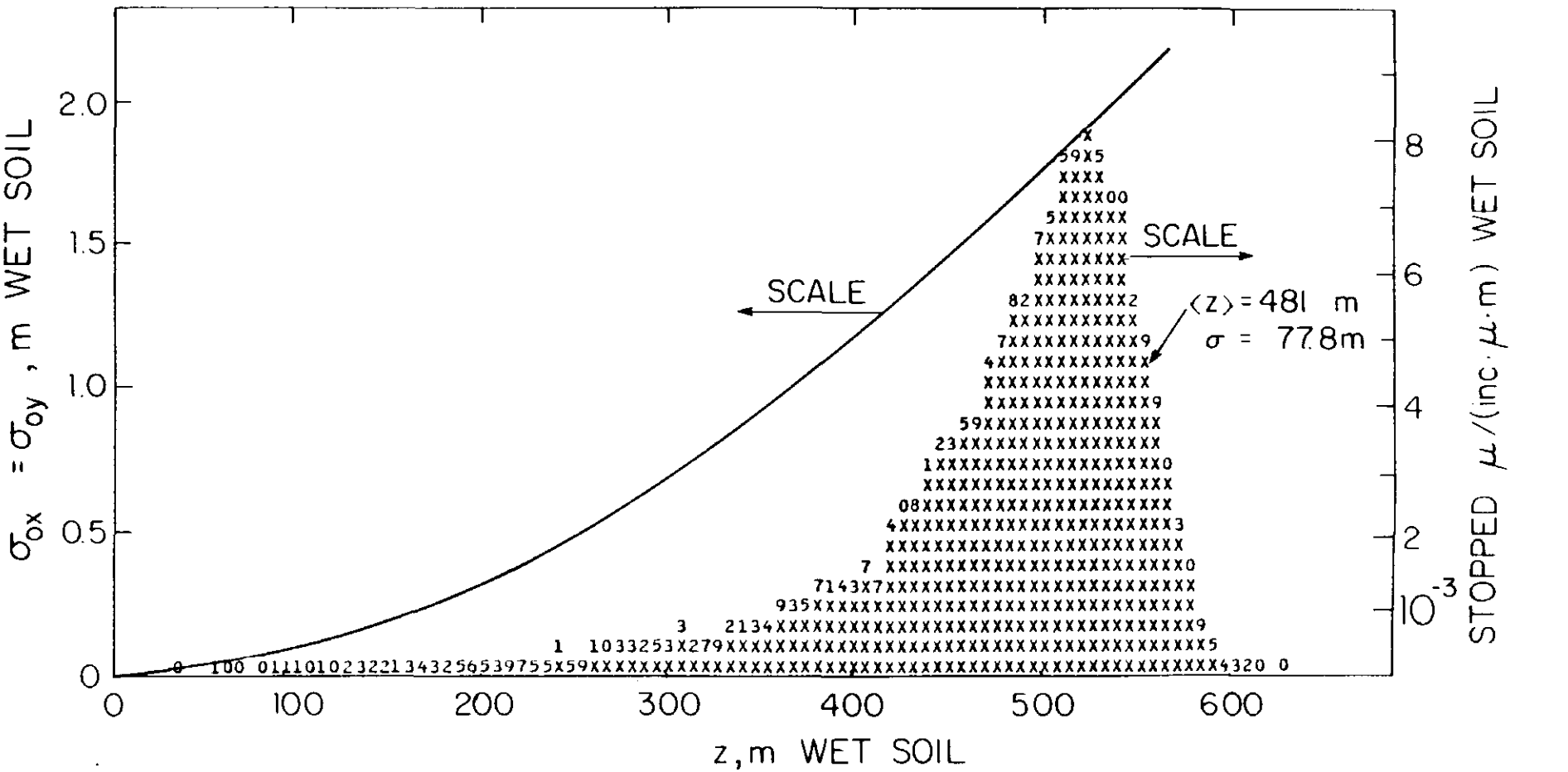

Fig. 79. Distribution in z of a pencil beam of 0.30 TeV muons stopped in soil (histogram, right scale, in m^{-1}). Projected rms spread of beam as a function of penetration (curve, left scale, in m).

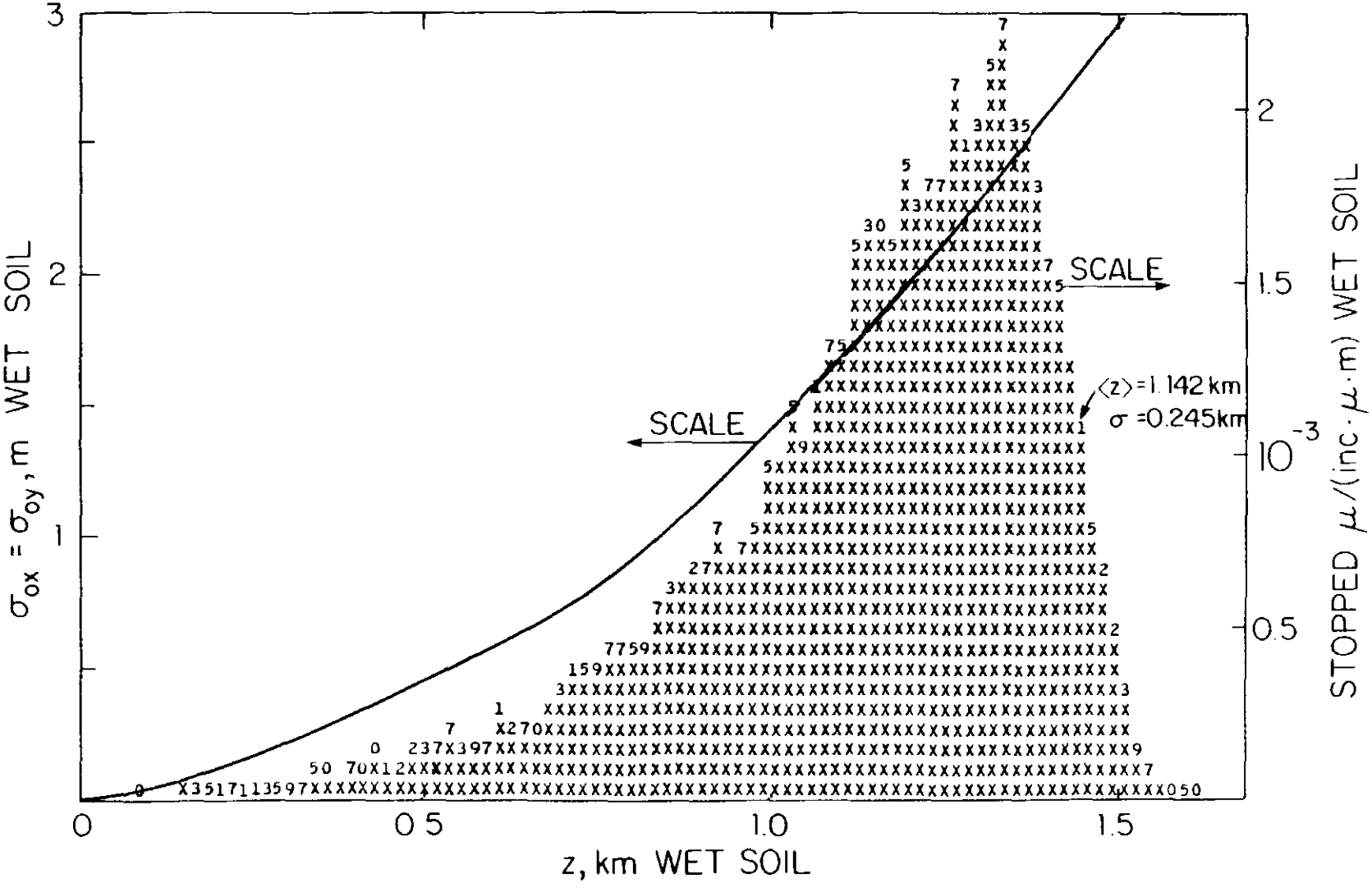

Fig. 80. Distribution in z of a pencil beam of 1.0 TeV muons stopped in soil (histogram, right scale, in m^{-1}). Projected rms spread of beam as a function of penetration (curve, left scale, in m).

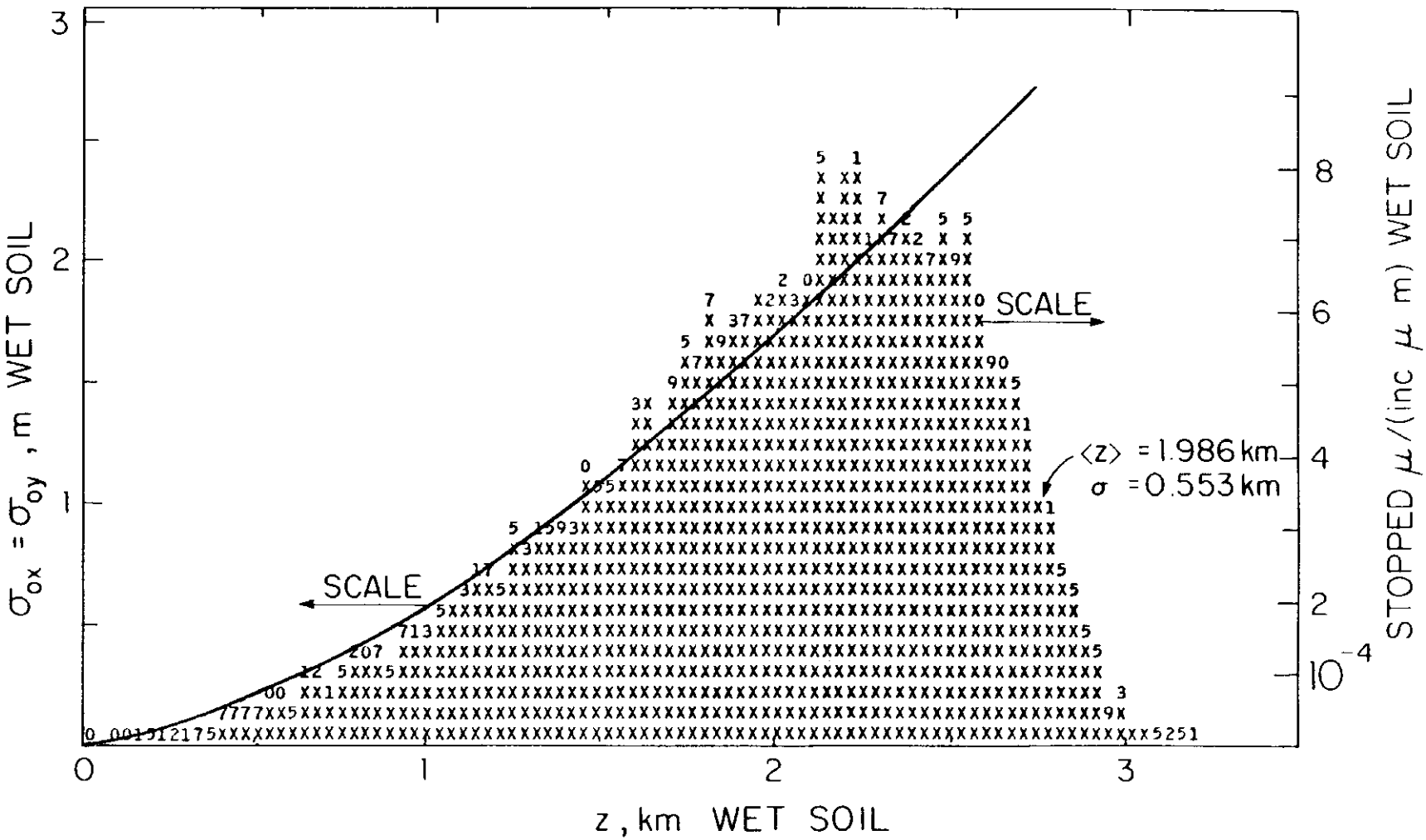

Fig. 81. Distribution in z of a pencil beam of 3.0 TeV muons stopped in soil (histogram, right scale, in m^{-1}). Projected rms spread of beam as a function of penetration (curve, left scale, in m).

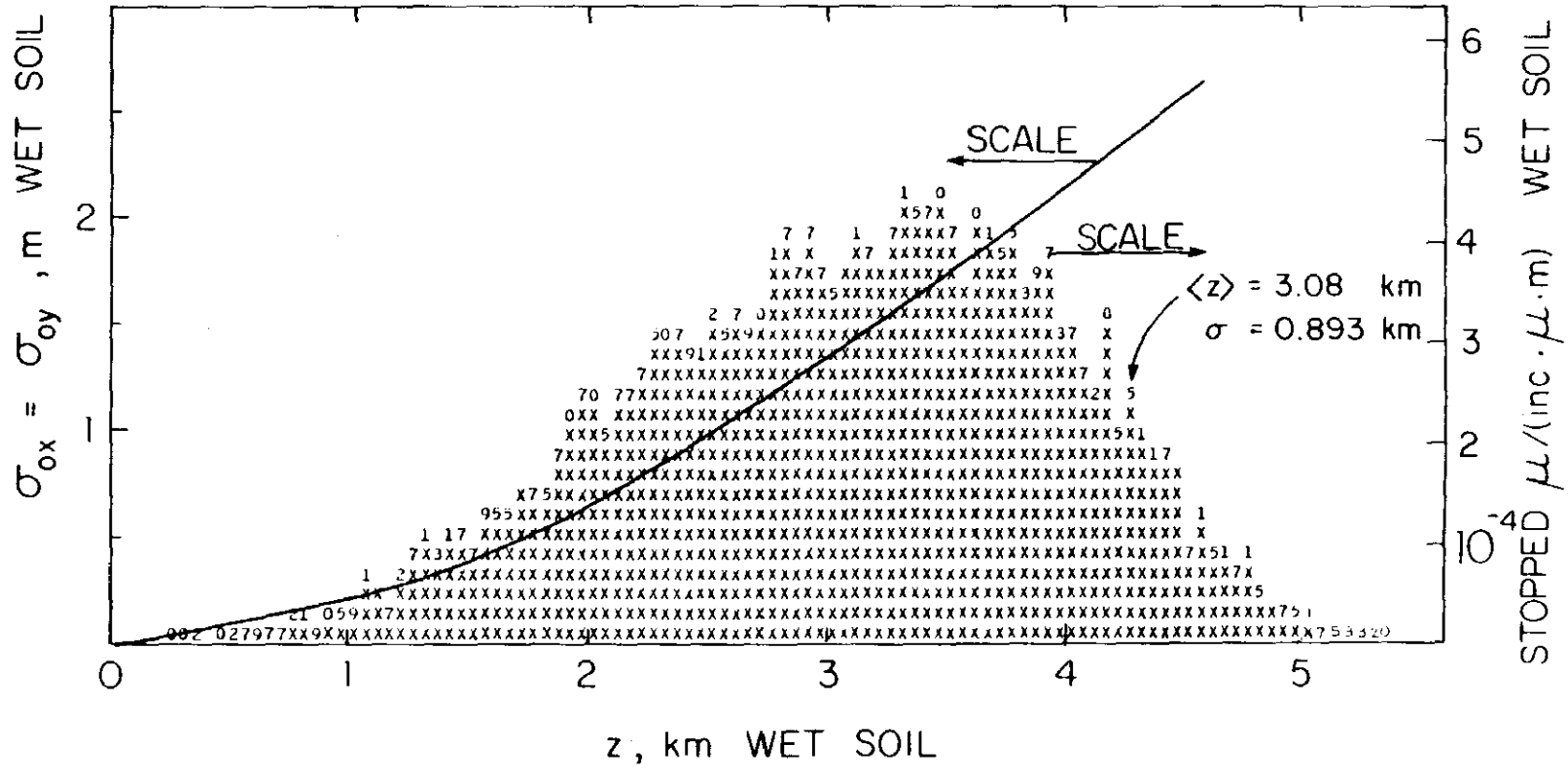

Fig. 82. Distribution in z of a pencil beam of 10.0 TeV muons stopped in soil (histogram, right scale, in m^{-1}). Projected rms spread of beam as a function of penetration (curve, left scale, in m).

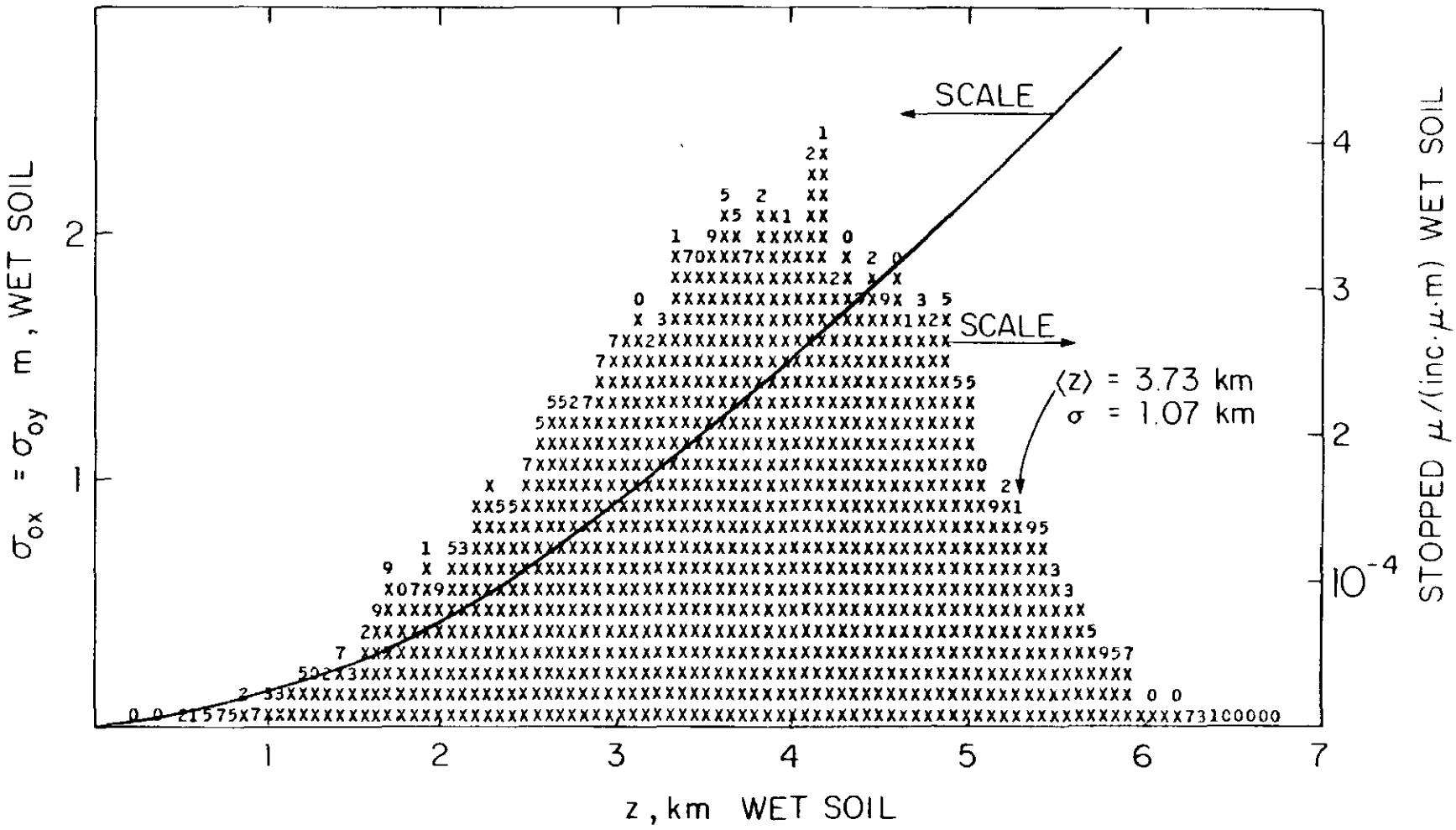

Fig. 83. Distribution in z of a pencil beam of 20.0 TeV muons stopped in soil (histogram, right scale, in m^{-1}). Projected rms spread of beam as a function of penetration (curve, left scale, in m).

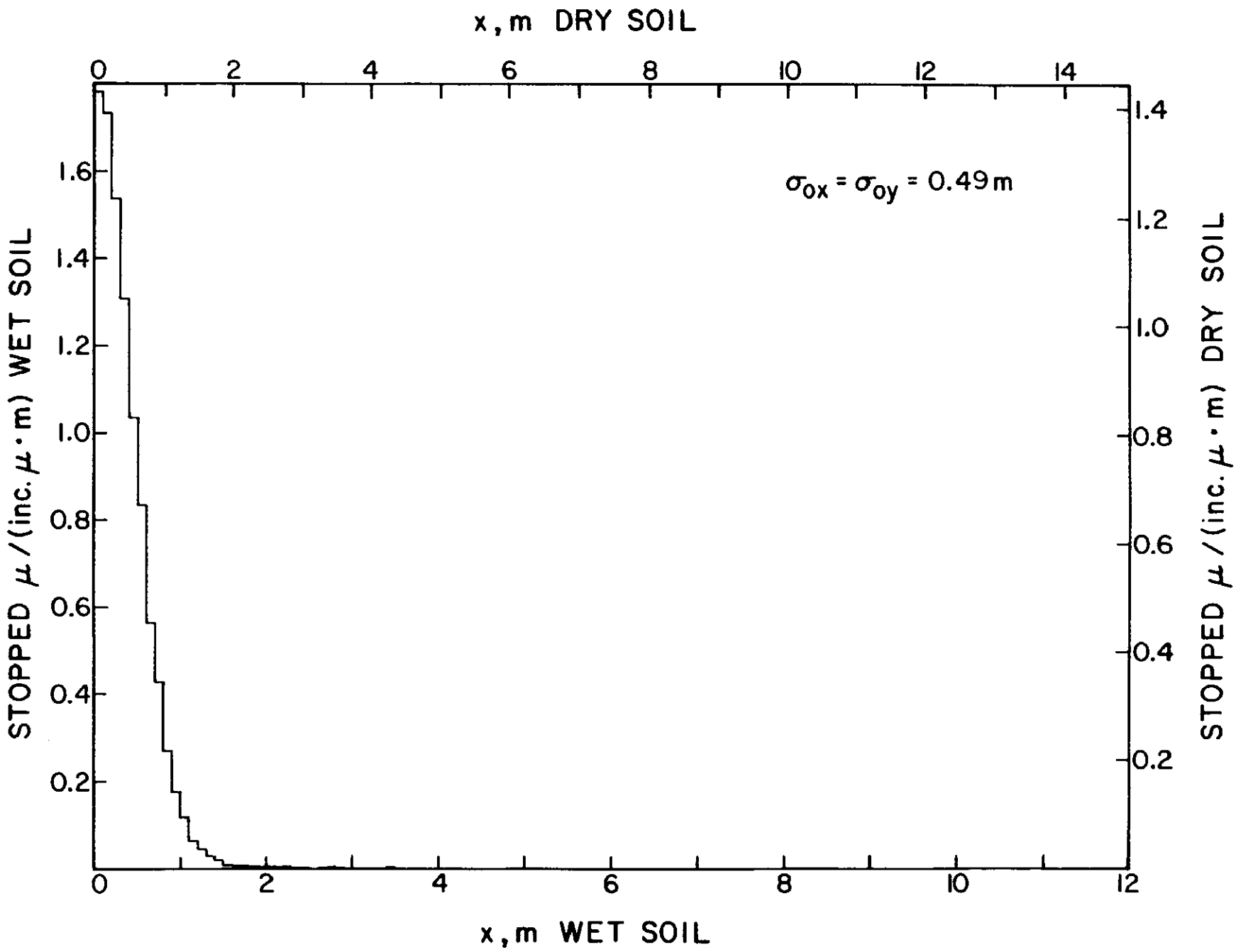

Fig. 84. Distribution in x of a pencil beam of 0.01 TeV muons stopped in soil (in m^{-1}). For wet soil use left & bottom axes and for dry soil use right & top axes.

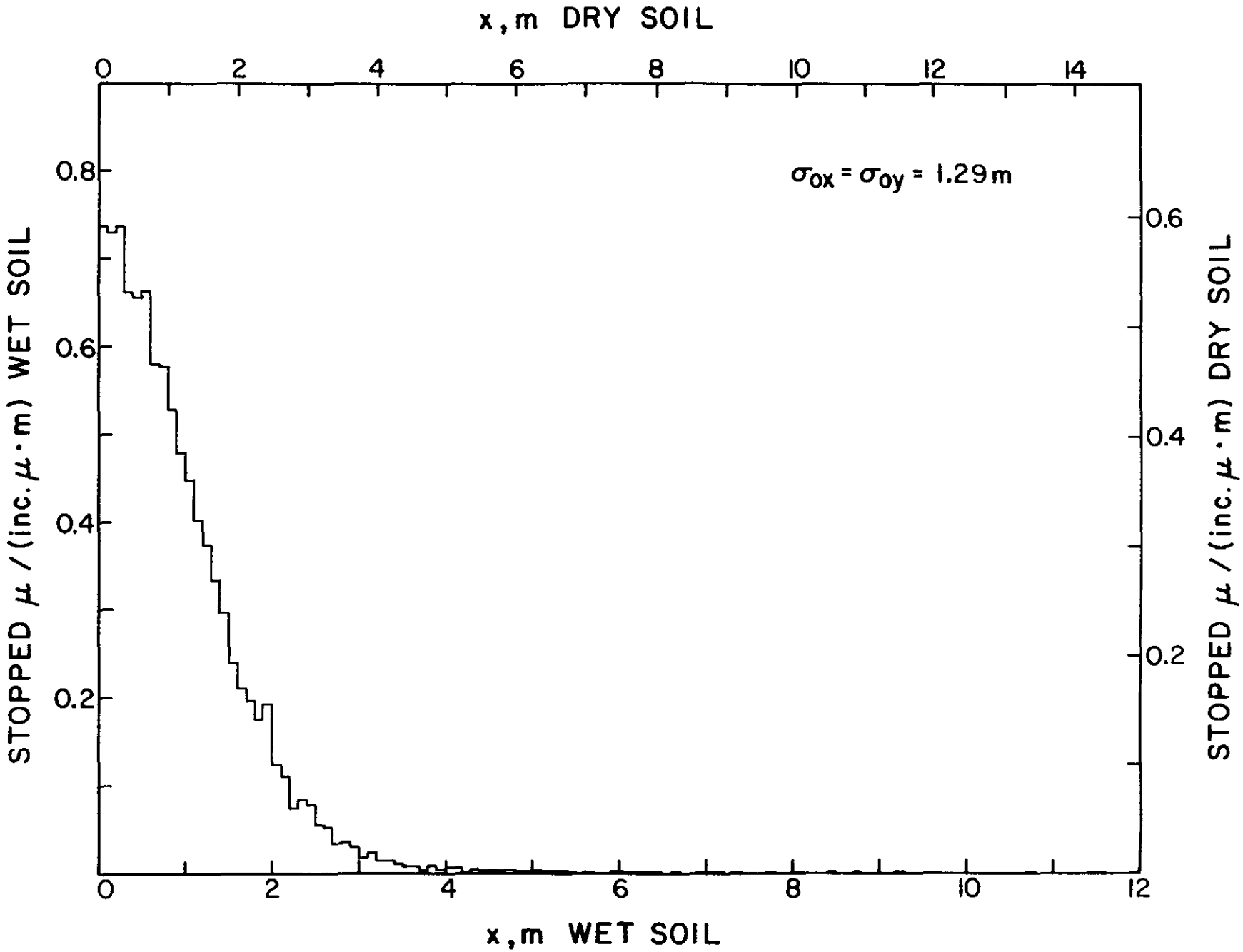

Fig. 85. Distribution in x of a pencil beam of 0.10 TeV muons stopped in soil (in m^{-1}). For wet soil use left & bottom axes and for dry soil use right & top axes.

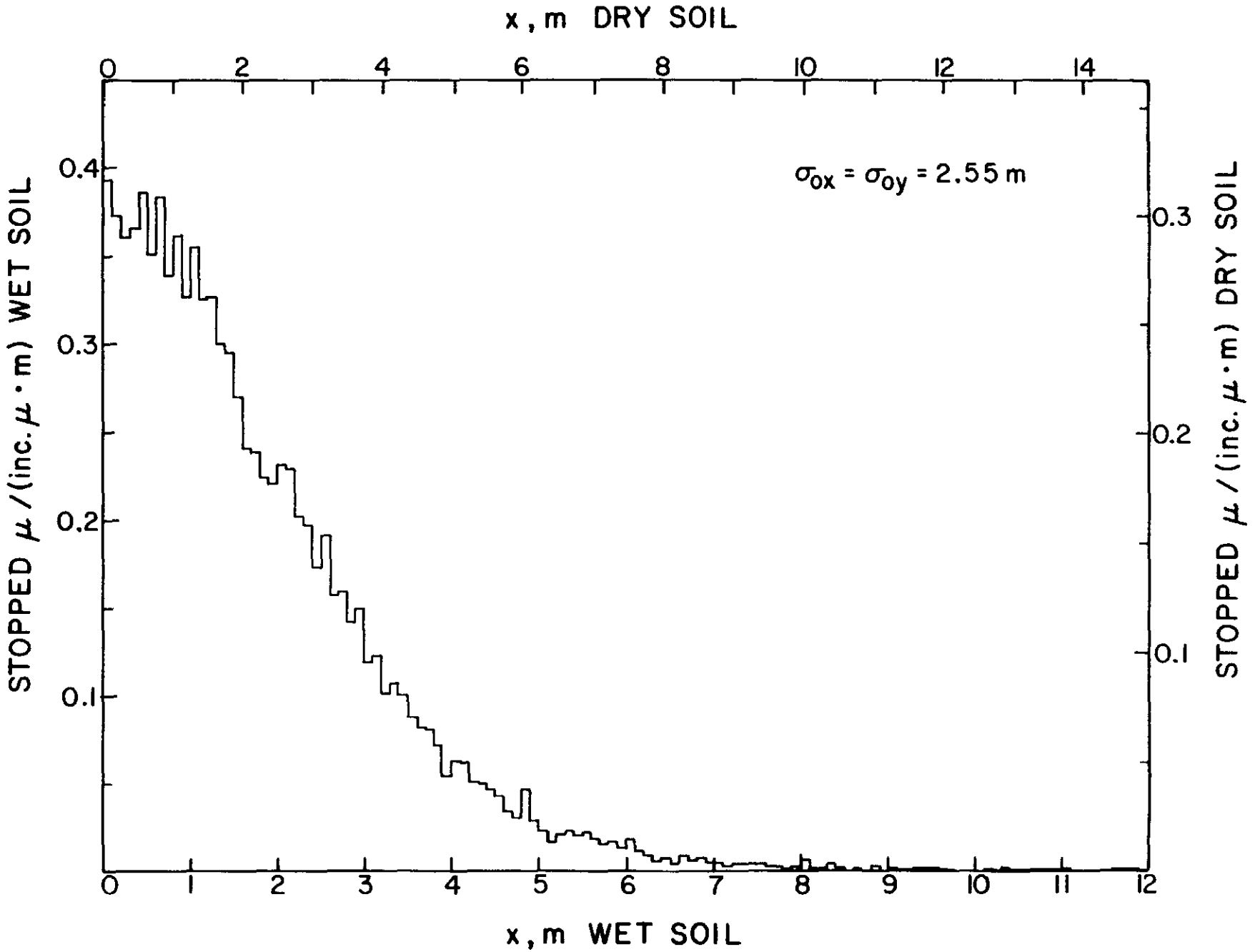

Fig. 86. Distribution in x of a pencil beam of 1.0 TeV muons stopped in soil (in m^{-1}). For wet soil use left & bottom axes and for dry soil use right & top axes.

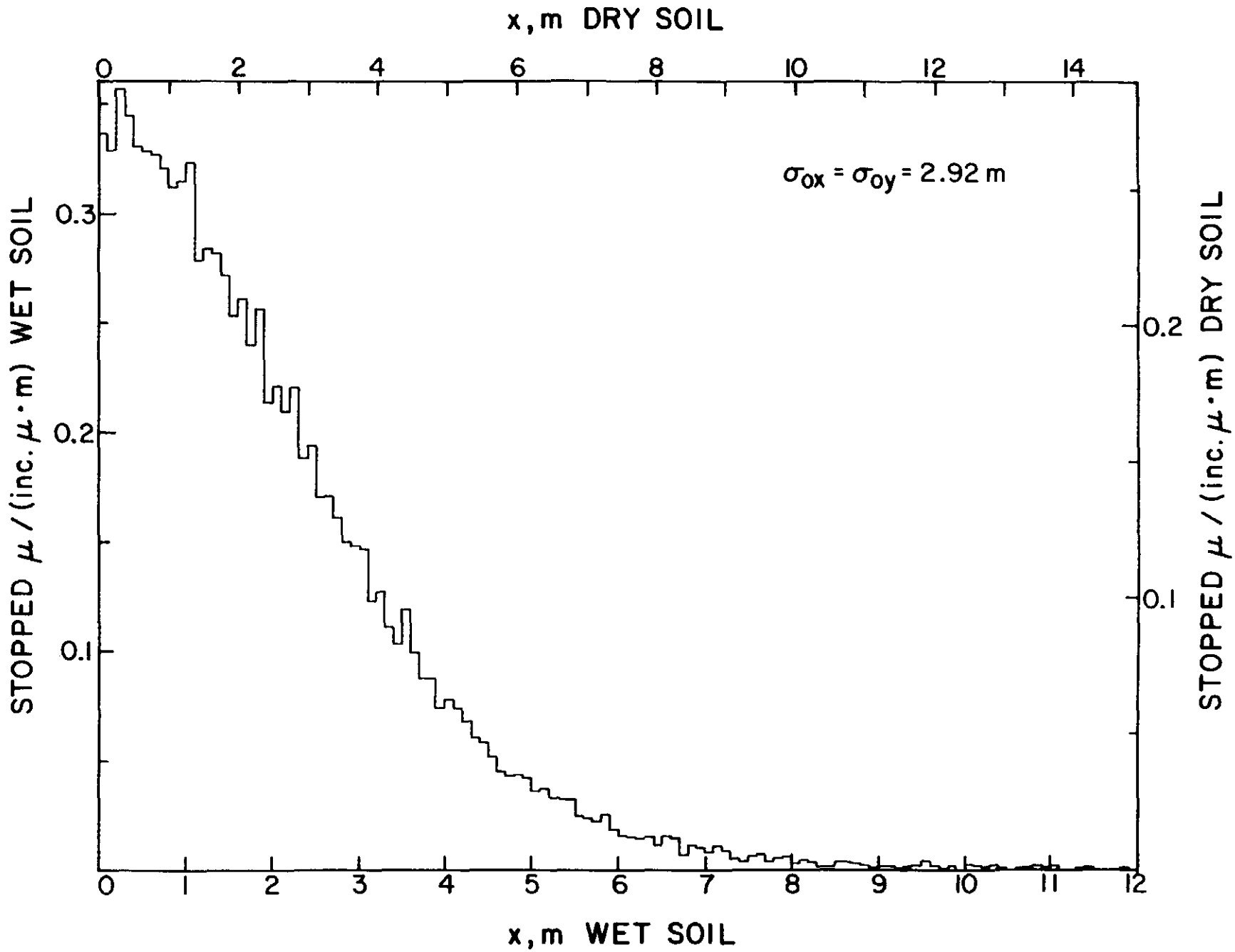

Fig. 87. Distribution in x of a pencil beam of 10.0 TeV muons stopped in soil (in m^{-1}) For wet soil use left & bottom axes and for dry soil use right & top axes.

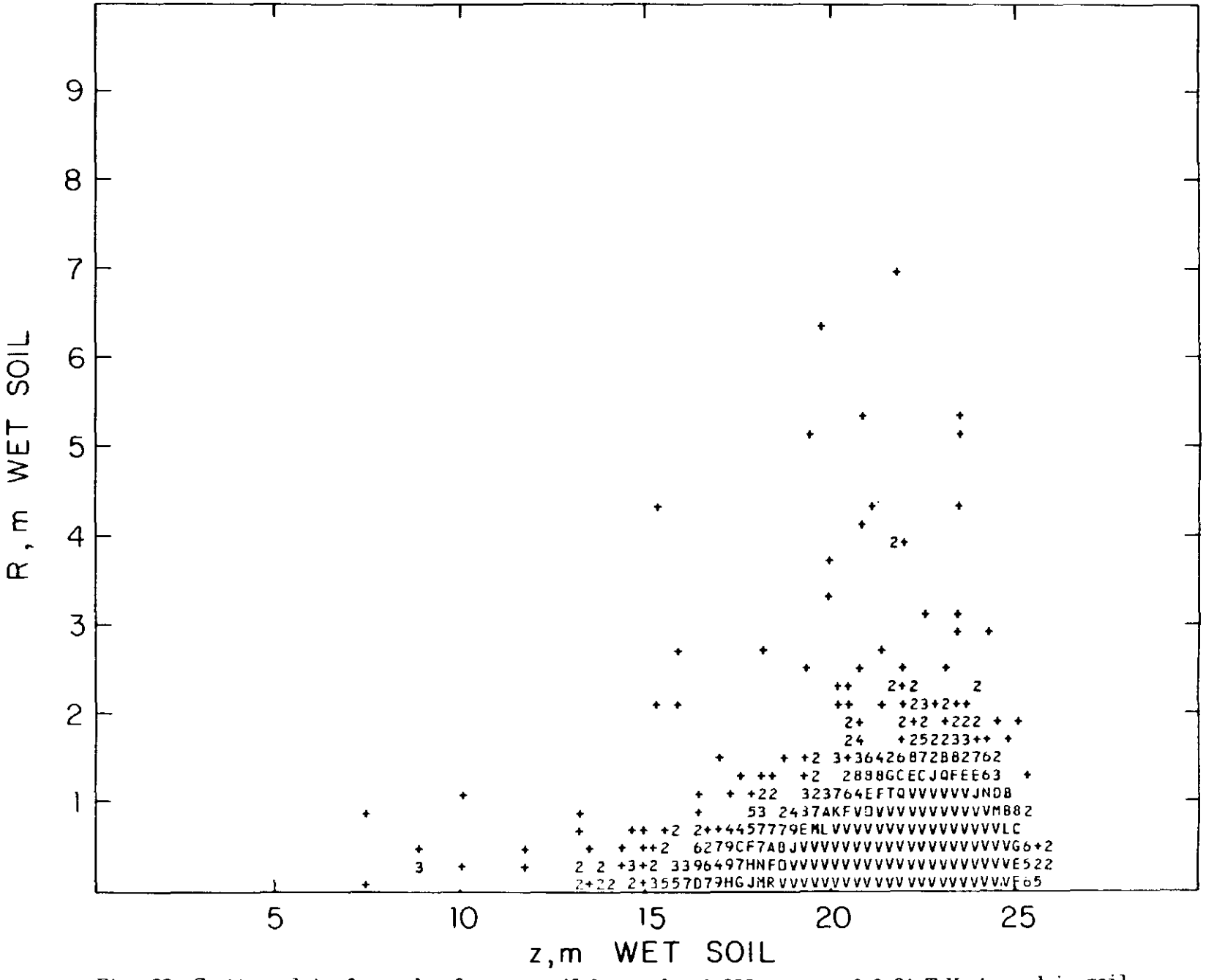

Fig. 88. Scatter plot of z and x for a pencil beam of 10 000 muons of 0.01 TeV stopped in soil.

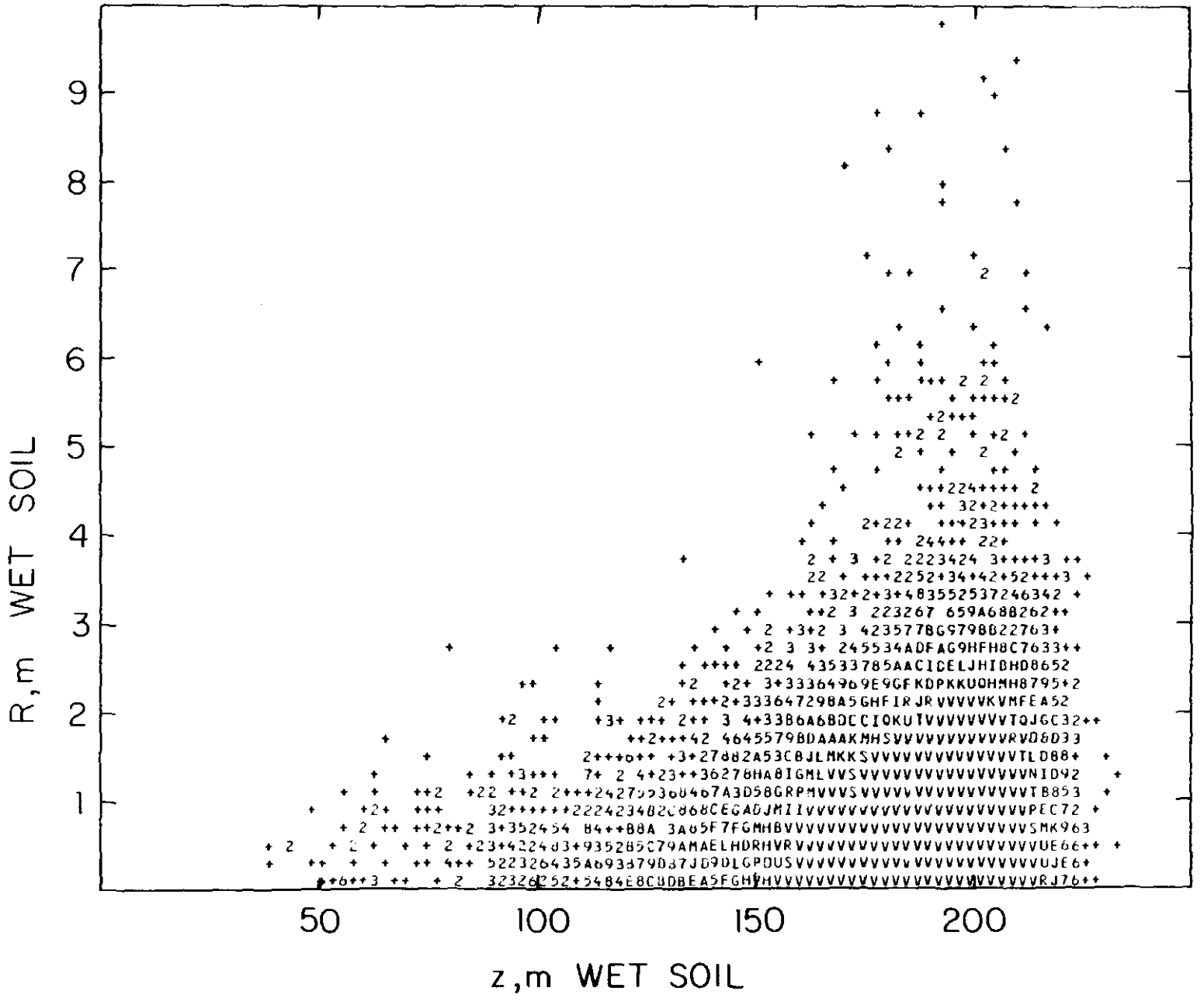

Fig. 89. Scatter plot of z and x for a pencil beam of 10 000 muons of 0.1 TeV stopped in soil.

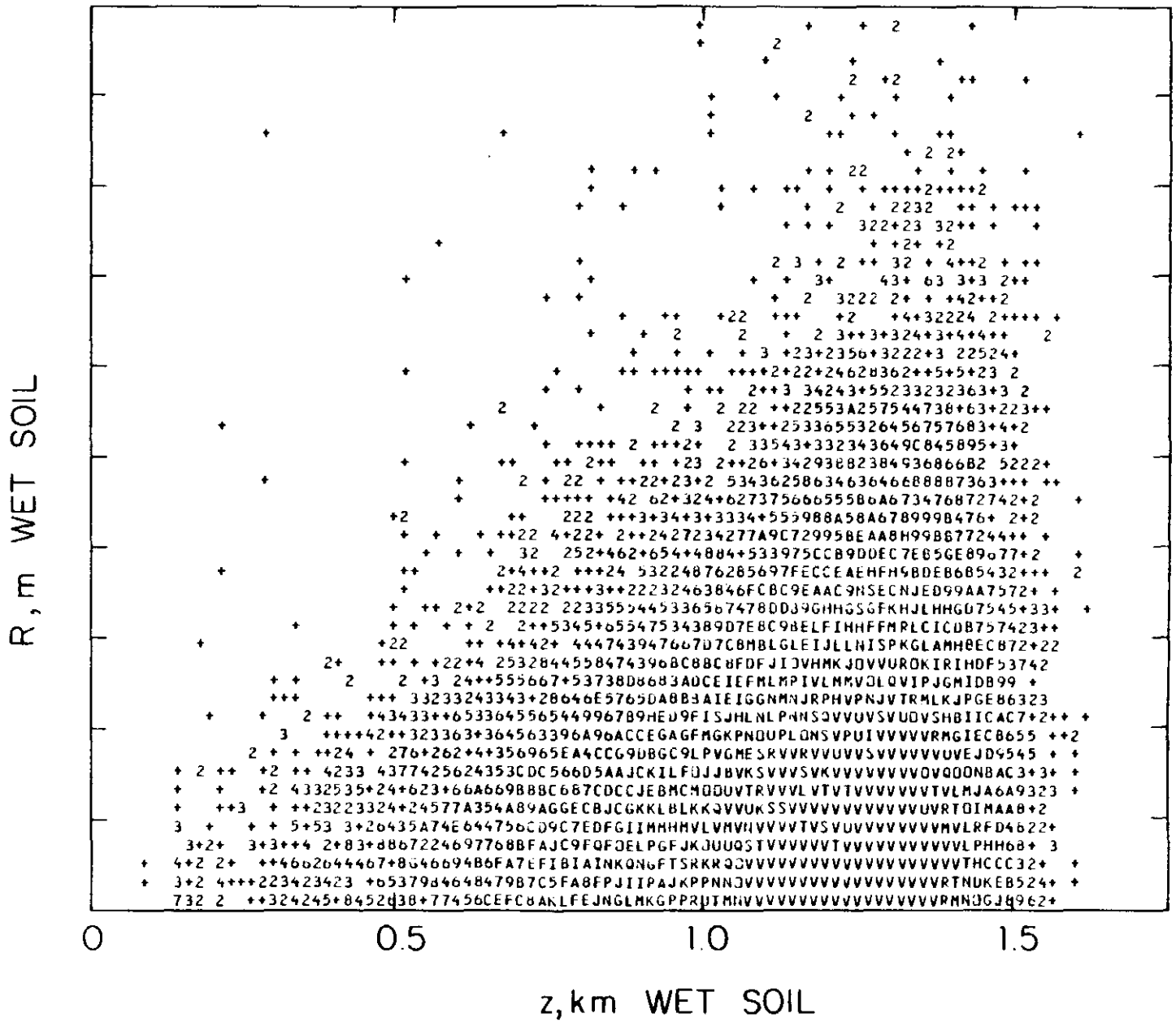

Fig. 90. Scatter plot of z and x for a pencil beam of 10 000 muons of 1.0 TeV stopped in soil.

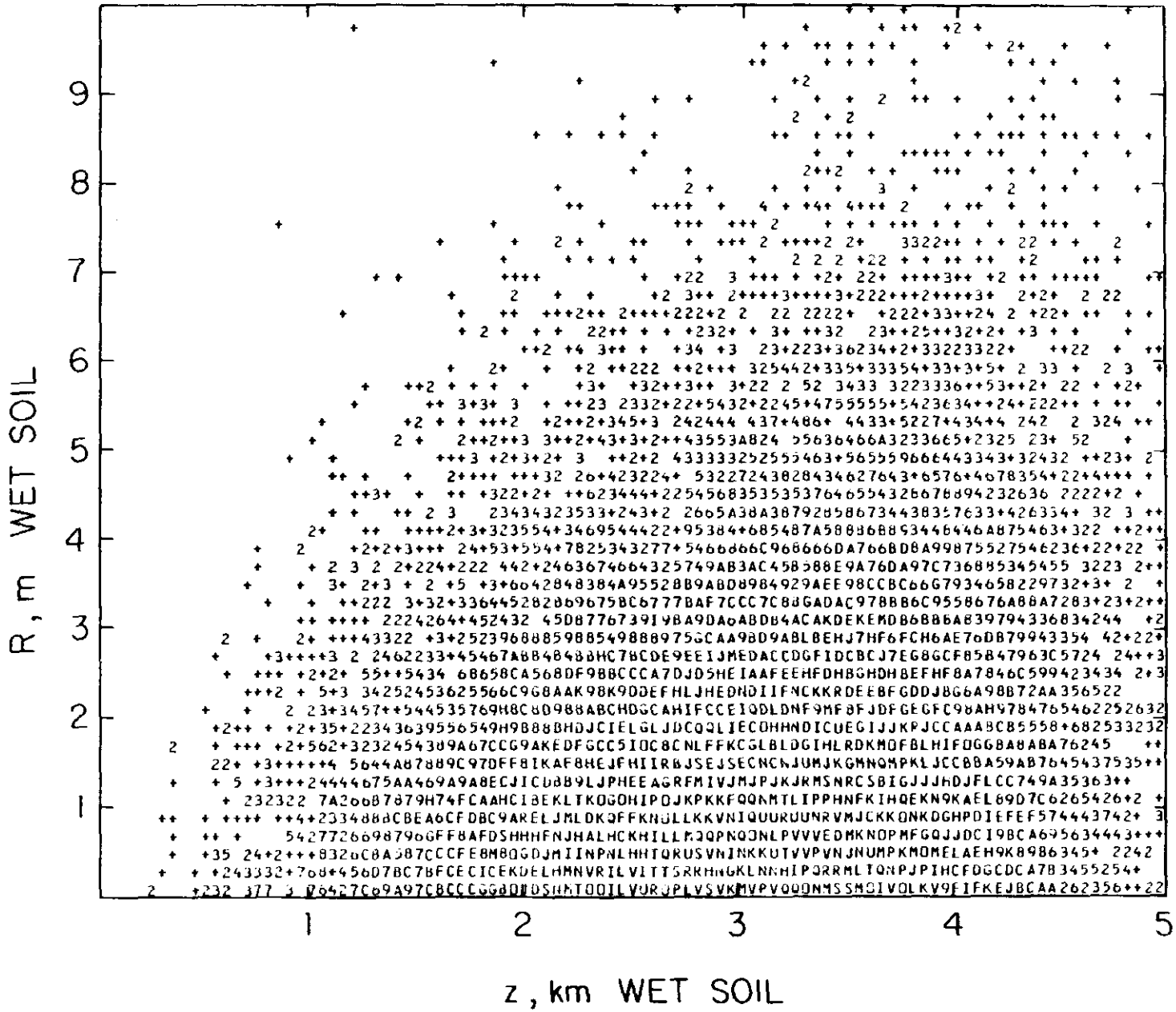

Fig. 91. Scatter plot of z and x for a pencil beam of 10 000 muons of 10.0 TeV stopped in soil.

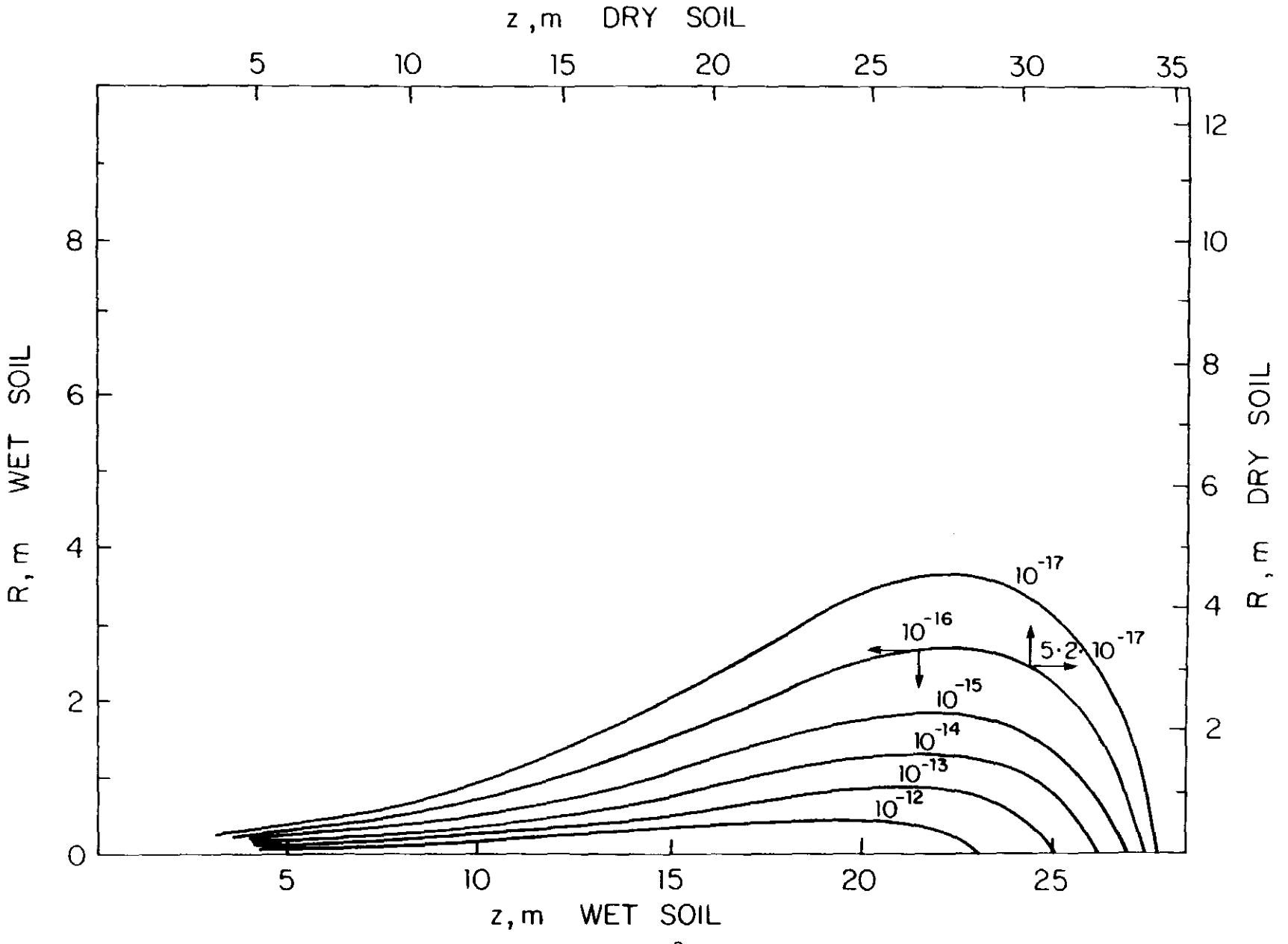

Fig. 92. Contours of equal energy density (in GeV/cm^3•incident muon) for a pencil beam of 0.01 TeV muons incident on solid soil cylinder along the axis. Contours for wet soil (left & bottom axes) are integral powers of ten. Contours for dry soil (right & top axes) must be scaled down by 0.52 as shown for one example. Some contours may be omitted for clarity or due to statistical uncertainty.

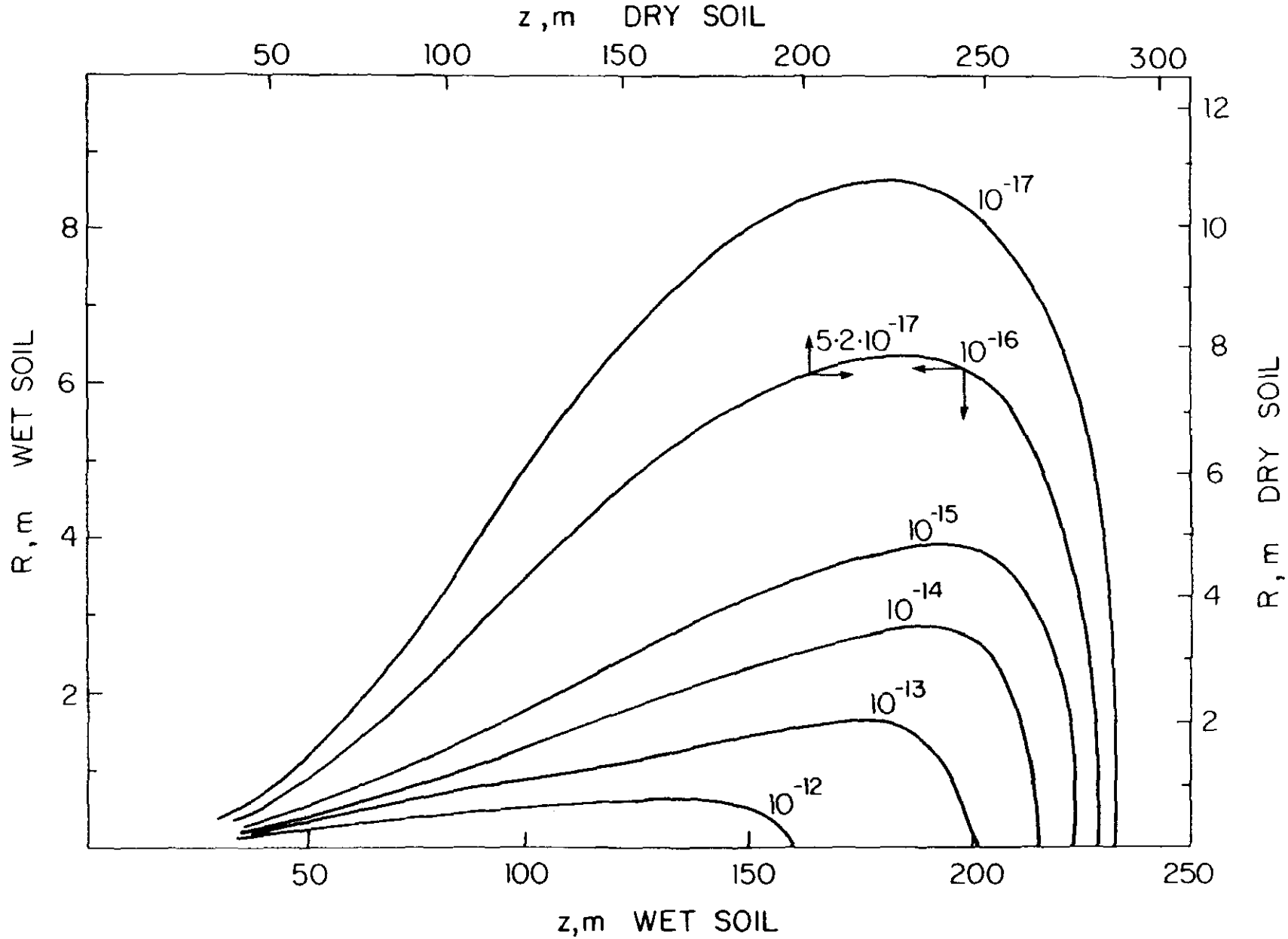

Fig. 93. Contours of equal energy density (in GeV/cm^3•incident muon) for a pencil beam of 0.10 TeV muons incident on solid soil cylinder along the axis. Contours for wet soil (left & bottom axes) are integral powers of ten. Contours for dry soil (right & top axes) must be scaled down by 0.52 as shown for one example. Some contours may be omitted for clarity or due to statistical uncertainty.

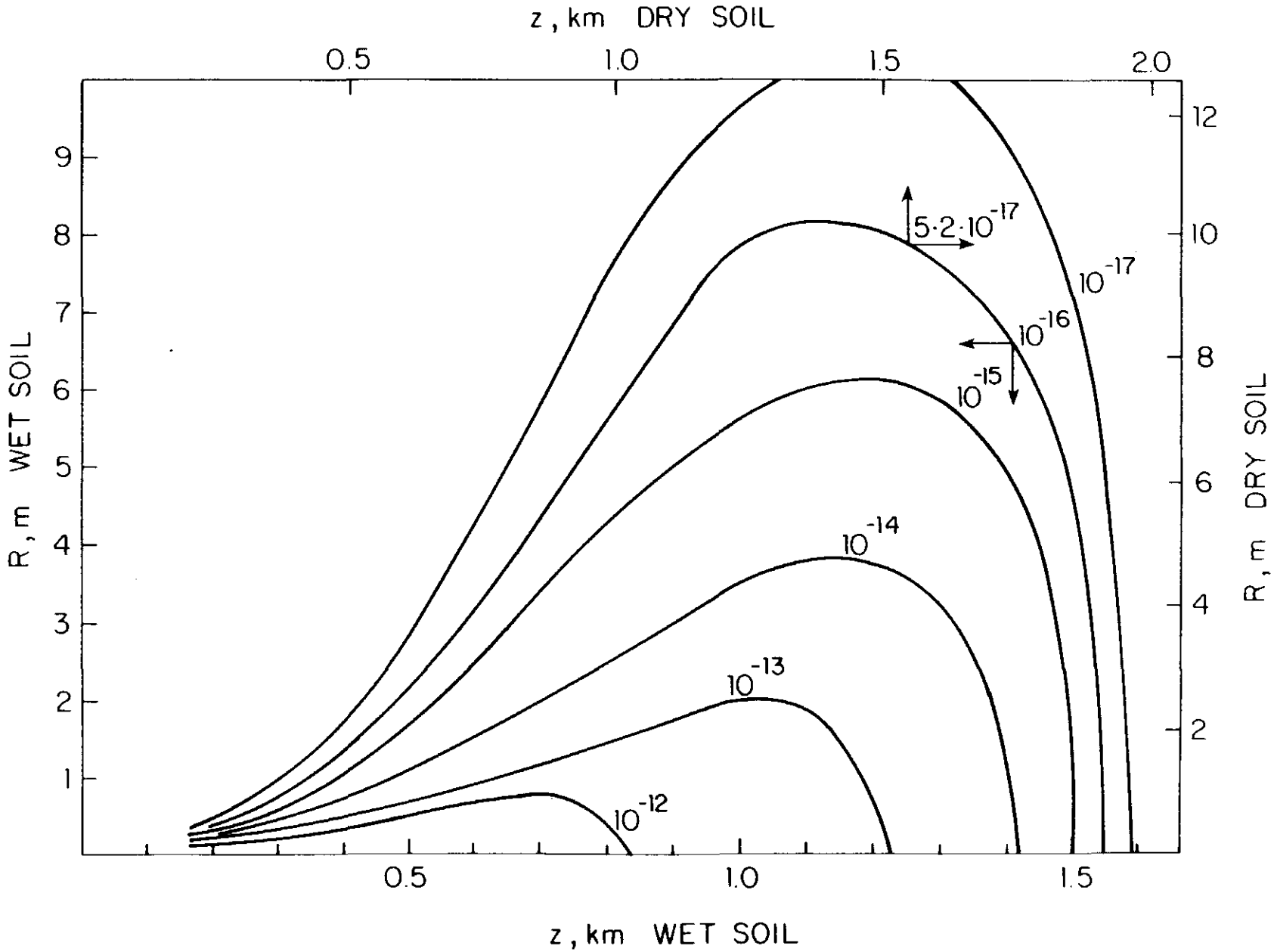

Fig. 94. Contours of equal energy density (in GeV/cm^3•incident muon) for a pencil beam of 1.0 TeV muons incident on solid soil cylinder along the axis. Contours for wet soil (left & bottom axes) are integral powers of ten. Contours for dry soil (right & top axes) must be scaled down by 0.52 as shown for one example. Some contours may be omitted for clarity or due to statistical uncertainty.

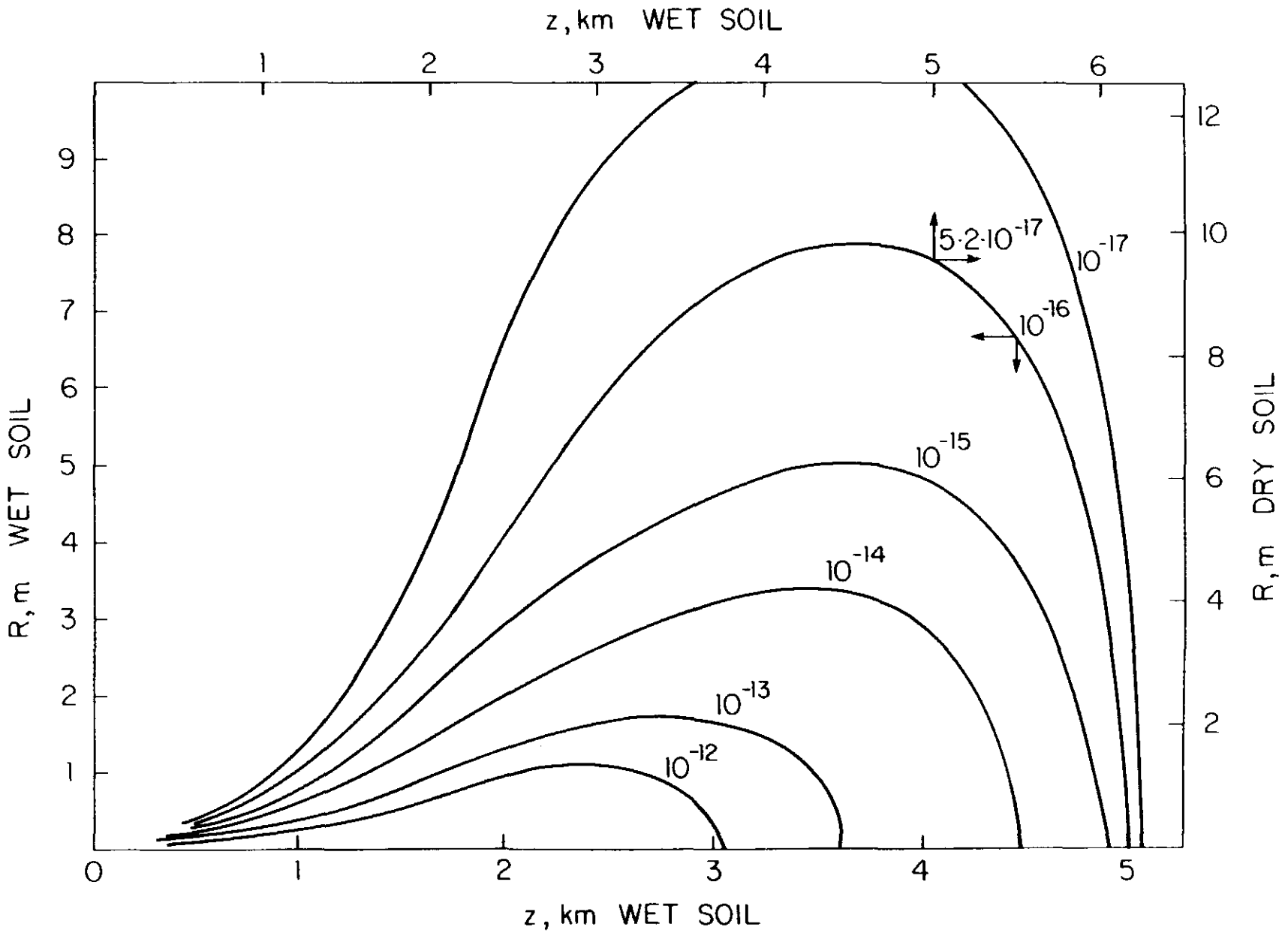

Fig. 95. Contours of equal energy density (in GeV/cm^3•incident muon) for a pencil beam of 10.0 TeV muons incident on solid soil cylinder along the axis. Contours for wet soil (left & bottom axes) are integral powers of ten. Contours for dry soil (right & top axes) must be scaled down by 0.52 as shown for one example. Some contours may be omitted for clarity or due to statistical uncertainty.

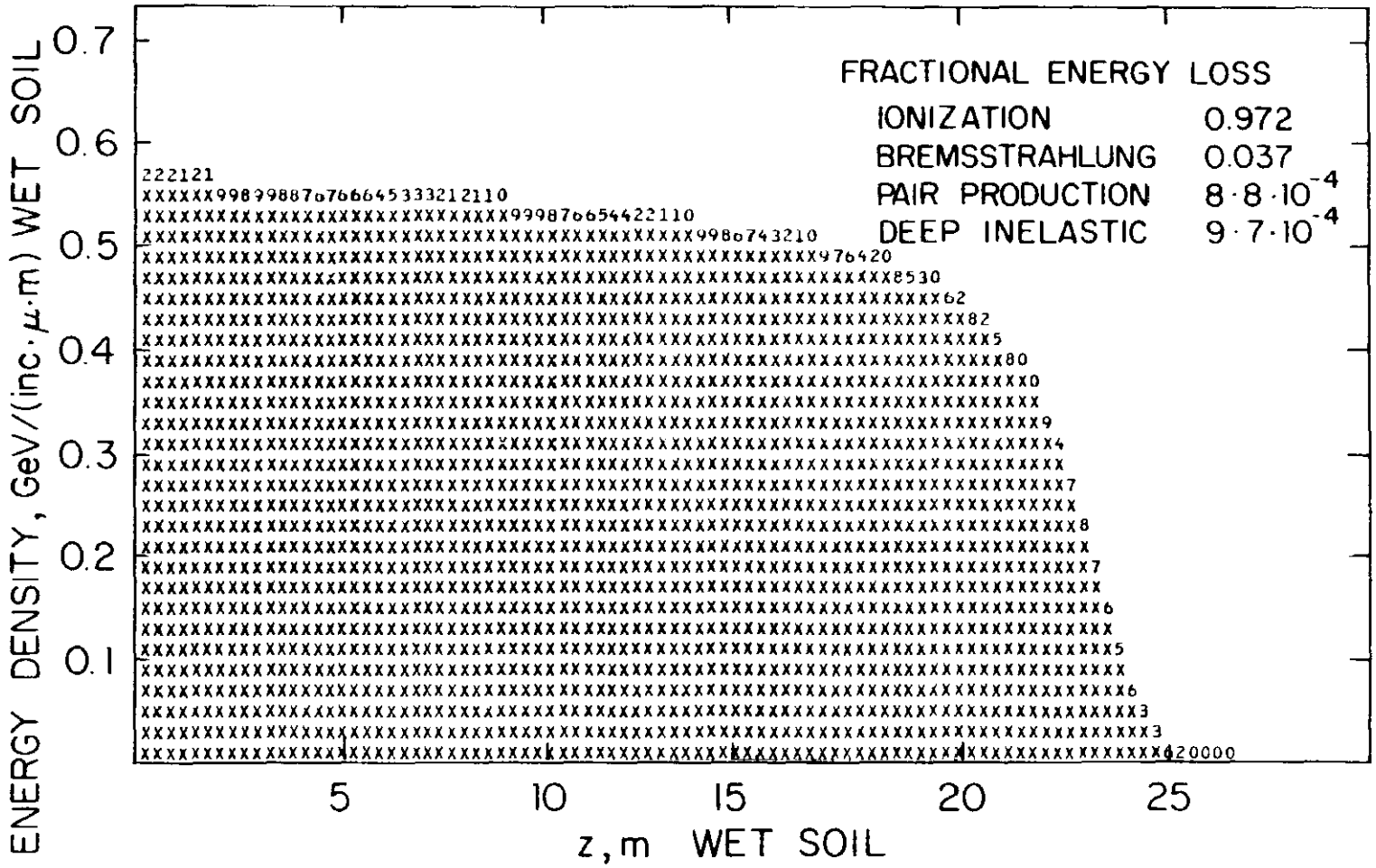

Fig. 96. Radially integrated energy density (in GeV/cm•incident muon) for a pencil beam of 0.01 TeV muons incident on solid soil cylinder (of infinite radius).

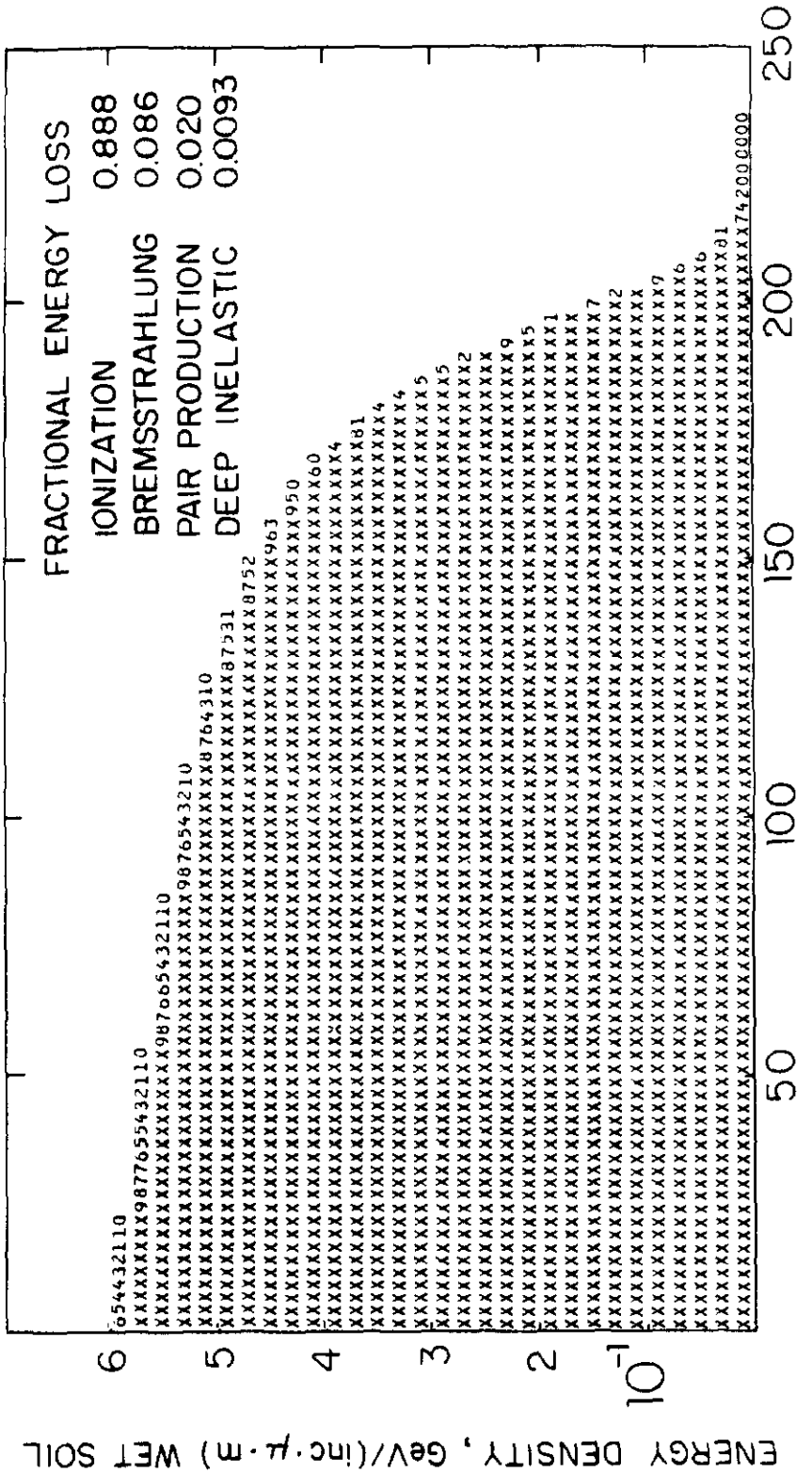

Fig. 97. Radially integrated energy density (in GeV/cm²·incident muon) for a pencil beam of 0.10 TeV muons incident on solid soil cylinder (of infinite radius).

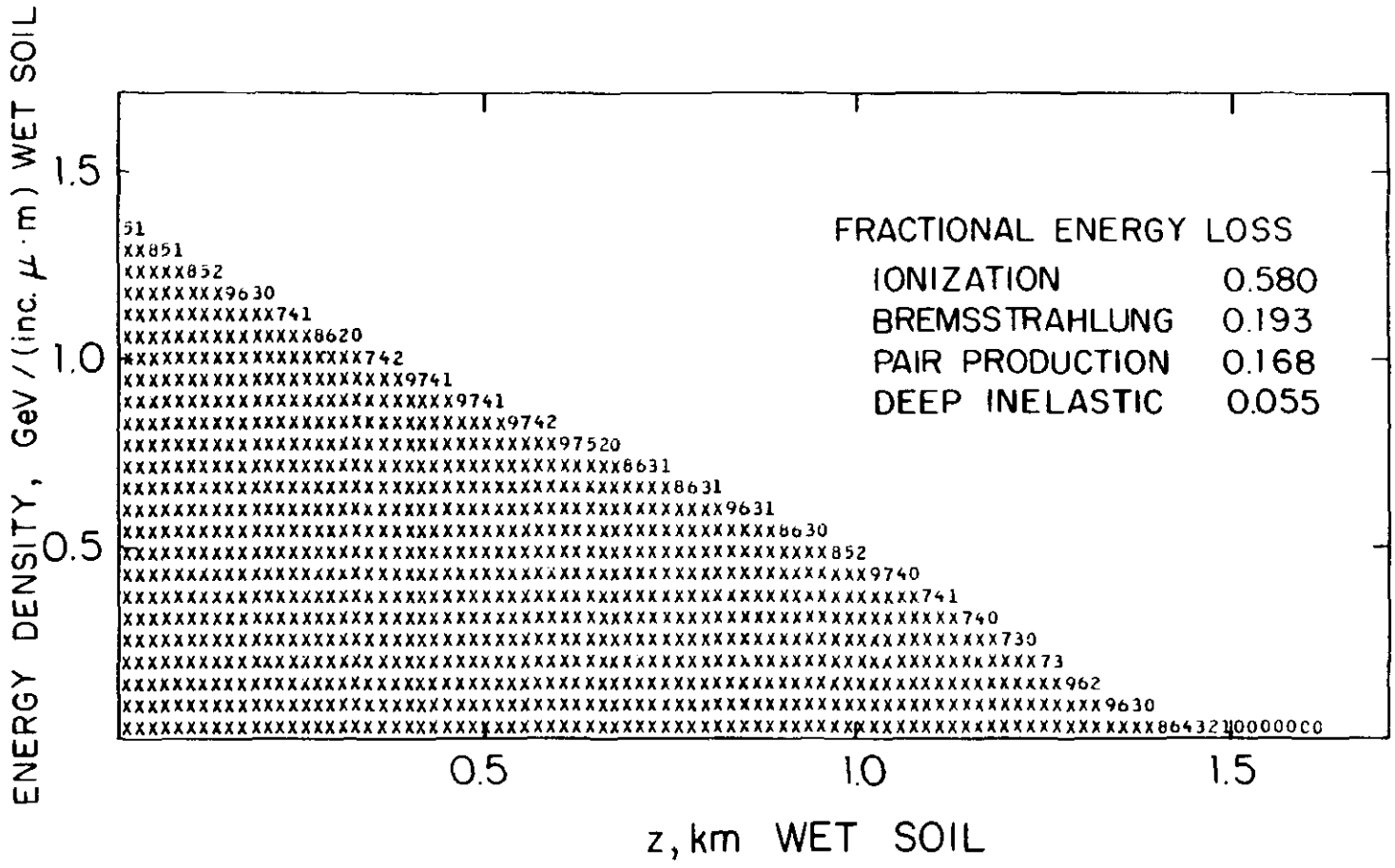

Fig. 98. Radially integrated energy density (in GeV/cm•incident muon) for a pencil beam of 1.0 TeV muons incident on solid soil cylinder (of infinite radius).

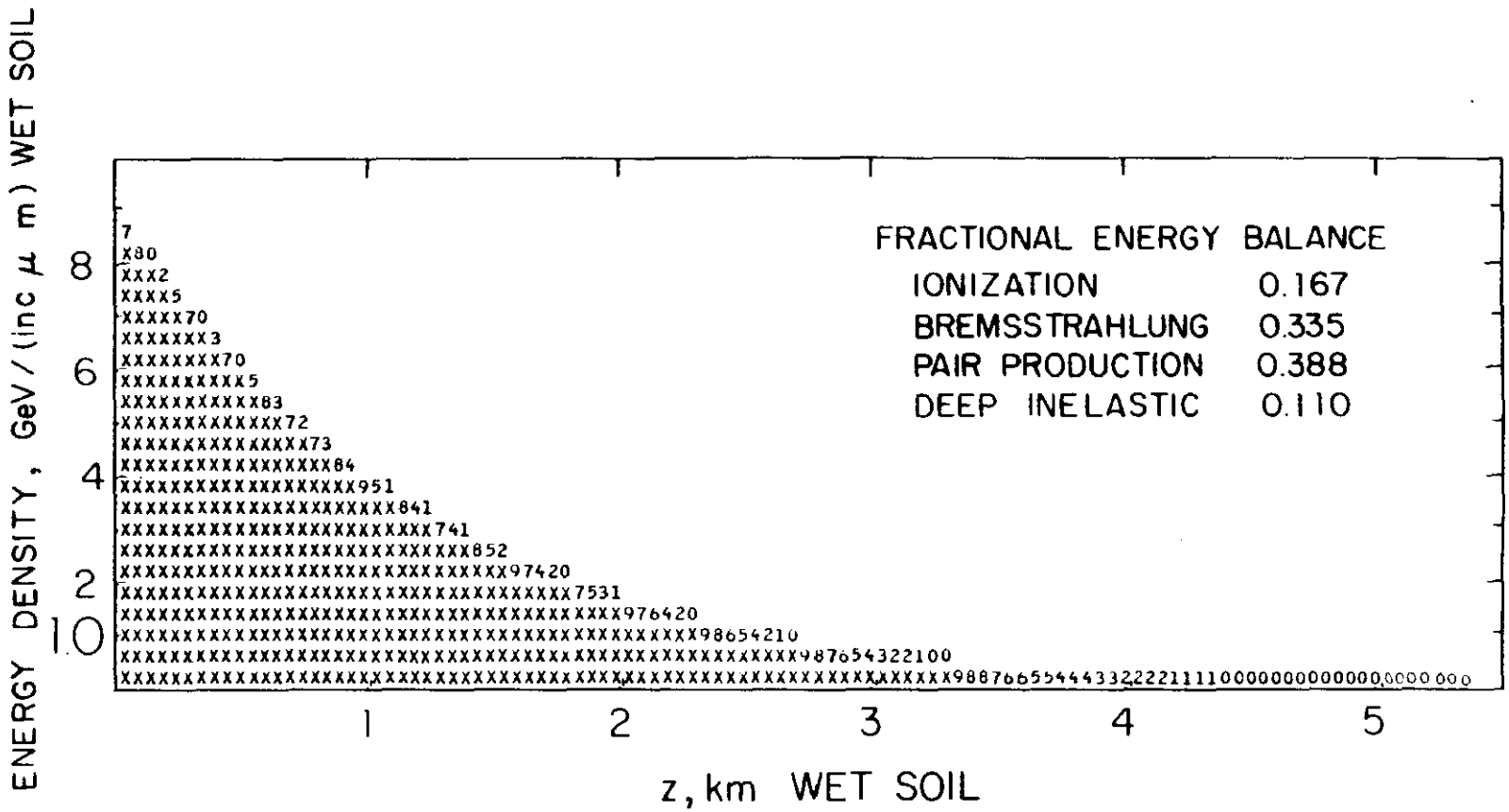

Fig. 99. Radially integrated energy density (in GeV/cm•incident muon) for a pencil beam of 10.0 TeV muons incident on solid soil cylinder (of infinite radius).

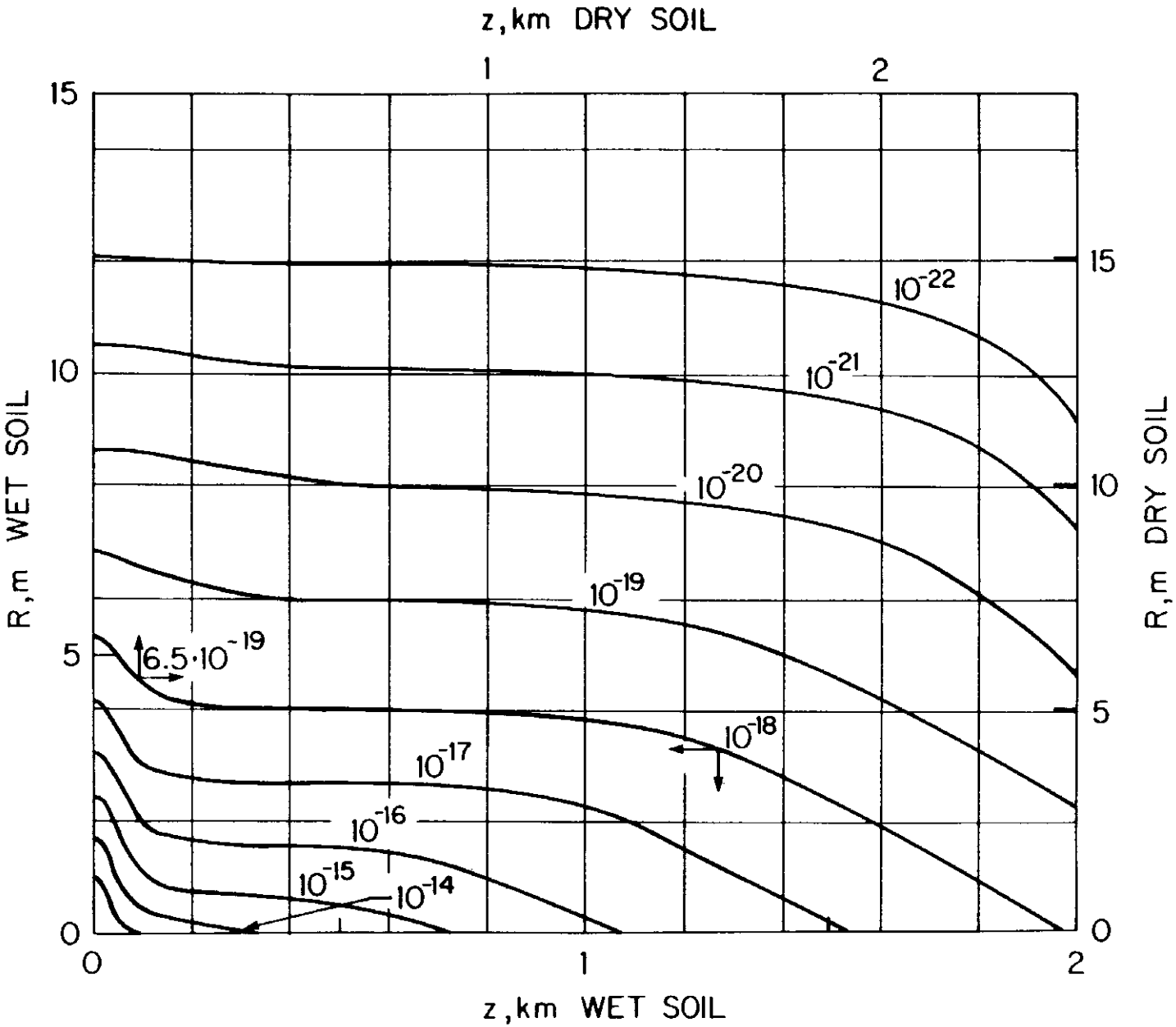

Fig. 100. Contours of equal dose equivalent (in rem/incident proton) due to muons for a beam of 5 TeV protons incident on a solid soil cylinder. Muons generated by both hadron and electromagnetic cascades are included. Contours for wet soil (left & bottom axes) are integral powers of ten. Contours for dry soil (right & top axes) must be scaled down by 0.65 as shown for one example. Some contours may be omitted for clarity or due to statistical uncertainty.

F100

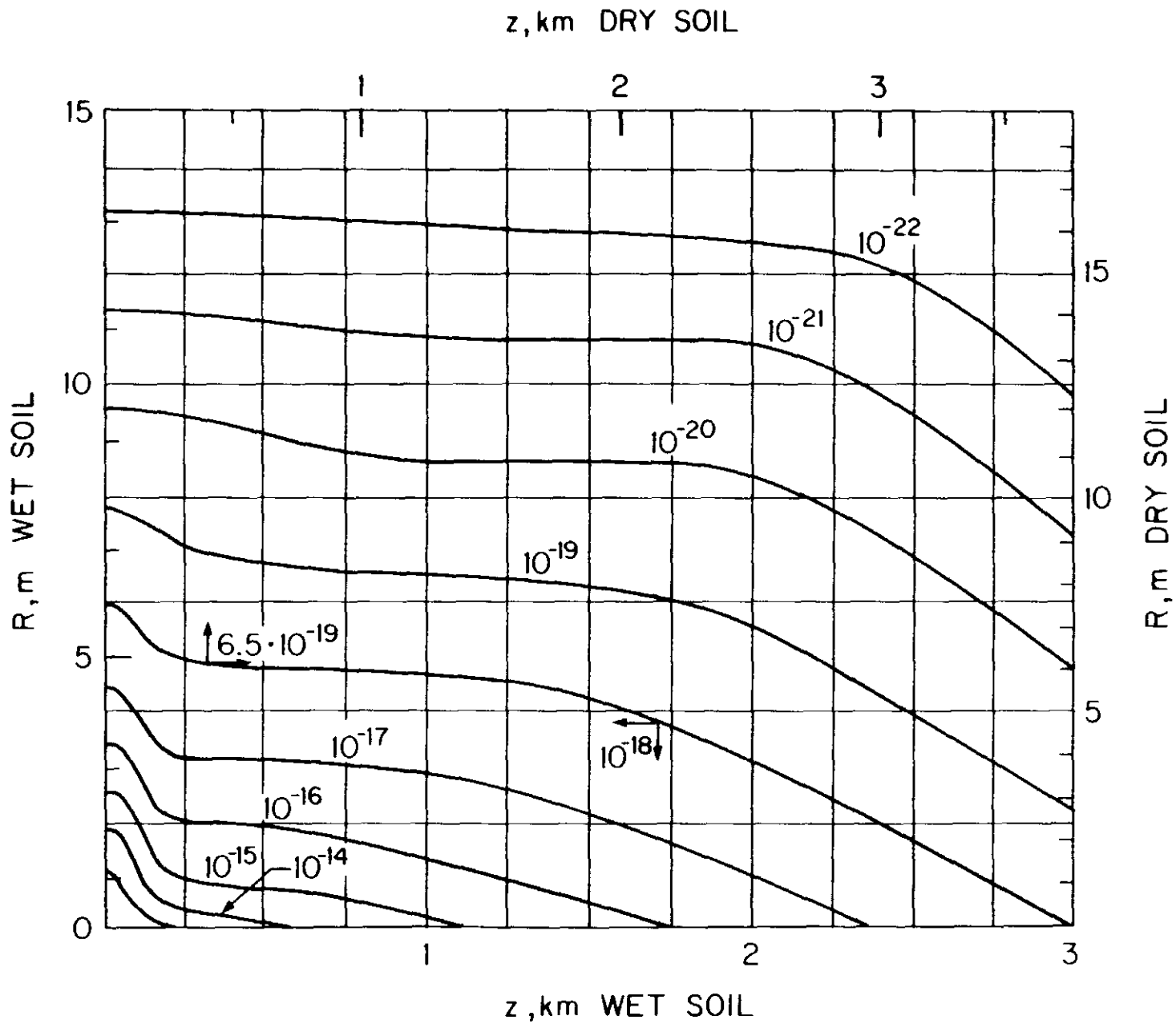

Fig. 101. Contours of equal dose equivalent (in rem/incident proton) due to muons for a beam of 10 TeV protons incident on a solid soil cylinder. Muons generated by both hadron and electromagnetic cascades are included. Contours for wet soil (left & bottom axes) are integral powers of ten. Contours for dry soil (right & top axes) must be scaled down by 0.65 as shown for one example. Some contours may be omitted for clarity or due to statistical uncertainty.

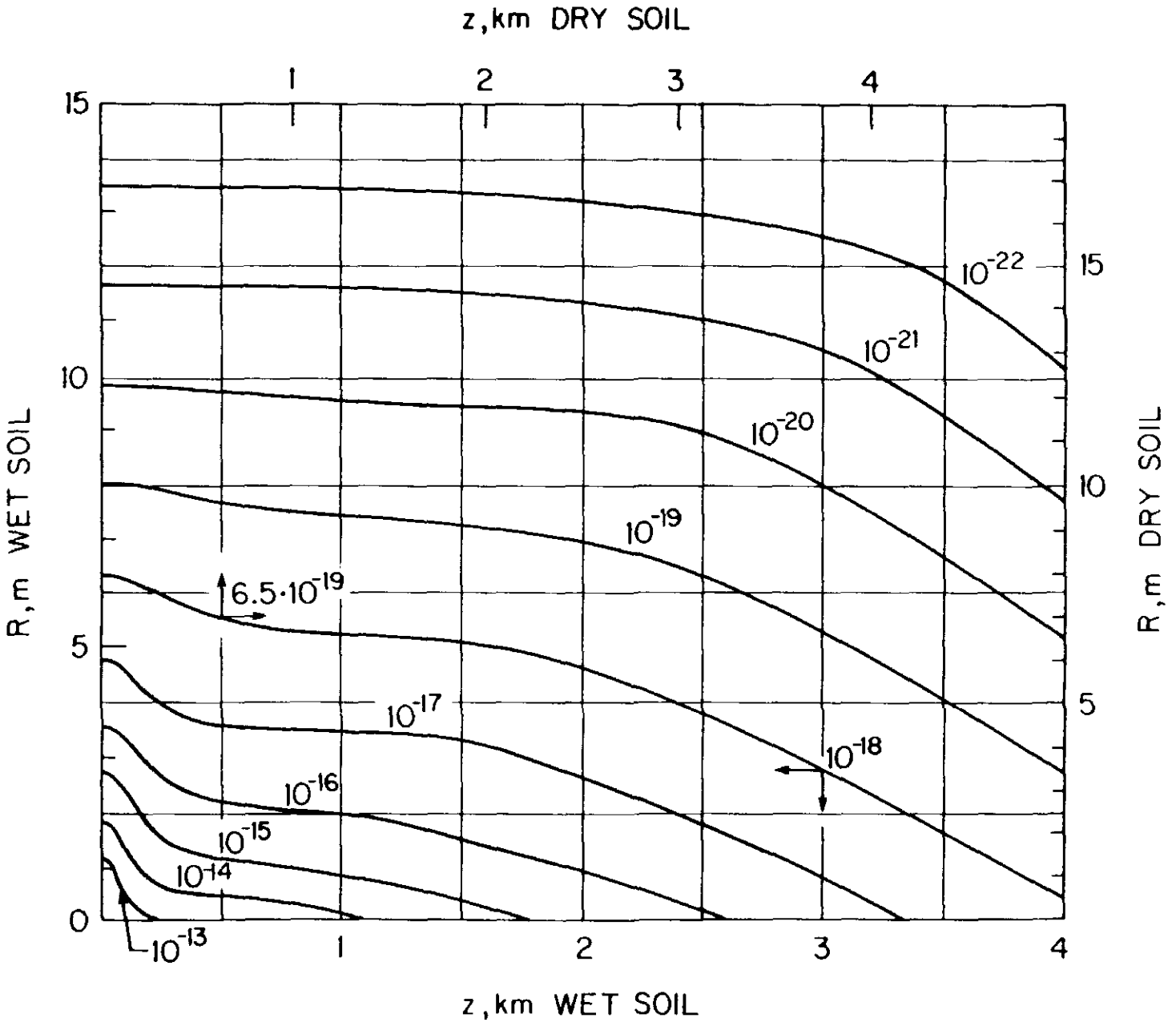

Fig. 102. Contours of equal dose equivalent (in rem/incident proton) due to muons for a beam of 20 TeV protons incident on a solid soil cylinder. Muons generated by both hadron and electromagnetic cascades are included. Contours for wet soil (left & bottom axes) are integral powers of ten. Contours for dry soil (right & top axes) must be scaled down by 0.65 as shown for one example. Some contours may be omitted for clarity or due to statistical uncertainty.

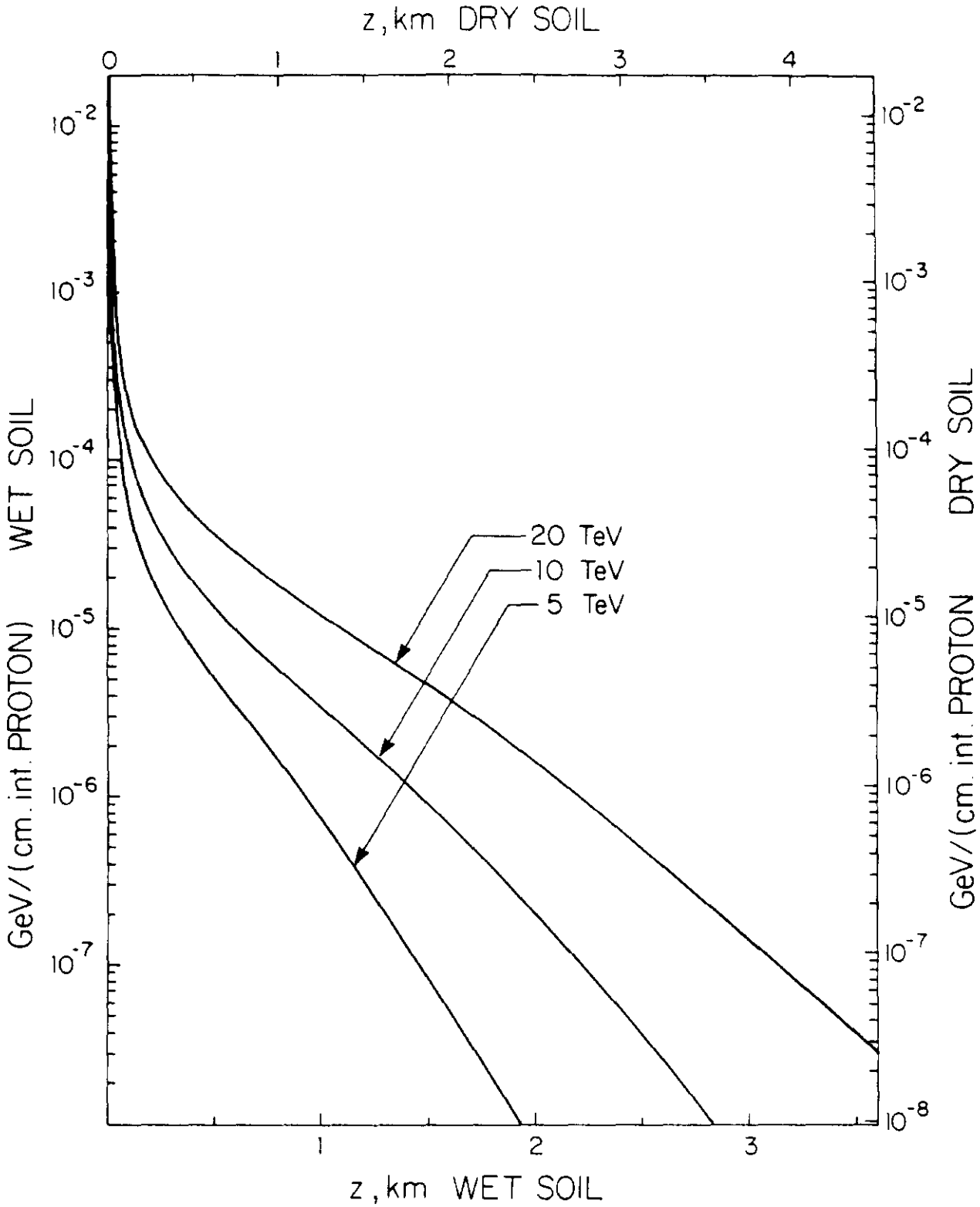

Fig. 103. Radially integrated energy density (in GeV/cm•interacting proton) due to muons from cascades initiated by 5, 10 and 20 TeV protons in infinite soil. For wet soil use left & bottom axes and for dry soil right & top axes.

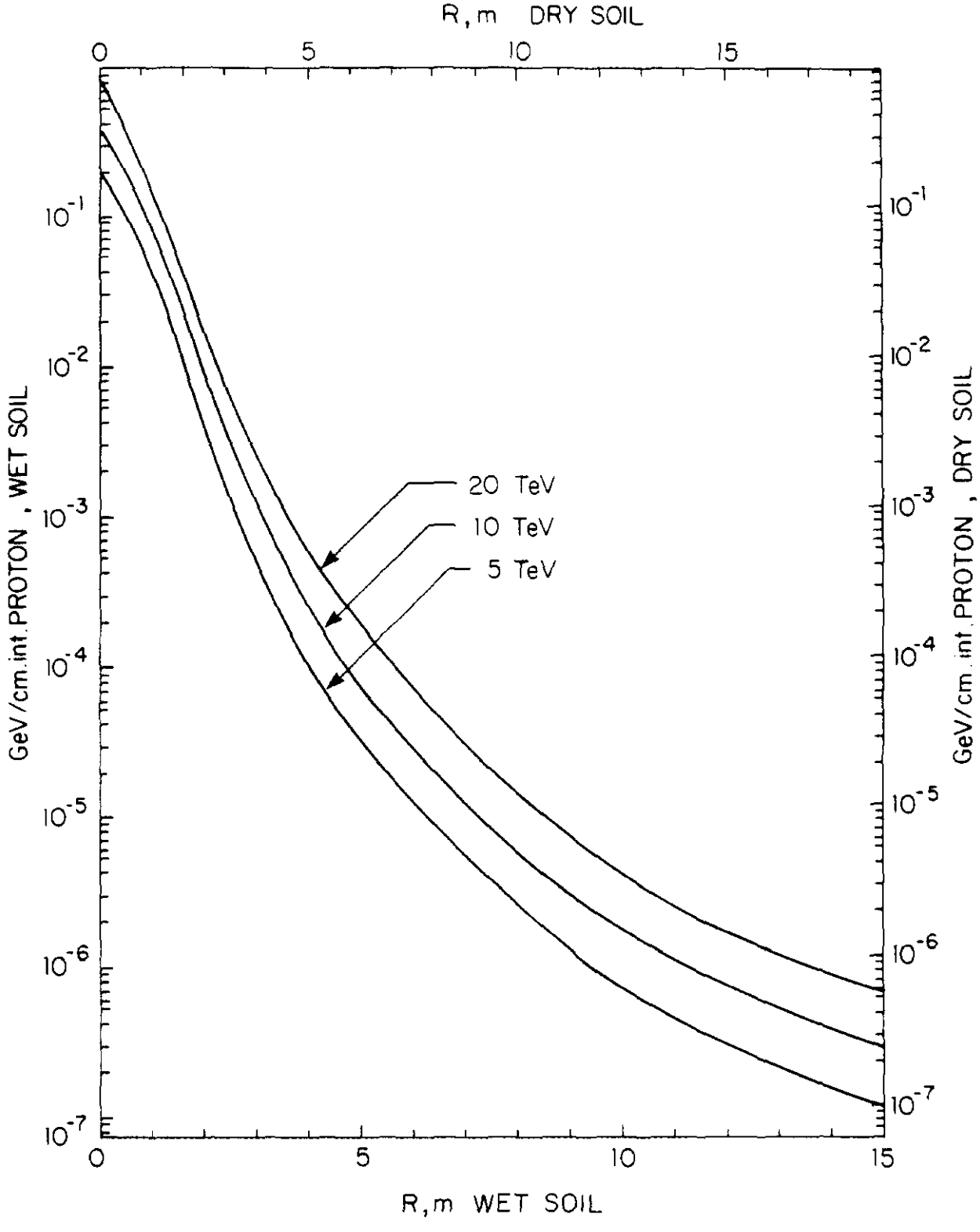

Fig. 104. Longitudinally integrated energy density (in GeV/cm•interacting proton) due to muons from cascades initiated by 5, 10 and 20 TeV protons in infinite soil. For wet soil use left & bottom axes and for dry soil right & top axes.

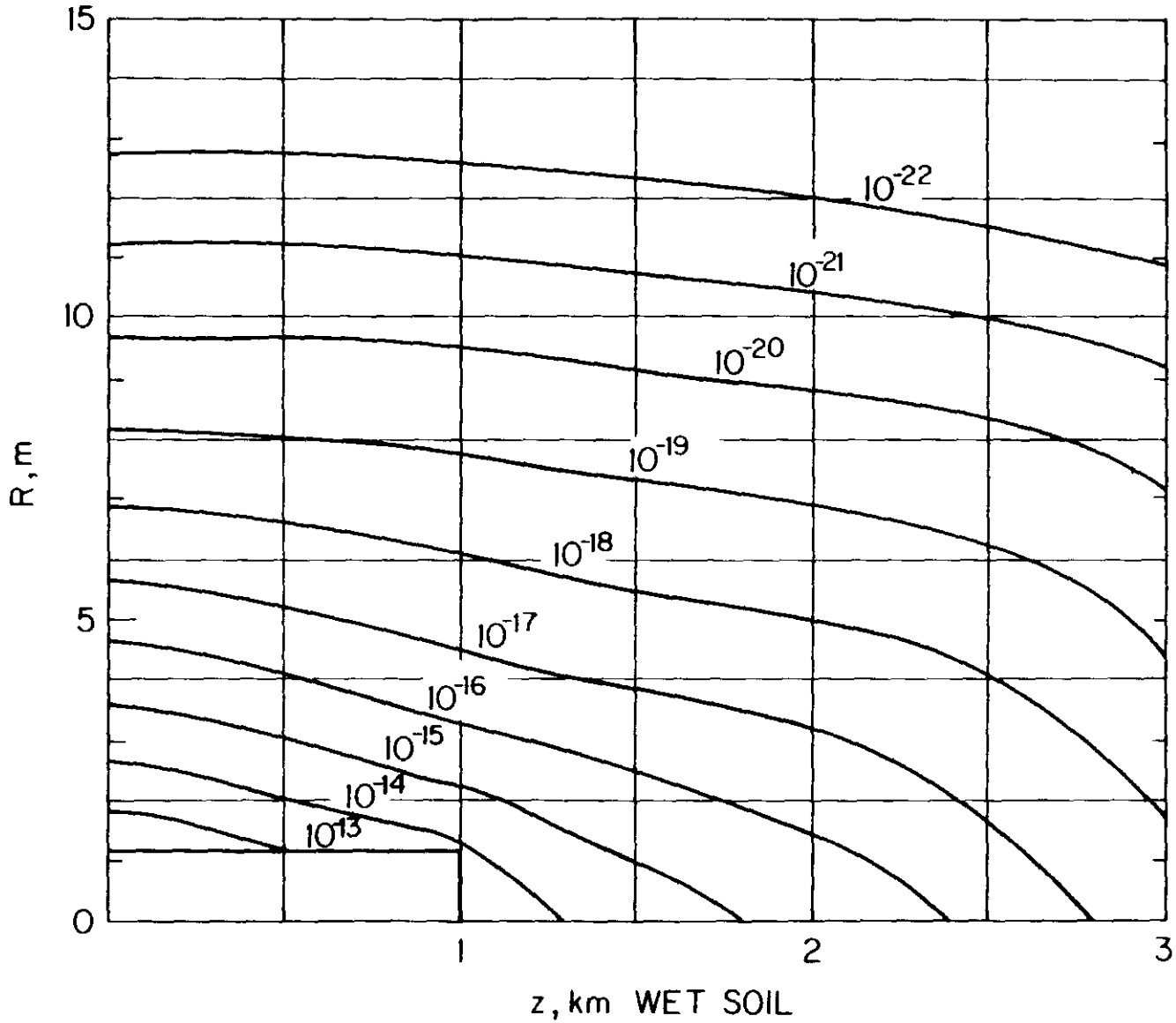

Fig. 105. Contours of equal dose equivalent (in rem/interacting proton) in a (wet) soil shield, due to muons from interactions of 5 TeV protons lost on the side of a bare beampipe in a 1.2m radius, 1.0km long tunnel. Some contours may be omitted for clarity or due to statistical uncertainty.

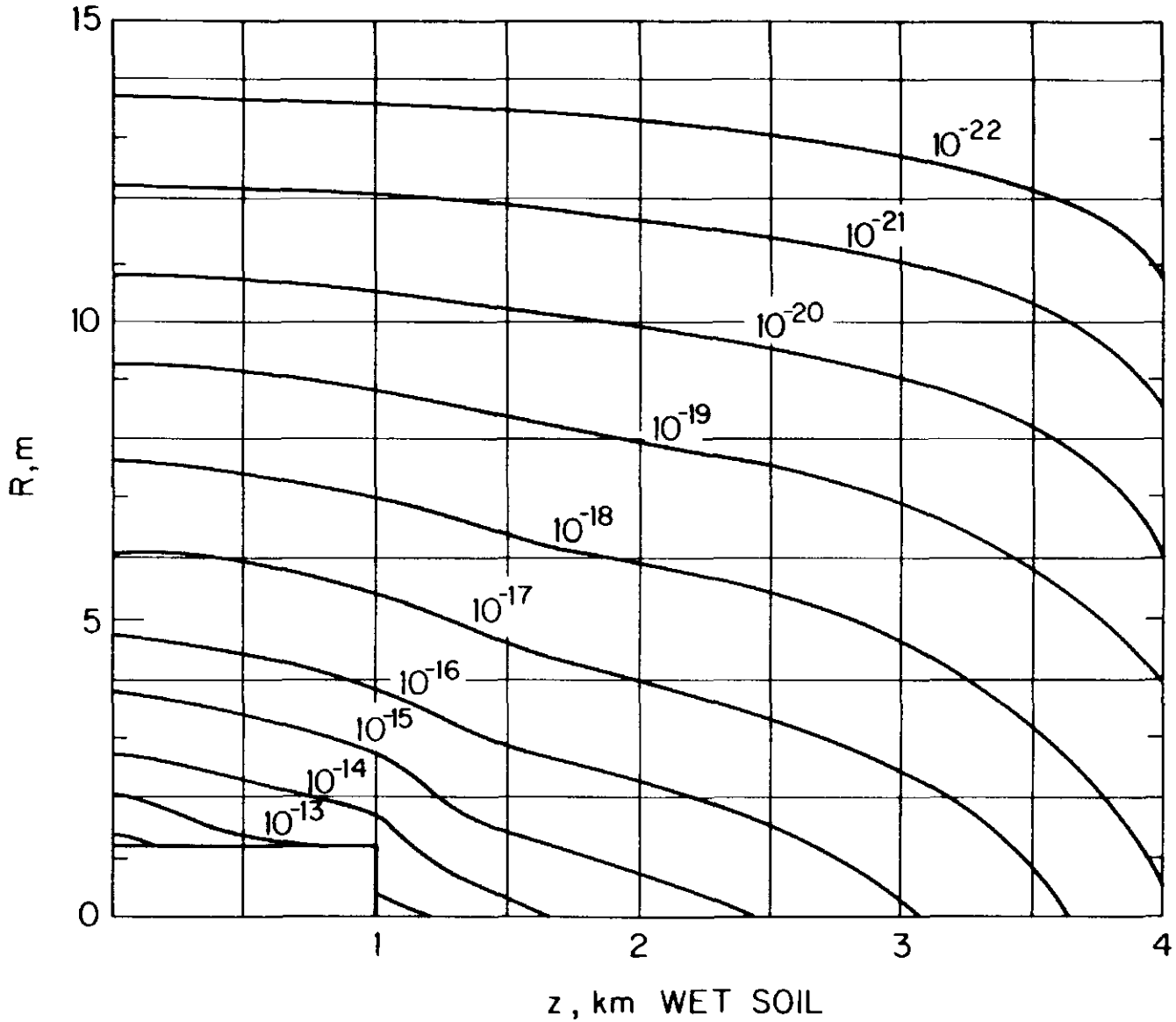

Fig. 106. Contours of equal dose equivalent (in rem/interacting proton) in a (wet) soil shield, due to muons from interactions of 10 TeV protons lost on the side of a bare beampipe in a 1.2m radius, 1.0km long tunnel. Some contours may be omitted for clarity or due to statistical uncertainty.

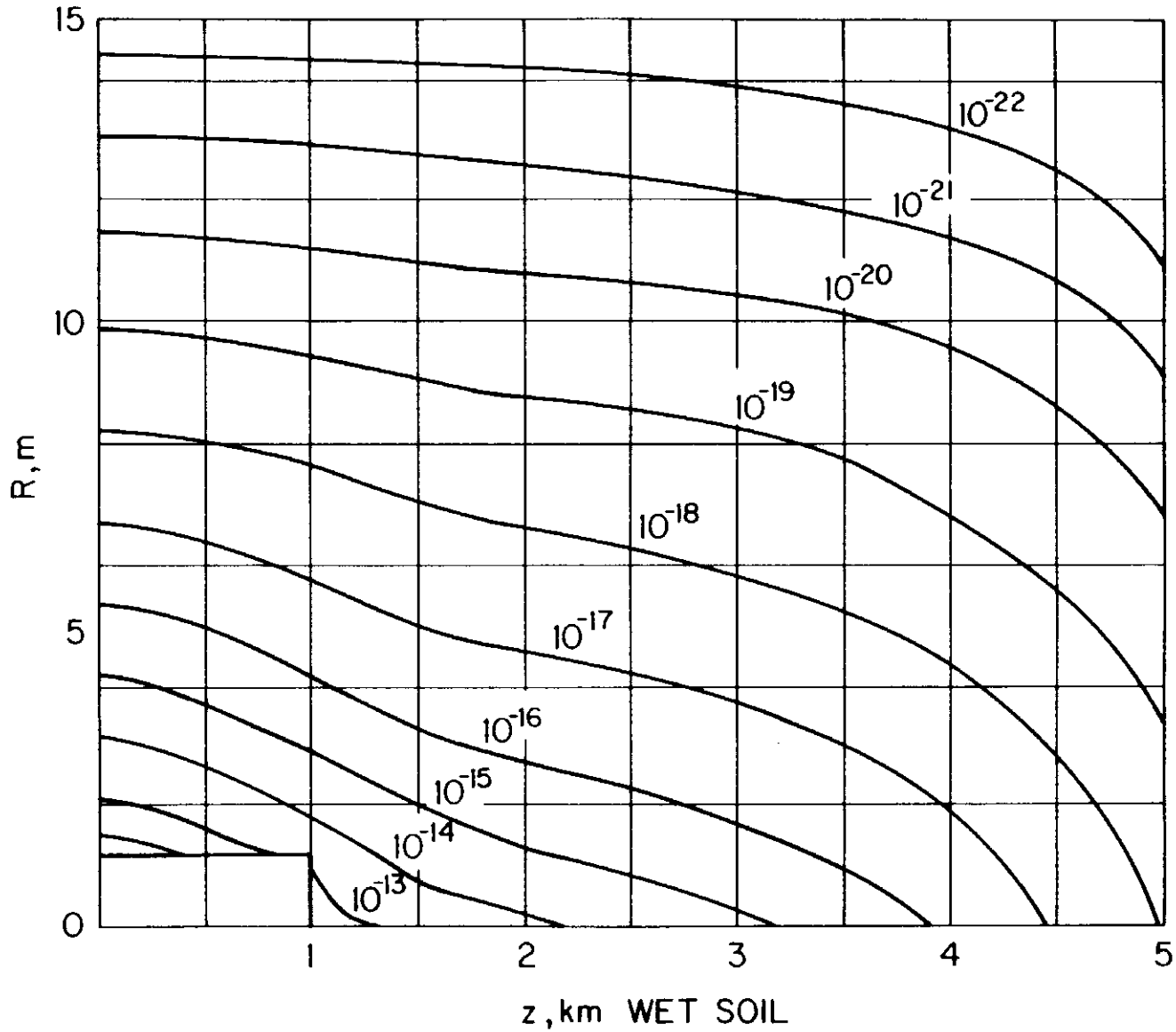

Fig. 107. Contours of equal dose equivalent (in rem/interacting proton) in a (wet) soil shield, due to muons from interactions of 20 TeV protons lost on the side of a bare beampipe in a 1.2m radius, 1.0km long tunnel. Some contours may be omitted for clarity or due to statistical uncertainty.

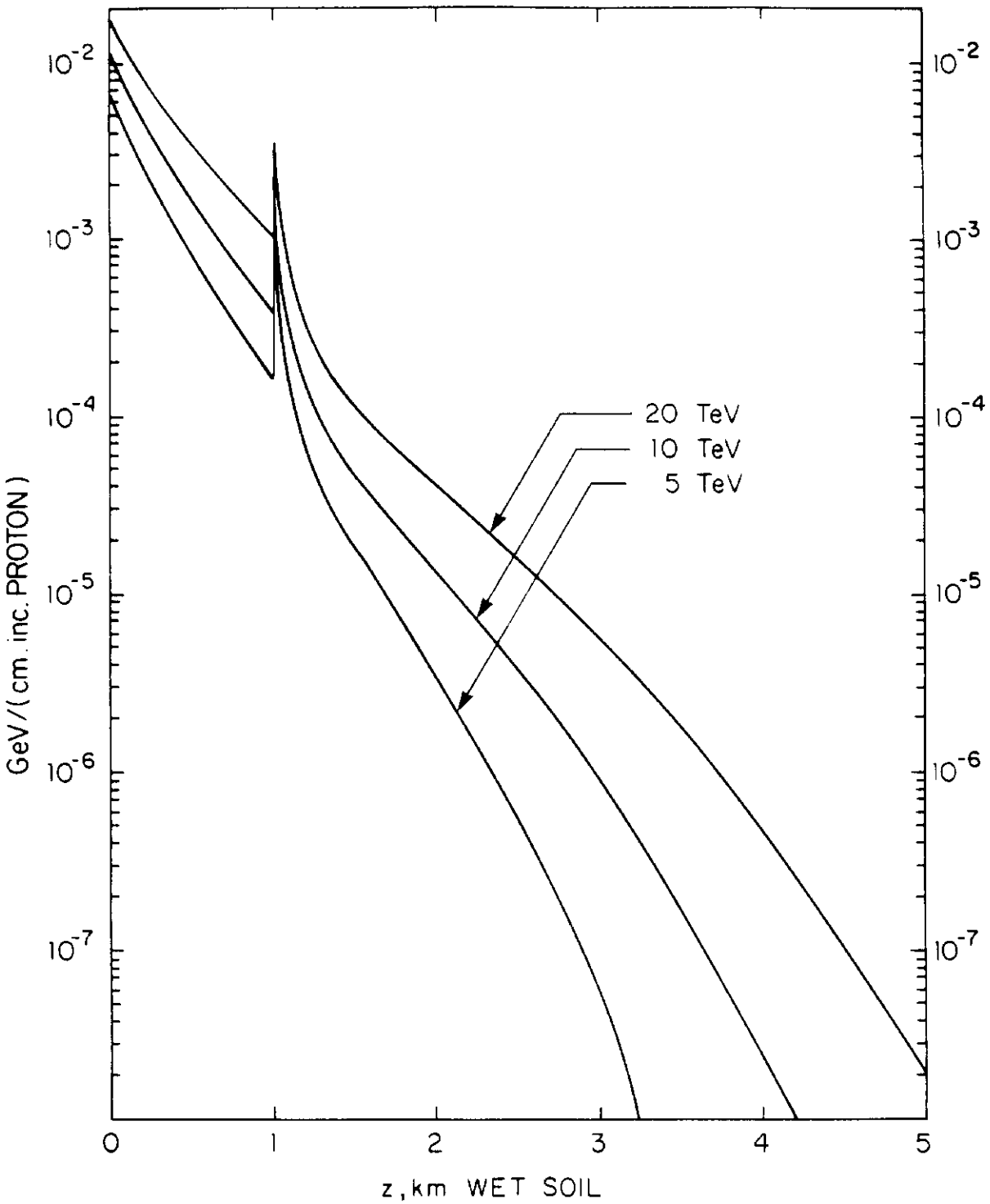

Fig. 108. Radially integrated energy density (in GeV/cm•interacting proton) in soil shield around a 1km long, 1.2m radius tunnel due to muons from interactions of 5, 10 and 20 TeV protons on the side of a bare beampipe inside the tunnel.

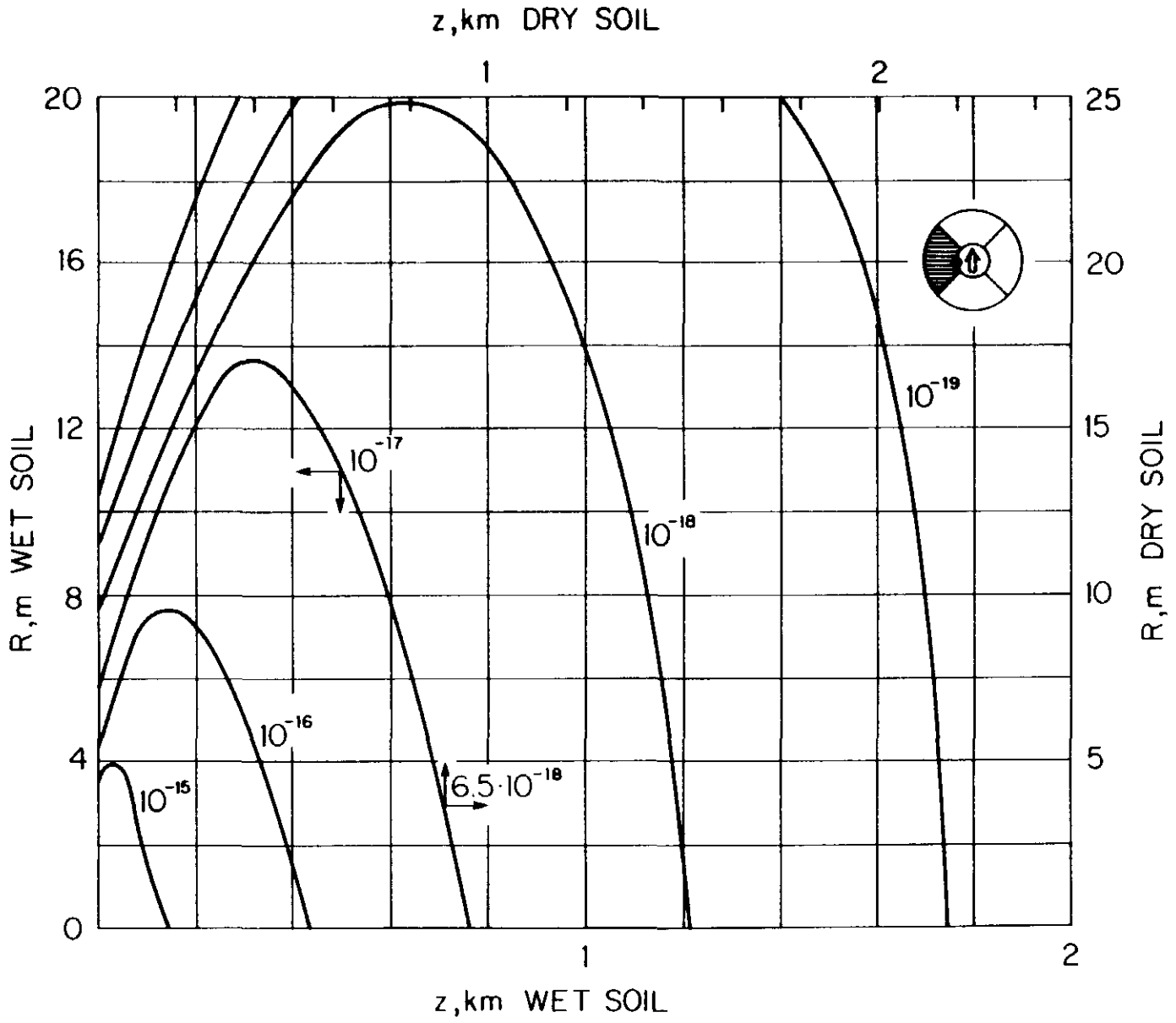

Fig. 109. Contours of equal dose-equivalent (in rem/interacting proton) in the inside quadrant (with respect to the ring) of a soil shield around a 1.2m radius tunnel due to muons from interactions of 5 TeV protons on the inside of the beampipe of a magnet inside the tunnel. The z-direction is tangential to the ring at the interaction point. Contours for wet soil (left & bottom axes) are integral powers of ten. Contours for dry soil (right & top axes) must be scaled down by 0.65 as shown for one example. Some contours may be omitted for clarity or due to statistical uncertainty.

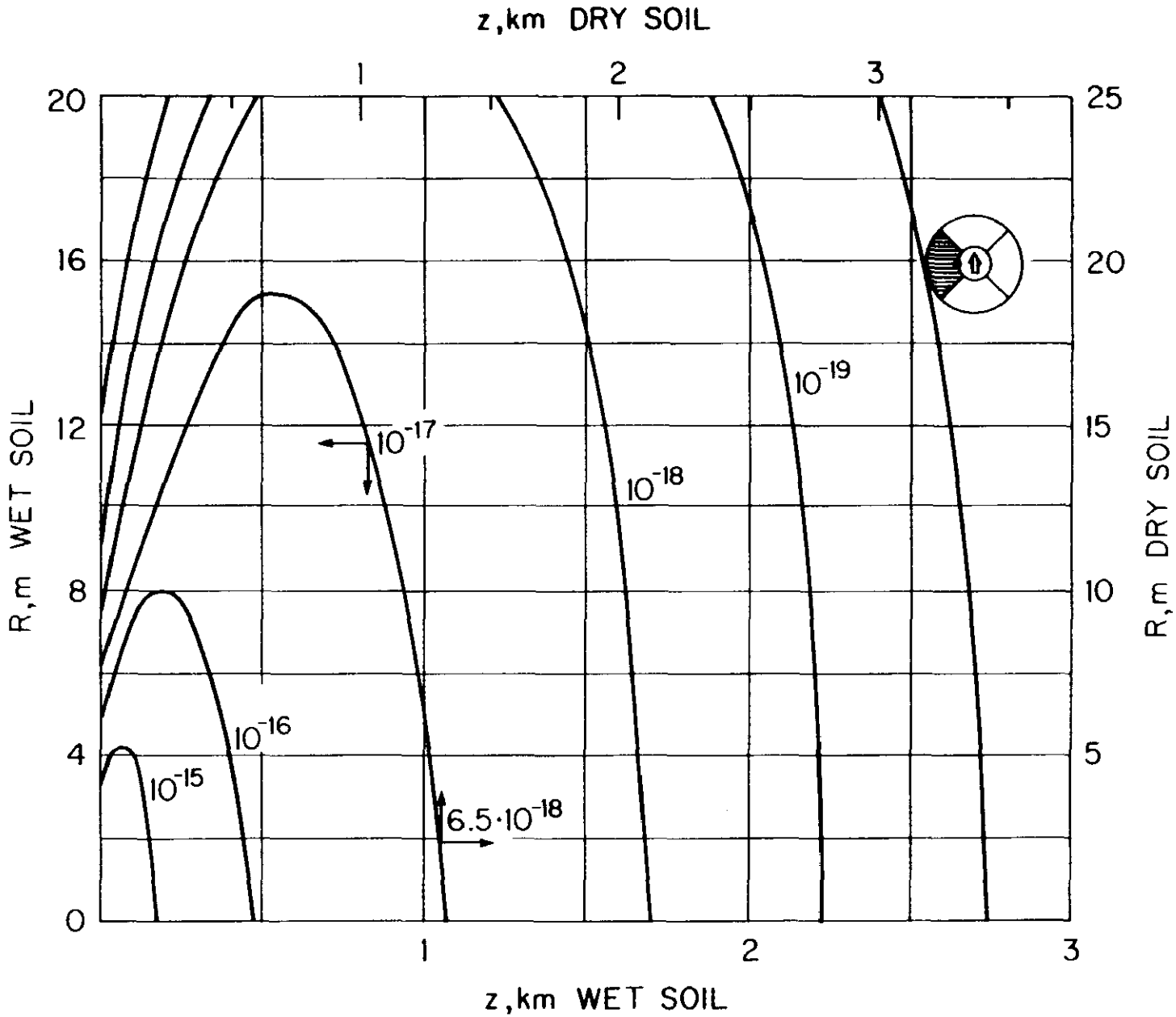

Fig. 110. Contours of equal dose-equivalent (in rem/interacting proton) in the inside quadrant (with respect to the ring) of a soil shield around a 1.2m radius tunnel due to muons from interactions of 10 TeV protons on the inside of the beampipe of a magnet inside the tunnel. The z-direction is tangential to the ring at the interaction point. Contours for wet soil (left & bottom axes) are integral powers of ten. Contours for dry soil (right & top axes) must be scaled down by 0.65 as shown for one example. Some contours may be omitted for clarity or due to statistical uncertainty.

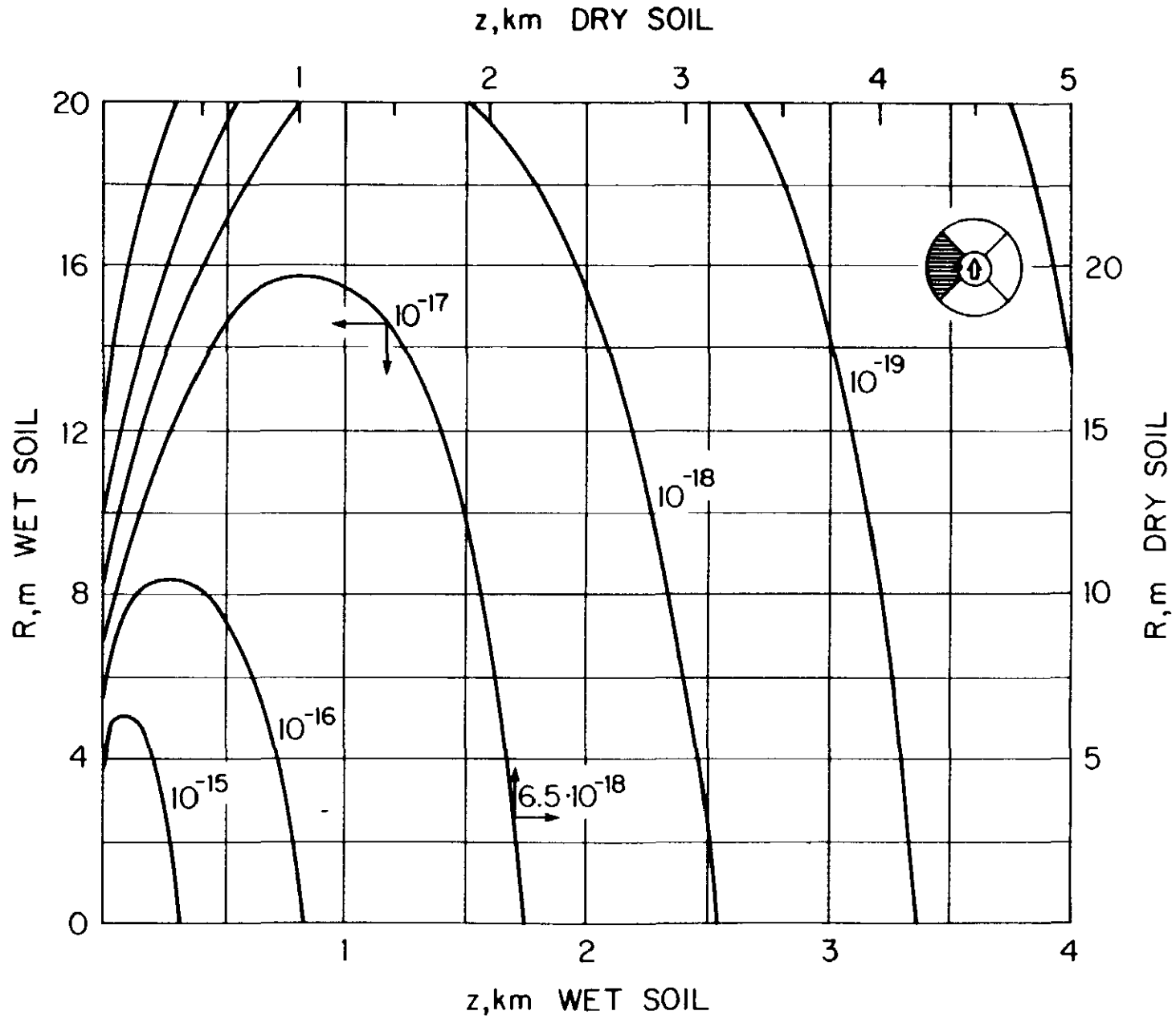

Fig. 111. Contours of equal dose-equivalent (in rem/interacting proton) in the inside quadrant (with respect to the ring) of a soil shield around a 1.2m radius tunnel due to muons from interactions of 20 TeV protons on the inside of the beampipe of a magnet inside the tunnel. The z-direction is tangential to the ring at the interaction point. Contours for wet soil (left & bottom axes) are integral powers of ten. Contours for dry soil (right & top axes) must be scaled down by 0.65 as shown for one example. Some contours may be omitted for clarity or due to statistical uncertainty.

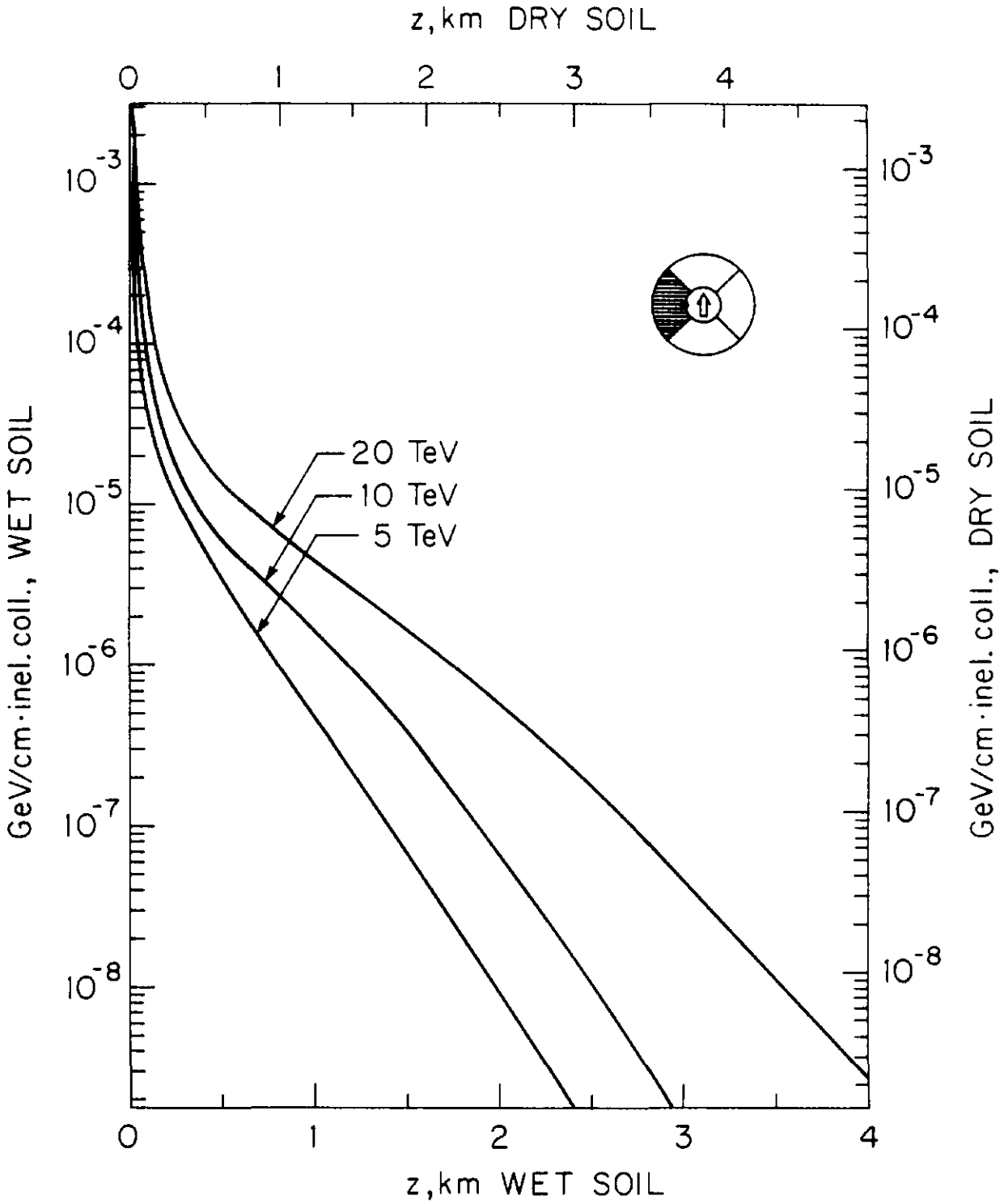

Fig. 112. Radially integrated energy density (in GeV/cm•interacting proton) in the inside quadrant (with respect to the ring) of a soil shield around a 1.2m radius tunnel due to muons from interactions of 5, 10 and 20 TeV protons on the inside of the beampipe of a continuous dipole inside the tunnel. The z-direction is tangential to the ring at the interaction point. For wet soil use left & bottom axes and for dry soil right & top axes.

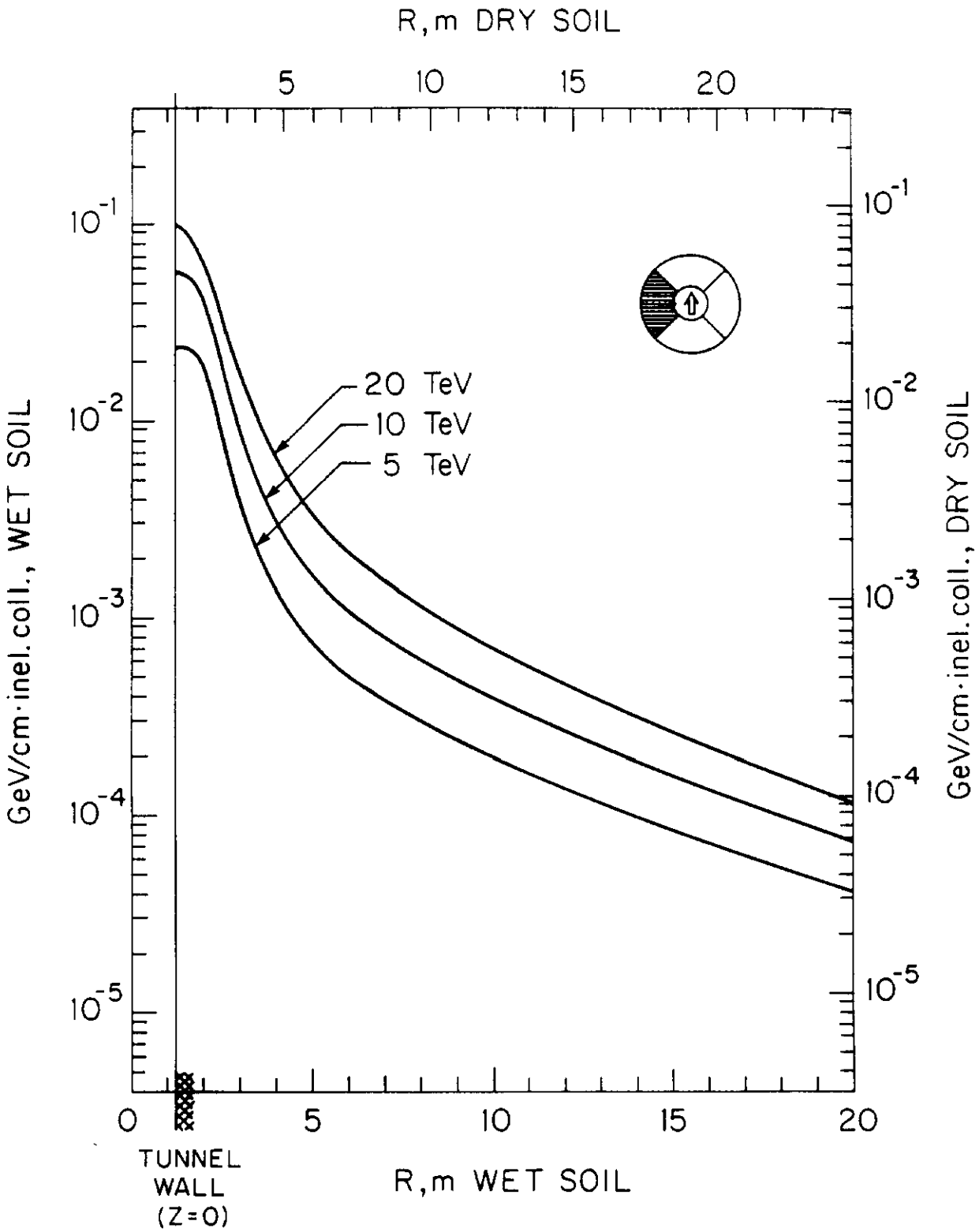

Fig. 113. Longitudinally integrated energy density (in GeV/cm•interacting proton) in the inside quadrant (with respect to the ring) of a soil shield around a 1.2m radius tunnel due to muons from interactions of 5, 10 and 20 TeV protons on the inside of the beam-pipe of a continuous dipole inside the tunnel. The R-direction is perpendicular to a tangent to the ring at the interaction point. For wet soil use left & bottom axes and for dry soil right & top axes.

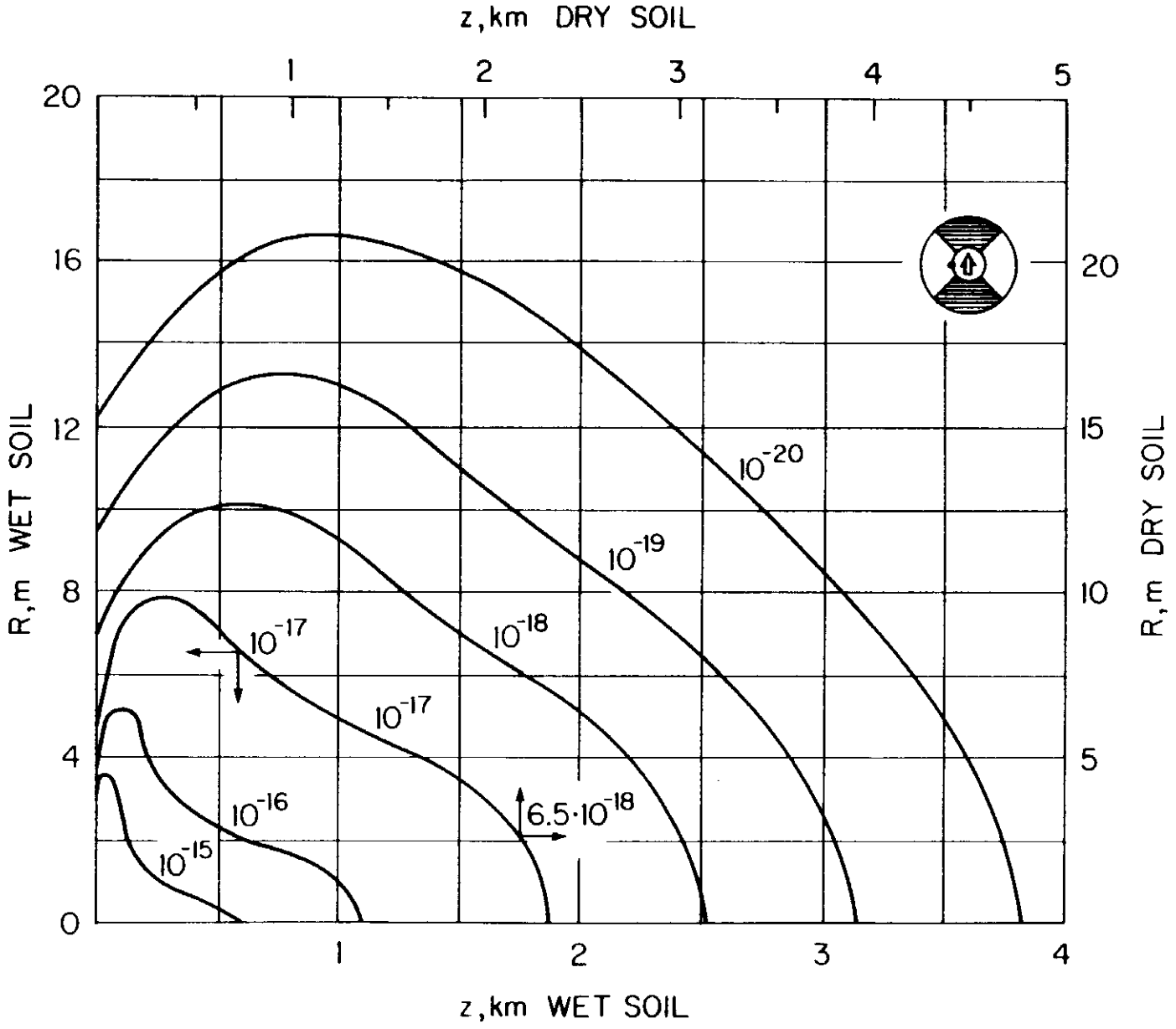

Fig. 114. Contours of equal dose-equivalent (in rem/interacting proton) in the top/bottom quadrant (with respect to the ring) of a soil shield around a 1.2m radius tunnel due to muons from interactions of 20 TeV protons on the inside of the beampipe of a magnet inside the tunnel. The z-direction is tangential to the ring at the interaction point. Contours for wet soil (left & bottom axes) are integral powers of ten. Contours for dry soil (right & top axes) must be scaled down by 0.65 as shown for one example. Some contours may be omitted for clarity or due to statistical uncertainty.

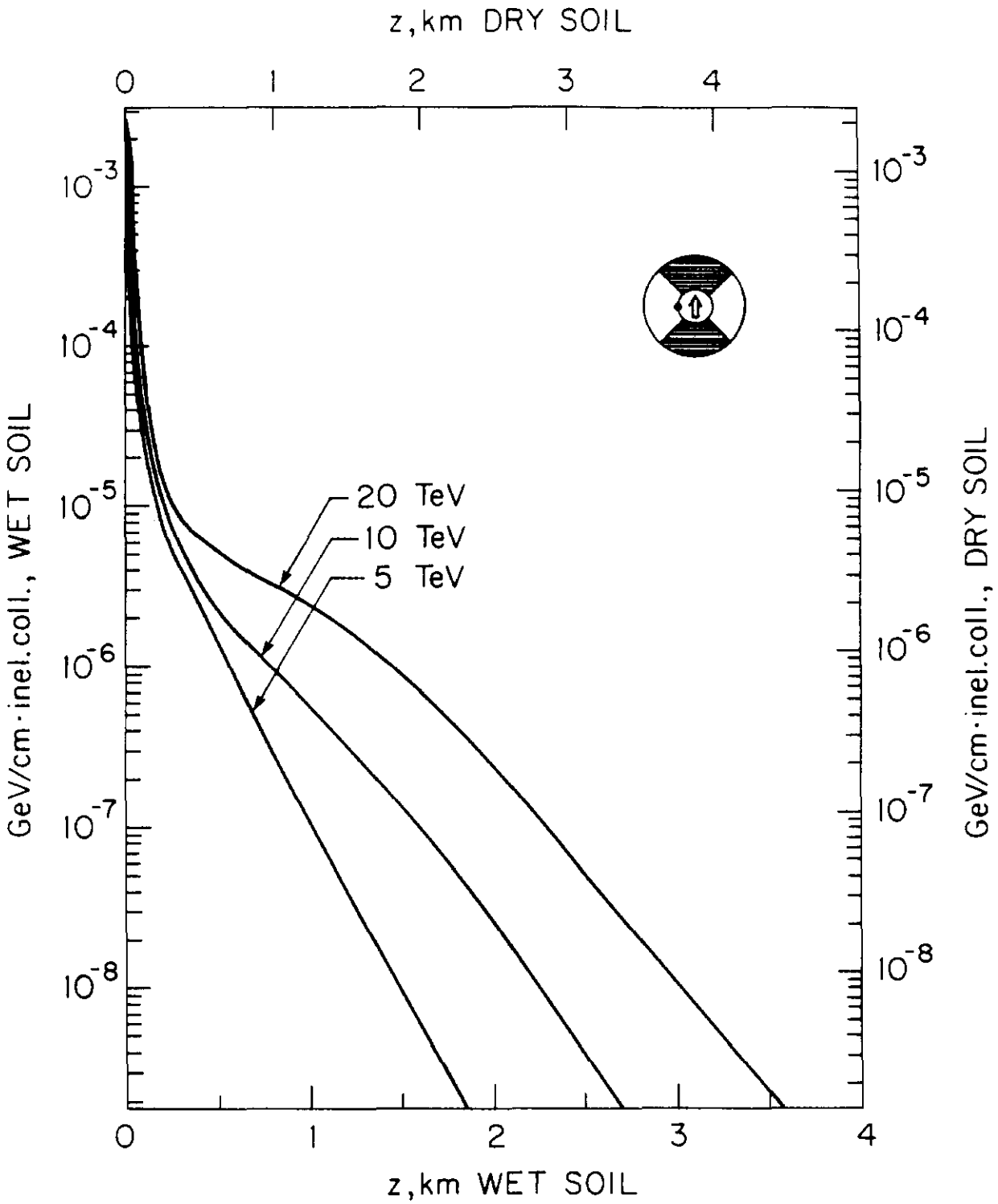

Fig. 115. Radially integrated energy density (in GeV/cm•interacting proton) in the top and bottom quadrant of a soil shield around a 1.2m radius tunnel due to muons from interactions of 5, 10 and 20 TeV protons on the inside of the beampipe of a continuous dipole inside the tunnel. The z-direction is tangential to the ring at the interaction point. For wet soil use left & bottom axes and for dry soil right & top axes.

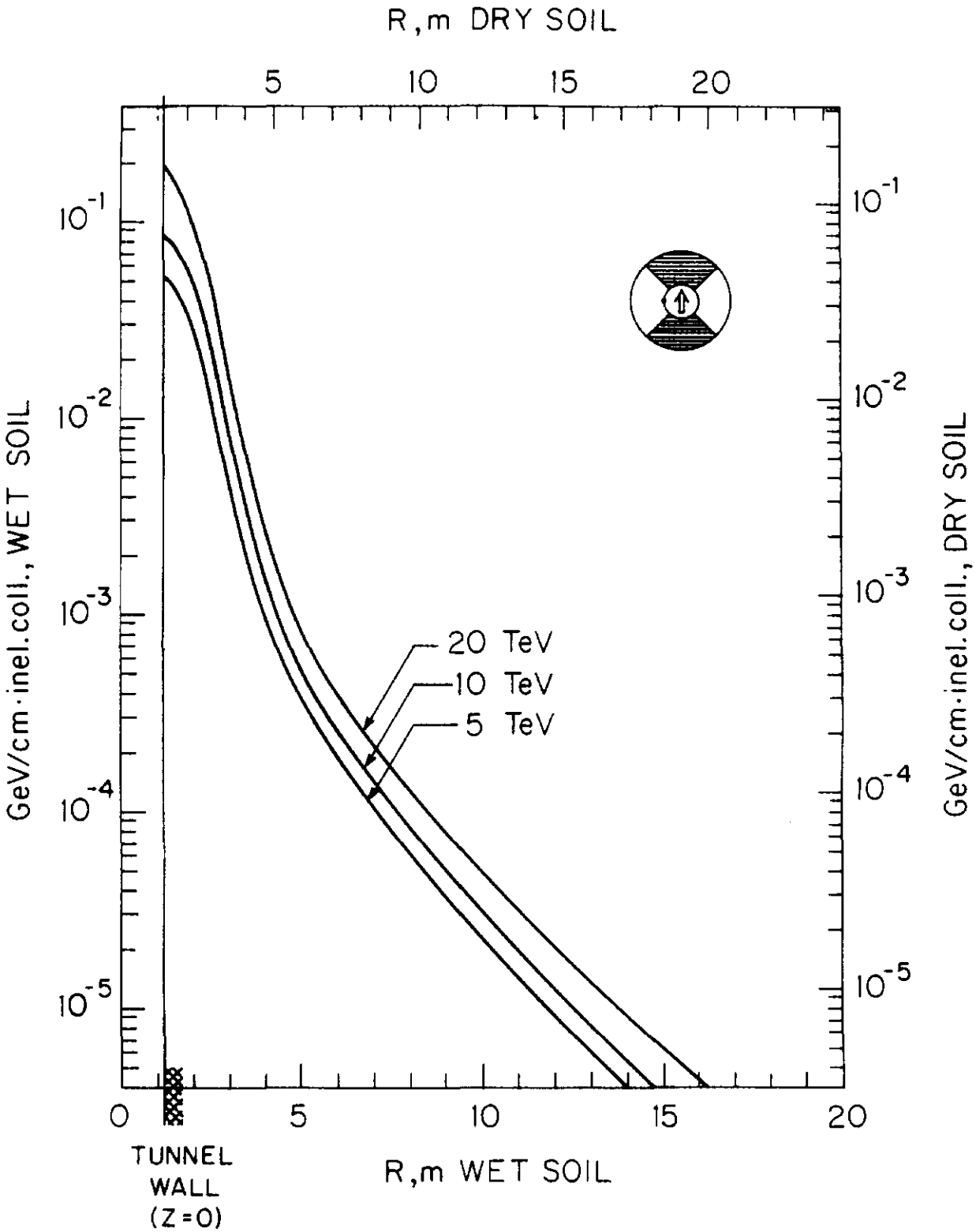

Fig. 116. Longitudinally integrated energy density (in GeV/cm•interacting proton) in the top and bottom quadrant of a soil shield around a 1.2m radius tunnel due to muons from interactions of 5, 10 and 20 TeV protons on the inside of the beampipe of a continuous dipole inside the tunnel. The R-direction is perpendicular to a tangent to the ring at the interaction point. For wet soil use left & bottom axes and for dry soil right & top axes.

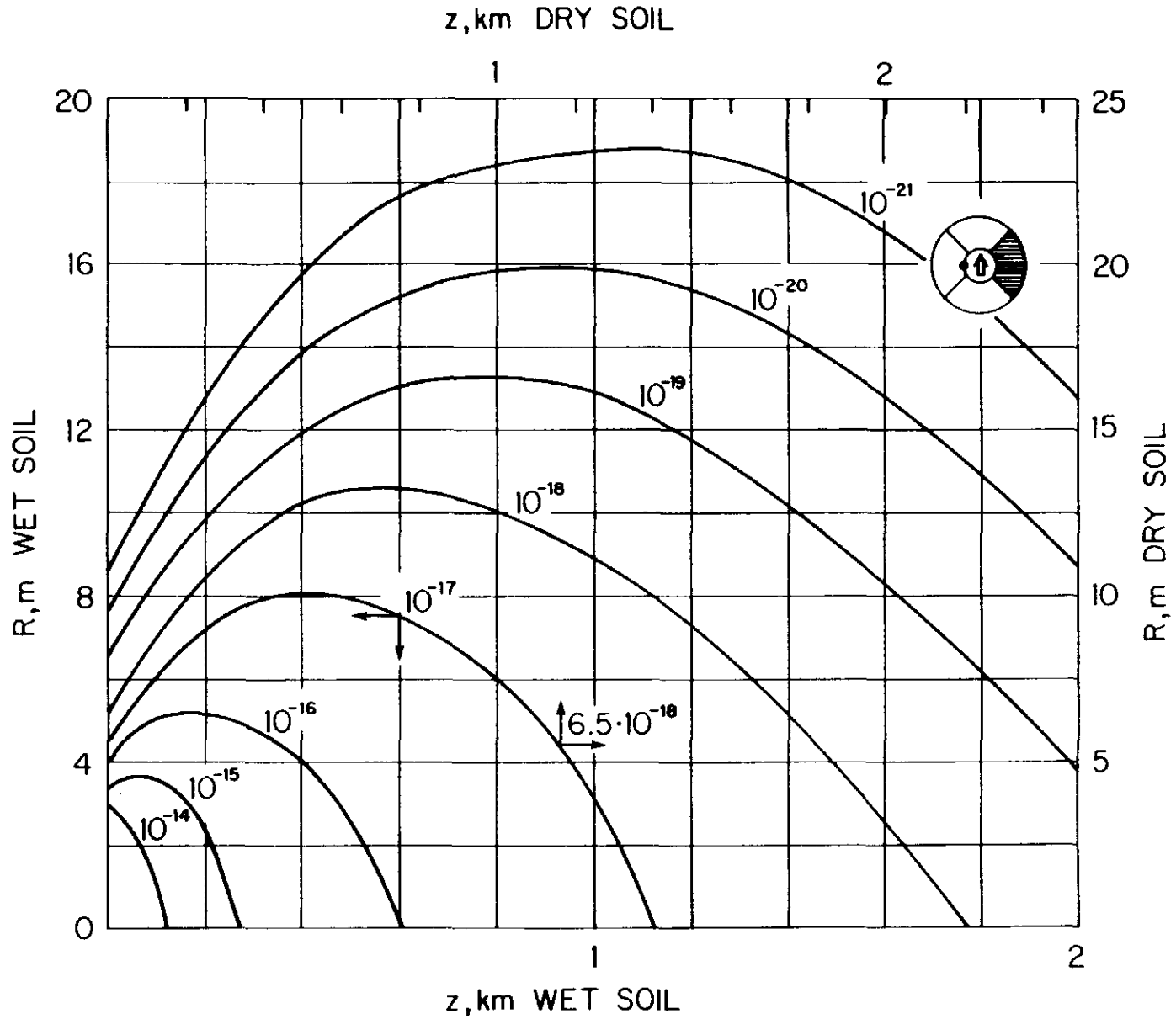

Fig. 117. Contours of equal dose-equivalent (in rem/interacting proton) in the outside quadrant (with respect to the ring) of a soil shield around a 1.2m radius tunnel due to muons from interactions of 5 TeV protons on the inside of the beampipe of a magnet inside the tunnel. The z-direction is tangential to the ring at the interaction point. Contours for wet soil (left & bottom axes) are integral powers of ten. Contours for dry soil (right & top axes) must be scaled down by 0.65 as shown for one example. Some contours may be omitted for clarity or due to statistical uncertainty.

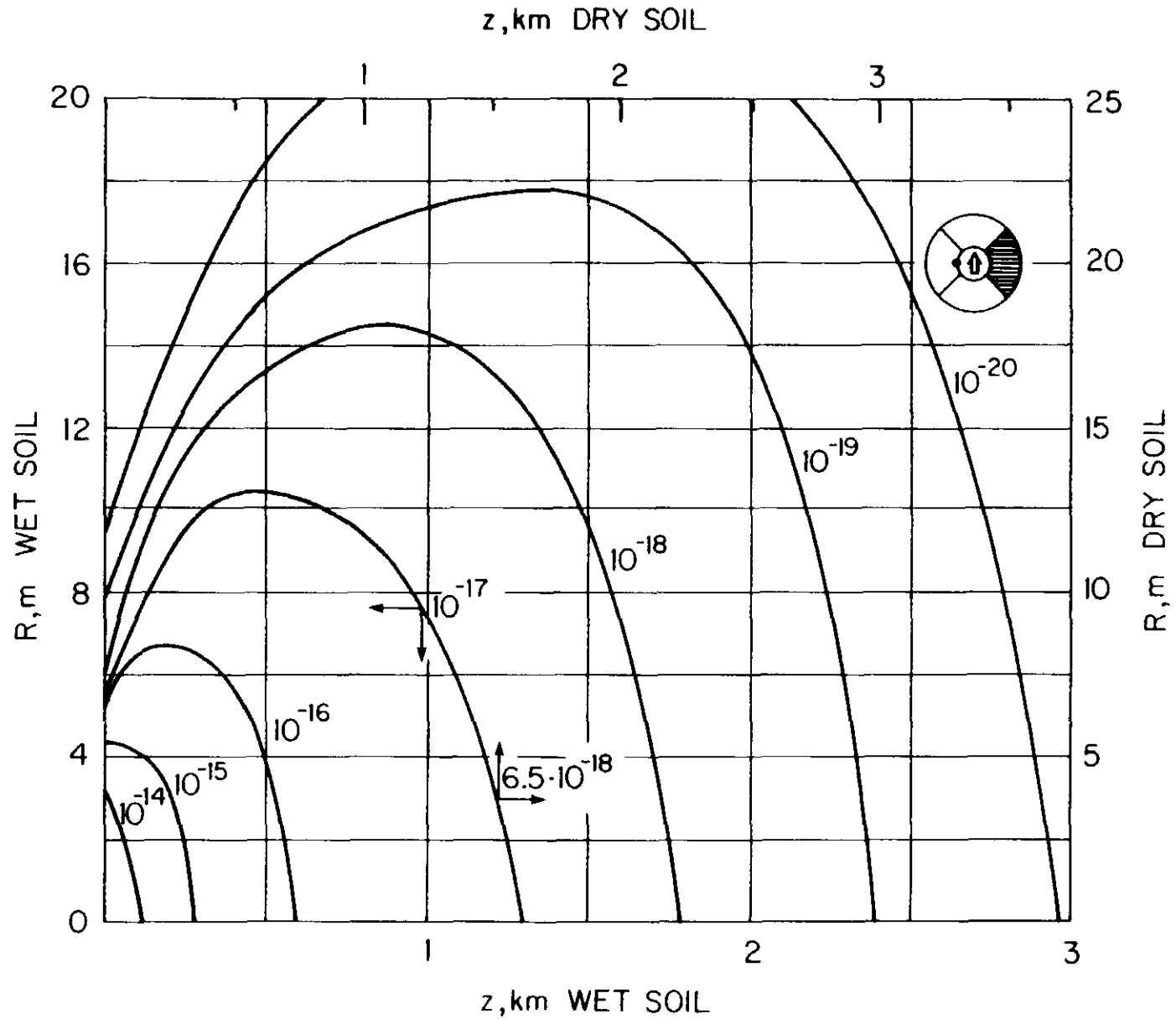

Fig. 118. Contours of equal dose-equivalent (in rem/interacting proton) in the outside quadrant (with respect to the ring) of a soil shield around a 1.2m radius tunnel due to muons from interactions of 10 TeV protons on the inside of the beampipe of a magnet inside the tunnel. The z-direction is tangential to the ring at the interaction point. Contours for wet soil (left & bottom axes) are integral powers of ten. Contours for dry soil (right & top axes) must be scaled down by 0.65 as shown for one example. Some contours may be omitted for clarity or due to statistical uncertainty.

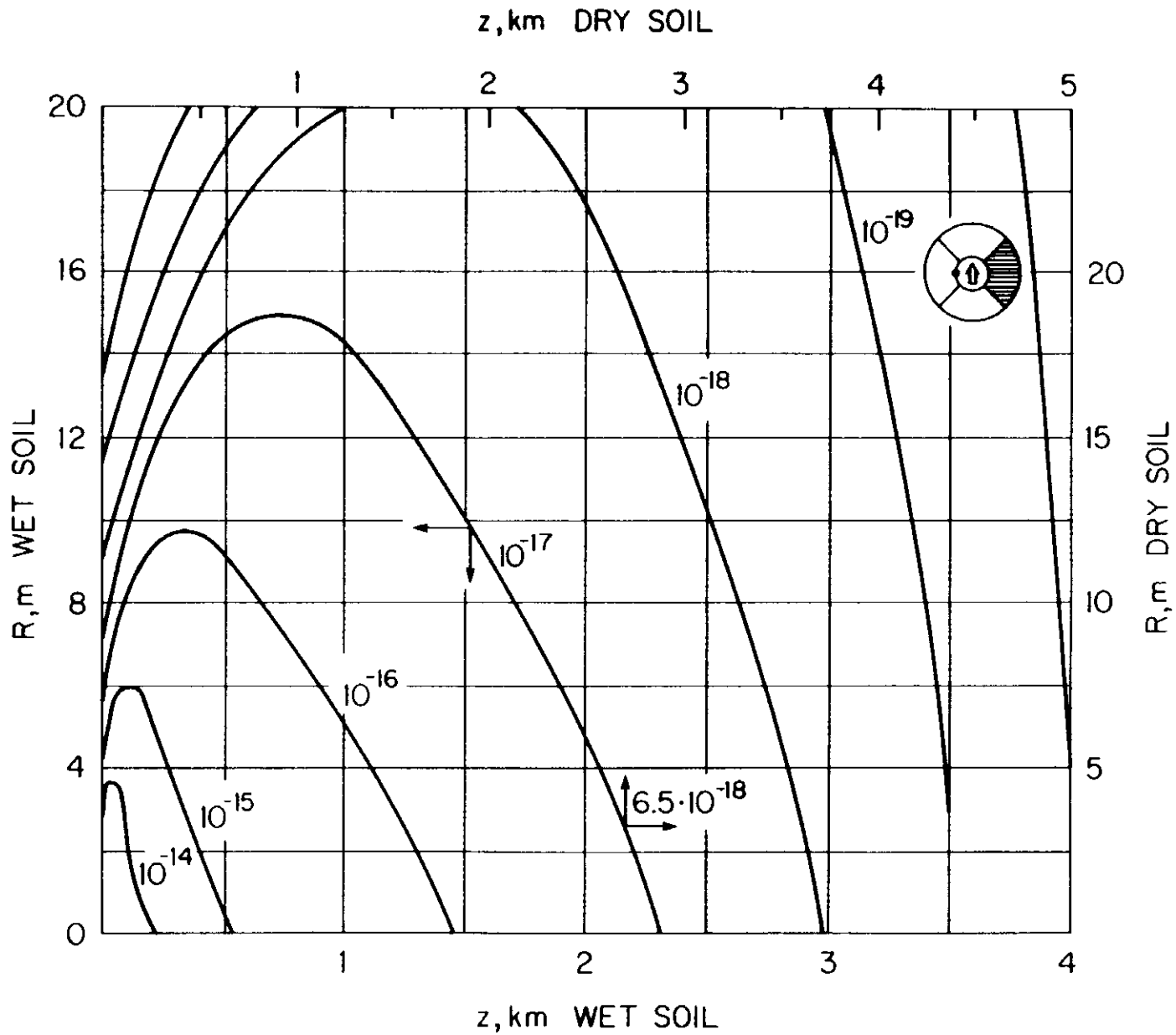

Fig. 119. Contours of equal dose-equivalent (in rem/interacting proton) in the outside quadrant (with respect to the ring) of a soil shield around a 1.2m radius tunnel due to muons from interactions of 20 TeV protons on the inside of the beampipe of a magnet inside the tunnel. The z-direction is tangential to the ring at the interaction point. Contours for wet soil (left & bottom axes) are integral powers of ten. Contours for dry soil (right & top axes) must be scaled down by 0.65 as shown for one example. Some contours may be omitted for clarity or due to statistical uncertainty.

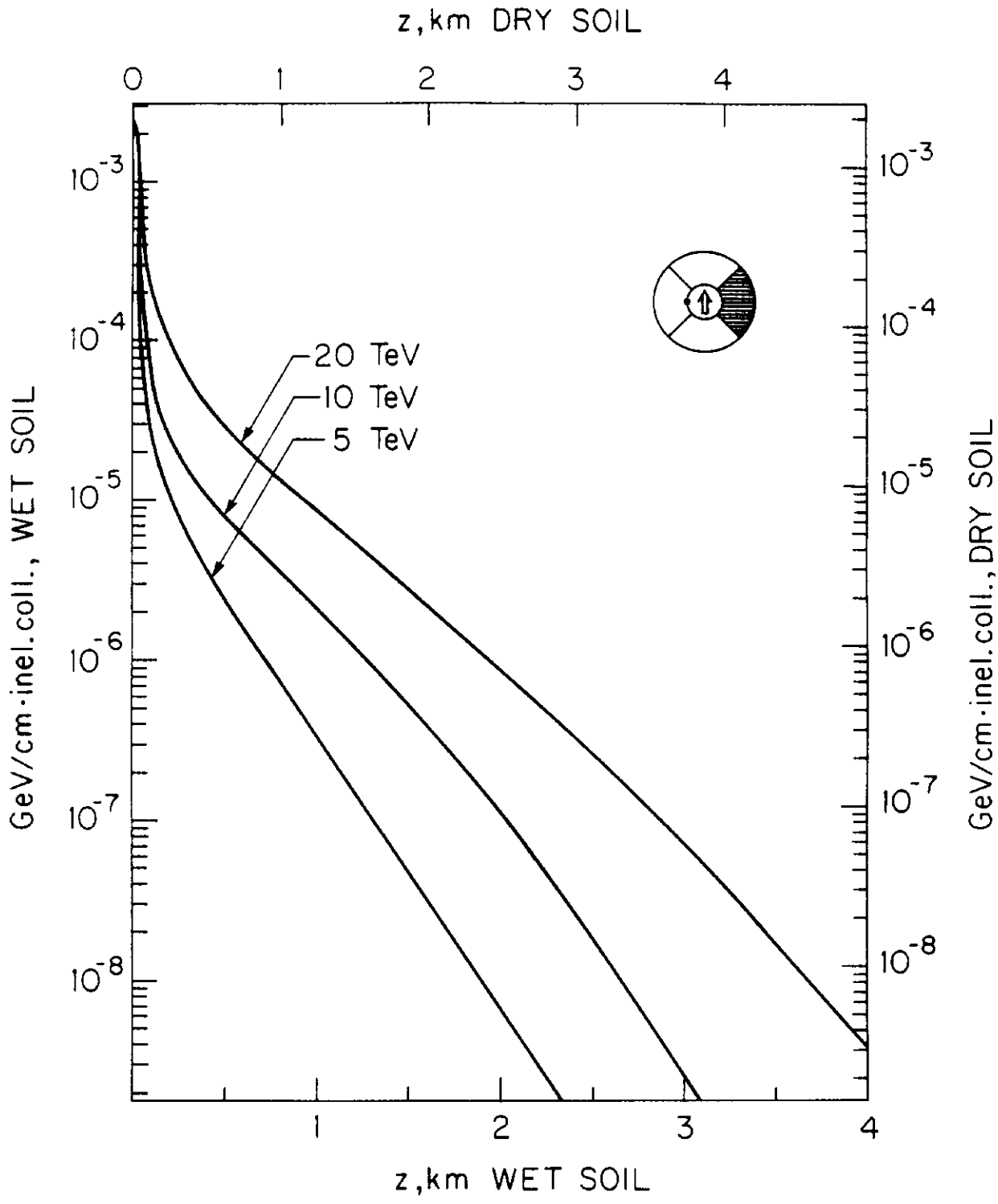

Fig. 120. Radially integrated energy density (in GeV/cm•interacting proton) in the outside quadrant (with respect to the ring) of a soil shield around a 1.2m radius tunnel due to muons from interactions of 5, 10 and 20 TeV protons on the inside of the beampipe of a continuous dipole inside the tunnel. The z-direction is tangential to the ring at the interaction point. For wet soil use left & bottom axes and for dry soil right & top axes.

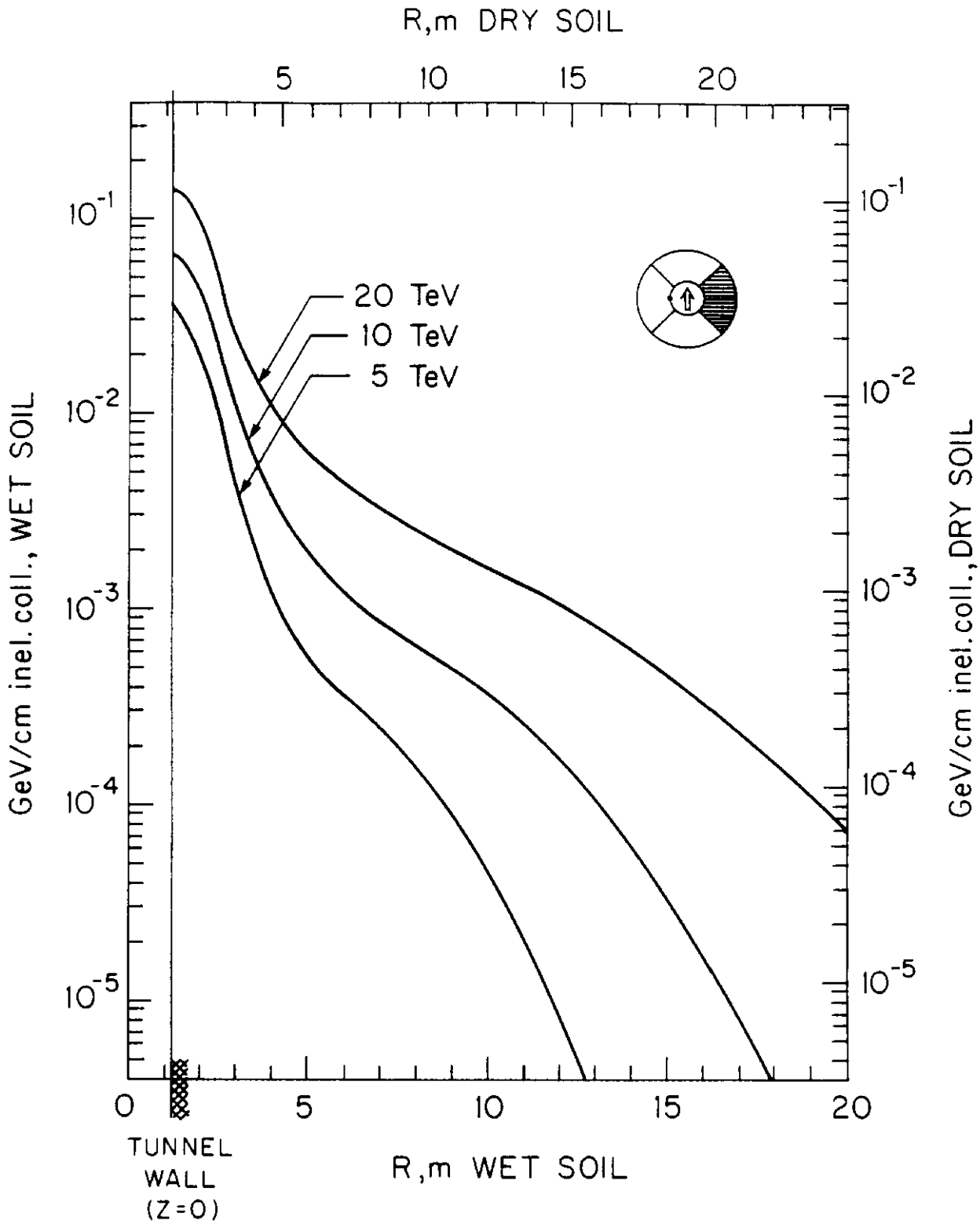

Fig. 121. Longitudinally integrated energy density (in GeV/cm•interacting proton) in the outside quadrant (with respect to the ring) of a soil shield around a 1.2m radius tunnel due to muons from interactions of 5, 10 and 20 TeV protons on the inside of the beampipe of a continuous dipole inside the tunnel. The R-direction is perpendicular to a tangent to the ring at the interaction point. For wet soil use left & bottom axes and for dry soil right & top axes.

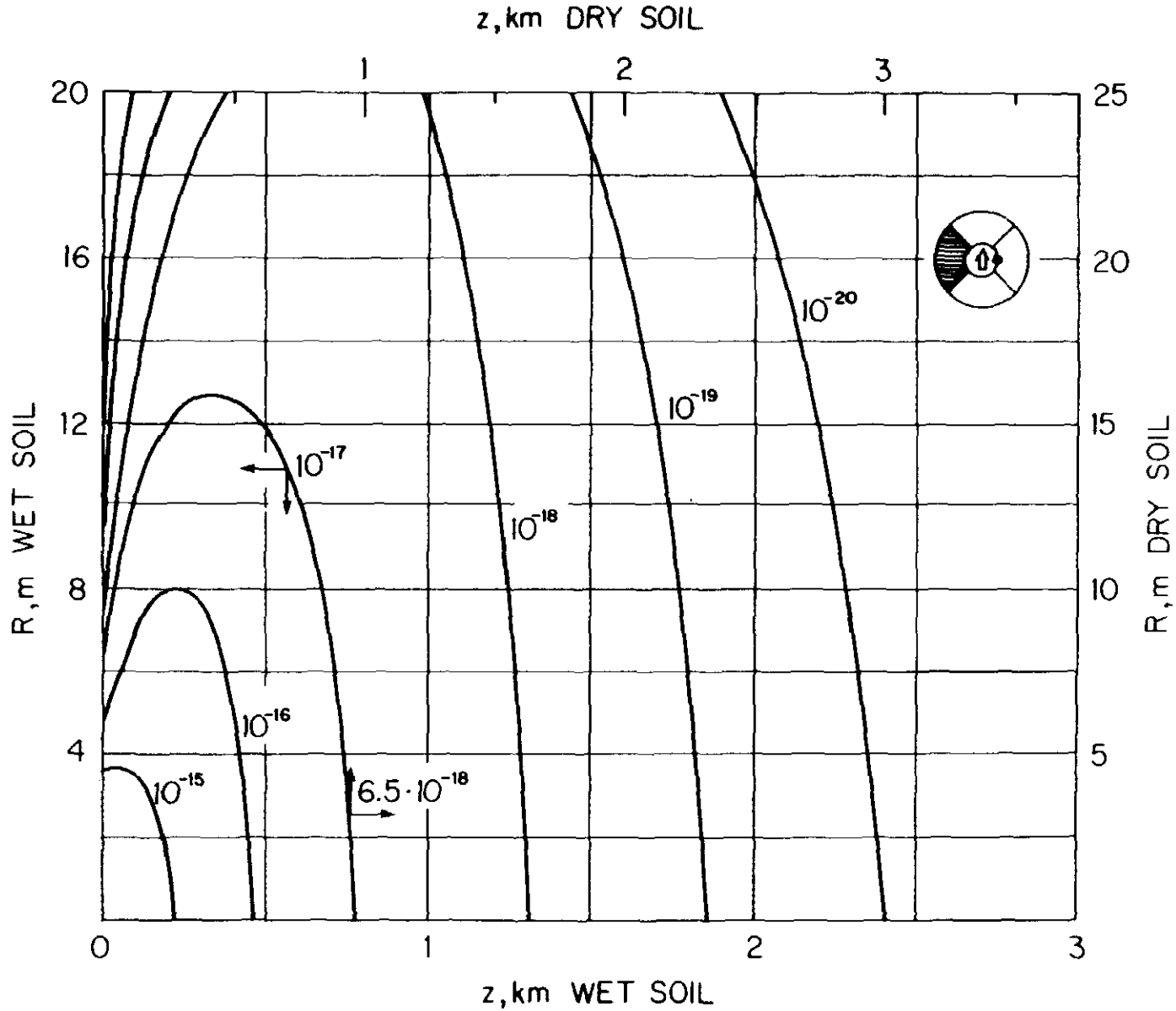

Fig. 122. Contours of equal dose-equivalent (in rem/interacting proton) in the inside quadrant (with respect to the ring) of a soil shield aroud a 1.2m radius tunnel due to muons from interactions of 5 TeV protons on the outside of the beampipe of a magnet inside the tunnel. The z-direction is tangential to the ring at the interaction point. Contours for wet soil (left & bottom axes) are integral powers of ten. Contours for dry soil (right & top axes) must be scaled down by 0.65 as shown for one example. Some contours may be omitted for clarity or due to statistical uncertainty.

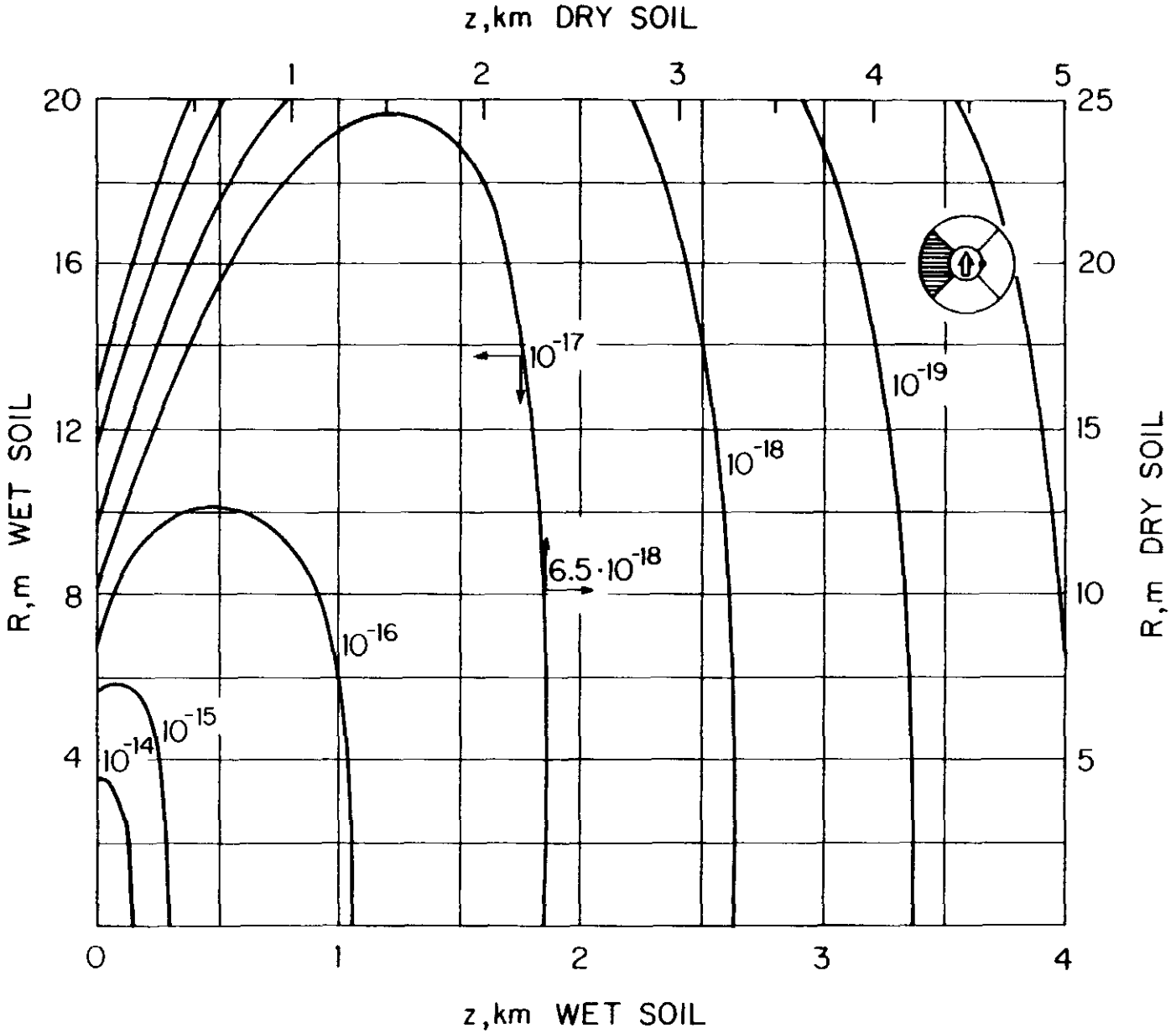

Fig. 123. Contours of equal dose-equivalent (in rem/interacting proton) in the inside quadrant (with respect to the ring) of a soil shield aroud a 1.2m radius tunnel due to muons from interactions of 20 TeV protons on the outside of the beampipe of a magnet inside the tunnel. The z-direction is tangential to the ring at the interaction point. Contours for wet soil (left & bottom axes) are integral powers of ten. Contours for dry soil (right & top axes) must be scaled down by 0.65 as shown for one example. Some contours may be omitted for clarity or due to statistical uncertainty.

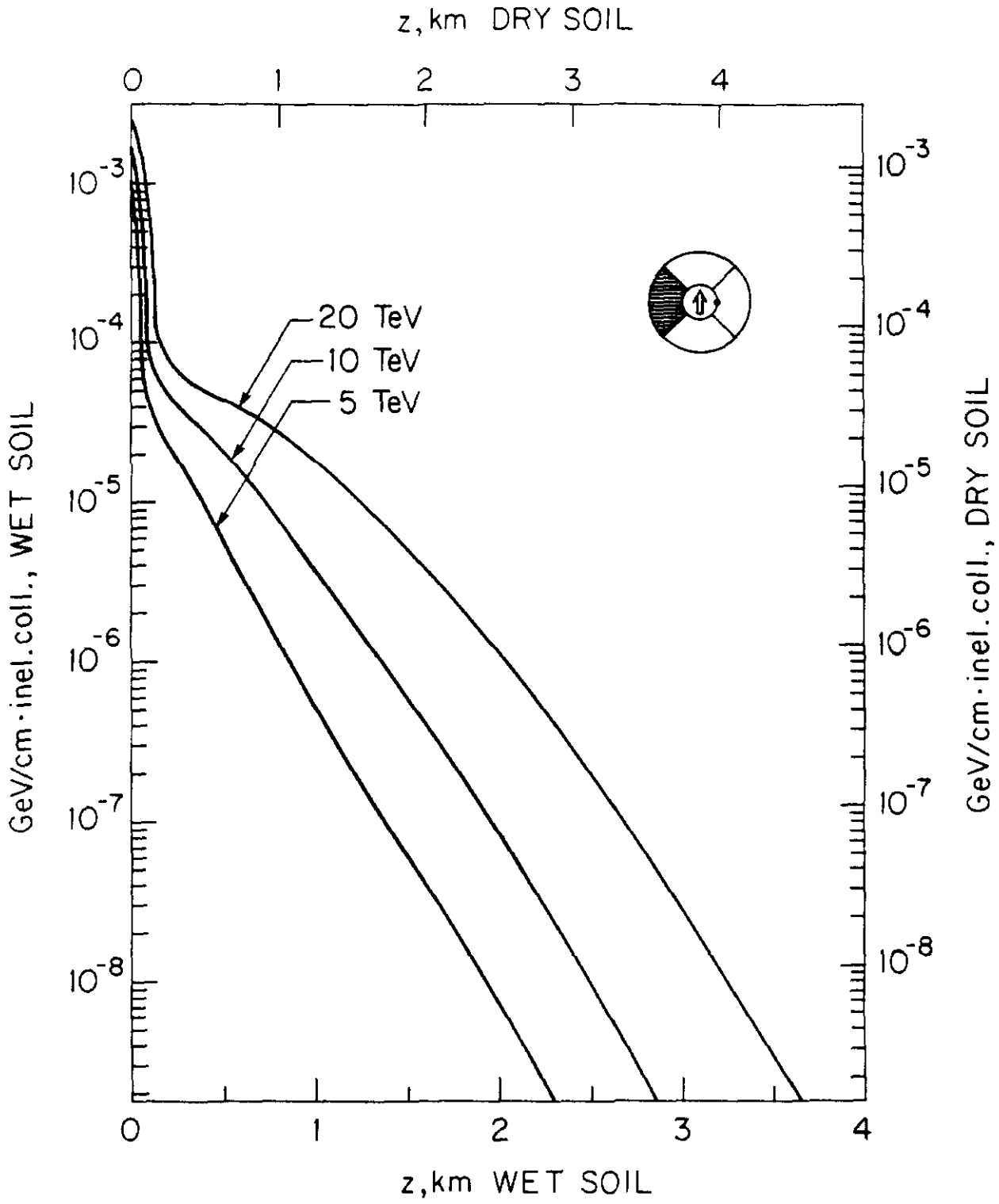

Fig. 124. Radially integrated energy density (in GeV/cm•interacting proton) in the inside quadrant (with respect to the ring) of a soil shield around a 1.2m radius tunnel due to muons from interactions of 5, 10 and 20 TeV protons on the outside of the beampipe of a continuous dipole inside the tunnel. The z-direction is tangential to the ring at the interaction point. For wet soil use left & bottom axes and for dry soil right & top axes.

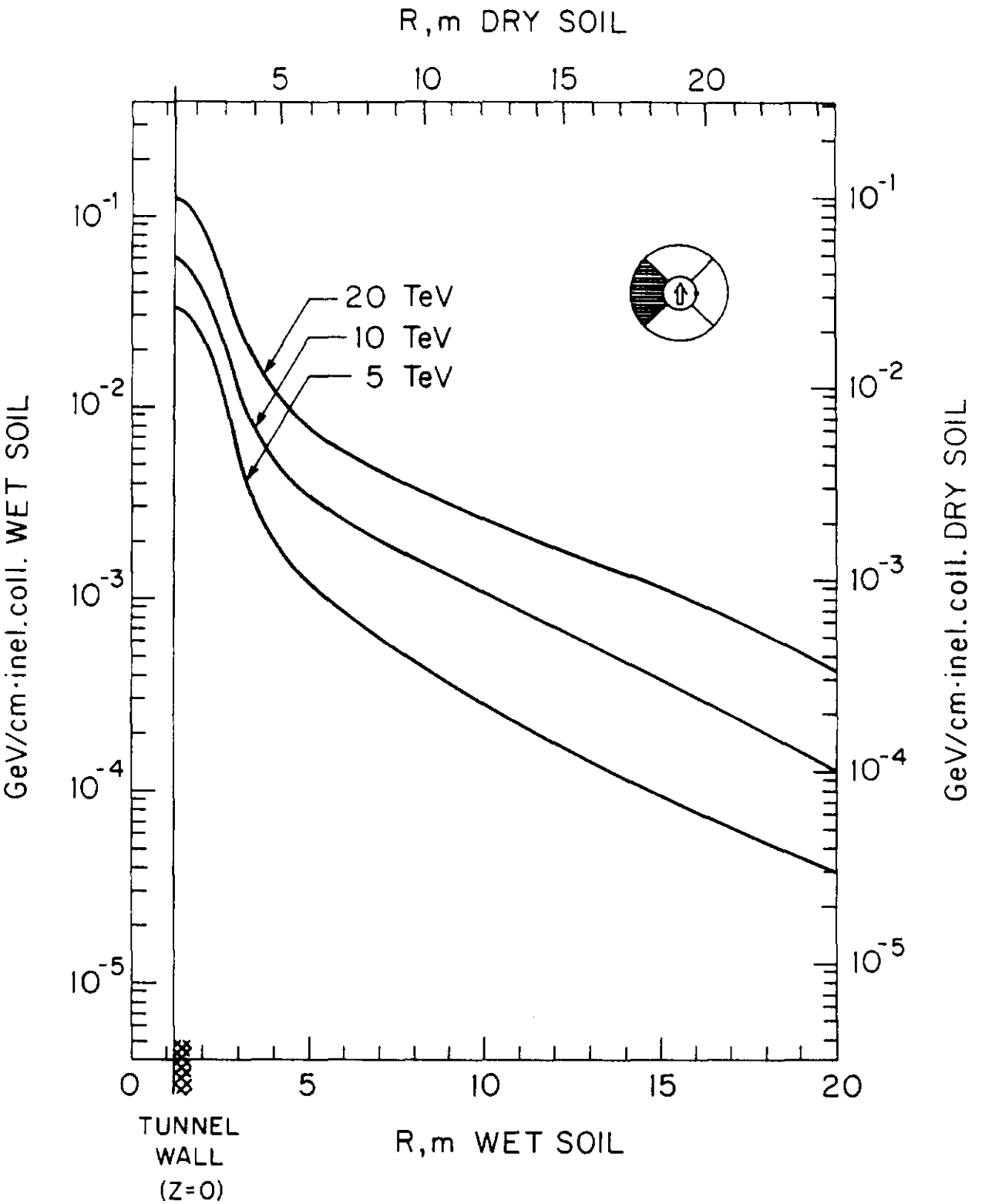

Fig. 125. Longitudinally integrated energy density (in GeV/cm•interacting proton) in the inside quadrant (with respect to the ring) of a soil shield around a 1.2m radius tunnel due to muons from interactions of 5, 10 and 20 TeV protons on the outside of the beampipe of a continuous dipole inside the tunnel. The R-direction is perpendicular to a tangent to the ring at the interaction point. For wet soil use left & bottom axes and for dry soil right & top axes.

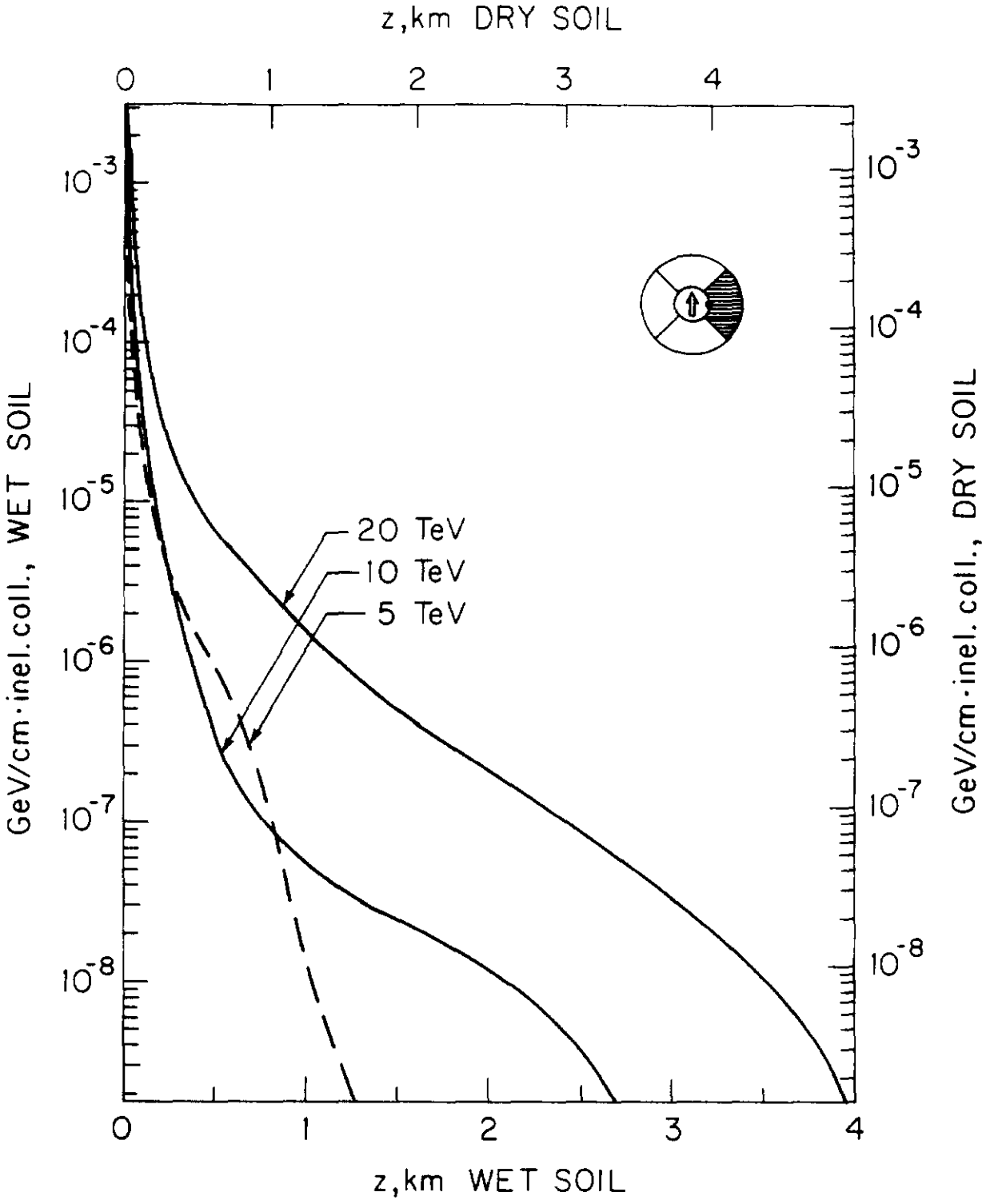

Fig. 126. Radially integrated energy density (in GeV/cm•interacting proton) in the outside quadrant (with respect to the ring) of a soil shield around a 1.2m radius tunnel due to muons from interactions of 5, 10 and 20 TeV protons on the outside of the beampipe of a continuous dipole inside the tunnel. The z-direction is tangential to the ring at the interaction point. For wet soil use left & bottom axes and for dry soil right & top axes.

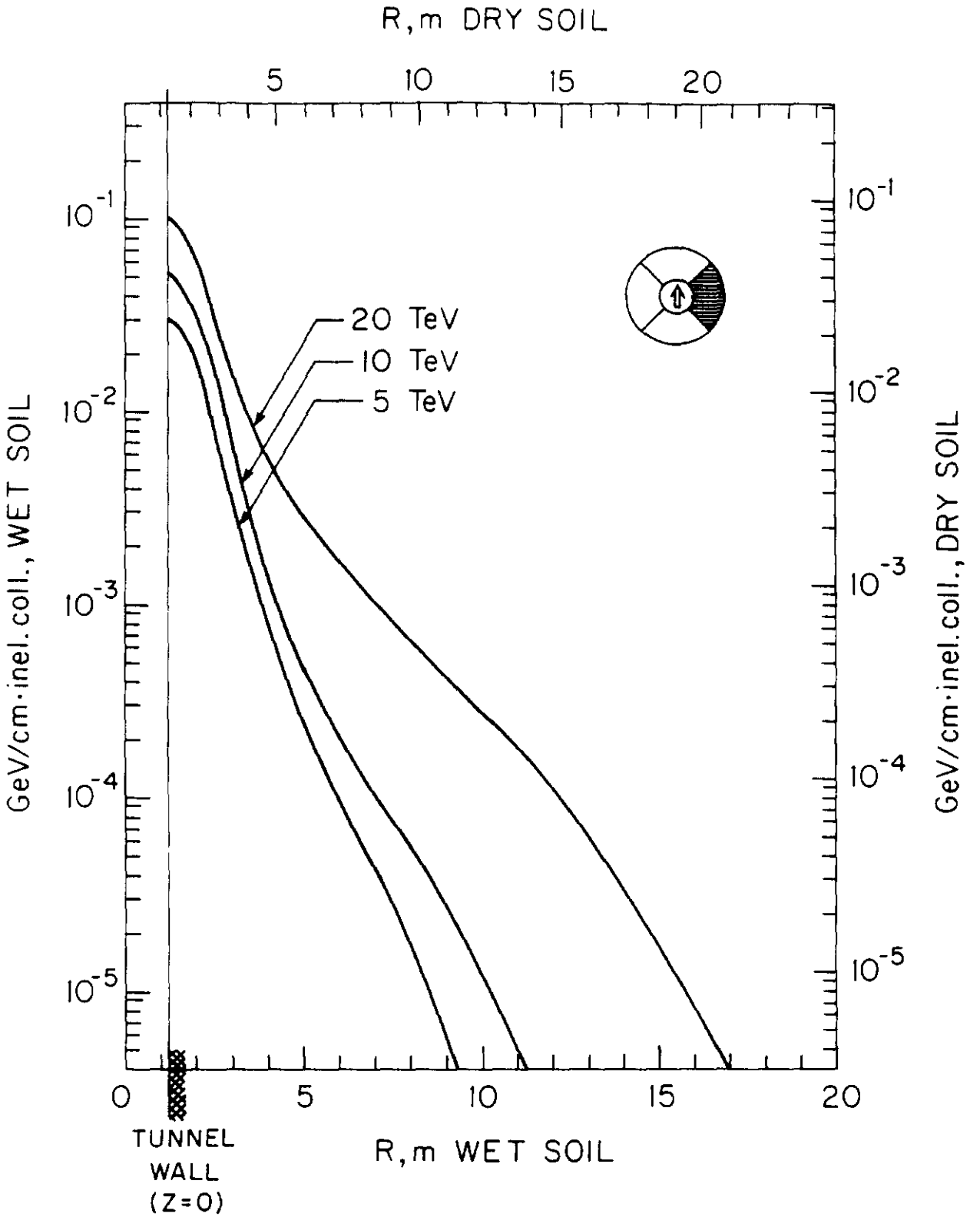

Fig. 127. Longitudinally integrated energy density (in GeV/cm•interacting proton) in the outside quadrant (with respect to the ring) of a a soil shield around a 1.2m radius tunnel due to muons from interactions of 5, 10 and 20 TeV protons on the outside of the beampipe of a continuous dipole inside the tunnel. The R-direction is perpendicular to a tangent to the ring at the interaction point. For wet soil use left & bottom axes and for dry soil right & top axes.

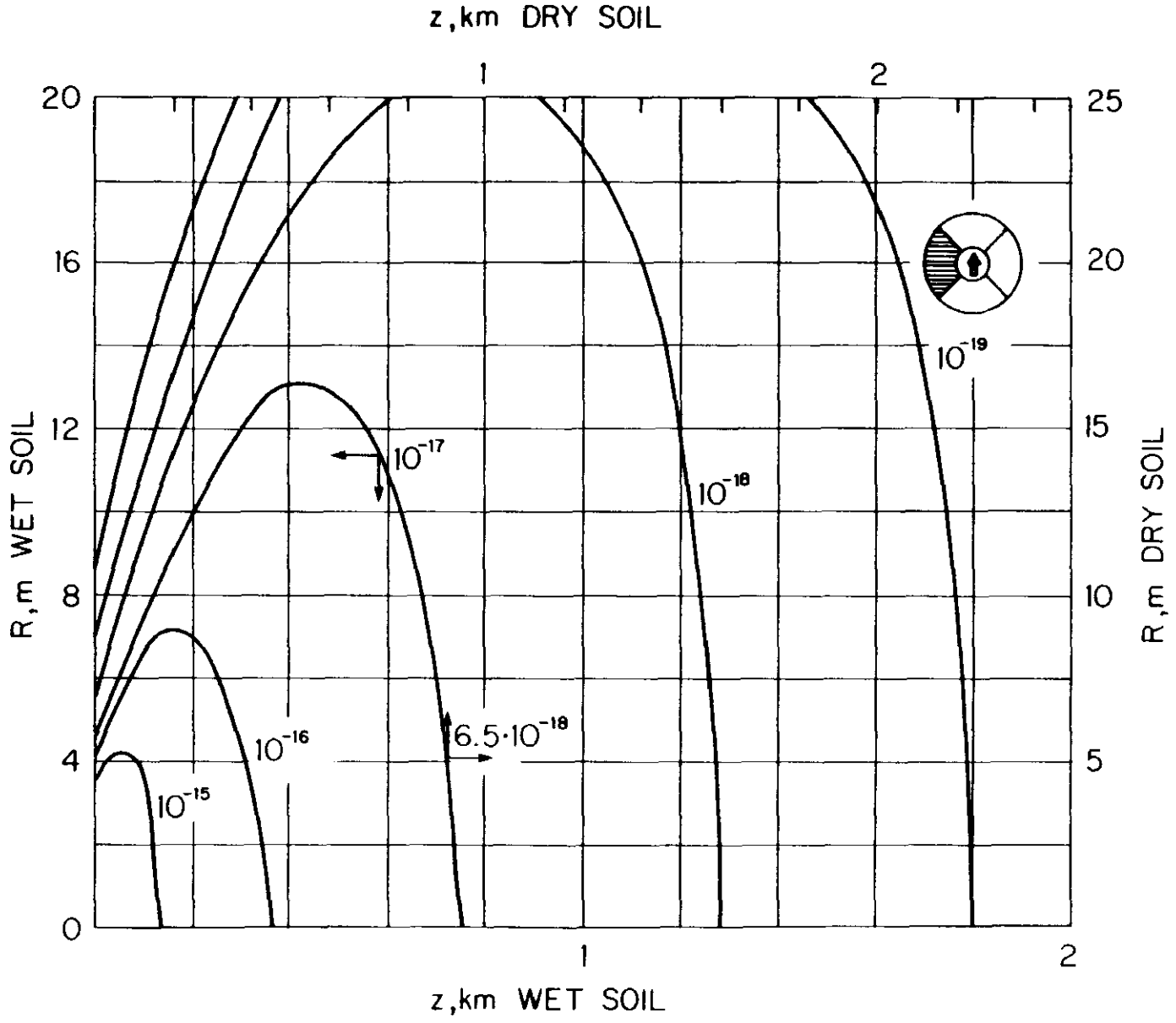

Fig. 128. Contours of equal dose-equivalent (in rem/interacting proton) in the inside quadrant (with respect to the ring) of a soil shield aroud a 1.2m radius tunnel due to muons from interactions of 5 TeV protons in the middle of the beampipe of a magnet inside the tunnel. The z-direction is tangential to the ring at the interaction point. Contours for wet soil (left & bottom axes) are integral powers of ten. Contours for dry soil (right & top axes) must be scaled down by 0.65 as shown for one example. Some contours may be omitted for clarity or due to statistical uncertainty.

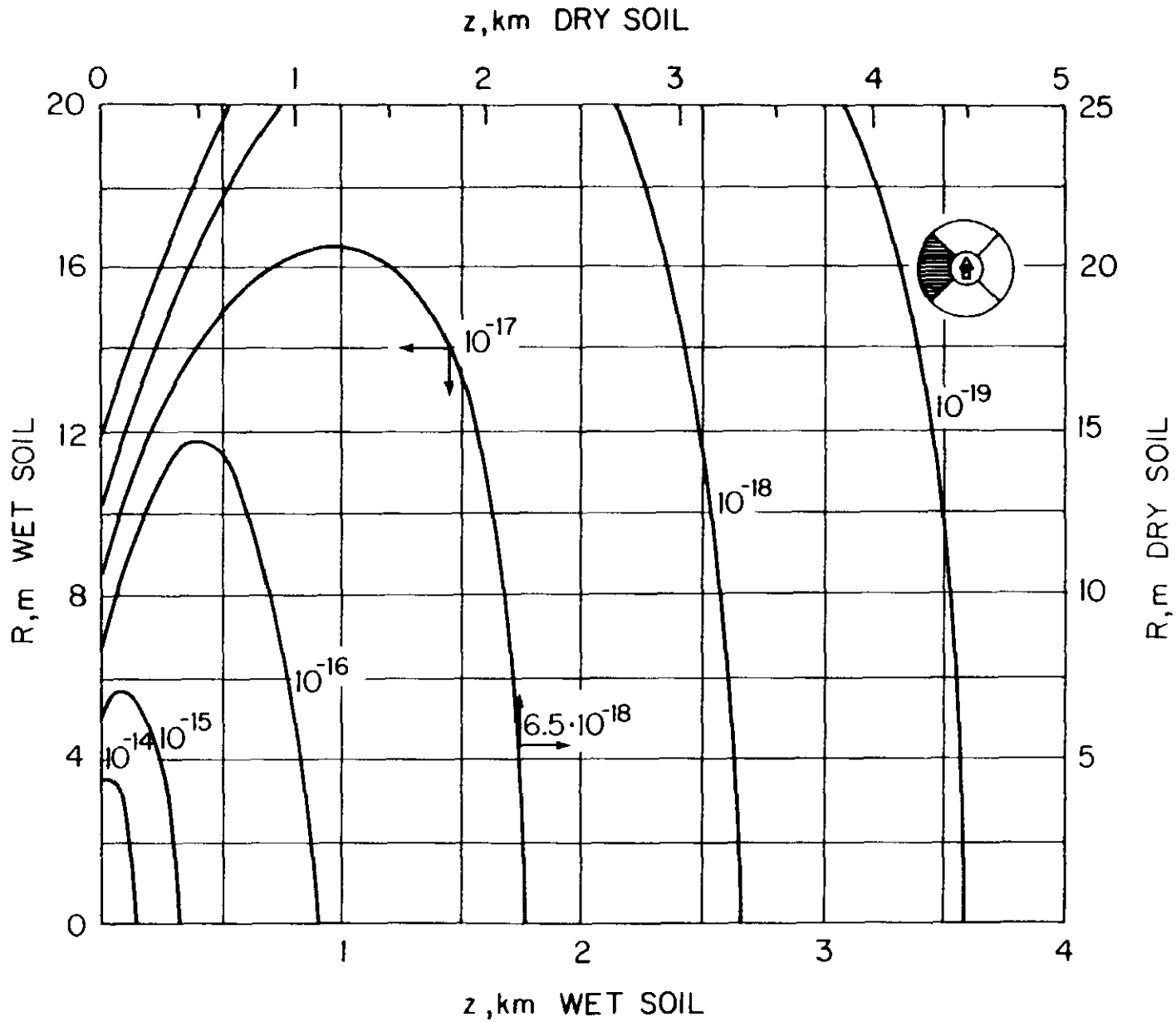

Fig. 129. Contours of equal dose-equivalent (in rem/interacting proton) in the inside quadrant (with respect to the ring) of a soil shield aroud a 1.2m radius tunnel due to muons from interactions of 20 TeV protons in the middle of the beampipe of a magnet inside the tunnel. The z-direction is tangential to the ring at the interaction point. Contours for wet soil (left & bottom axes) are integral powers of ten. Contours for dry soil (right & top axes) must be scaled down by 0.65 as shown for one example. Some contours may be omitted for clarity or due to statistical uncertainty.

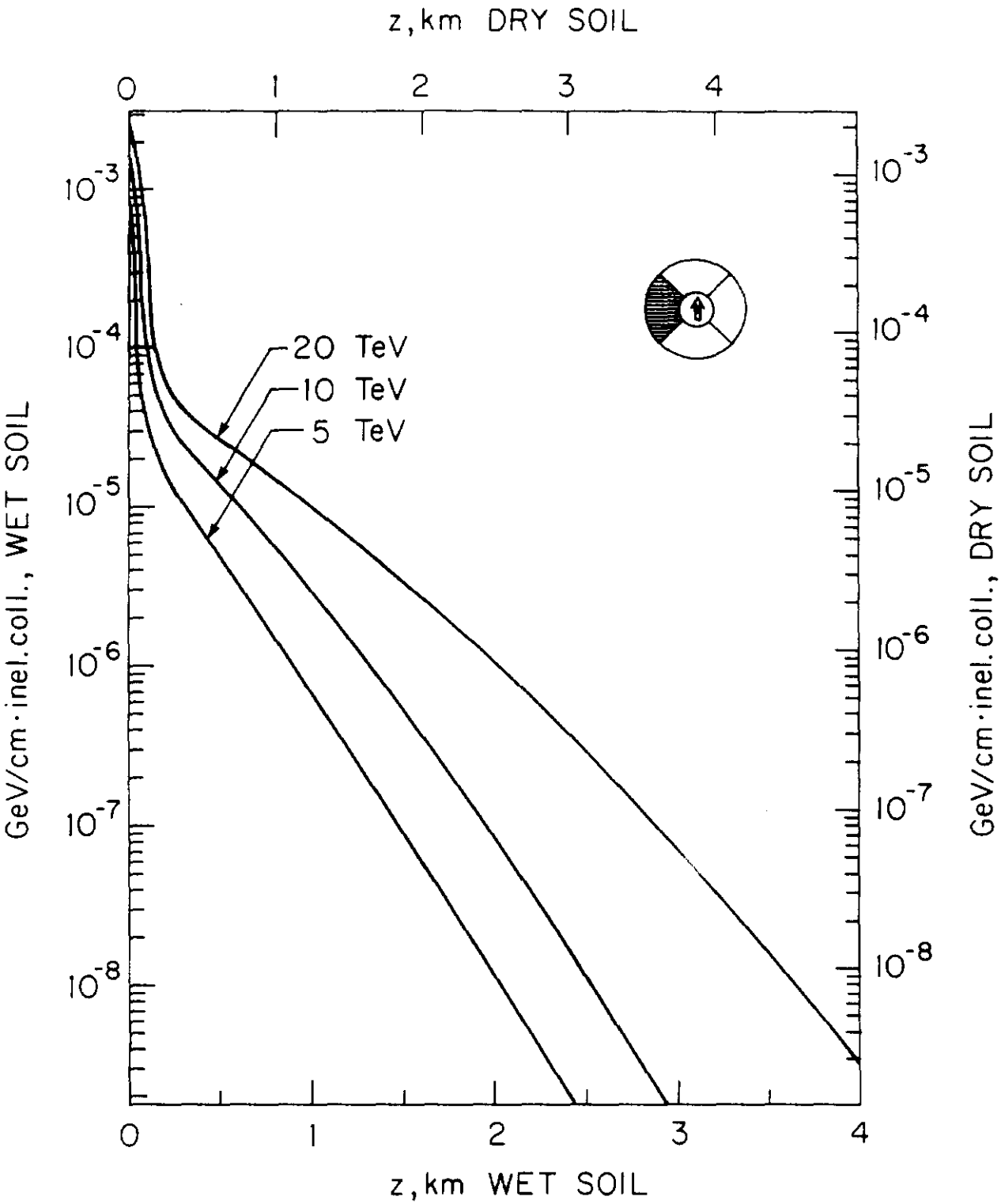

Fig. 130. Radially integrated energy density (in GeV/cm•interacting proton) in the inside quadrant (with respect to the ring) of a soil shield around a 1.2m radius tunnel due to muons from interactions of 5, 10 and 20 TeV protons in the middle of the beampipe of a continuous dipole inside the tunnel. The z-direction is tangential to the ring at the interaction point. For wet soil use left & bottom axes and for dry soil right & top axes.

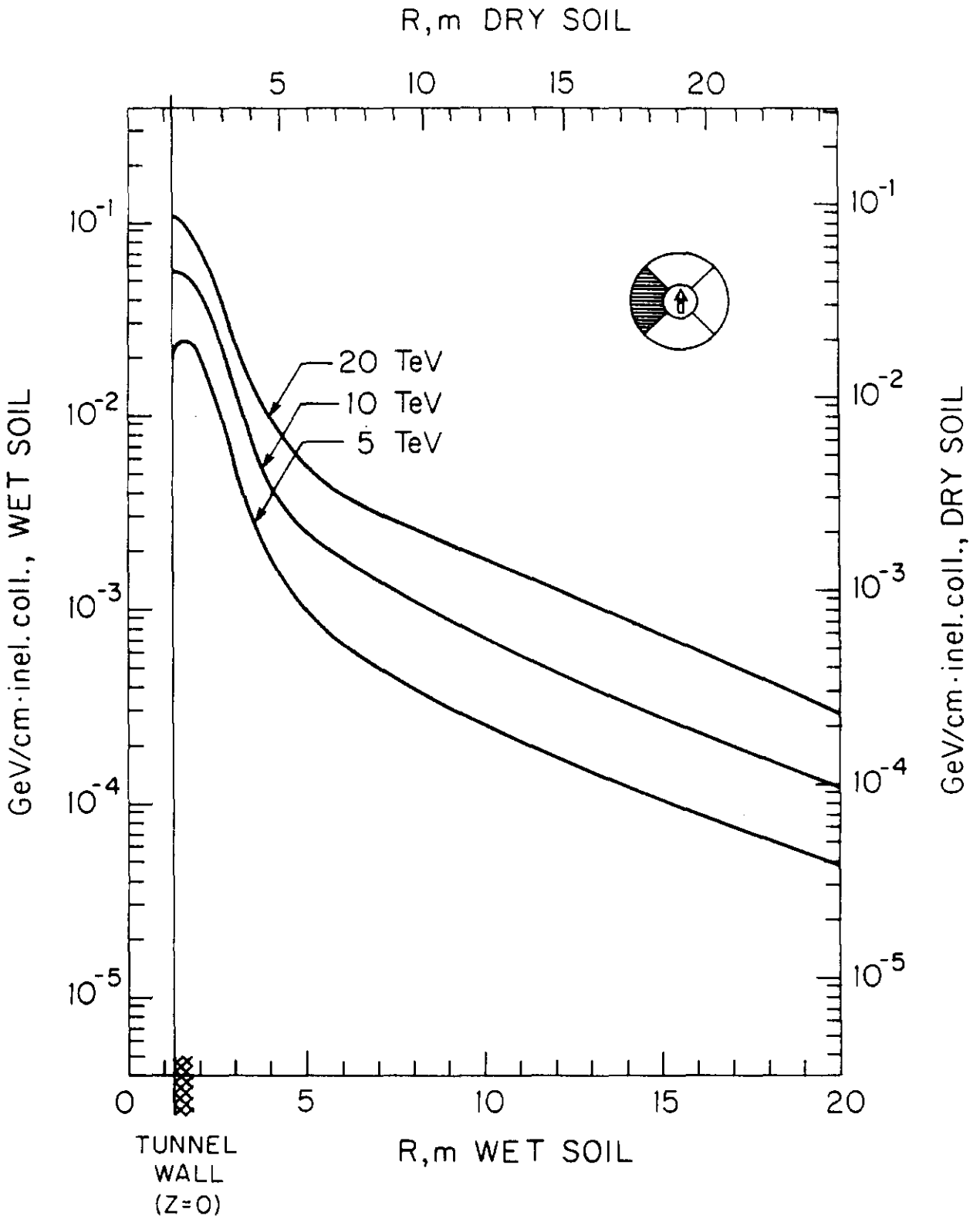

Fig. 131. Longitudinally integrated energy density (in GeV/cm•interacting proton) in the inside quadrant (with respect to the ring) of a soil shield around a 1.2m radius tunnel due to muons from interactions of 5, 10 and 20 TeV protons on the middle of the beampipe of a continuous dipole inside the tunnel. The R-direction is perpendicular to a tangent to the ring at the interaction point. For wet soil use left & bottom axes and for dry soil right & top axes.

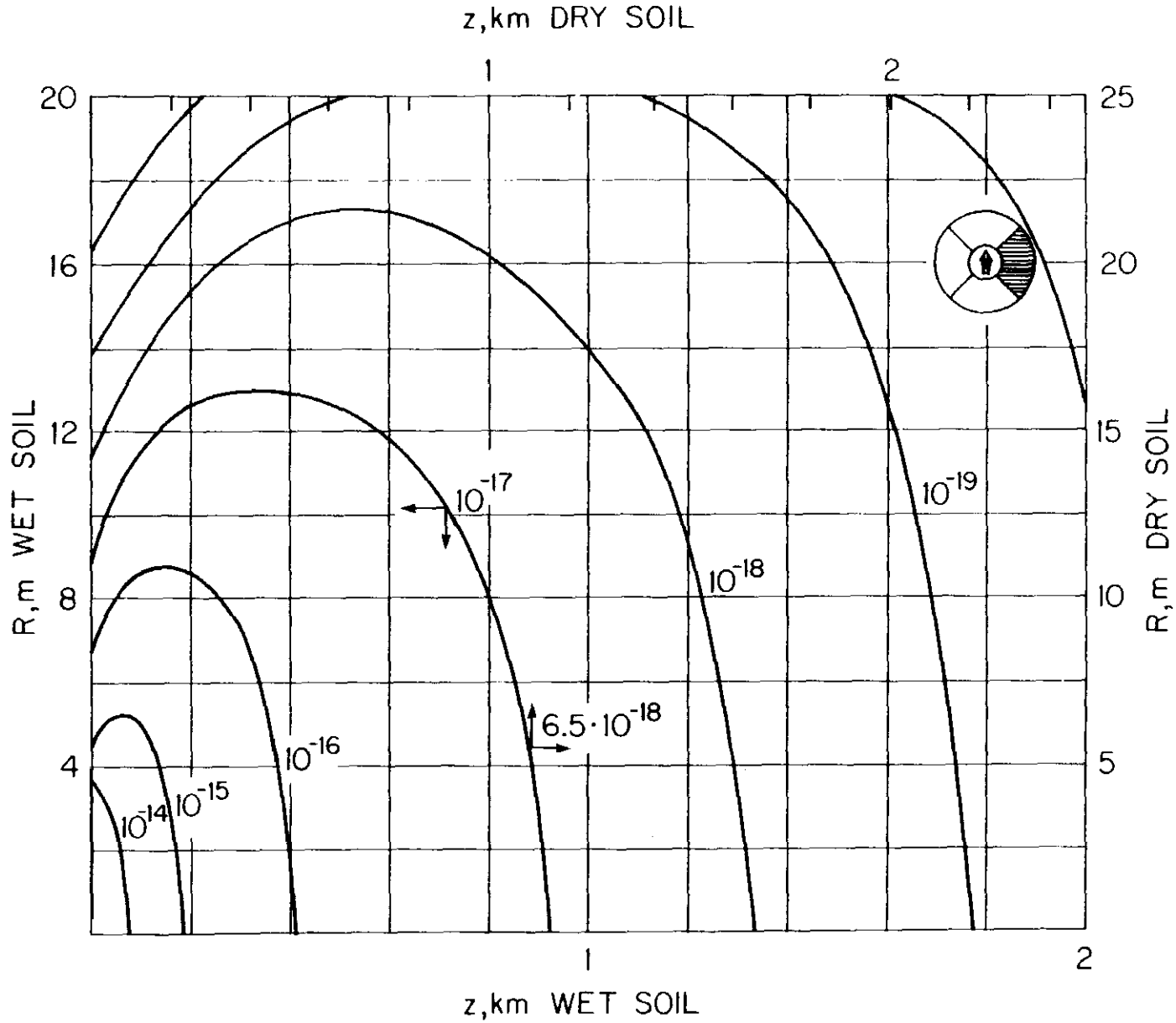

Fig. 132. Contours of equal dose-equivalent (in rem/interacting proton) in the outside quadrant (with respect to the ring) of a soil shield around a 1.2m radius tunnel due to muons from interactions of 20 TeV protons in the middle of the beampipe of a magnet inside the tunnel. The z-direction is tangential to the ring at the interaction point. Contours for wet soil (left & bottom axes) are integral powers of ten. Contours for dry soil (right & top axes) must be scaled down by 0.65 as shown for one example. Some contours may be omitted for clarity or due to statistical uncertainty.

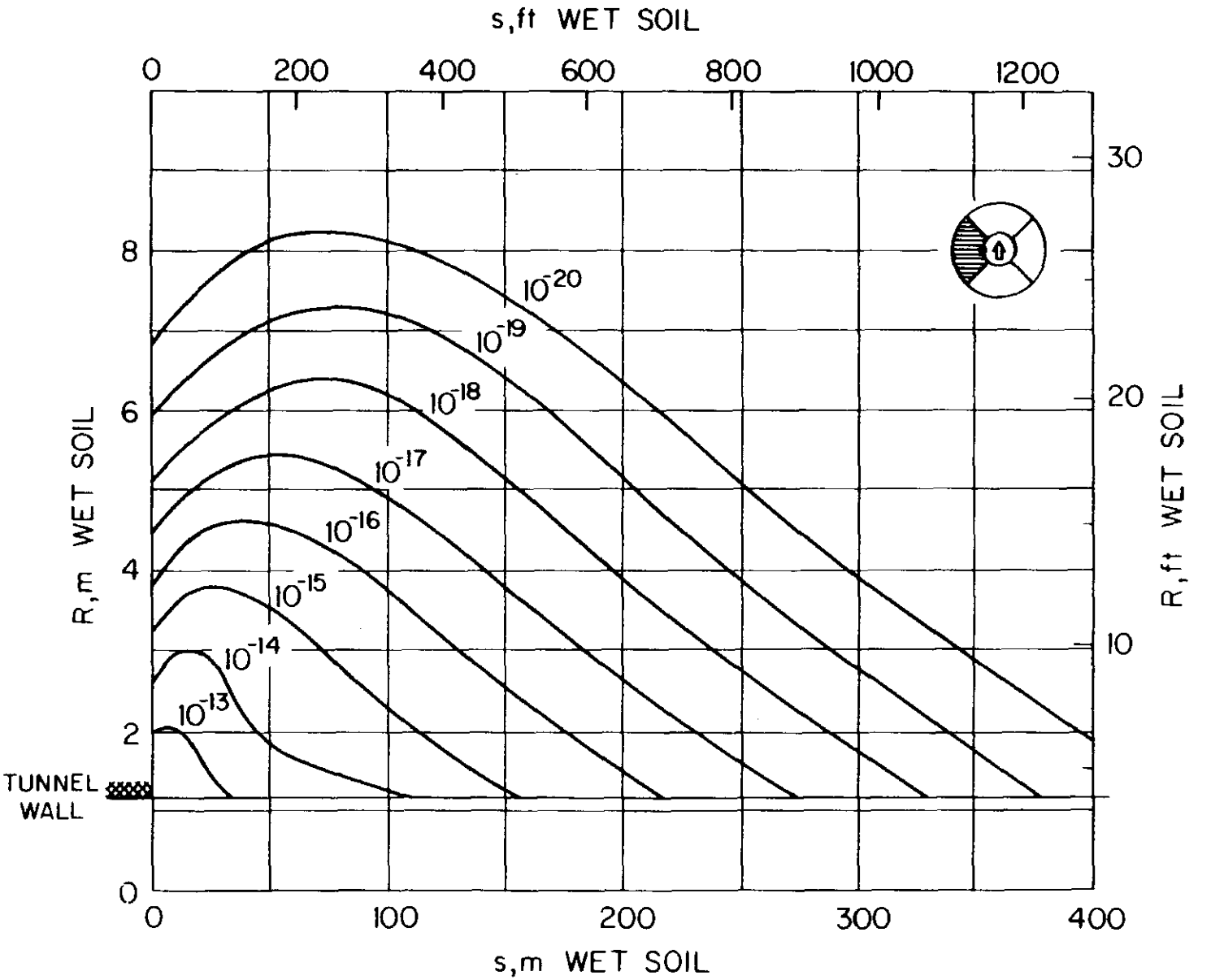

Fig. 133. Contours of equal dose-equivalent (in rem/interacting proton) in the inside quadrant (with respect to the ring) of a soil shield around a 1.2m radius tunnel due to muons from interactions of 5 TeV protons on the inside of the beampipe of a magnet inside the tunnel. The abcissa, s, is the distance along the ring from the interaction point. Some contours may be omitted for clarity or due to statistical uncertainty.

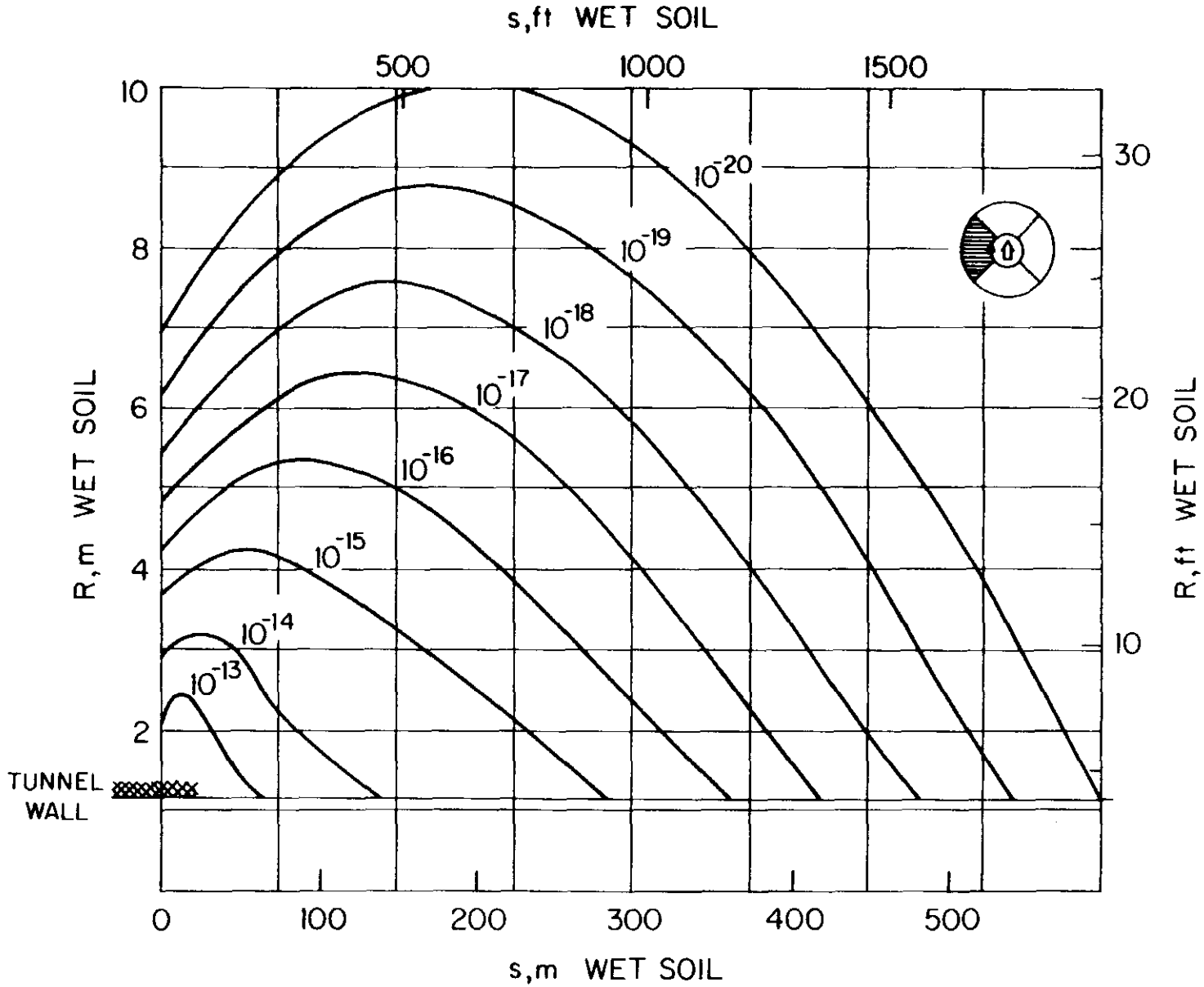

Fig. 134. Contours of equal dose-equivalent (in rem/interacting proton) in the inside quadrant (with respect to the ring) of a soil shield around a 1.2m radius tunnel due to muons from interactions of 10 TeV protons on the inside of the beampipe of a magnet inside the tunnel. The abcissa, s, is the distance along the ring from the interaction point. Some contours may be omitted for clarity or due to statistical uncertainty.

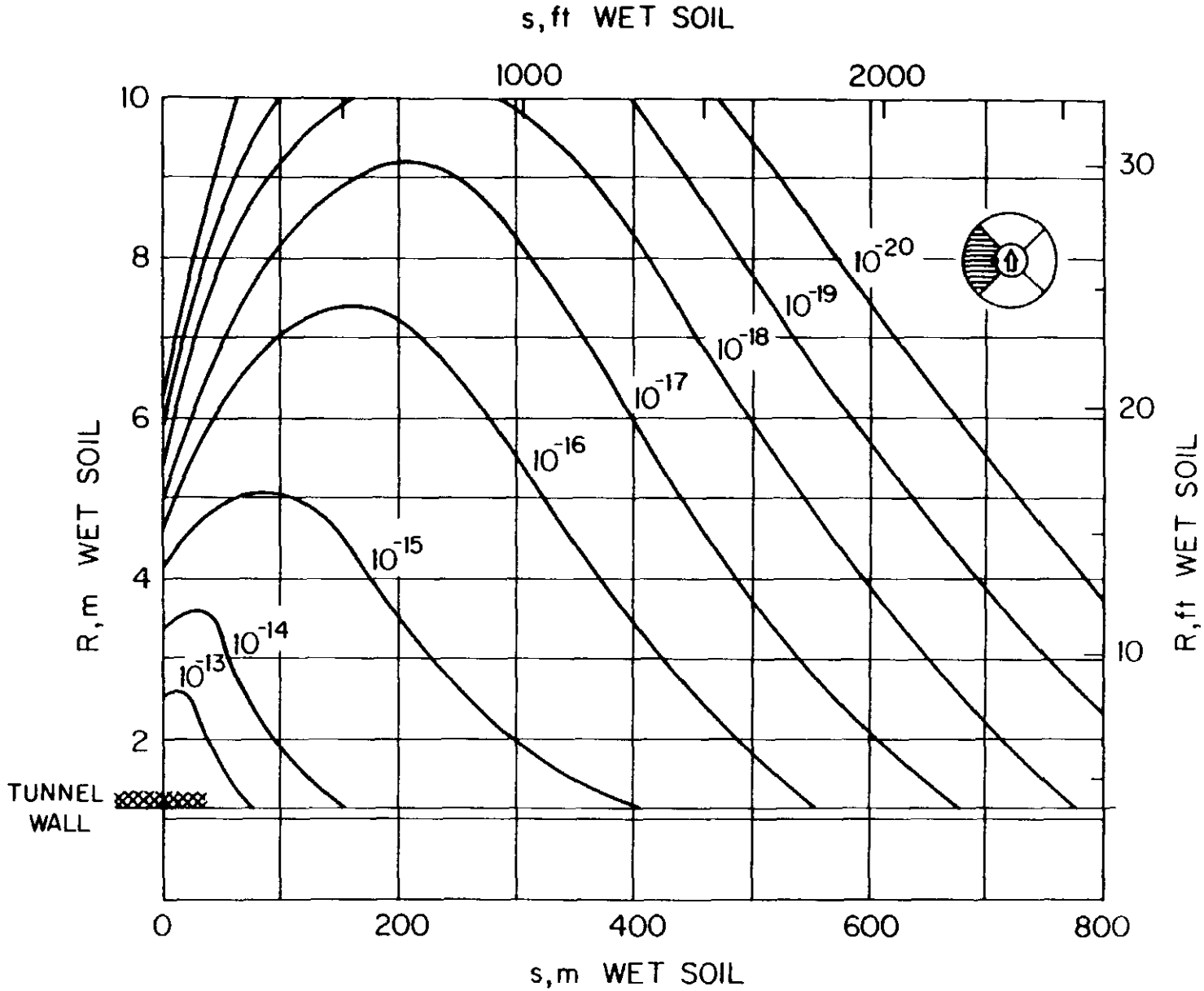

Fig. 135. Contours of equal dose-equivalent (in rem/interacting proton) in the inside quadrant (with respect to the ring) of a soil shield around a 1.2m radius tunnel due to muons from interactions of 20 TeV protons on the inside of the beampipe of a magnet inside the tunnel. The abcissa, s, is the distance along the ring from the interaction point. Some contours may be omitted for clarity or due to statistical uncertainty.

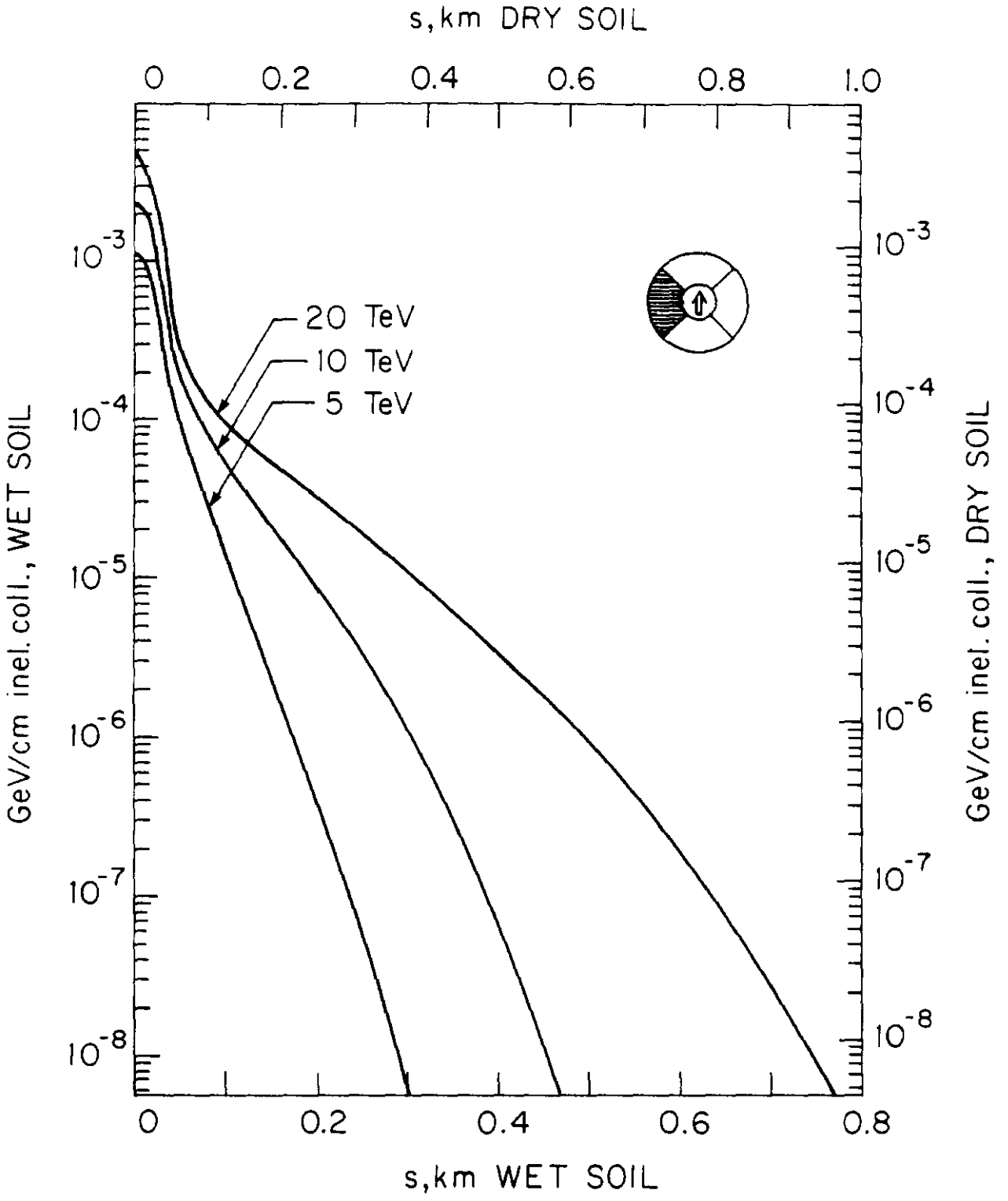

Fig. 136. Radially integrated energy density (in GeV/cm•interacting proton) in the inside quadrant (with respect to the ring) of a soil shield around a 1.2m radius tunnel due to muons from interactions of 5, 10 and 20 TeV protons on the inside of the beampipe of a continuous dipole inside the tunnel. The abcissa, s, is the distance along the ring from the interaction point. For wet soil use left & bottom axes and for dry soil right & top axes.

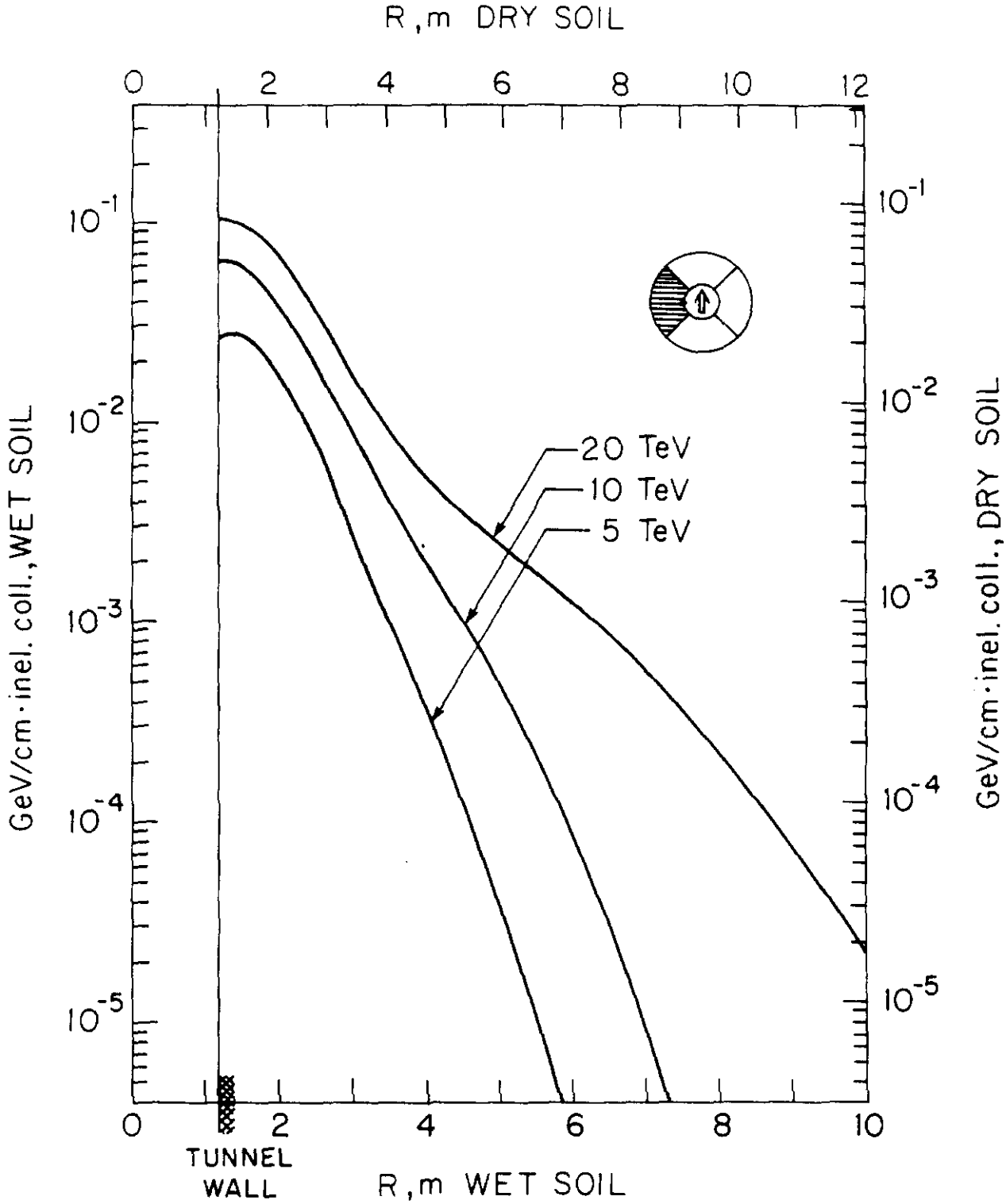

Fig. 137. Longitudinally integrated energy density (in GeV/cm•interacting proton) in the inside quadrant (with respect to the ring) of a soil shield around a 1.2m radius tunnel due to muons from interactions of 5, 10 and 20 TeV protons on the inside of the beampipe of a continuous dipole inside the tunnel. The abcissa, R, is the radial coordinate of the tunnel. For wet soil use left & bottom axes and for dry soil right & top axes.

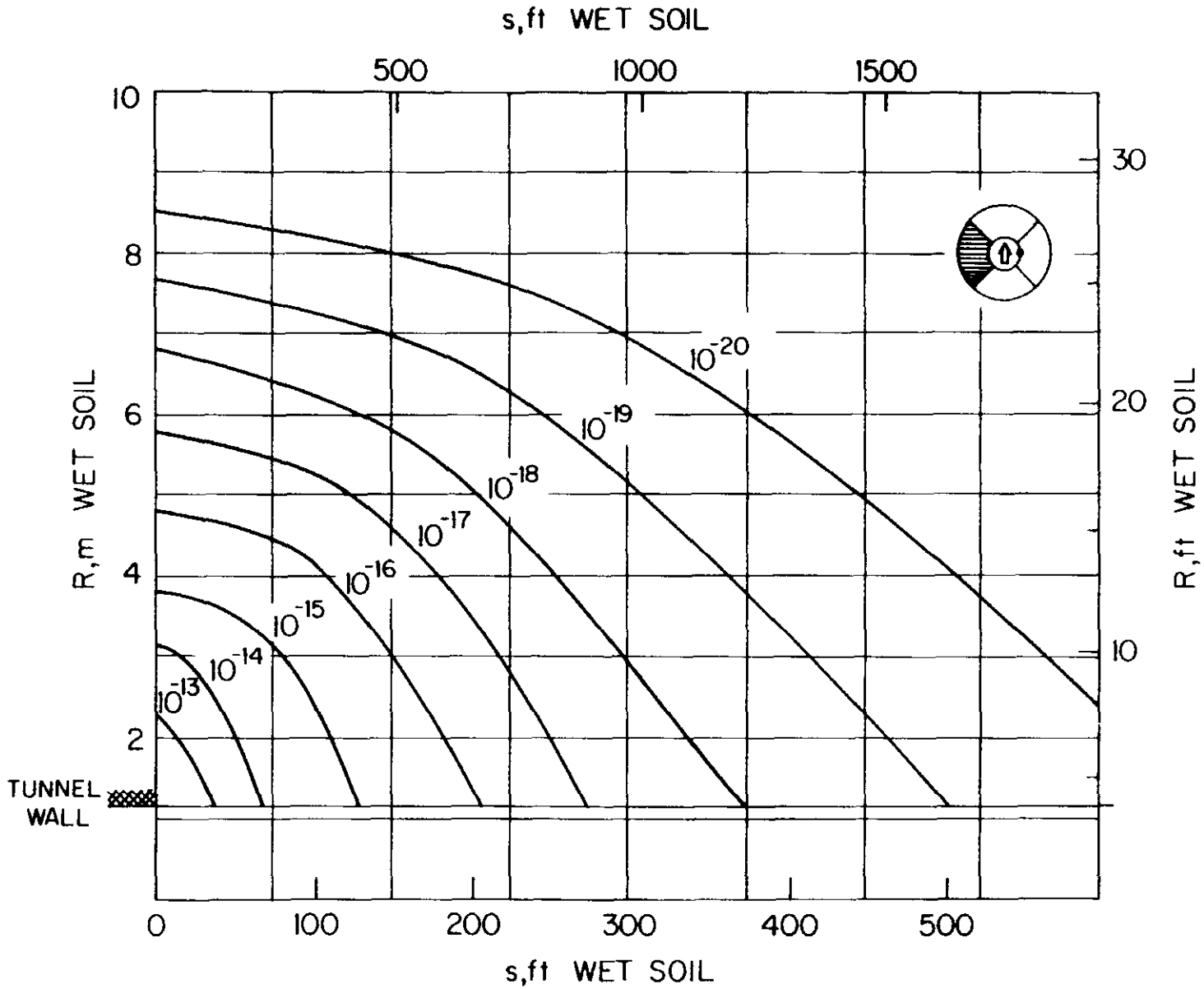

Fig. 138. Contours of equal dose-equivalent (in rem/interacting proton) in the inside quadrant (with respect to the ring) of a soil shield around a 1.2m radius tunnel due to muons from interactions of 5 TeV protons on the outside of the beampipe of a magnet inside the tunnel. The abcissa, s, is the distance along the ring from the interaction point. Some contours may be omitted for clarity or due to statistical uncertainty.

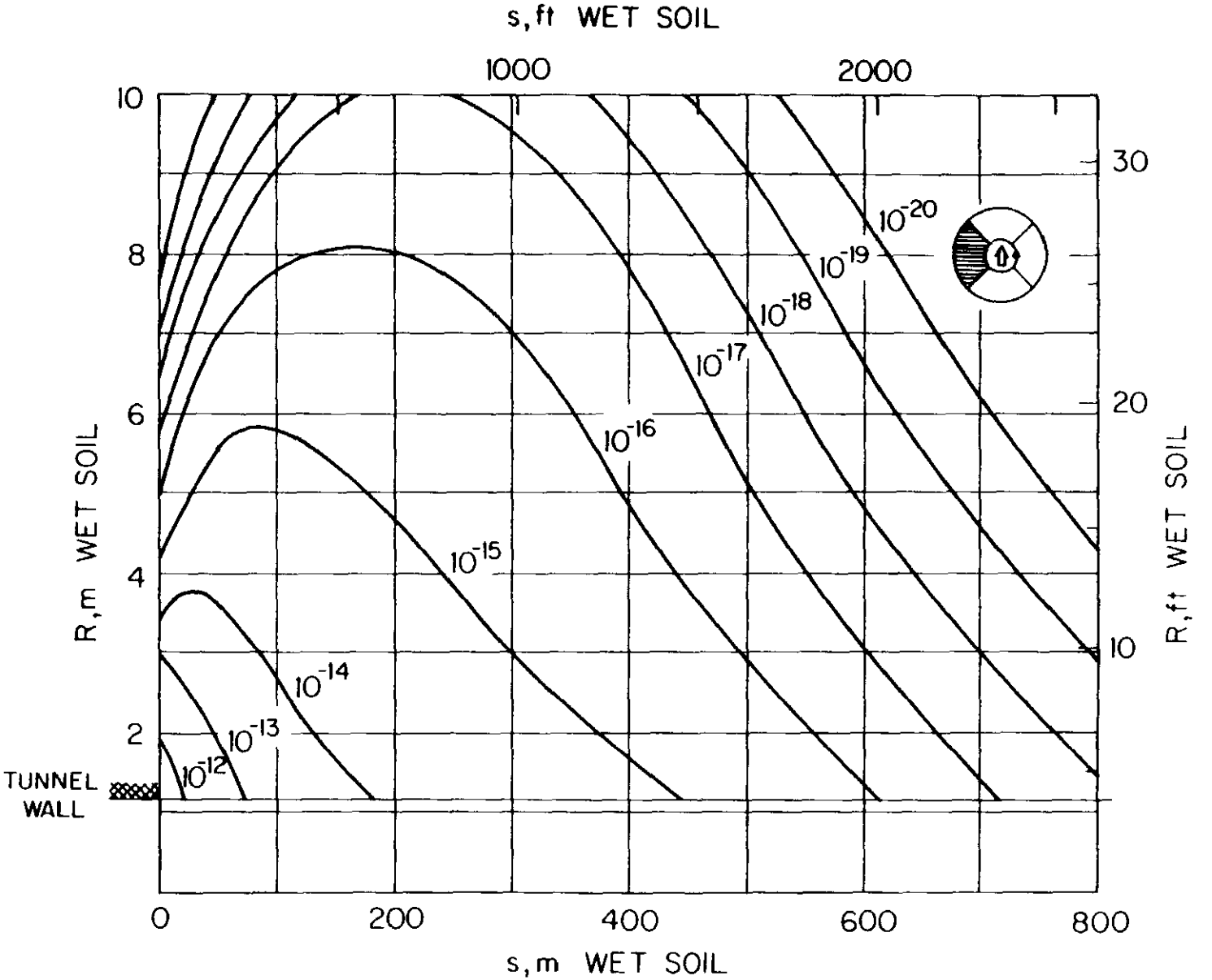

Fig. 139. Contours of equal dose-equivalent (in rem/interacting proton) in the inside quadrant (with respect to the ring) of a soil shield around a 1.2m radius tunnel due to muons from interactions of 20 TeV protons on the outside of the beampipe of a magnet inside the tunnel. The abcissa, s, is the distance along the ring from the interaction point. Some contours may be omitted for clarity or due to statistical uncertainty.

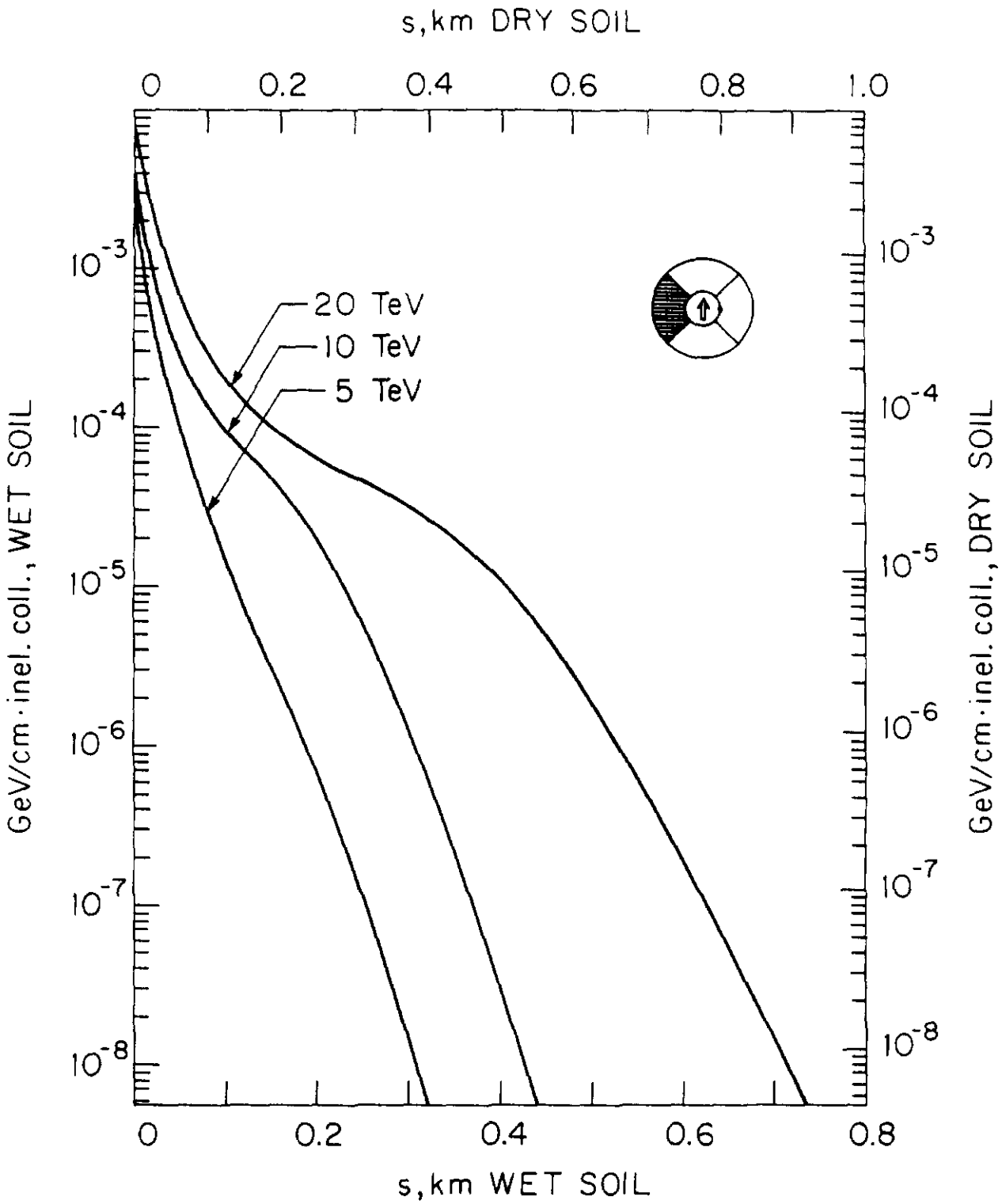

Fig. 140. Radially integrated energy density (in GeV/cm•interacting proton) in the inside quadrant (with respect to the ring) of a soil shield around a 1.2m radius tunnel due to muons from interactions of 5, 10 and 20 TeV protons on the outside of the beampipe of a continuous dipole inside the tunnel. The abcissa, s, is the distance along the ring from the interaction point. For wet soil use left & bottom axes and for dry soil right & top axes.

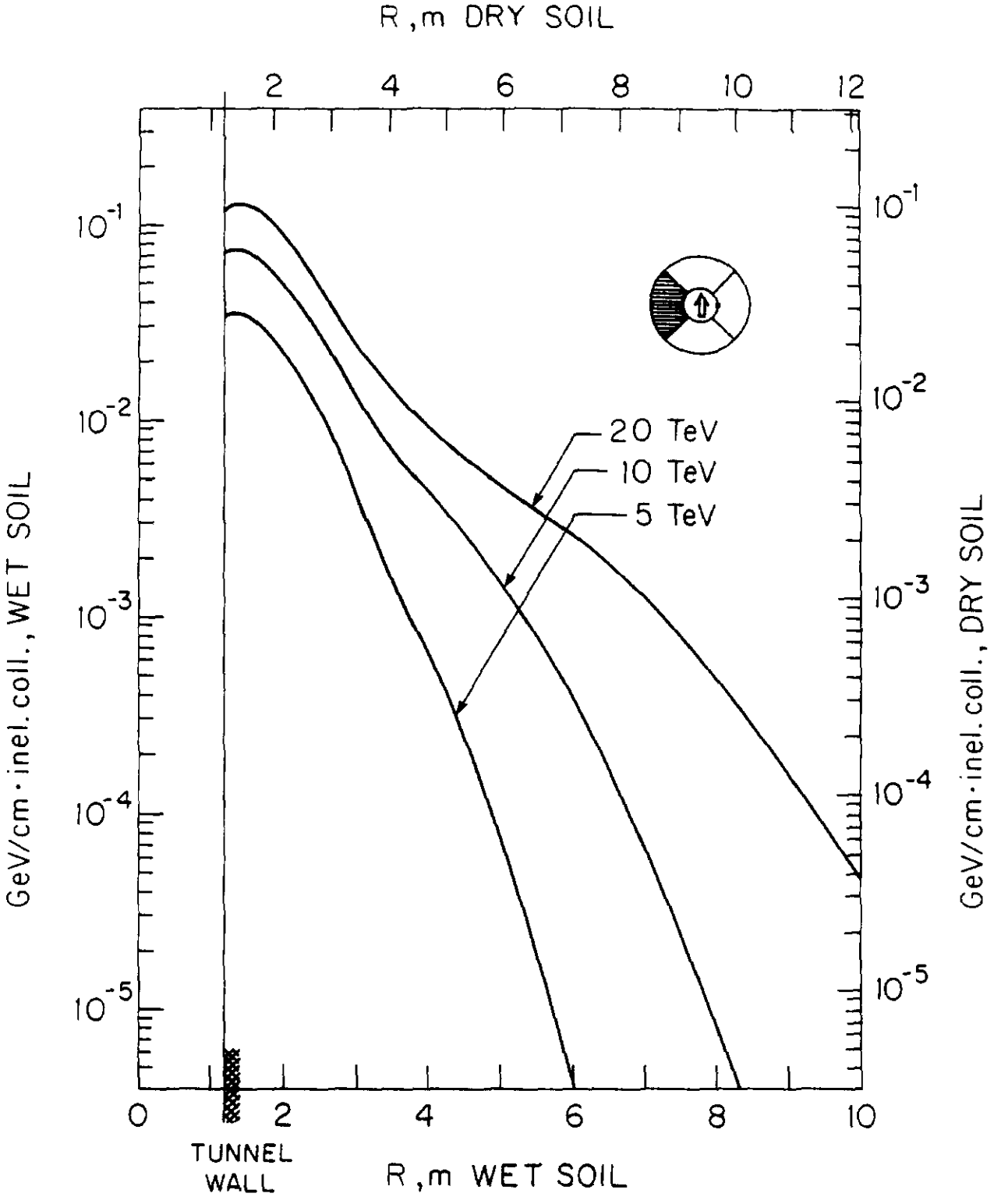

Fig. 141. Longitudinally integrated energy density (in GeV/cm•interacting proton) in the inside quadrant (with respect to the ring) of a soil shield around a 1.2m radius tunnel due to muons from interactions of 5, 10 and 20 TeV protons on the outside of the beampipe of a continuous dipole inside the tunnel. The abcissa, R, is the radial coordinate of the tunnel. For wet soil use left & bottom axes and for dry soil right & top axes.

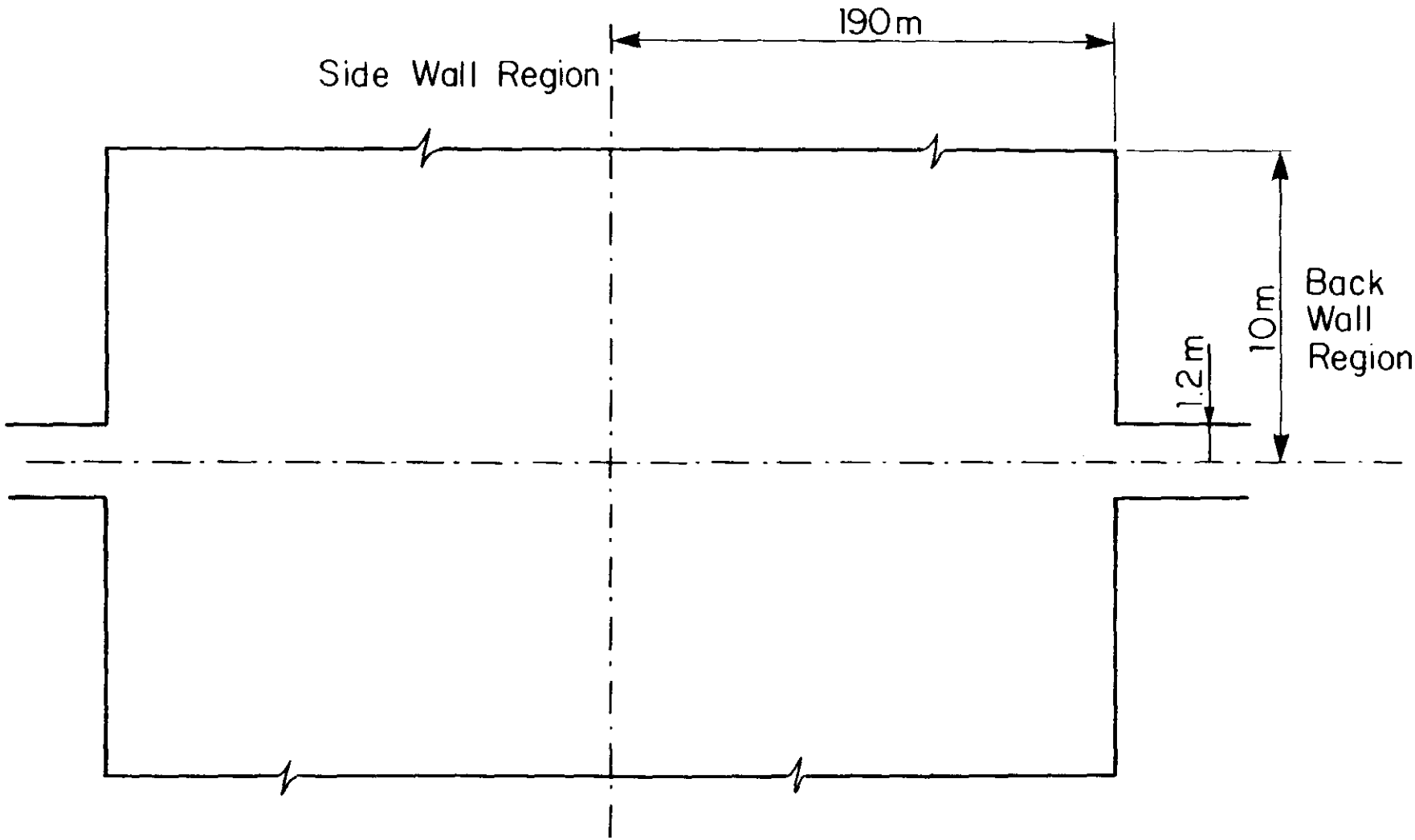

Fig. 142. Cross-section of collision hall as represented in program. For simplicity, the geometry is assumed to be cylindrically symmetric about the beam direction.

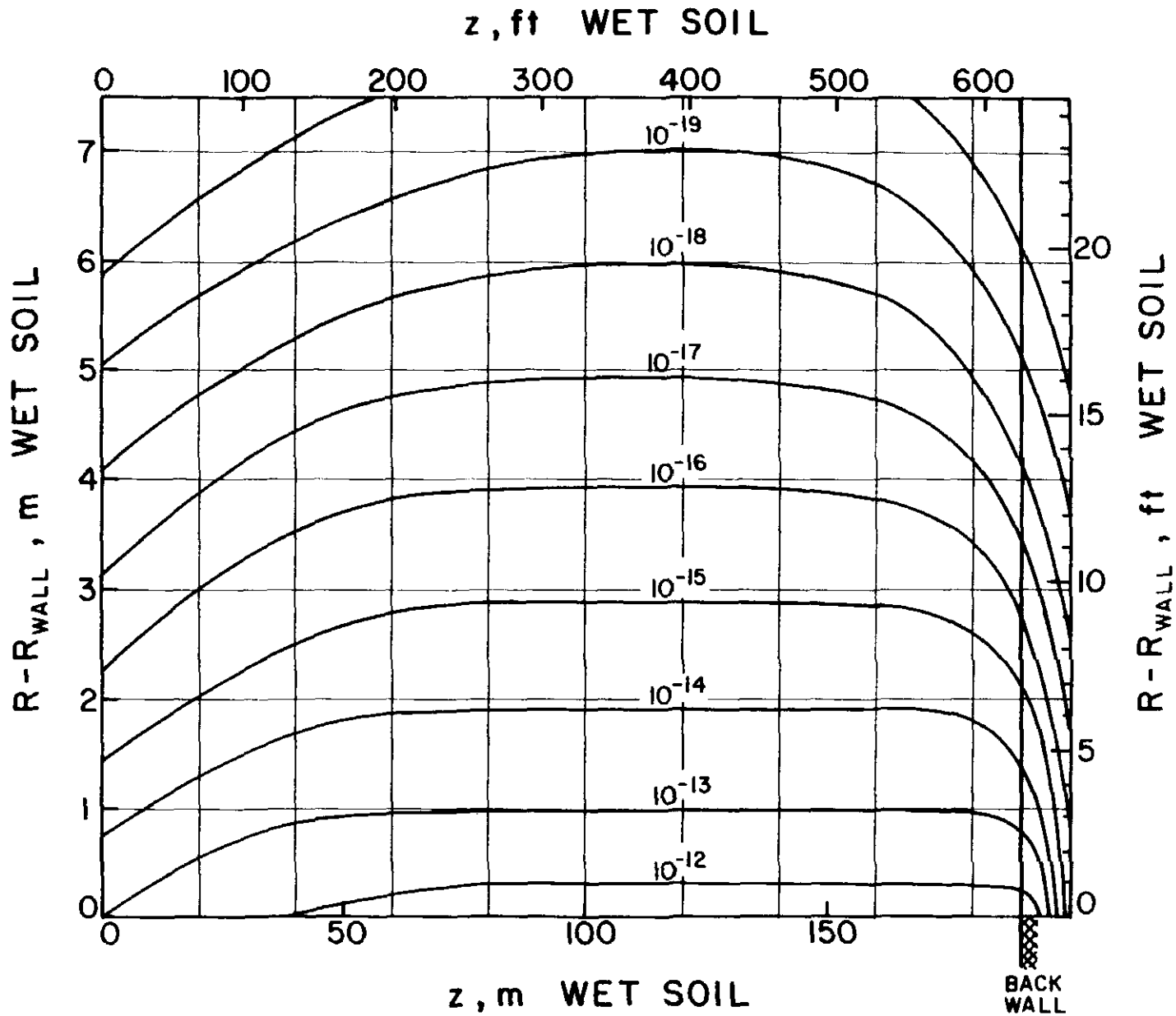

Fig. 143. Contours of equal dose equivalent (in rem/inelastic collision) in soil side wall of collision hall, due to hadrons from colliding beams of 5 TeV each. A 1mm thick beampipe is present. Some contours may be omitted for clarity or due to statistical uncertainty.

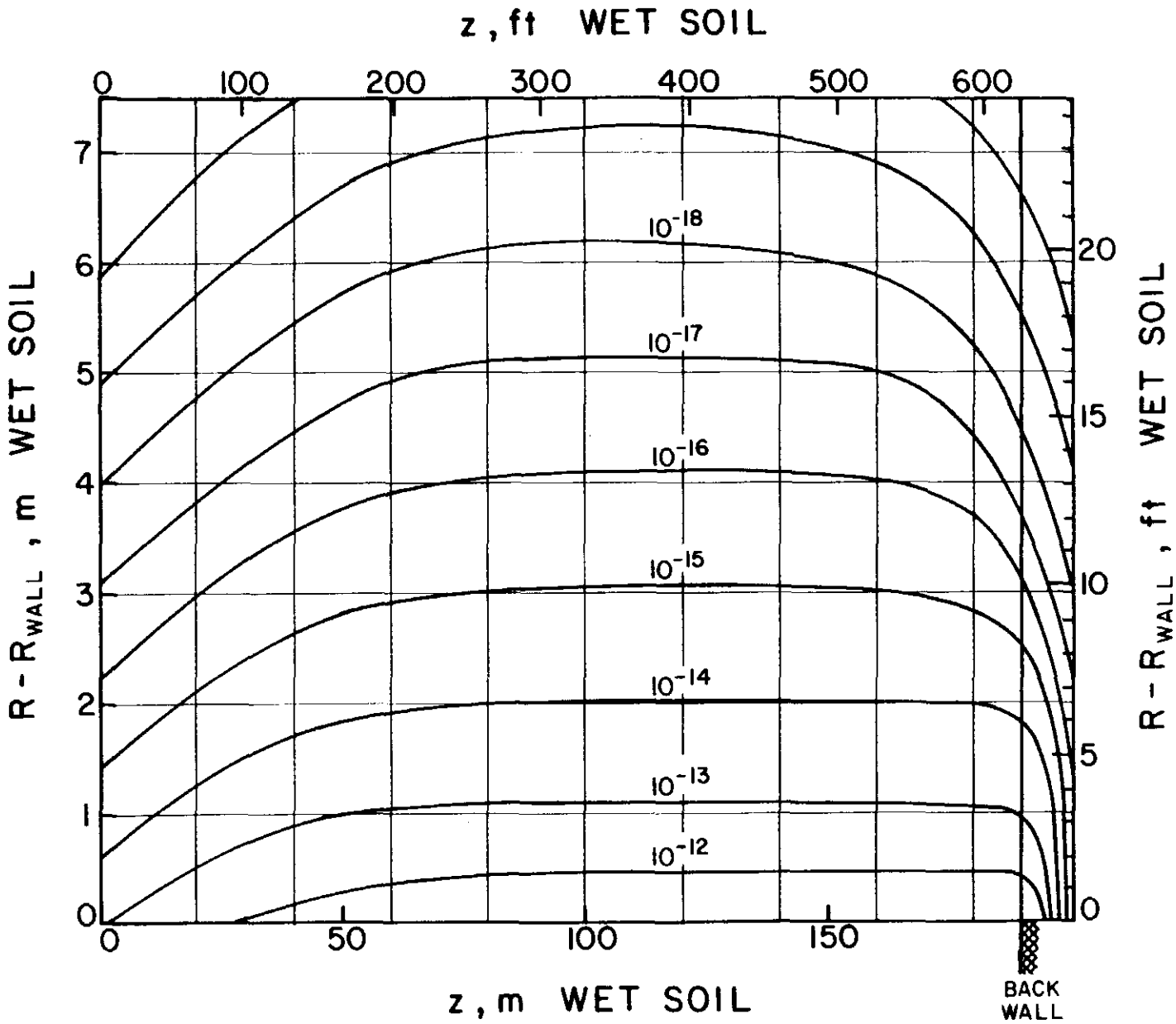

Fig. 144. Contours of equal dose equivalent (in rem/inelastic collision) in soil side wall of collision hall, due to hadrons from colliding beams of 20 TeV each. A 1mm thick beampipe is present. Some contours may be omitted for clarity or due to statistical uncertainty.

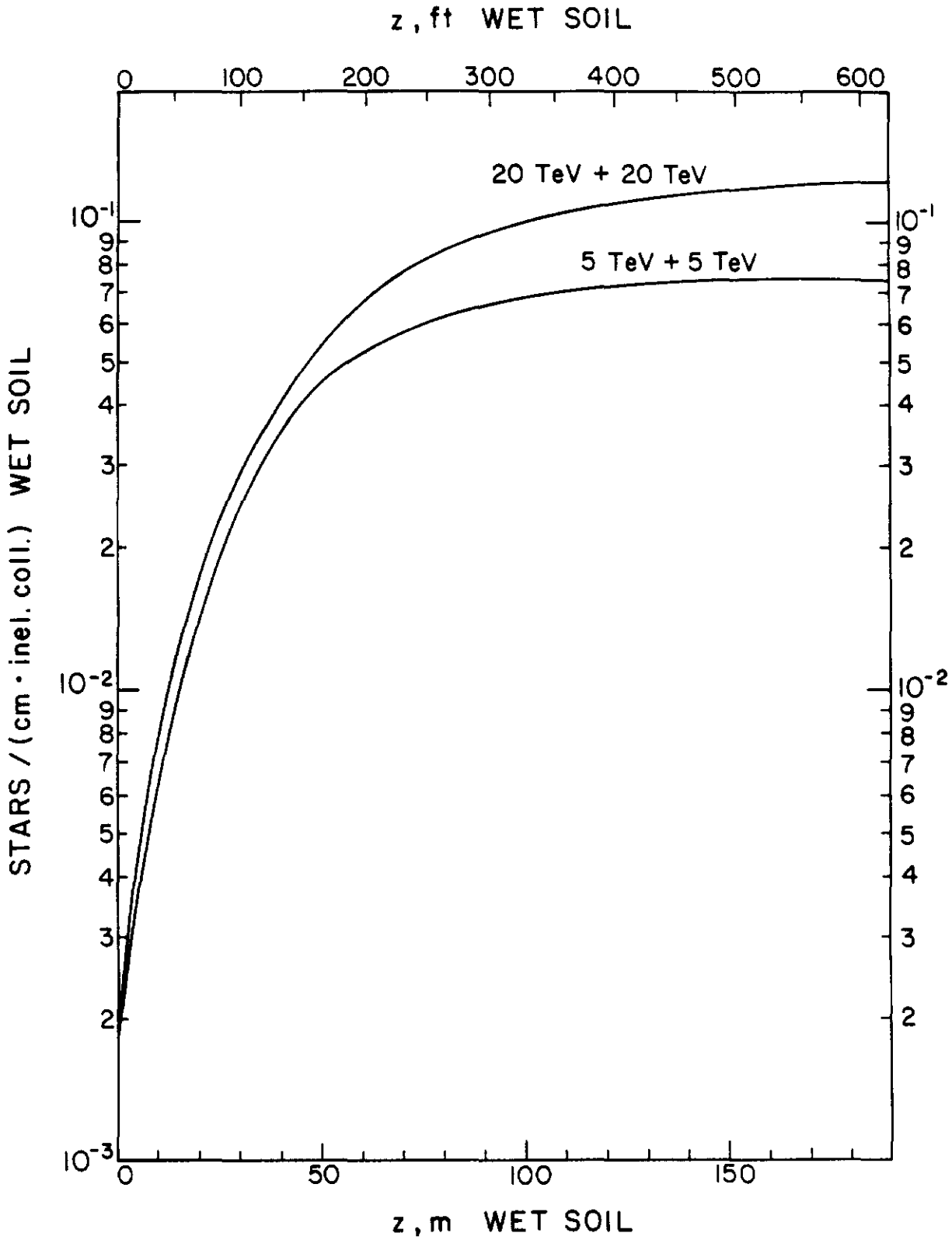

Fig. 145. Radially integrated star density (in stars/cm•inelastic collision) in side-wall of collision hall (see fig. 142) for colliding beams of 5, 10 and 20 TeV protons interacting at z=0. The calculation has a cut-off momentum of 0.3 GeV/c.

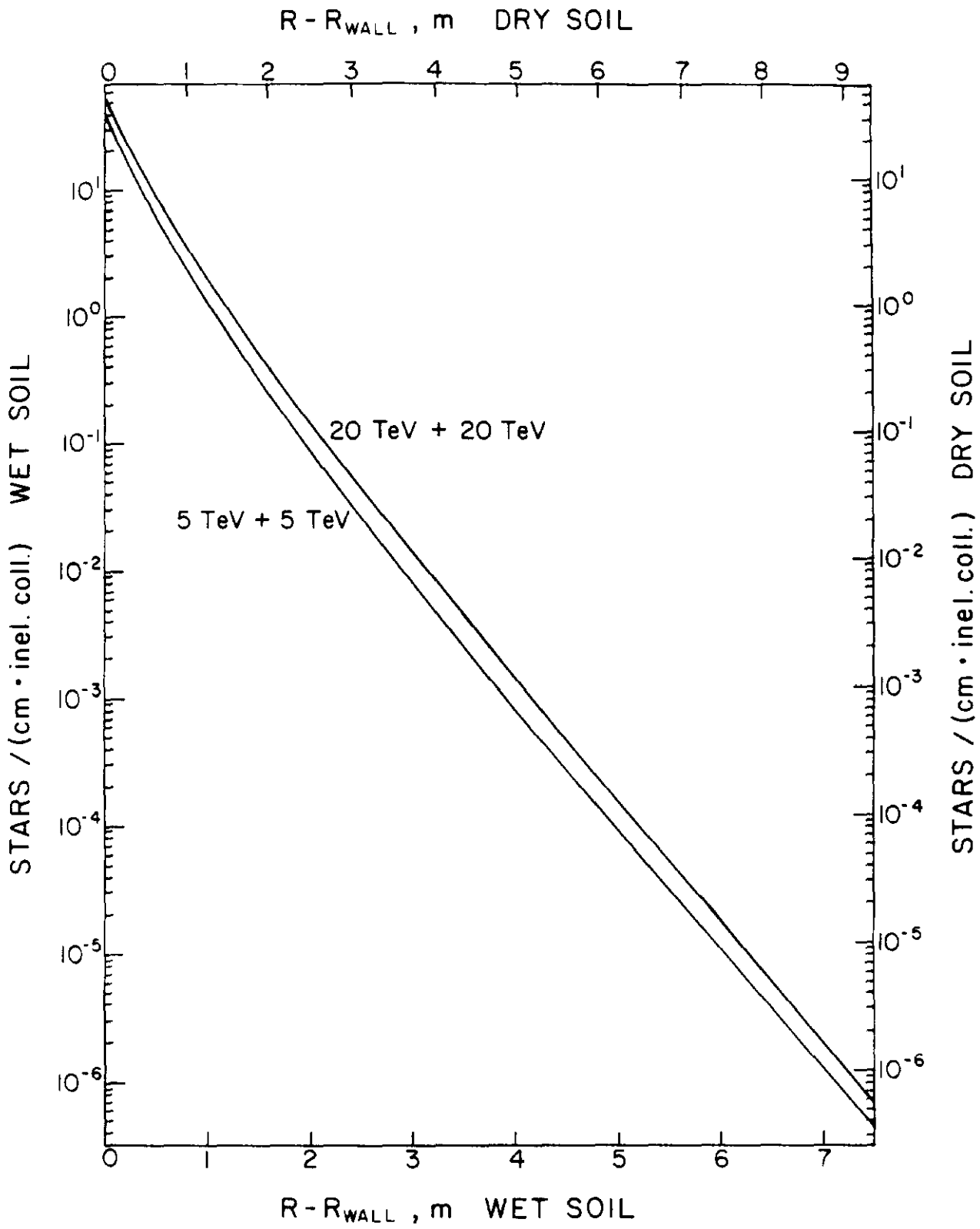

Fig. 146. Longitudinally integrated star density (in stars/cm•inelastic collision) in side-wall of collision hall (see fig. 142) for colliding beams of 5, 10 and 20 TeV protons interacting at z=0. The calculation has a cut-off momentum of 0.3 GeV/c. For wet soil use left & bottom axes and for dry soil right & top axes.

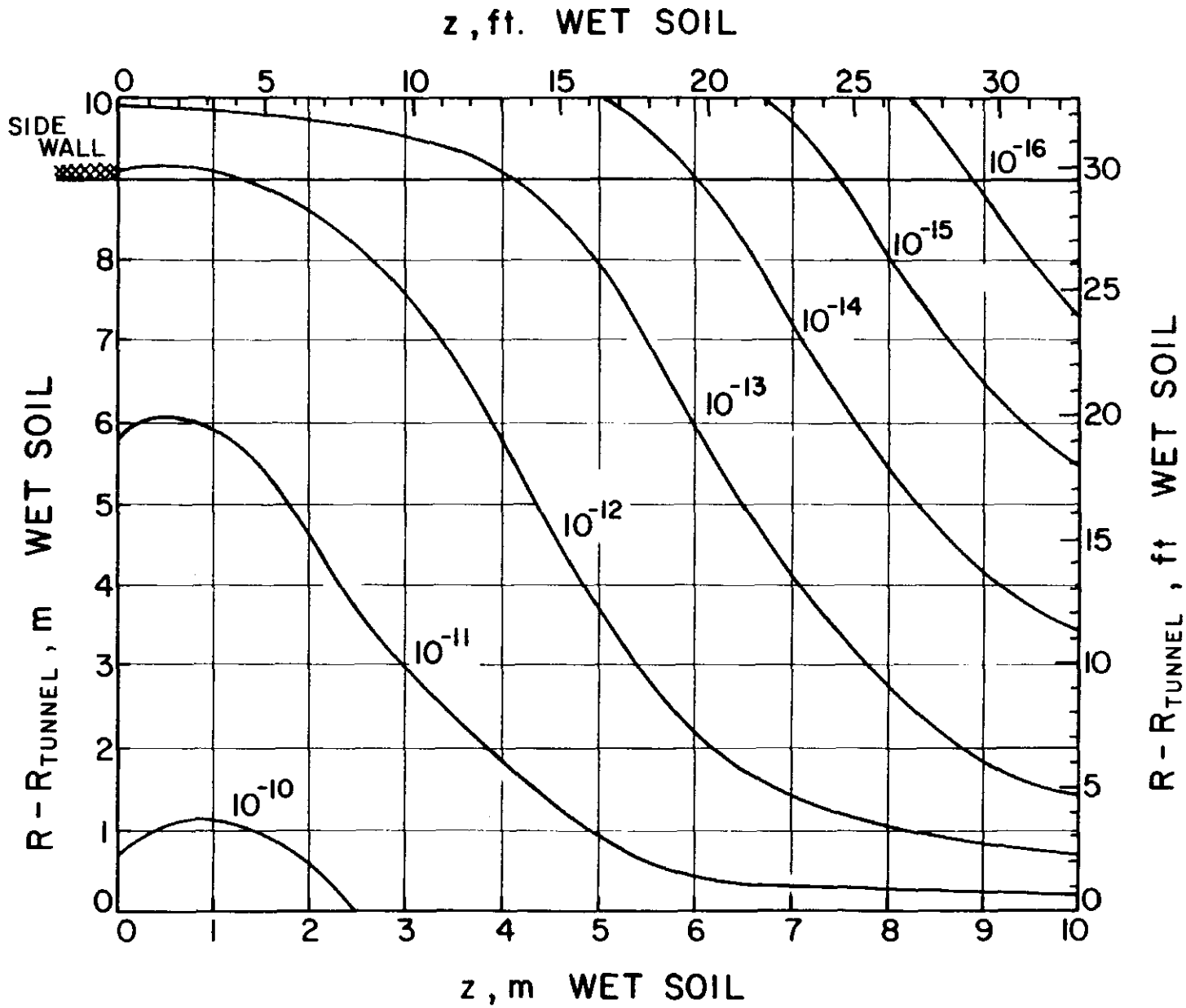

Fig. 147. Contours of equal dose equivalent (in rem/inelastic collision) in soil back wall of collision hall, due to hadrons from colliding beams of 5 TeV each. A 1mm thick beampipe is present. Some contours may be omitted for clarity or due to statistical uncertainty.

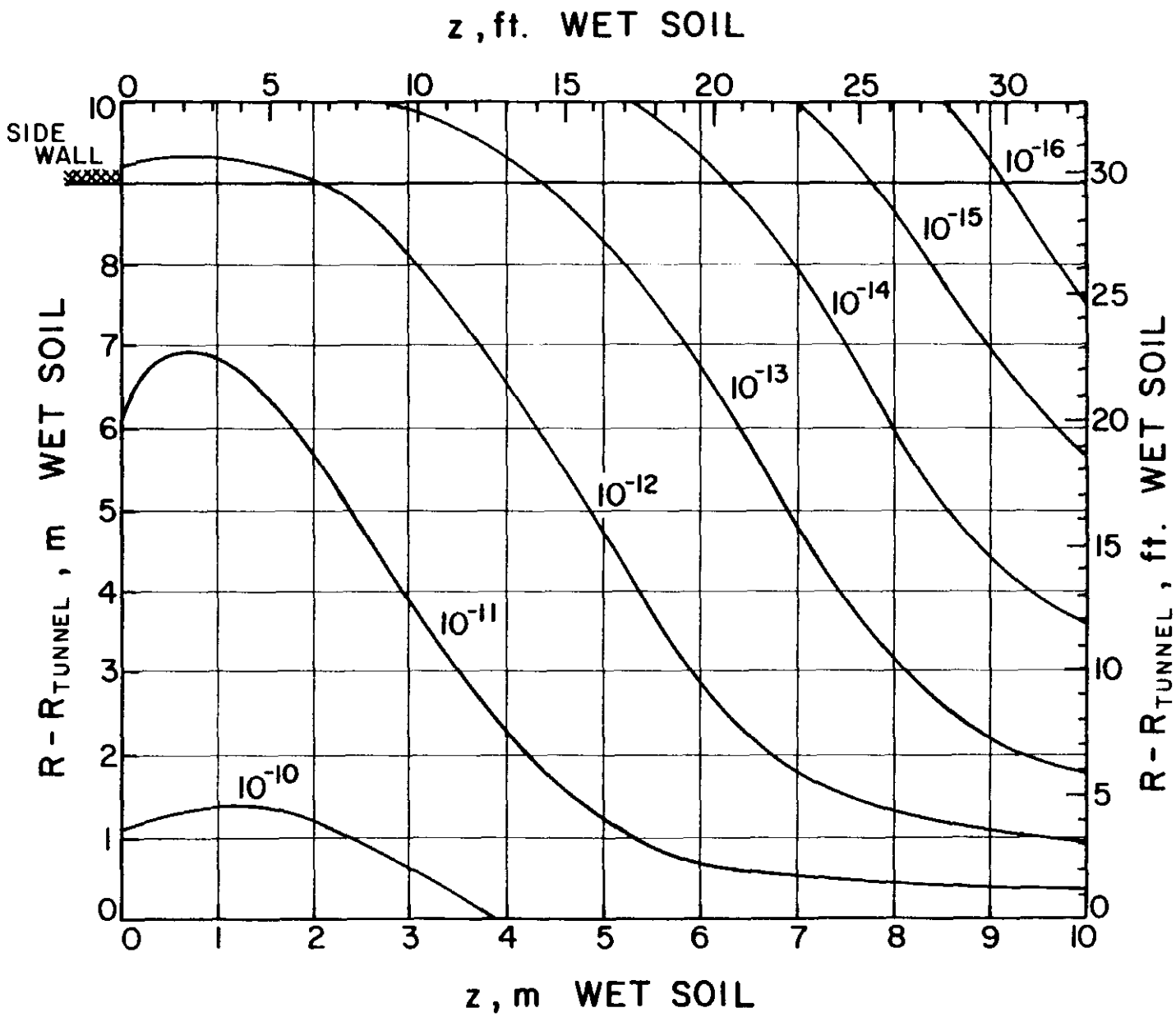

Fig. 148. Contours of equal dose equivalent (in rem/inelastic collision) in soil back wall of collision hall, due to hadrons from colliding beams of 20 TeV each. A 1mm thick beampipe is present. Some contours may be omitted for clarity or due to statistical uncertainty.

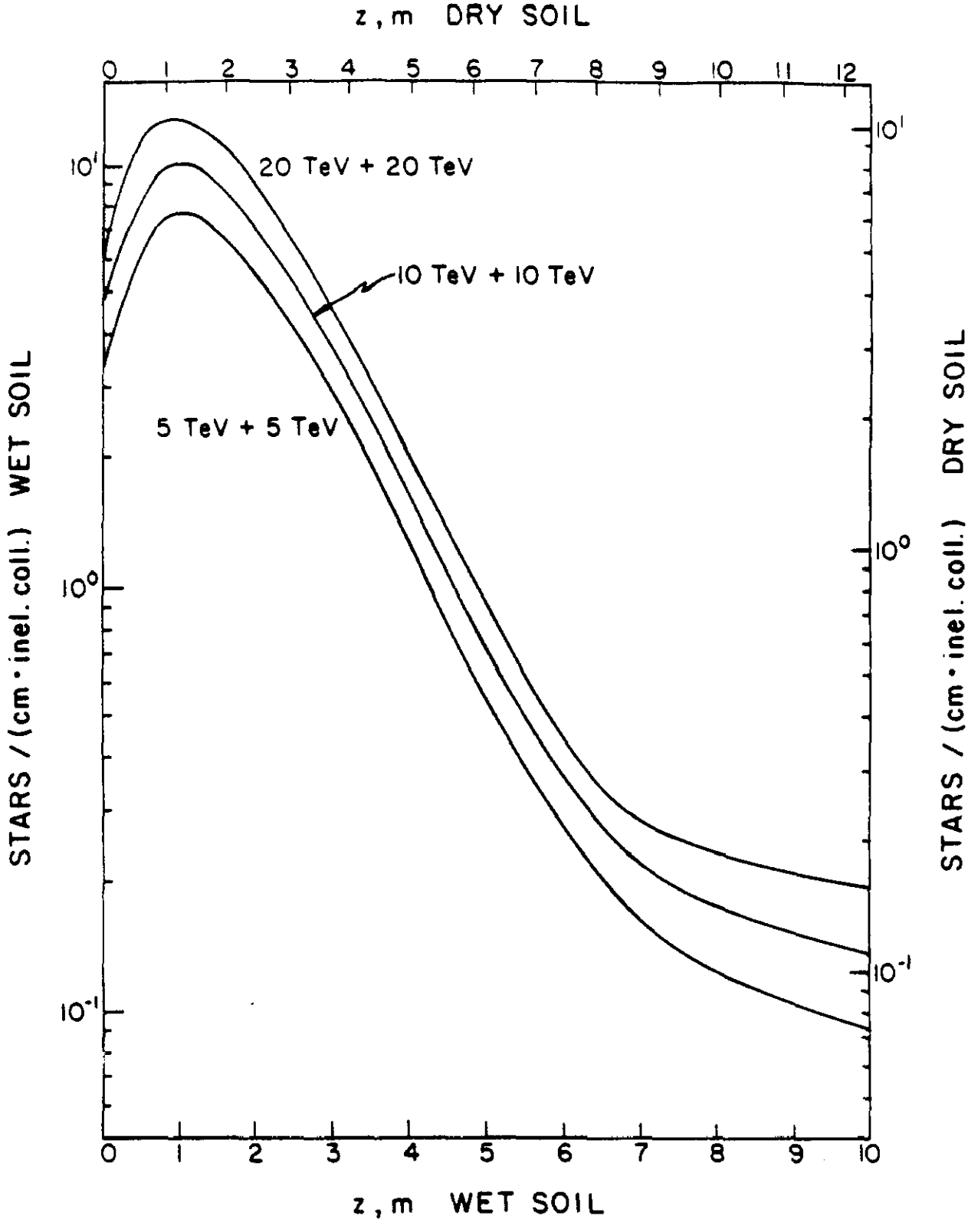

Fig. 149. Radially integrated star density (in stars/cm•inelastic collision) in back-wall of collision hall (see fig. 142) for colliding beams of 5, 10 and 20 TeV protons interacting at z=0. The calculation has a cut-off momentum of 0.3 GeV/c. For wet soil use left & bottom axes and for dry soil right & top axes.

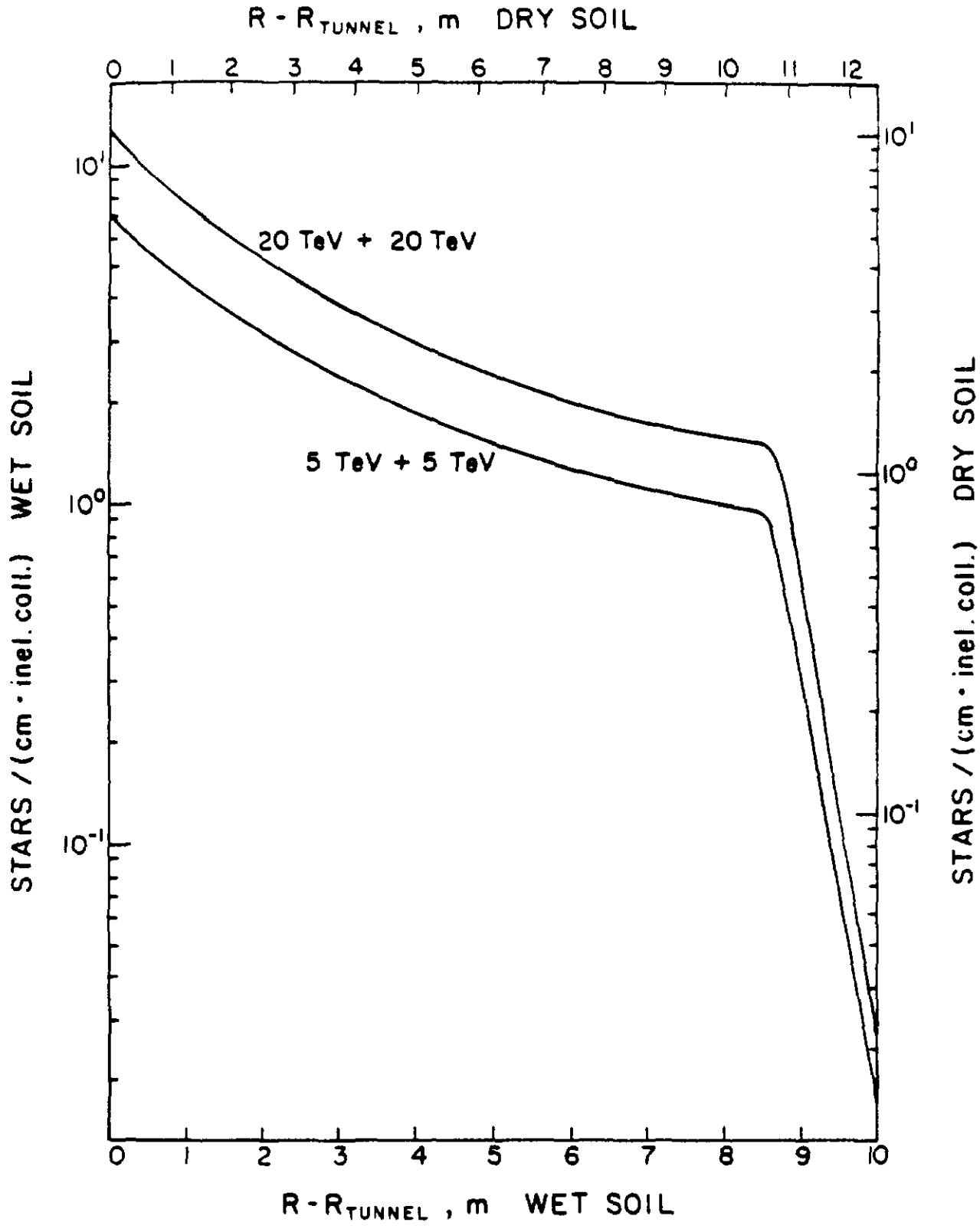

Fig. 150. Longitudinally integrated star density (in stars/cm•inelastic collision) in back-wall of collision hall (see fig. 142) for colliding beams of 5, 10 and 20 TeV protons interacting at z=0. The calculation has a cut-off momentum of 0.3 GeV/c. For wet soil use left & bottom axes and for dry soil right & top axes.

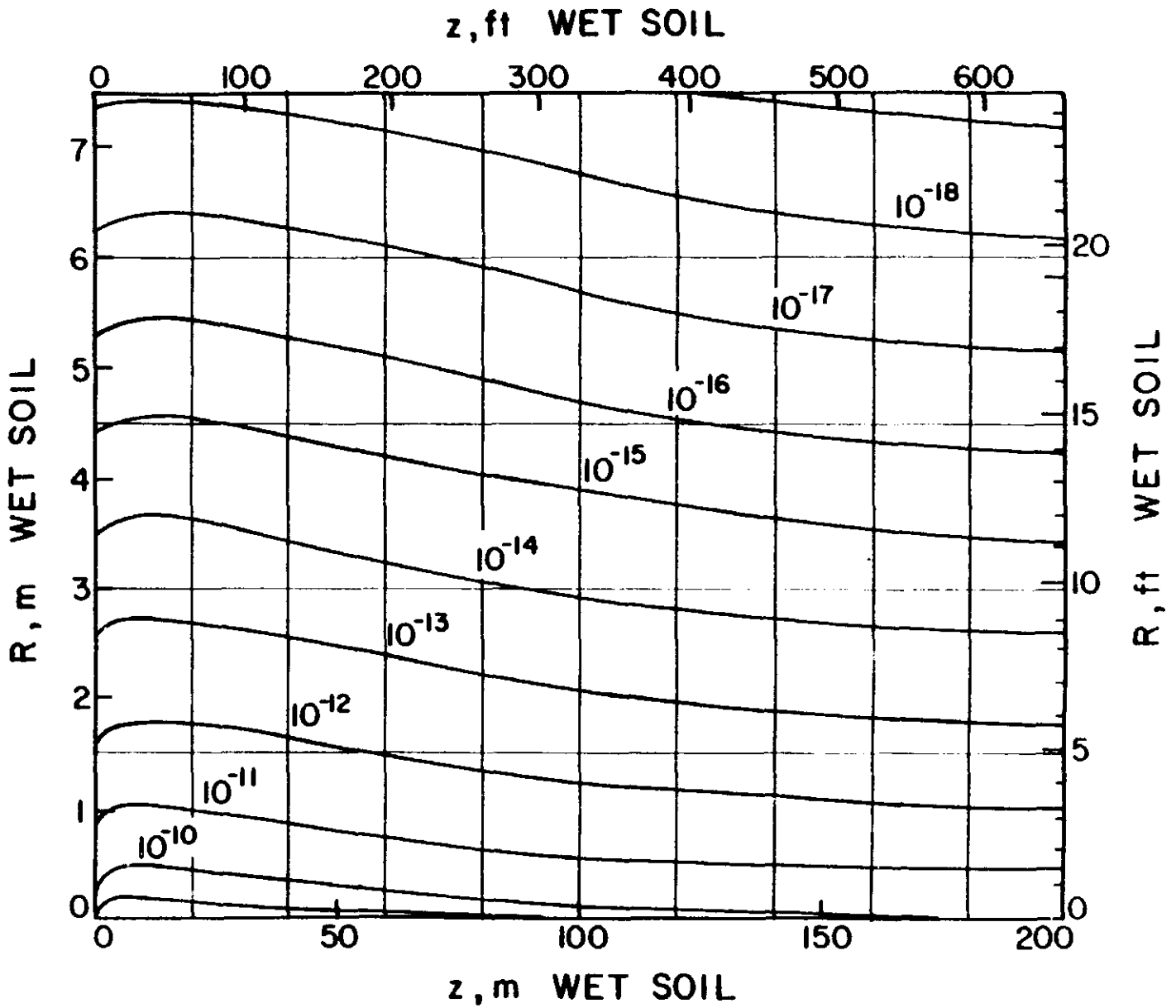

Fig. 151. Contours of equal dose equivalent (in rem/inelastic collision) in soil surrounding a beampipe, due to hadrons from colliding beams of 5 TeV each. Some contours may be omitted for clarity or due to statistical uncertainty.

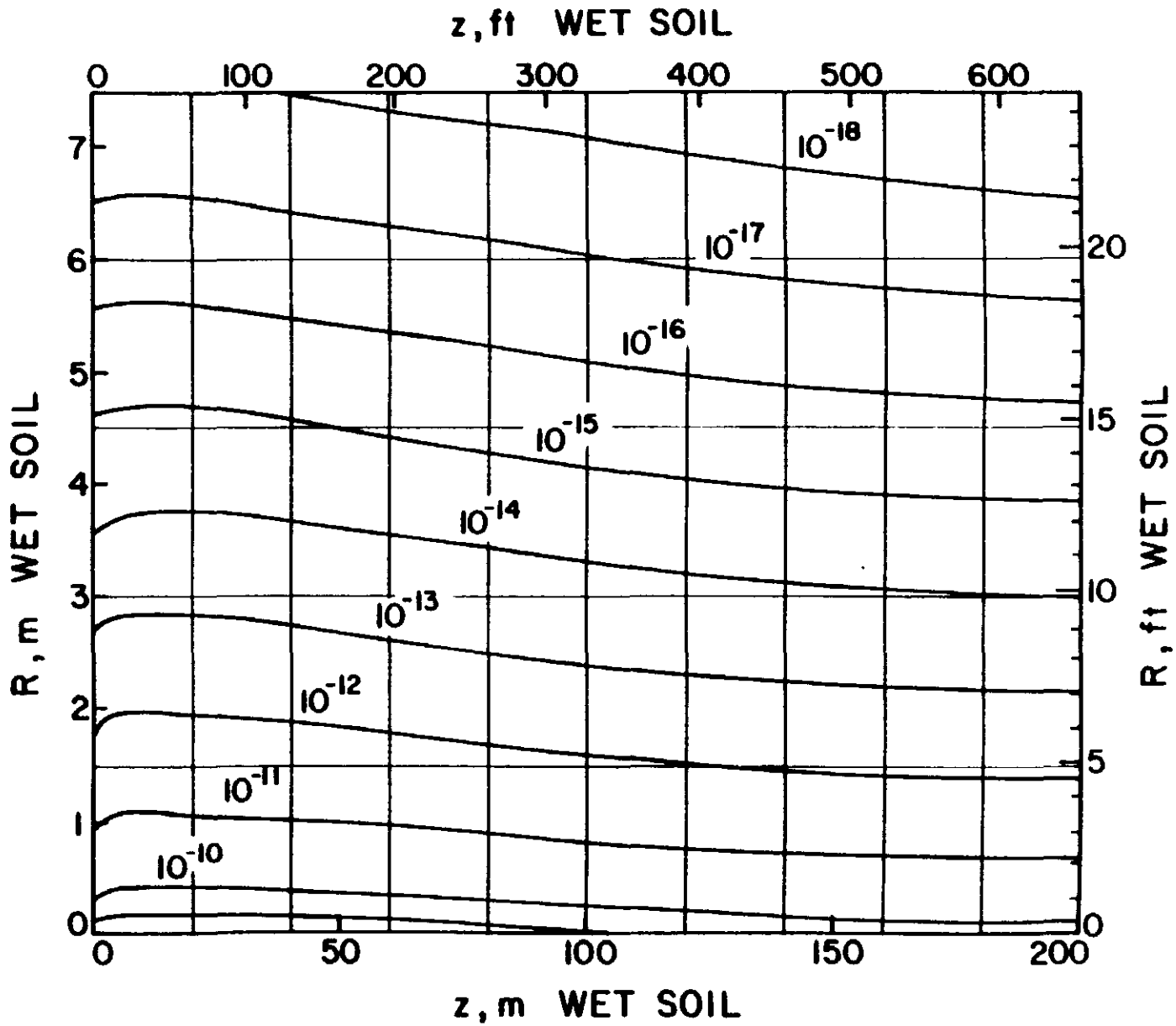

Fig. 152. Contours of equal dose equivalent (in rem/inelastic collision) in soil surrounding a beampipe, due to hadrons from colliding beams of 20 TeV each. Some contours may be omitted for clarity or due to statistical uncertainty.

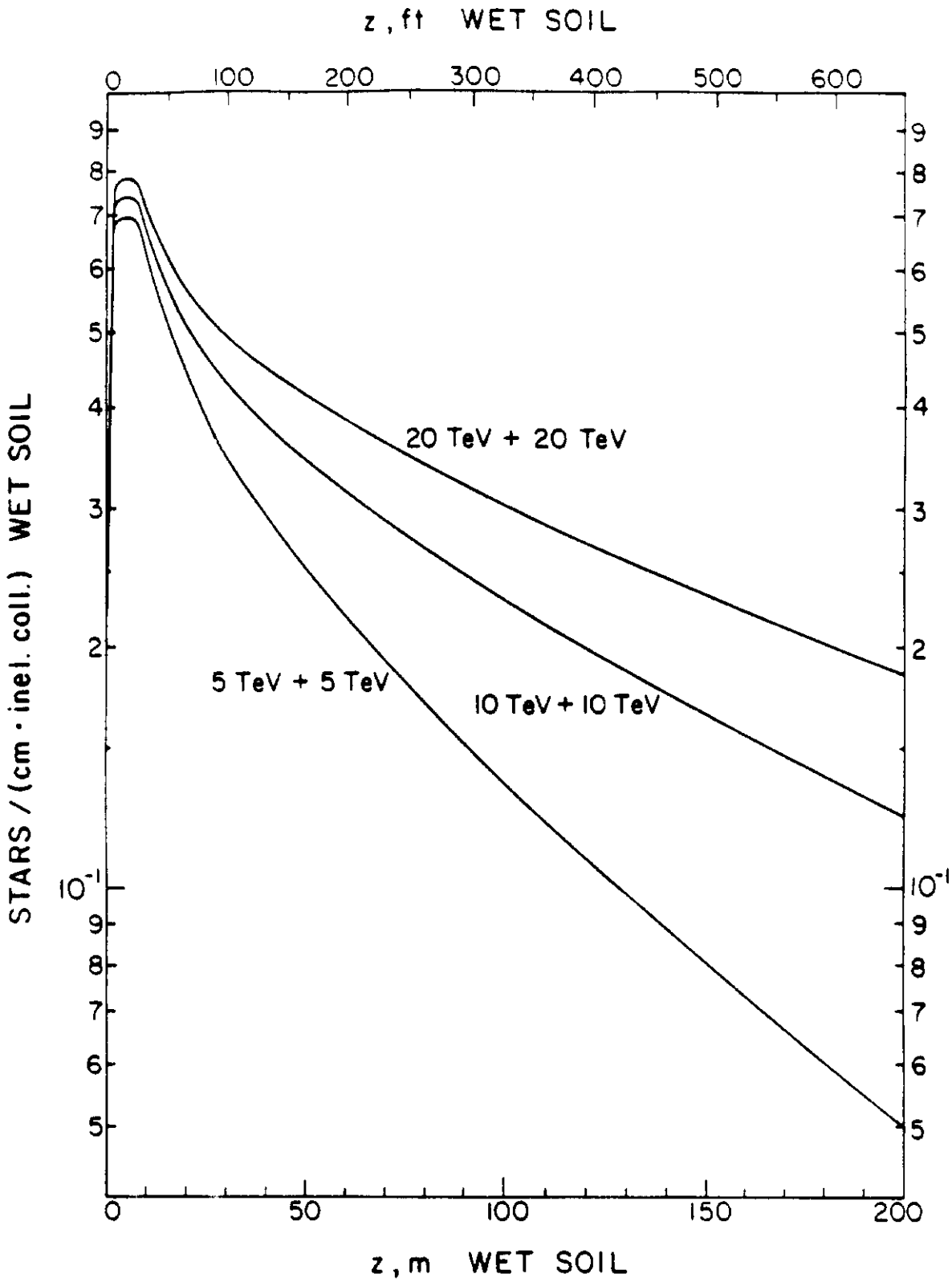

Fig. 153. Radially integrated star density (in stars/cm•inelastic collision) in soil surrounding a beampipe, for colliding beams of 5, 10 and 20 TeV protons interacting at z=0. The calculation has a cut-off momentum of 0.3 GeV/c.

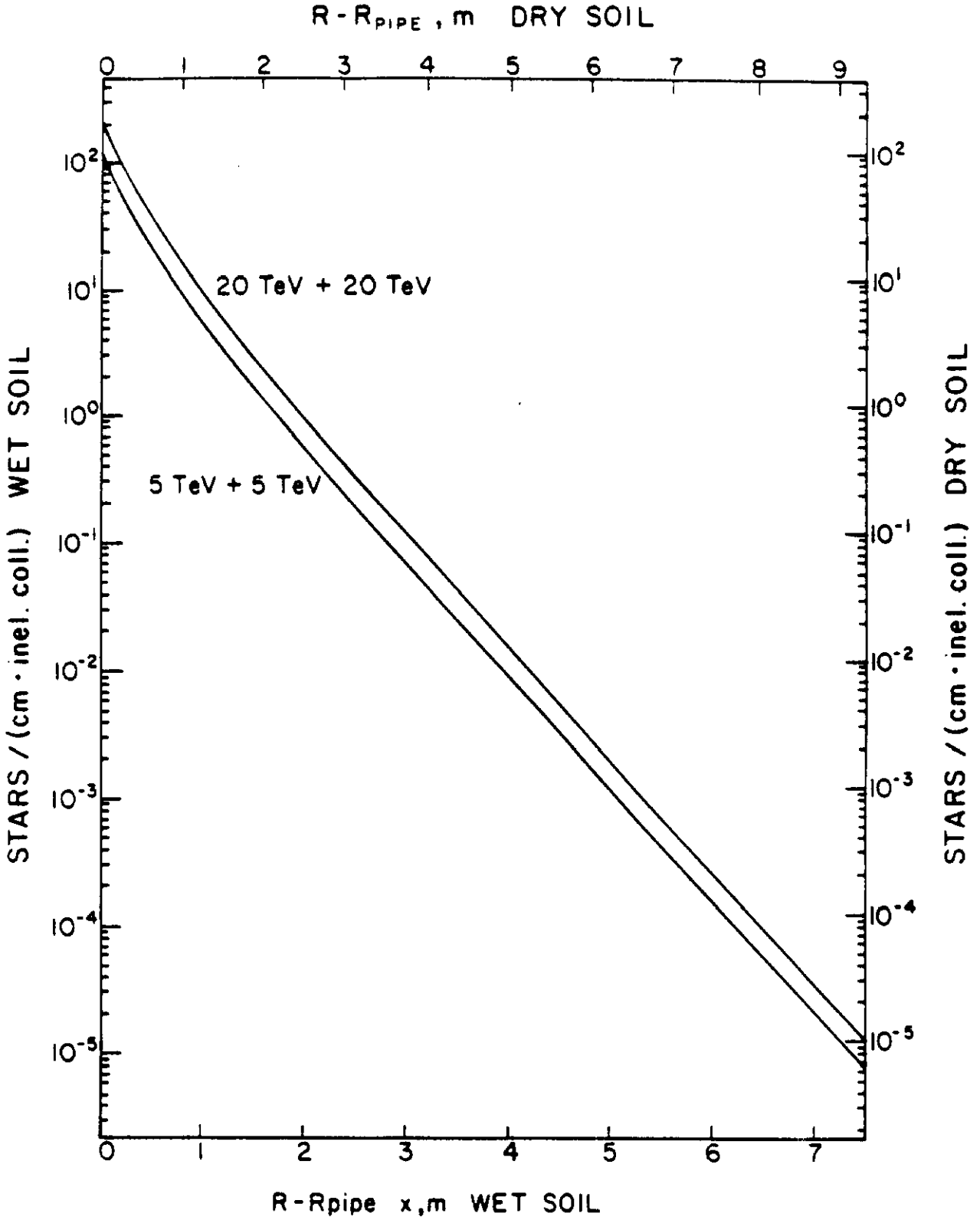

Fig. 154. Longitudinally integrated star density (in stars/cm•inelastic collision) in soil surrounding a beampipe, for colliding beams of 5, 10 and 20 TeV protons interacting at z=0. The calculation has a cut-off momentum of 0.3 GeV/c. For wet soil use left & bottom axes and for dry soil right & top axes.

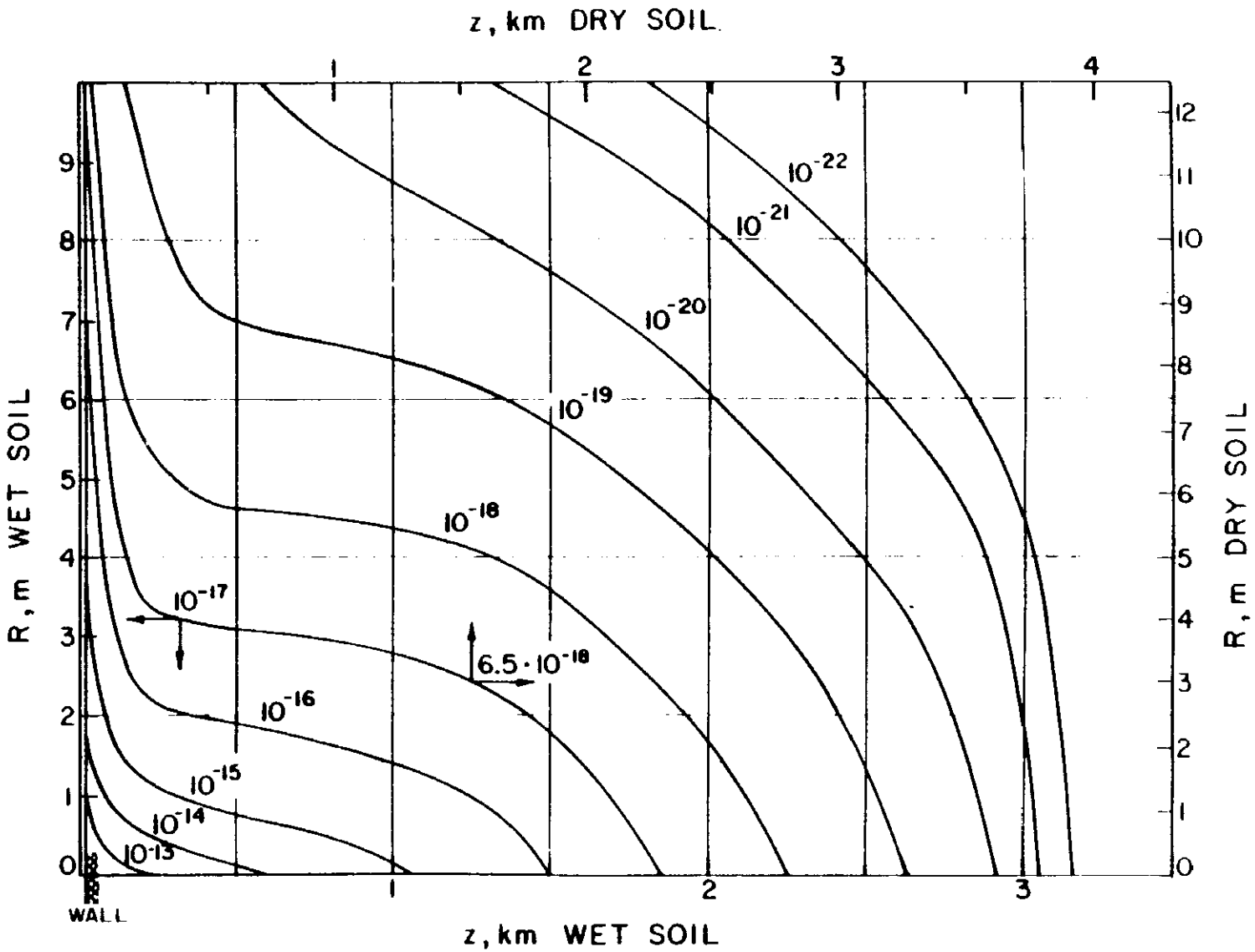

Fig. 155. Contours of equal dose equivalent (in rem/inelastic collision) in soil, due to muons for colliding beams of 5 TeV each followed by a 20m long decay space. Contours for wet soil (left & bottom axes) are integral powers of ten. Contours for dry soil (right & top axes) must be scaled down by 0.65 as shown for one example. Some contours may be omitted for clarity or due to statistical uncertainty.

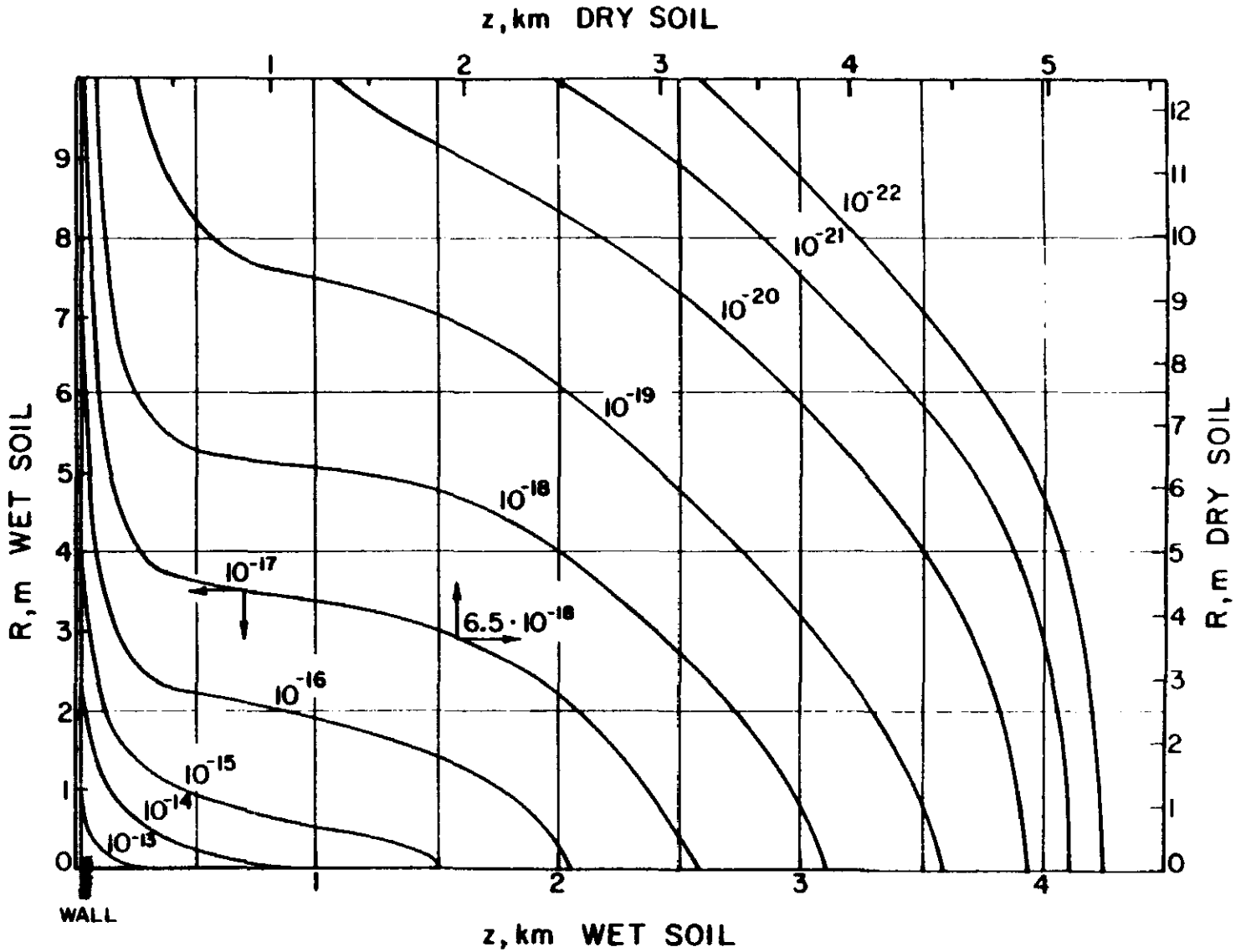

Fig. 156. Contours of equal dose equivalent (in rem/inelastic collision) in soil, due to muons for colliding beams of 10 TeV each followed by a 20m long decay space. Contours for wet soil (left & bottom axes) are integral powers of ten. Contours for dry soil (right & top axes) must be scaled down by 0.65 as shown for one example. Some contours may be omitted for clarity or due to statistical uncertainty.

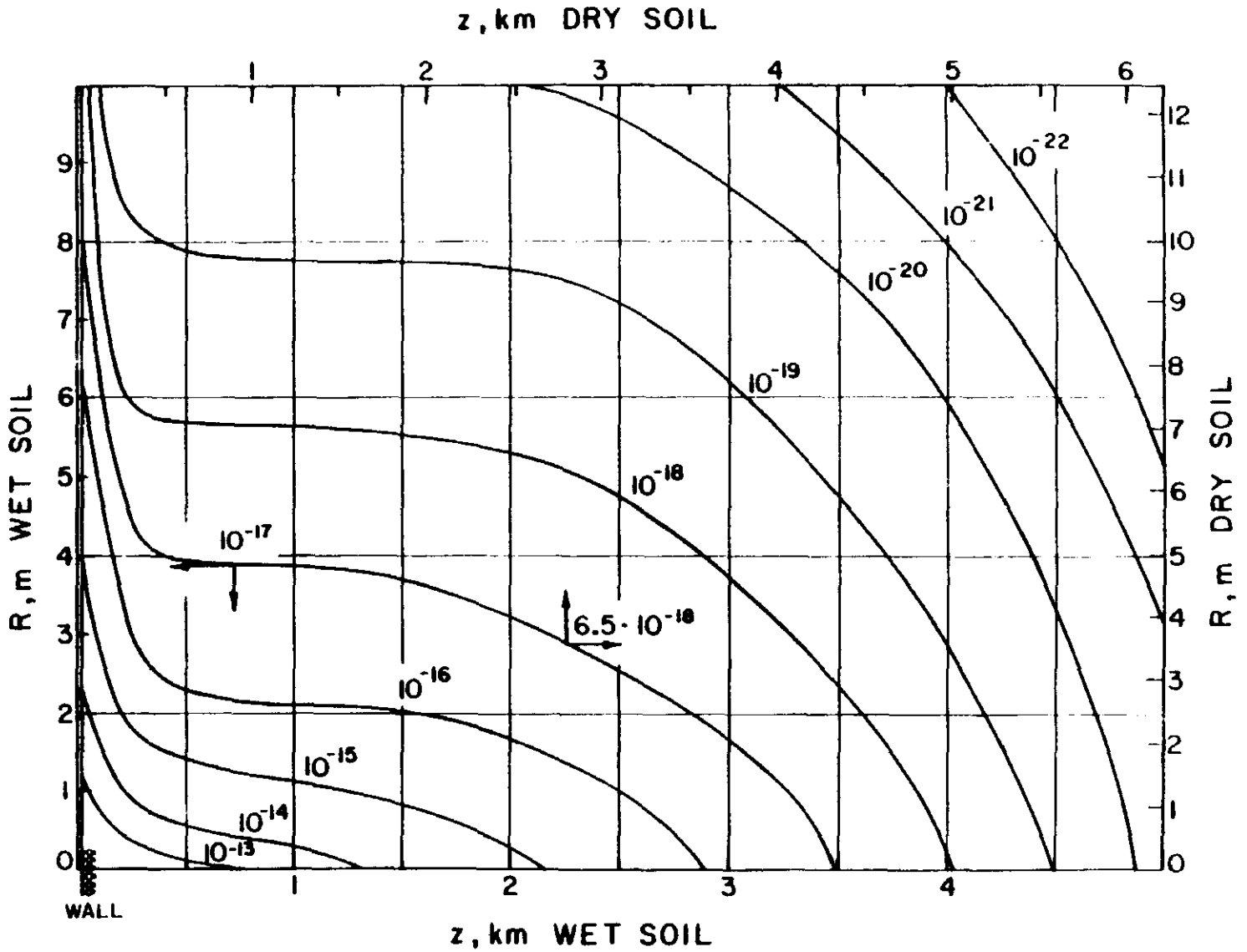

Fig. 157. Contours of equal dose equivalent (in rem/inelastic collision) in soil, due to muons for colliding beams of 20 TeV each followed by a 20m long decay space. Contours for wet soil (left & bottom axes) are integral powers of ten. Contours for dry soil (right & top axes) must be scaled down by 0.65 as shown for one example. Some contours may be omitted for clarity or due to statistical uncertainty.

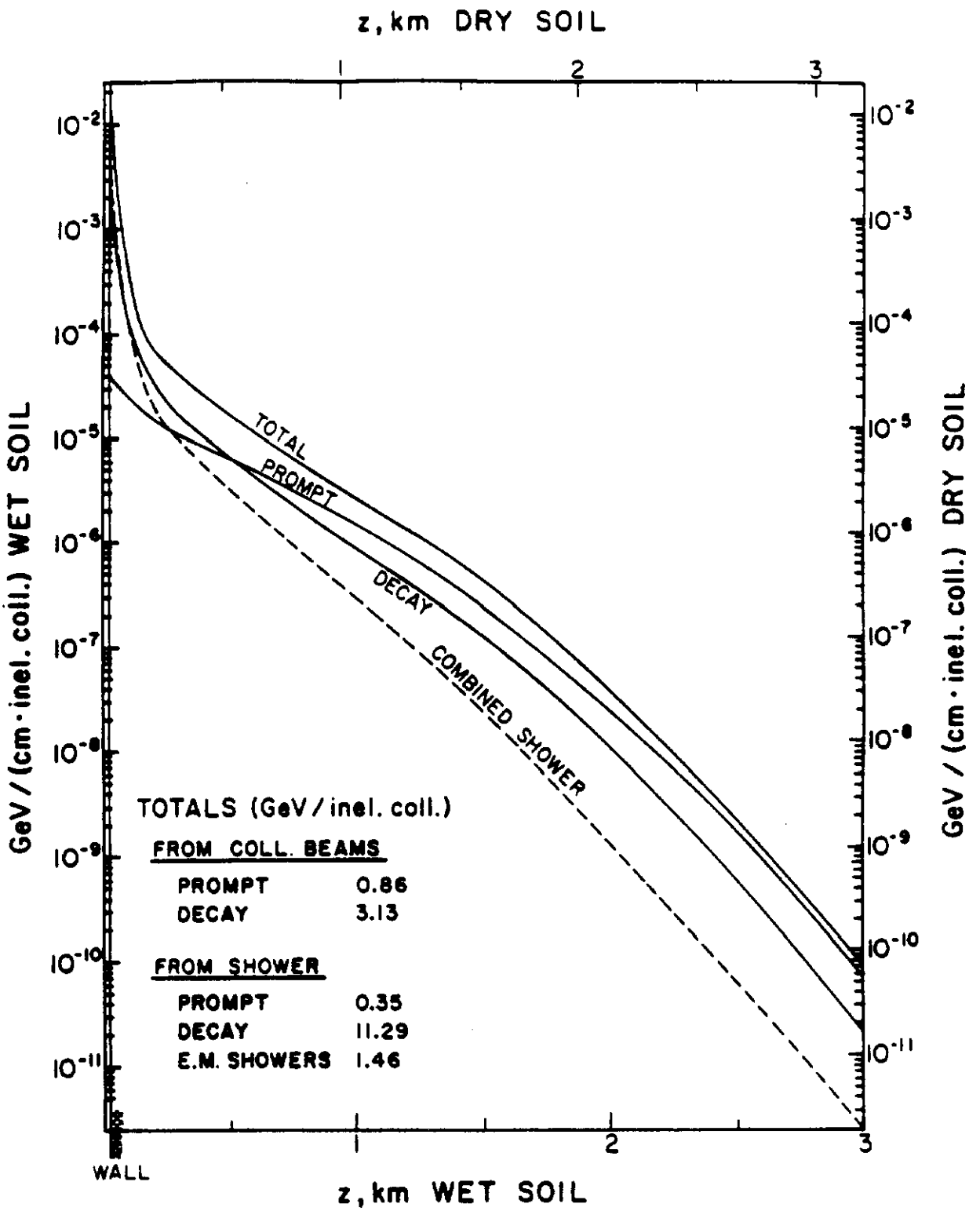

Fig. 158. Radially integrated energy density (in GeV/cm•inelastic collision) in soil of various muon components for colliding beams of 5 TeV protons with a 20m long decay space following the interaction region. For wet soil use left & bottom axes and for dry soil right & top axes.

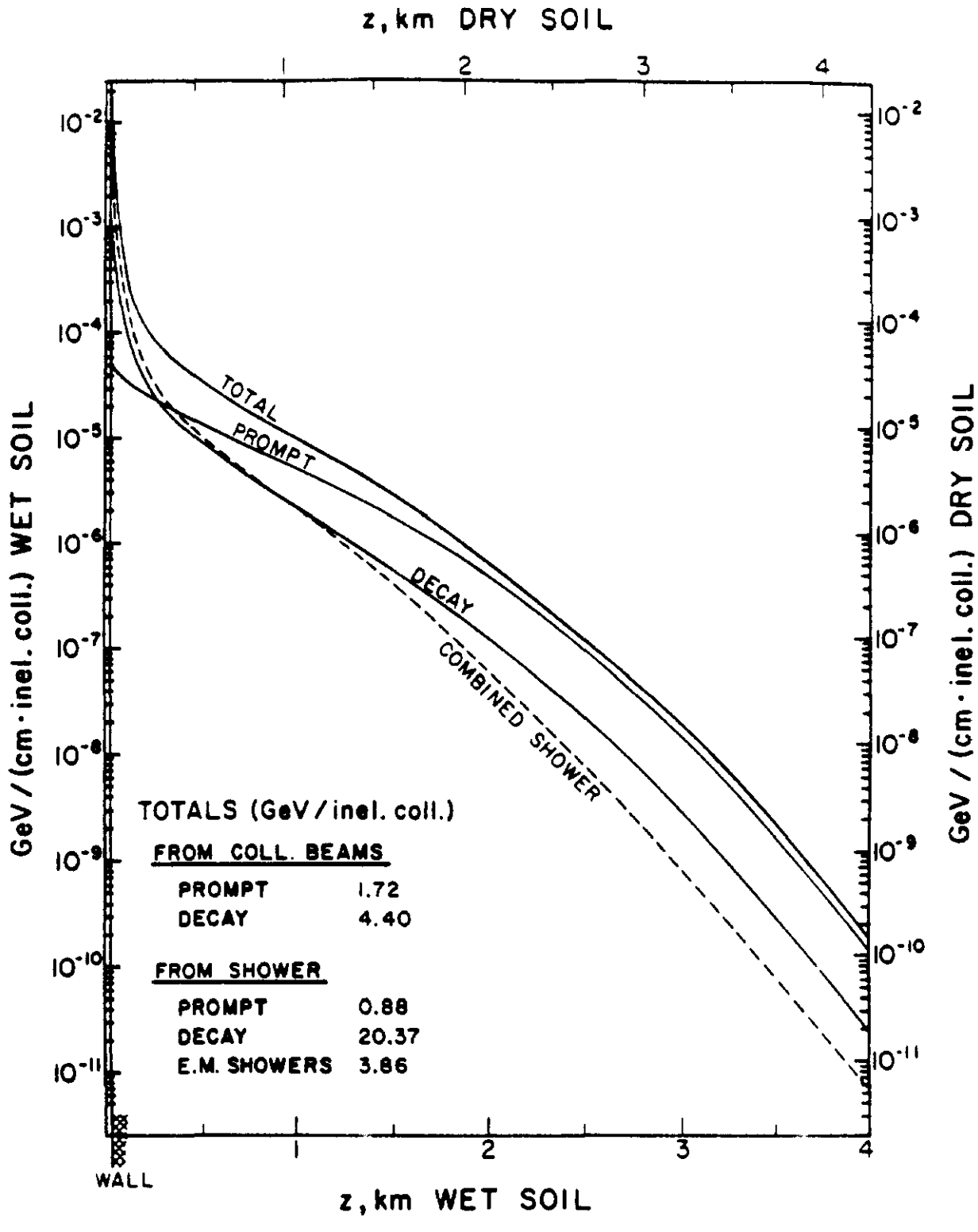

Fig. 159. Radially integrated energy density (in GeV/cm•inelastic collision) in soil of various muon components for colliding beams of 10 TeV protons with a 20m long decay space following the interaction region. For wet soil use left & bottom axes and for dry soil right & top axes.

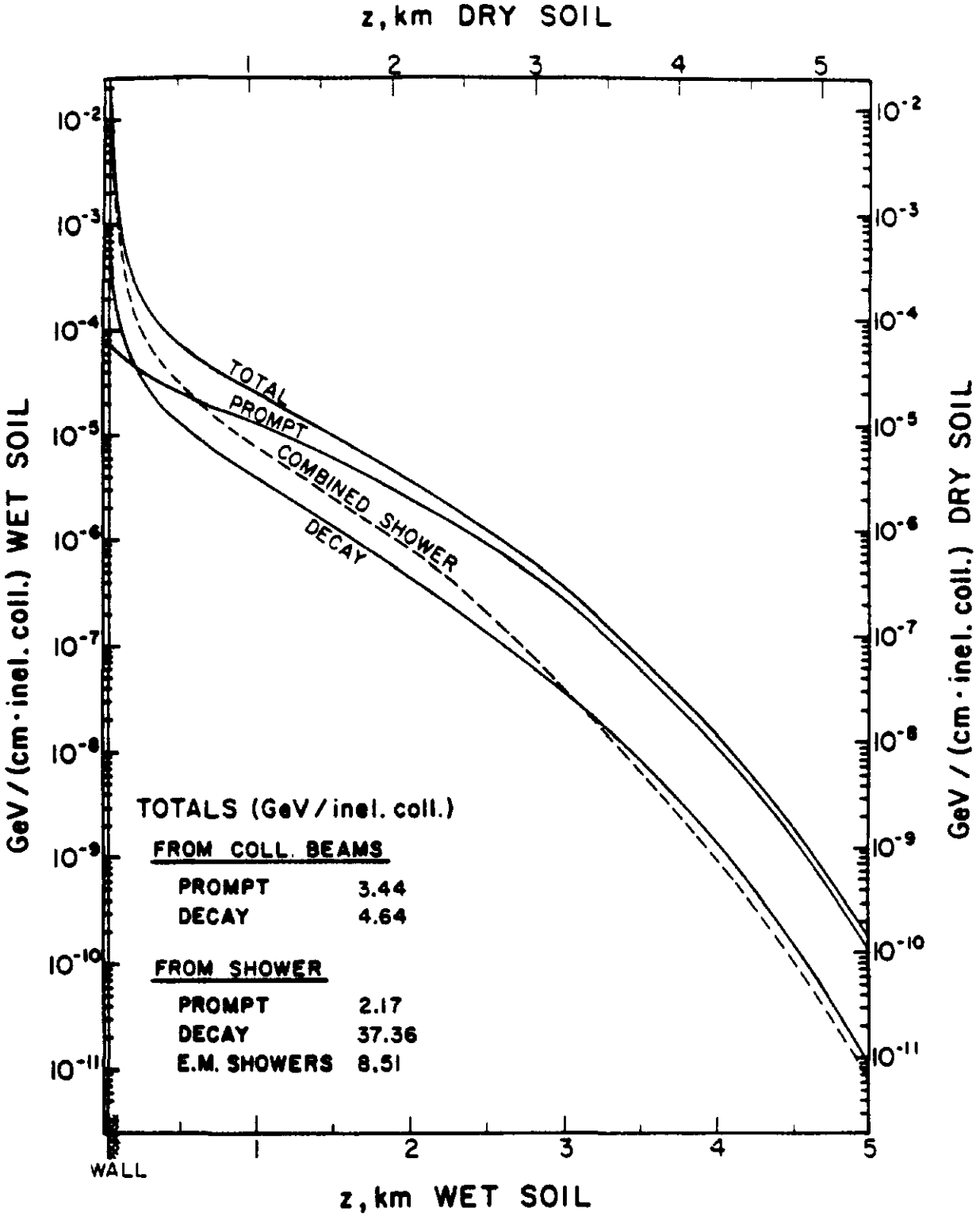

Fig. 160. Radially integrated energy density (in GeV/cm•inelastic collision) in soil of various muon components for colliding beams of 20 TeV protons with a 20m long decay space following the interaction region. For wet soil use left & bottom axes and for dry soil right & top axes.

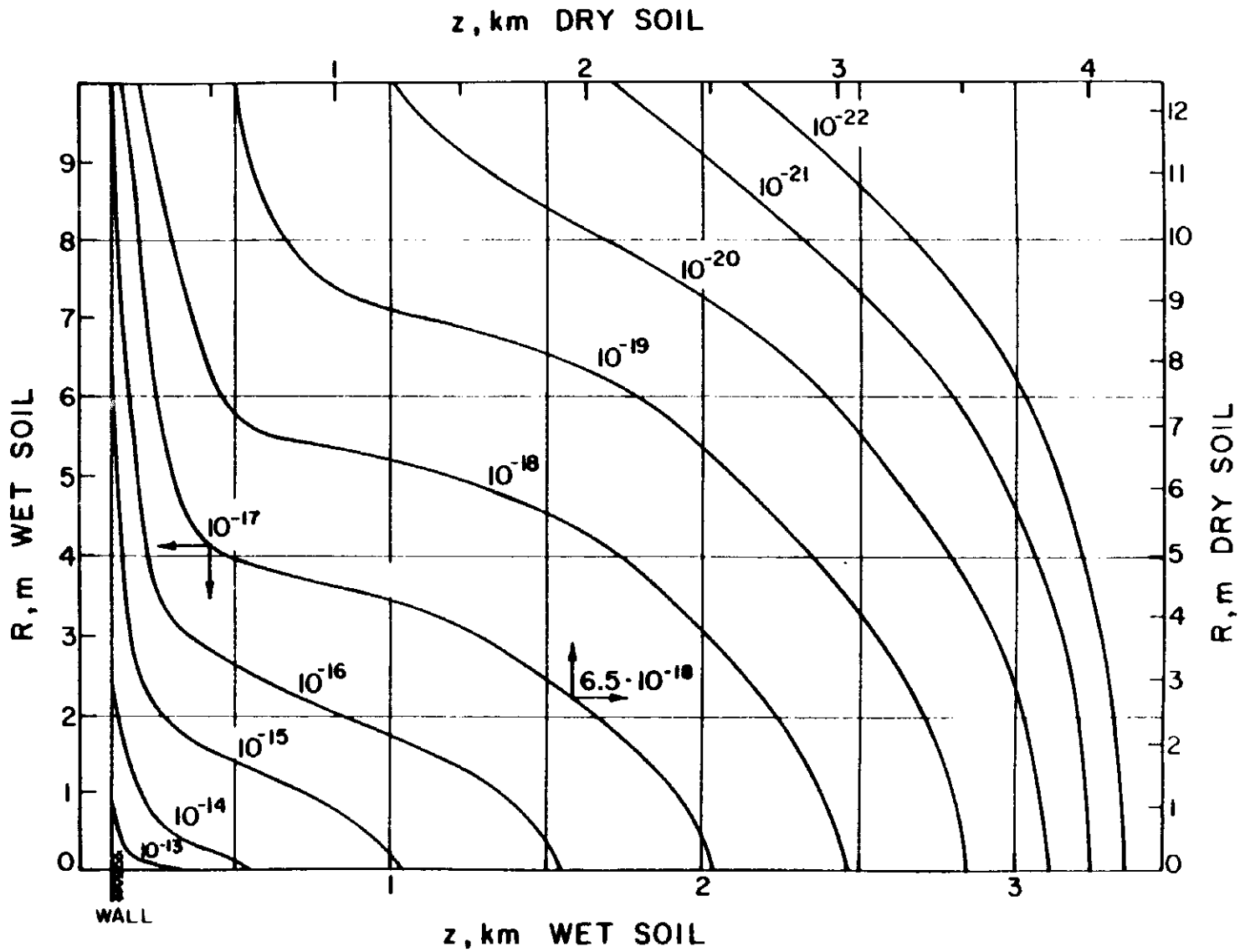

Fig. 161. Contours of equal dose equivalent (in rem/inelastic collision) in soil, due to muons for colliding beams of 5 TeV each followed by a 100m long decay space. Contours for wet soil (left & bottom axes) are integral powers of ten. Contours for dry soil (right & top axes) must be scaled down by 0.65 as shown for one example. Some contours may be omitted for clarity or due to statistical uncertainty.

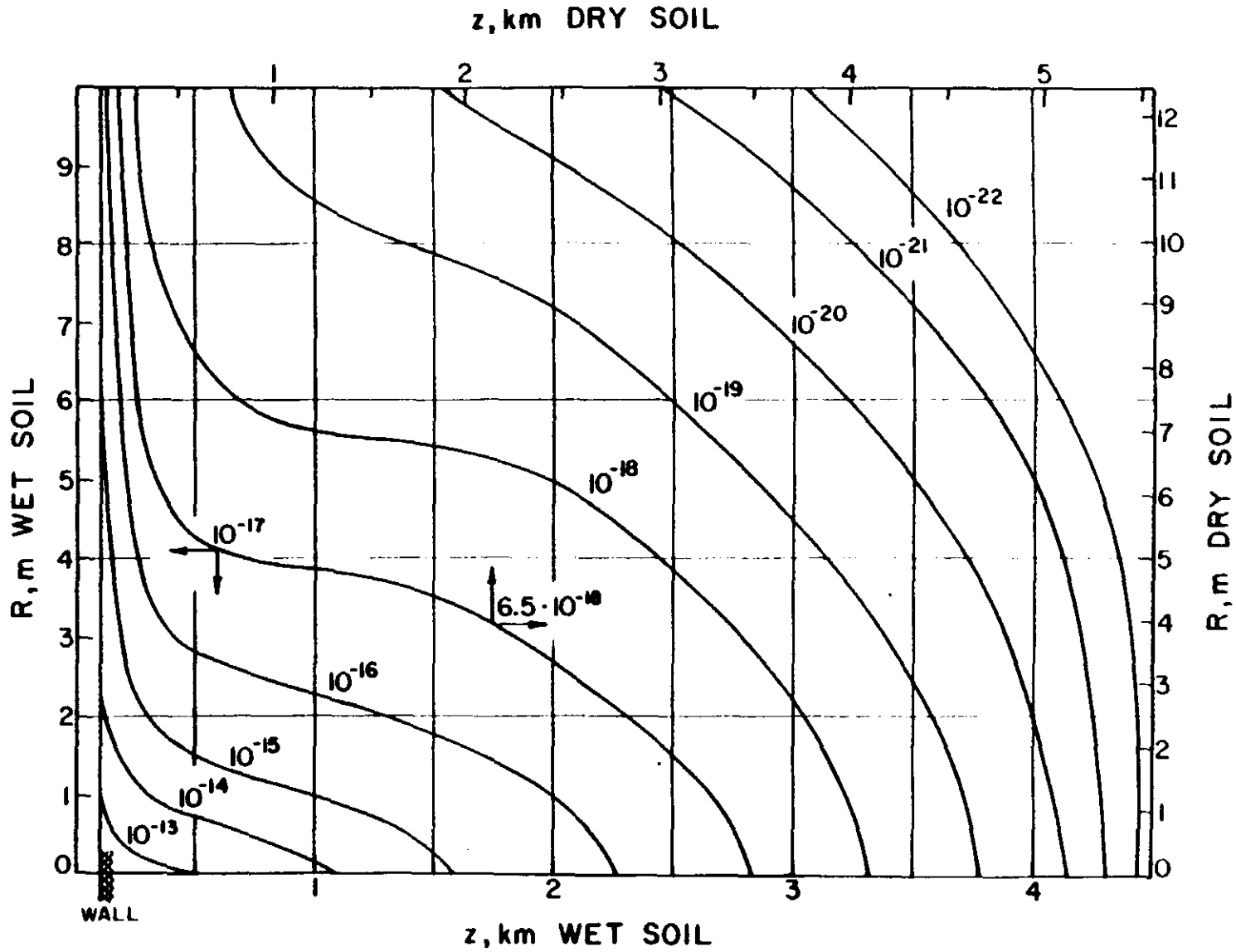

Fig. 162. Contours of equal dose equivalent (in rem/inelastic collision) in soil, due to muons for colliding beams of 10 TeV each followed by a 100m long decay space. Contours for wet soil (left & bottom axes) are integral powers of ten. Contours for dry soil (right & top axes) must be scaled down by 0.65 as shown for one example. Some contours may be omitted for clarity or due to statistical uncertainty.

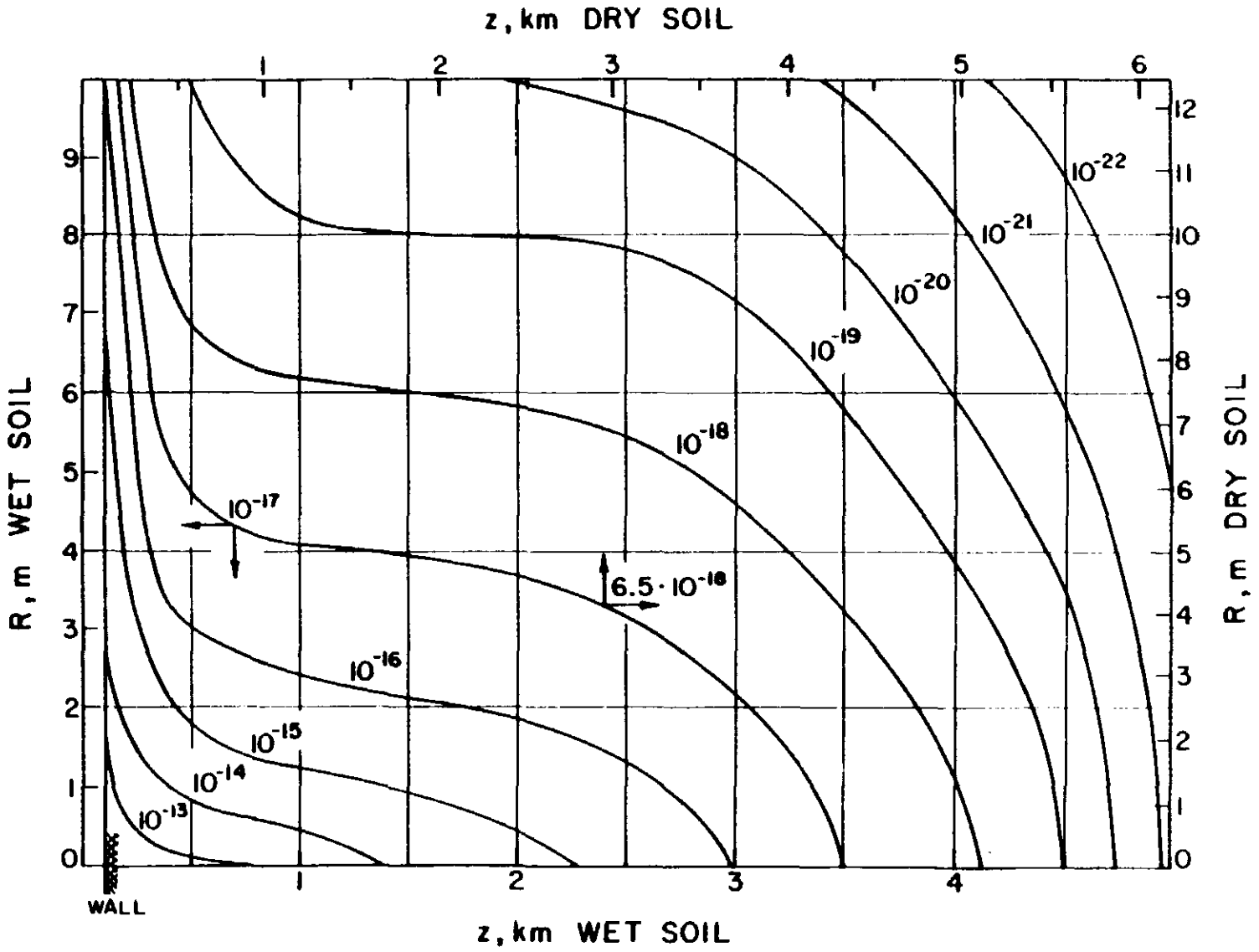

Fig. 163. Contours of equal dose equivalent (in rem/inelastic collision) in soil, due to muons for colliding beams of 20 TeV each followed by a 100m long decay space. Contours for wet soil (left & bottom axes) are integral powers of ten. Contours for dry soil (right & top axes) must be scaled down by 0.65 as shown for one example. Some contours may be omitted for clarity or due to statistical uncertainty.

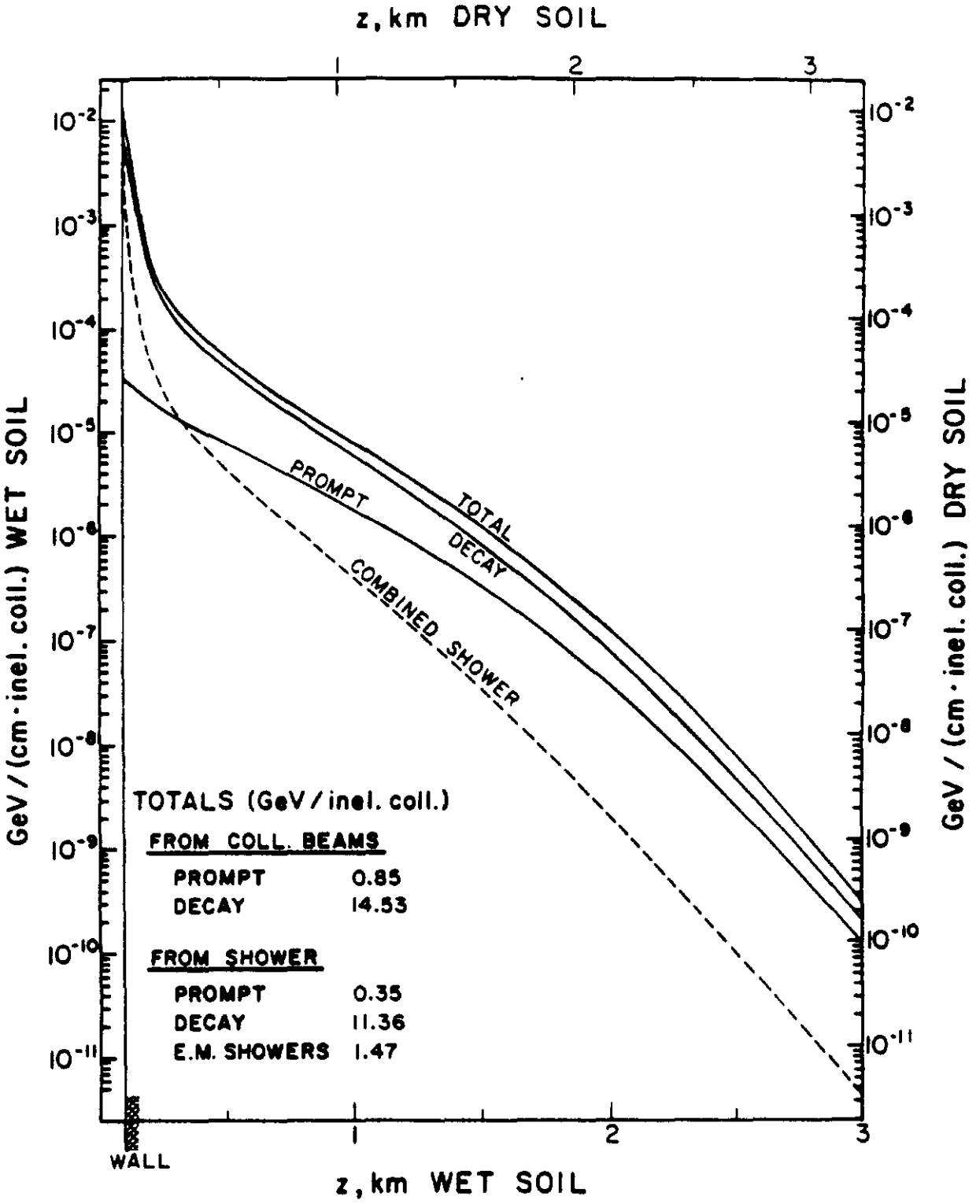

Fig. 164. Radially integrated energy density (in GeV/cm•inelastic collision) in soil of various muon components for colliding beams of 5 TeV protons with a 100m long decay space following the interaction region. For wet soil use left & bottom axes and for dry soil right & top axes.

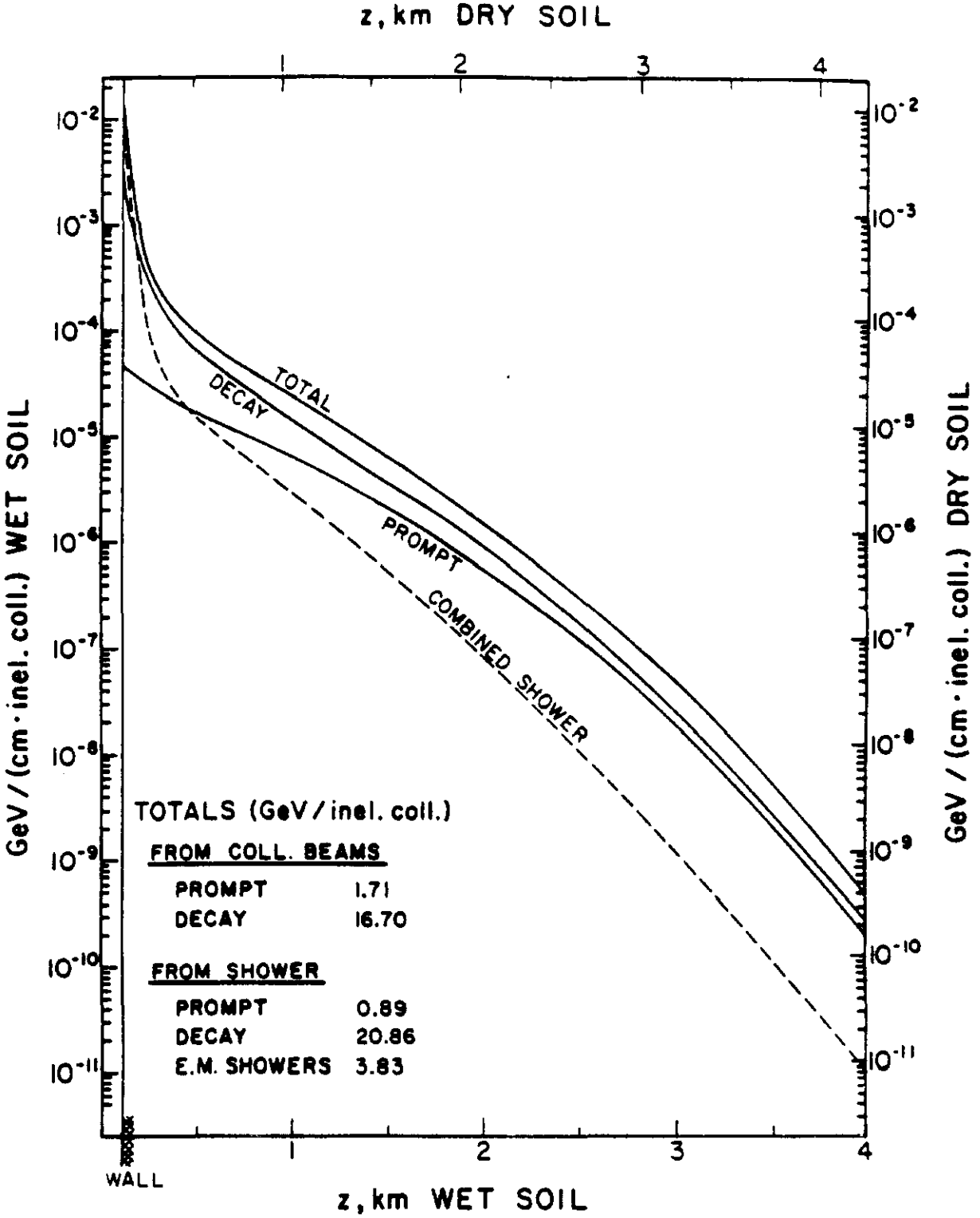

Fig. 165. Radially integrated energy density (in GeV/cm·inelastic collision) in soil of various muon components for colliding beams of 10 TeV protons with a 100m long decay space following the interaction region. For wet soil use left & bottom axes and for dry soil right & top axes.

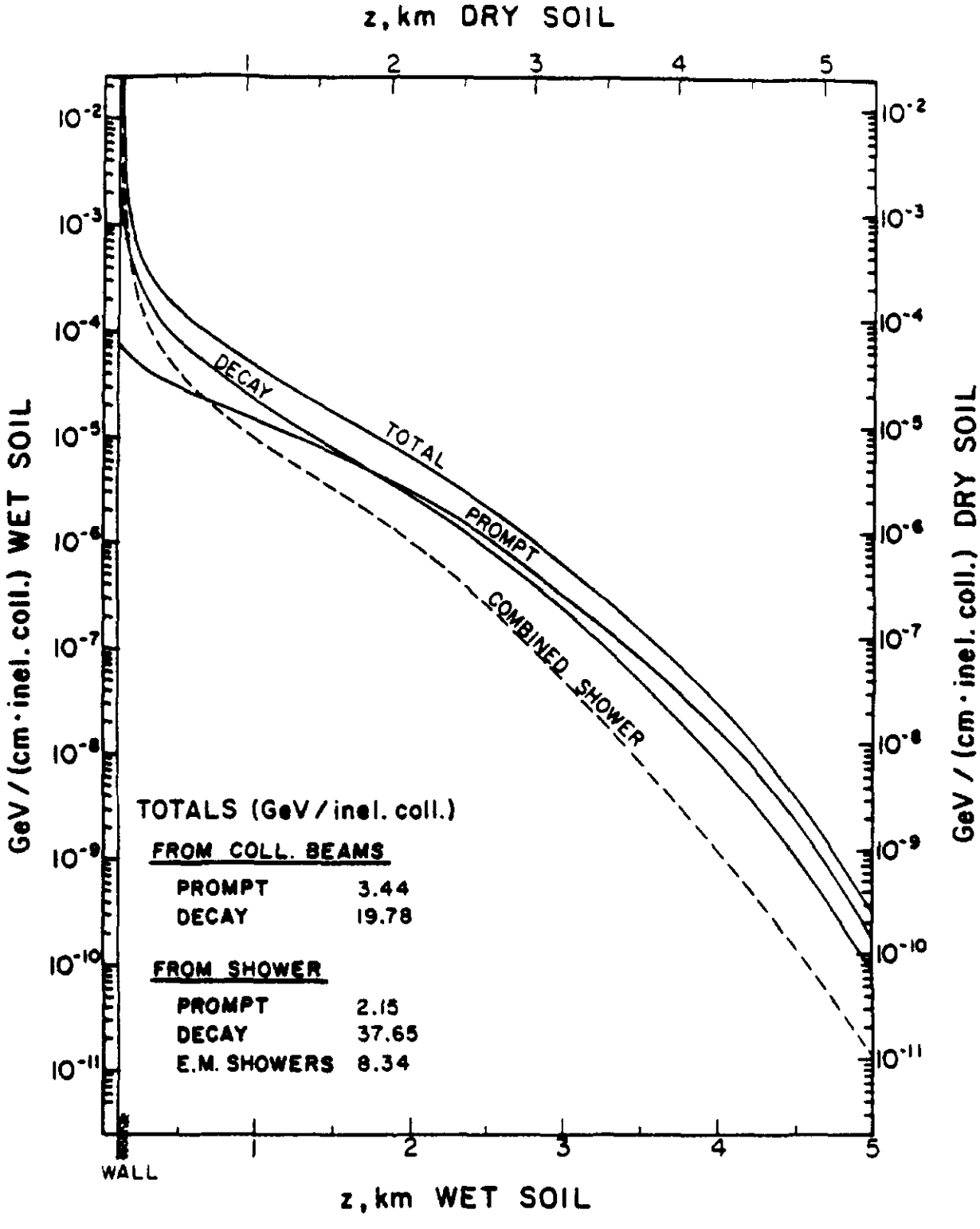

Fig. 166. Radially integrated energy density (in GeV/cm•inelastic collision) in soil of various muon components for colliding beams of 20 TeV protons with a 100m long decay space following the interaction region. For wet soil use left & bottom axes and for dry soil right & top axes.

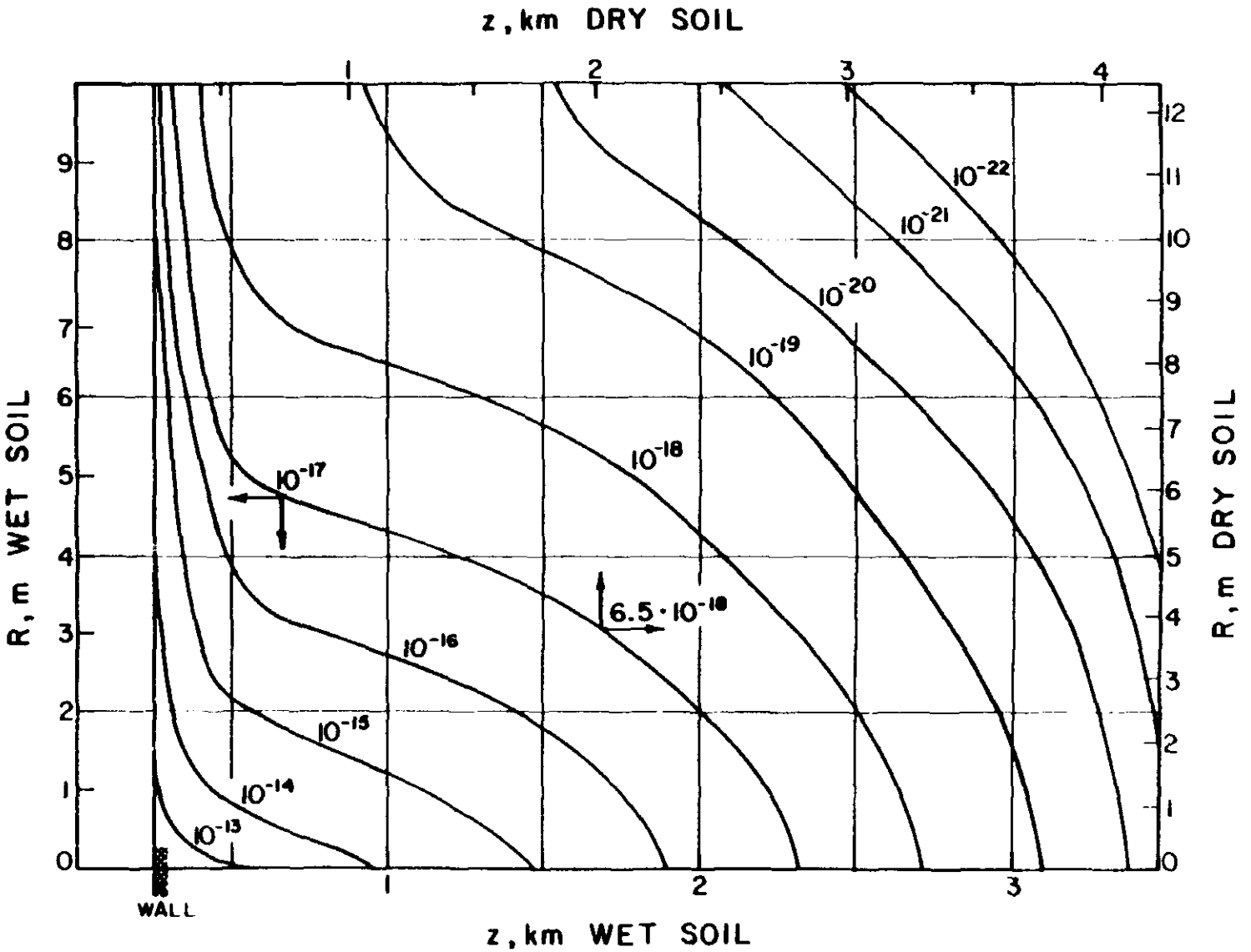

Fig 167. Contours of equal dose equivalent (in rem/inelastic collision) in soil, due to muons for colliding beams of 5 TeV each followed by a 250m long decay space. Contours for wet soil (left & bottom axes) are integral powers of ten. Contours for dry soil (right & top axes) must be scaled down by 0.65 as shown for one example. Some contours may be omitted for clarity or due to statistical uncertainty.

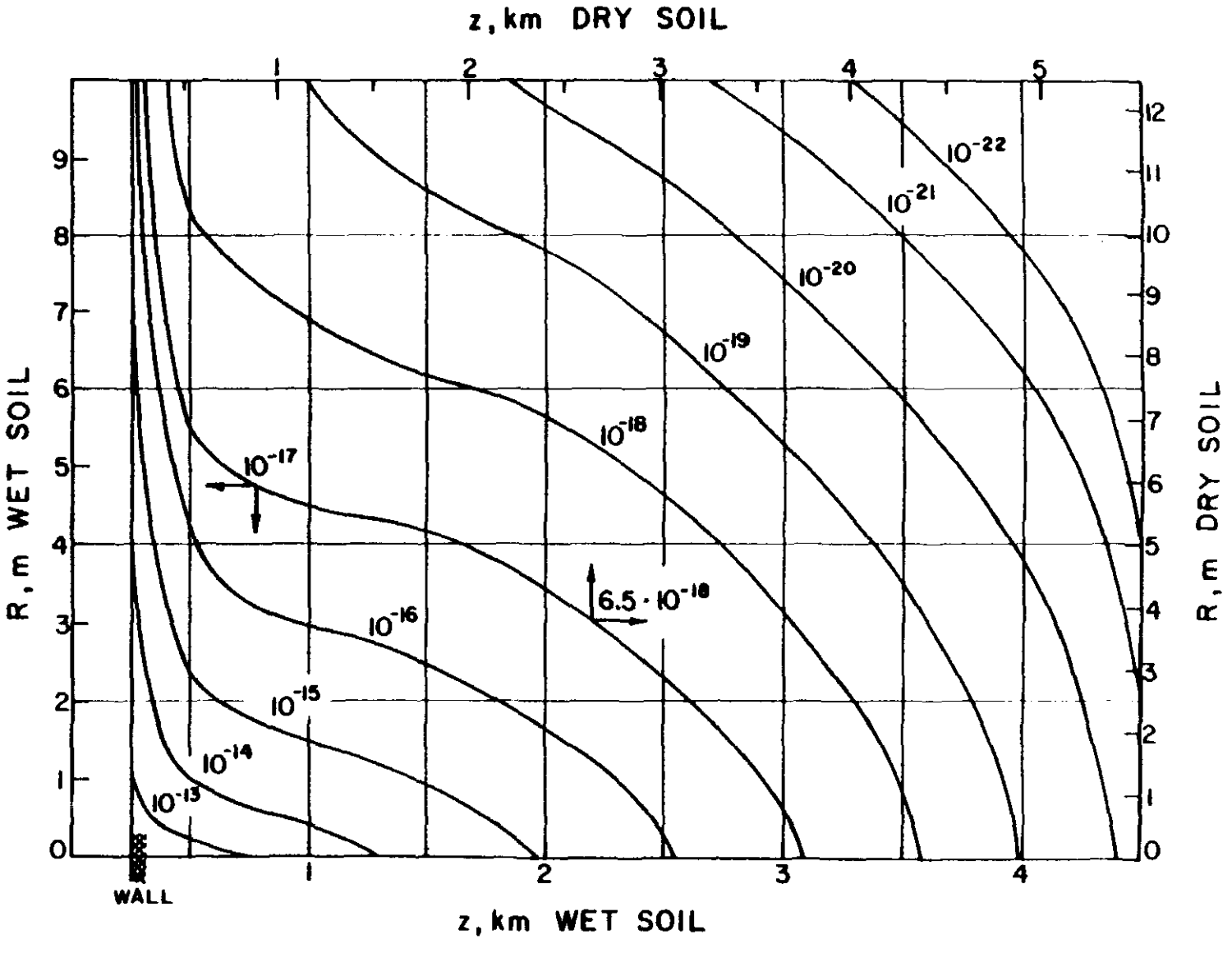

Fig. 168. Contours of equal dose equivalent (in rem/inelastic collision) in soil, due to muons for colliding beams of 10 TeV each followed by a 250m long decay space. Contours for wet soil (left & bottom axes) are integral powers of ten. Contours for dry soil (right & top axes) must be scaled down by 0.65 as shown for one example. Some contours may be omitted for clarity or due to statistical uncertainty.

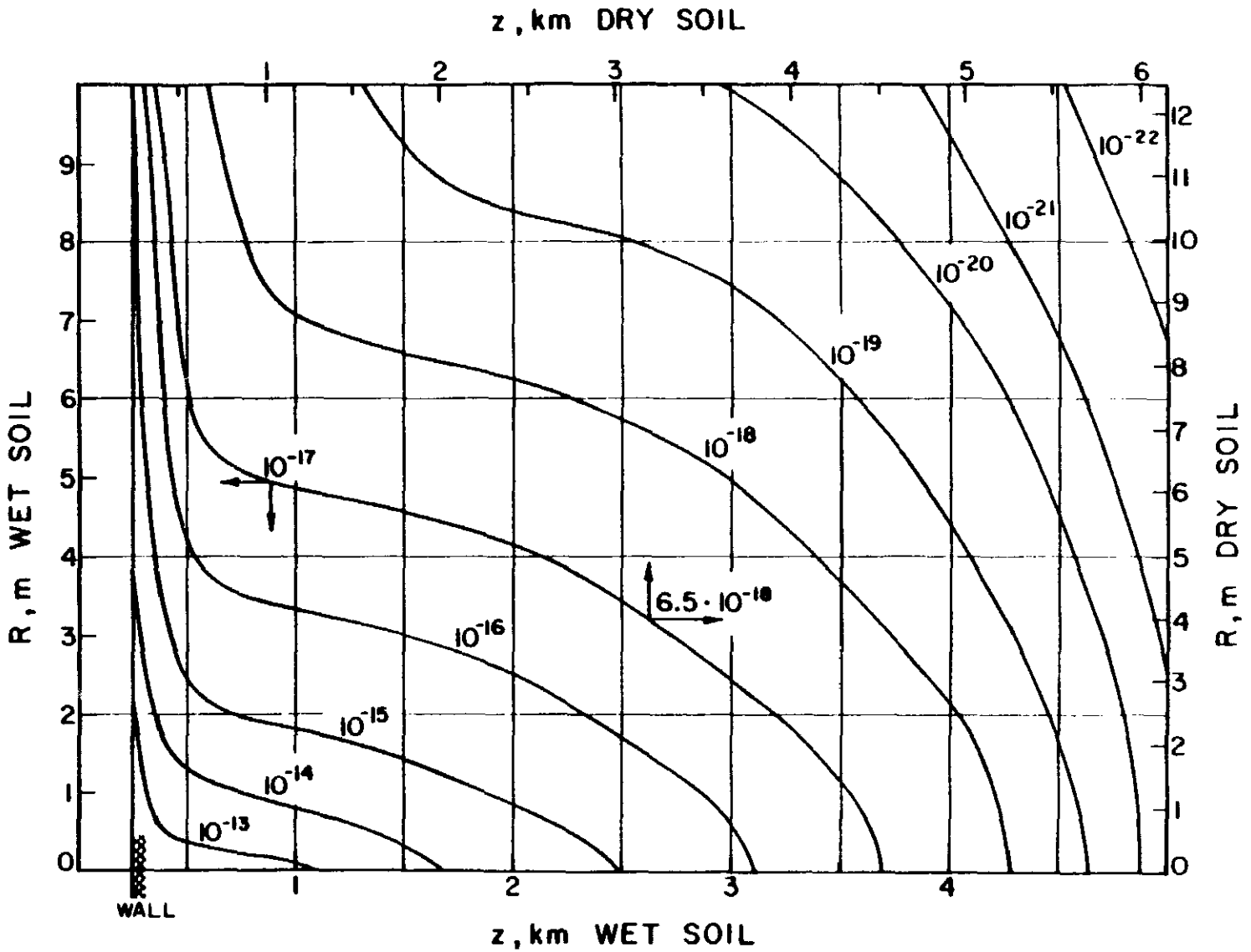

Fig. 169. Contours of equal dose equivalent (in rem/inelastic collision) in soil, due to muons for colliding beams of 20 TeV each followed by a 250m long decay space. Contours for wet soil (left & bottom axes) are integral powers of ten. Contours for dry soil (right & top axes) must be scaled down by 0.65 as shown for one example. Some contours may be omitted for clarity or due to statistical uncertainty.

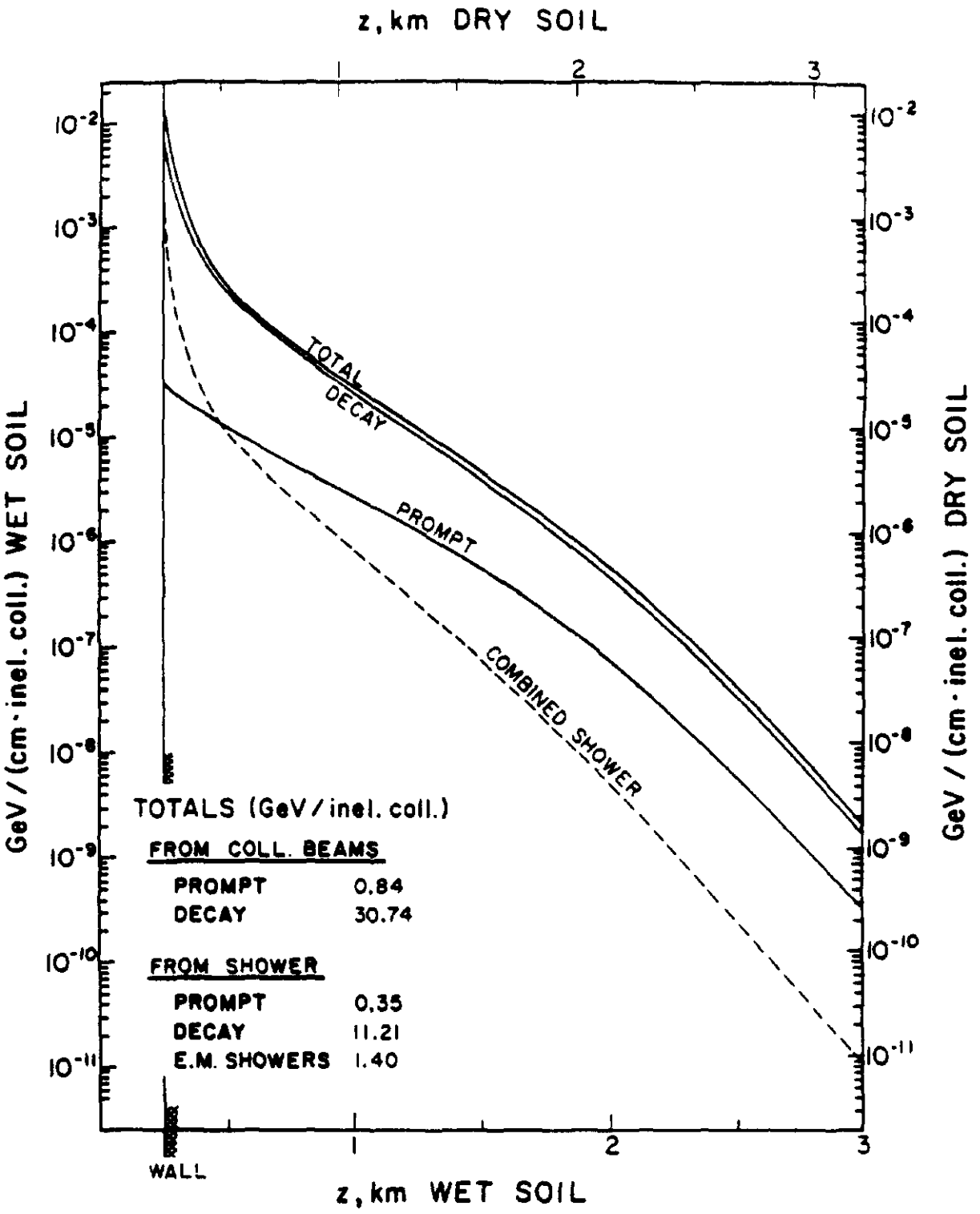

Fig. 170. Radially integrated energy density (in GeV/cm·inelastic collision) in soil of various muon components for colliding beams of 5 TeV protons with a 250m long decay space following the interaction region. For wet soil use left & bottom axes and for dry soil right & top axes.

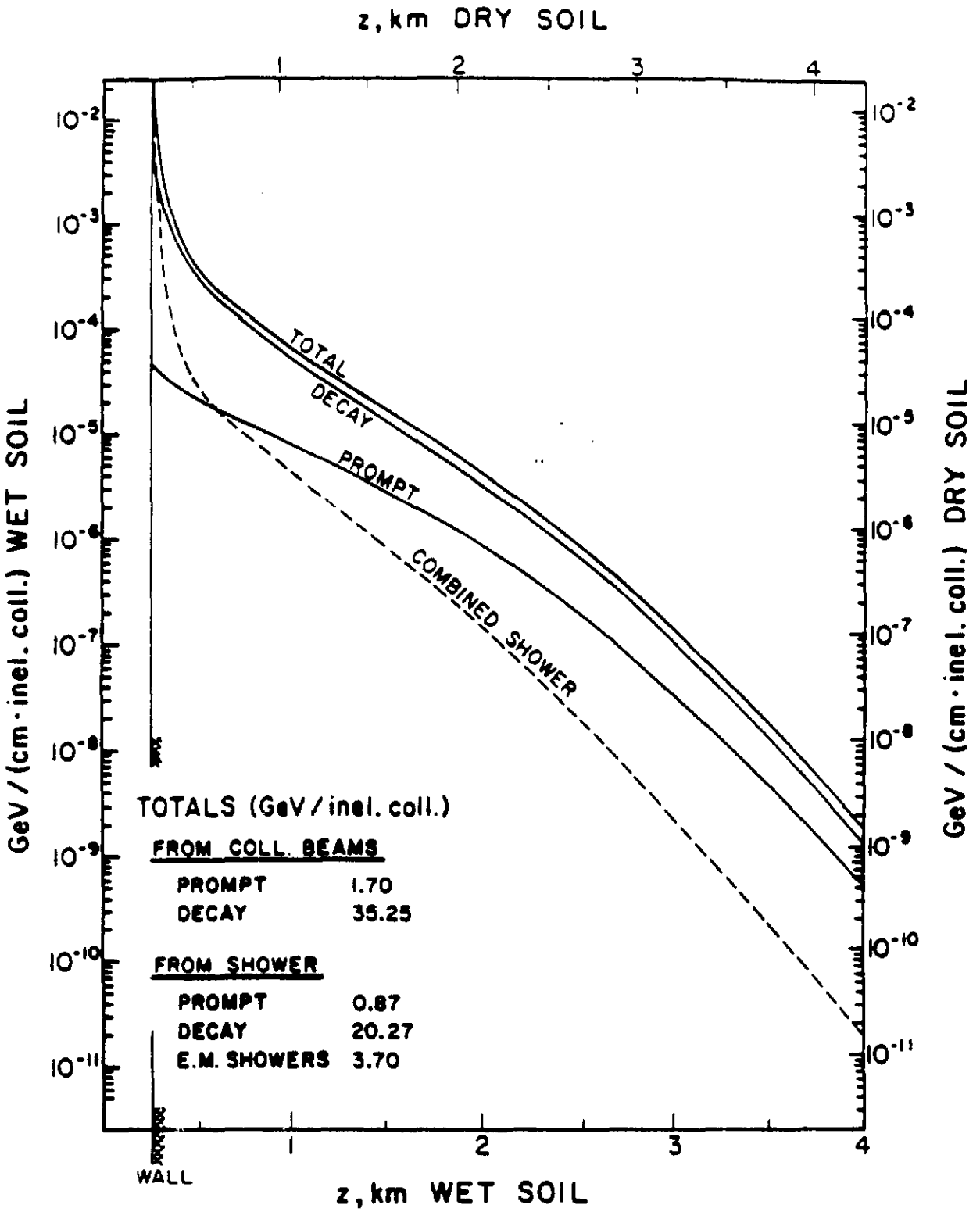

Fig. 171. Radially integrated energy density (in GeV/cm·inelastic collision) in soil of various muon components for colliding beams of 10 TeV protons with a 250m long decay space following the interaction region. For wet soil use left & bottom axes and for dry soil right & top axes.

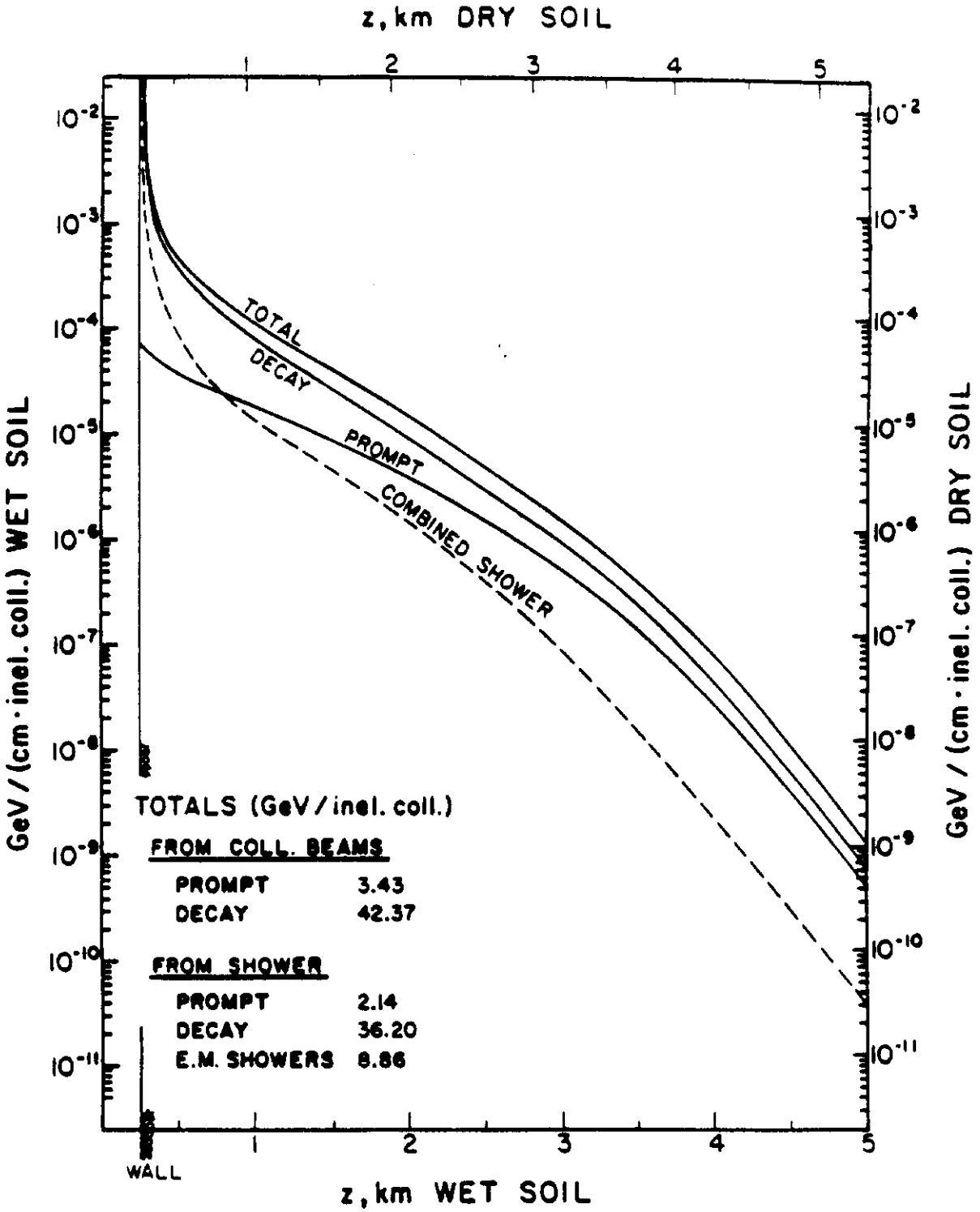

Fig. 172. Radially integrated energy density (in GeV/cm·inelastic collision) in soil of various muon components for colliding beams of 20 TeV protons with a 250m long decay space following the interaction region. For wet soil use left & bottom axes and for dry soil right & top axes.

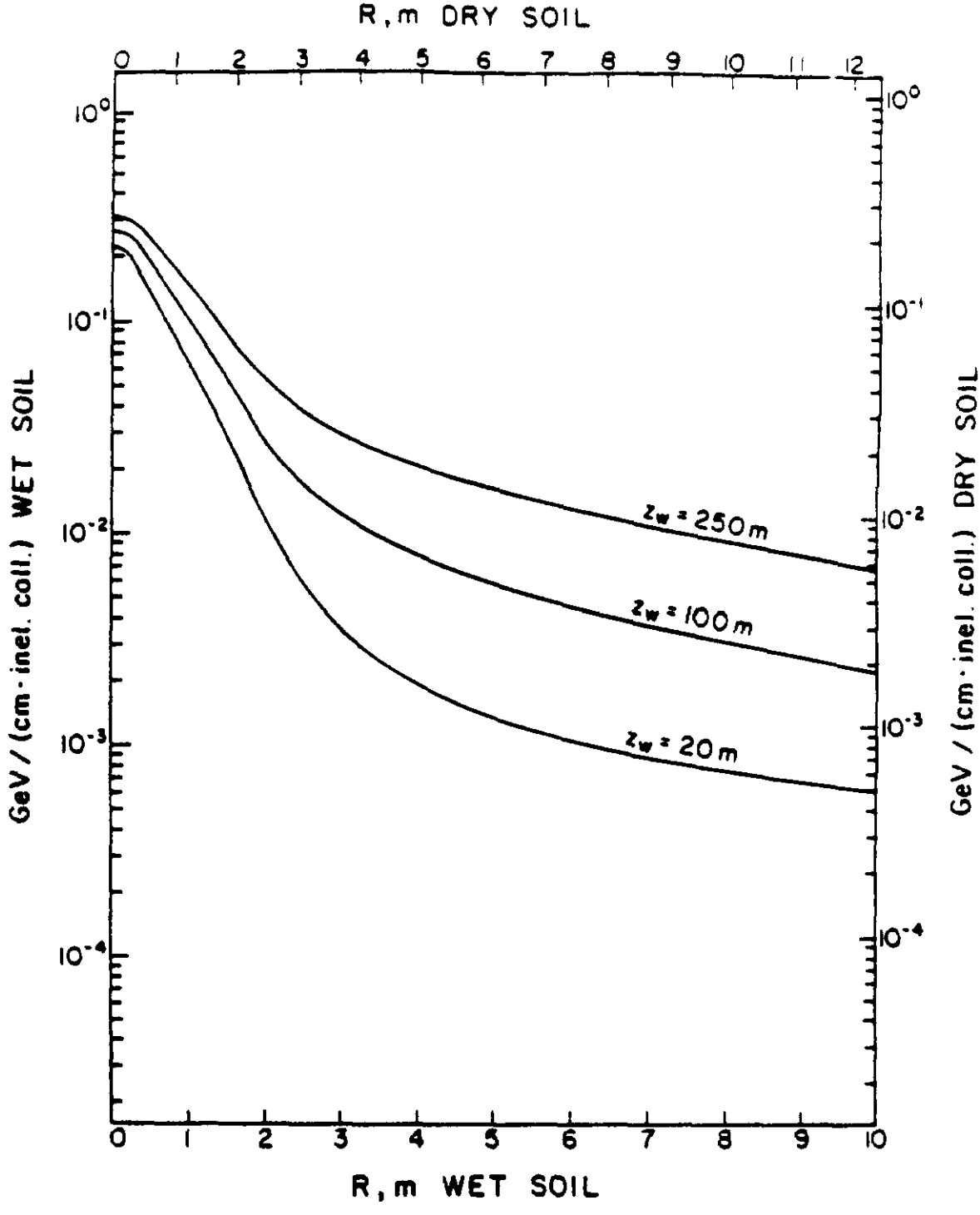

Fig. 173. Longitudinally integrated energy density (in GeV/cm·inelastic collision) in soil of various muon components for colliding beams of 5 TeV protons with a 20, 100 and 250m long decay space following the interaction region. For wet soil use left & bottom axes and for dry soil right & top axes.

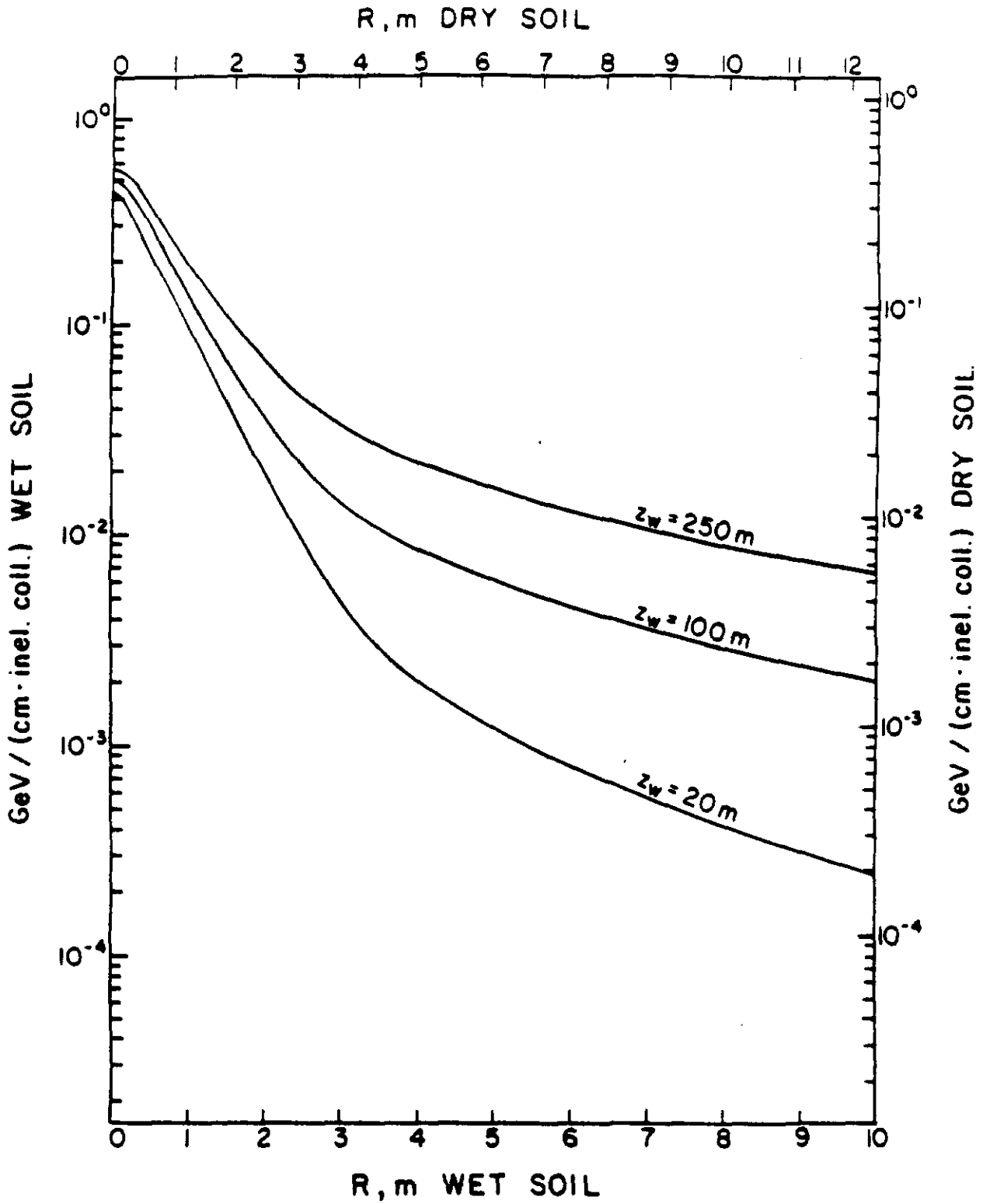

Fig. 174. Longitudinally integrated energy density (in GeV/cm·inelastic collision) in soil of various muon components for colliding beams of 10 TeV protons with a 20, 100 and 250m long decay space following the interaction region. For wet soil use left & bottom axes and for dry soil right & top axes.

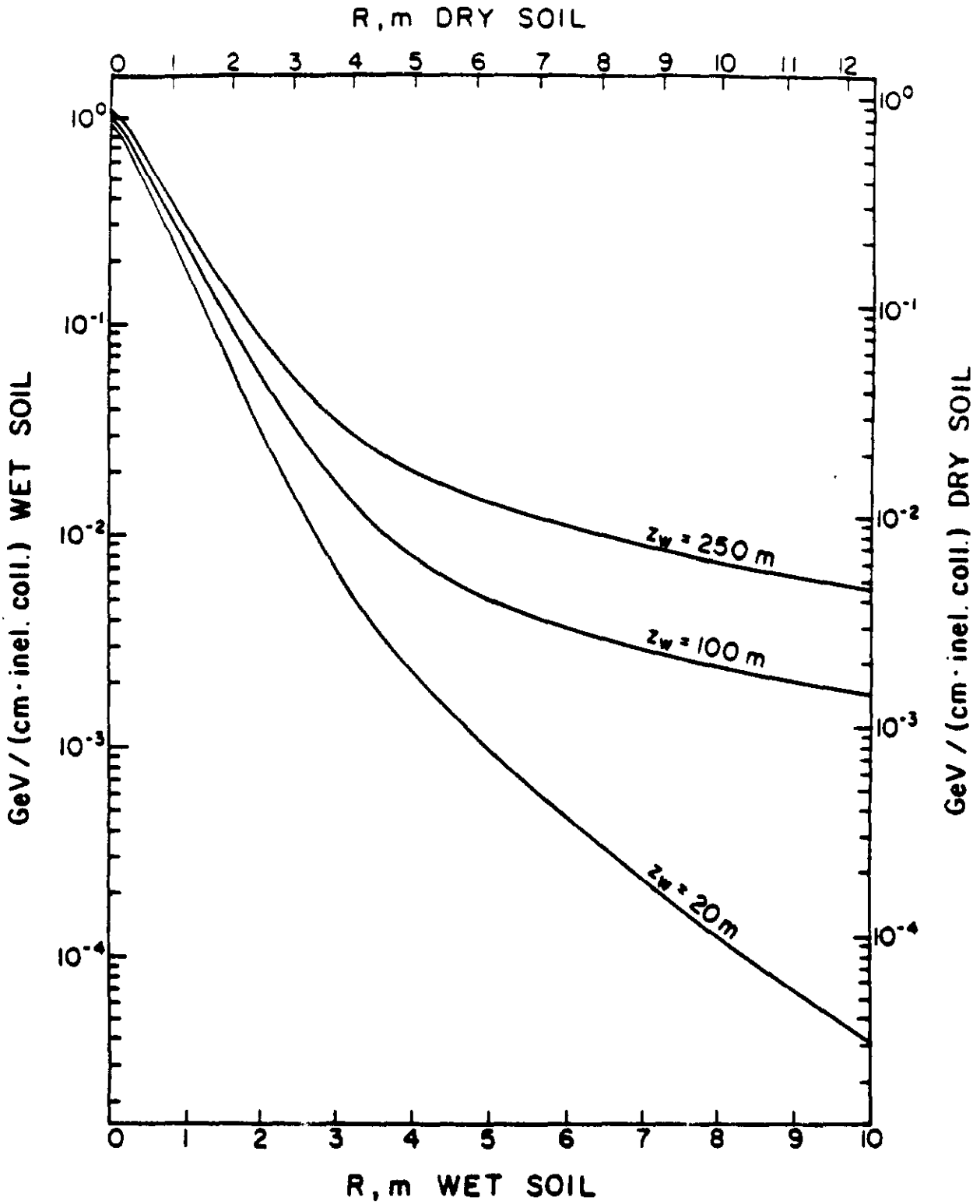

Fig. 175. Longitudinally integrated energy density (in GeV/cm•inelastic collision) in soil of various muon components for colliding beams of 20 TeV protons with a 20, 100 and 250m long decay space following the interaction region. For wet soil use left & bottom axes and for dry soil right & top axes.

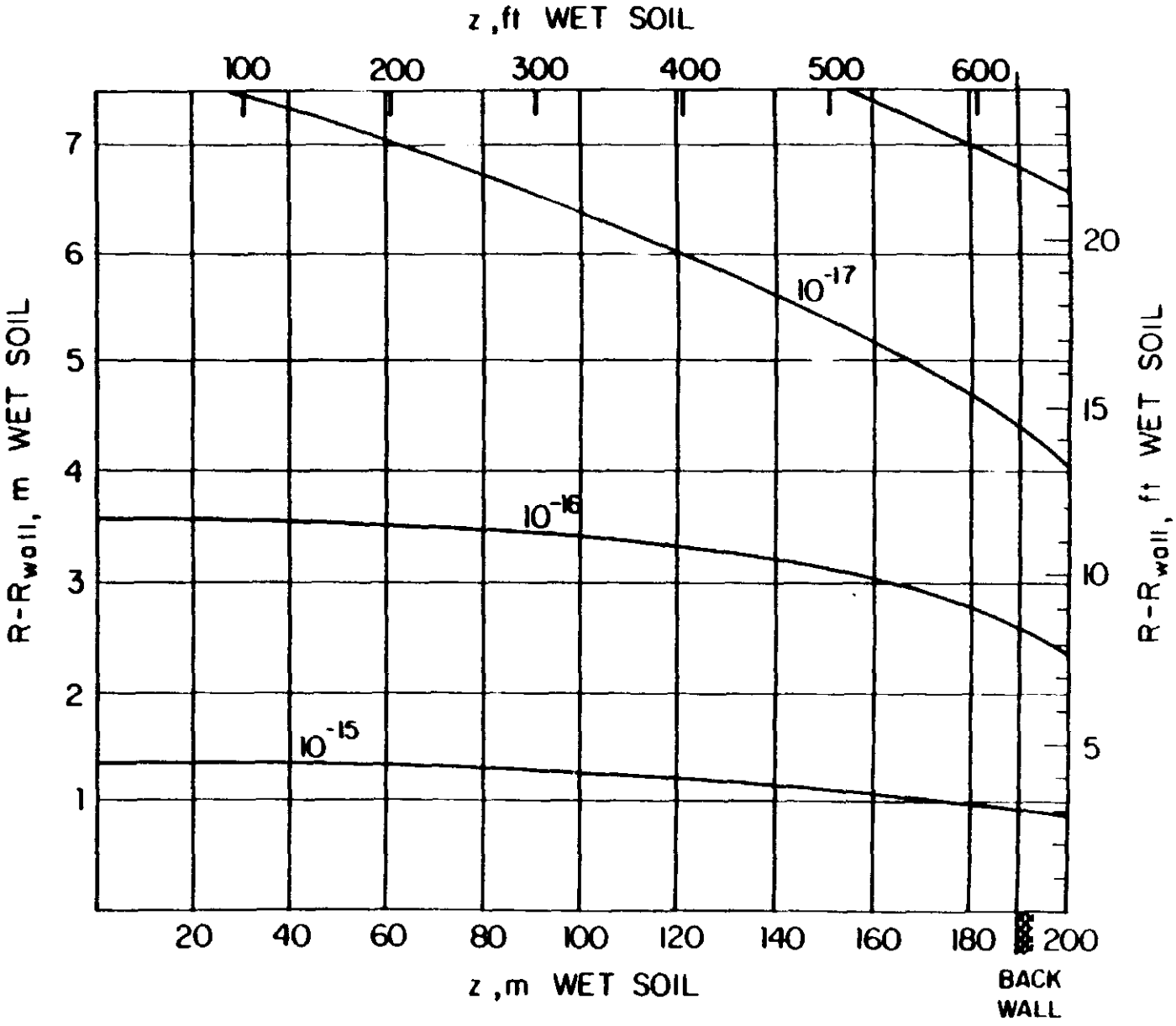

Fig. 176. Contours of equal dose equivalent (in rem/inelastic collision) in soil side wall of collision hall due to muons for colliding beams of 5 TeV each. A 1mm thick beampipe is present. Some contours may be omitted for clarity or due to statistical uncertainty

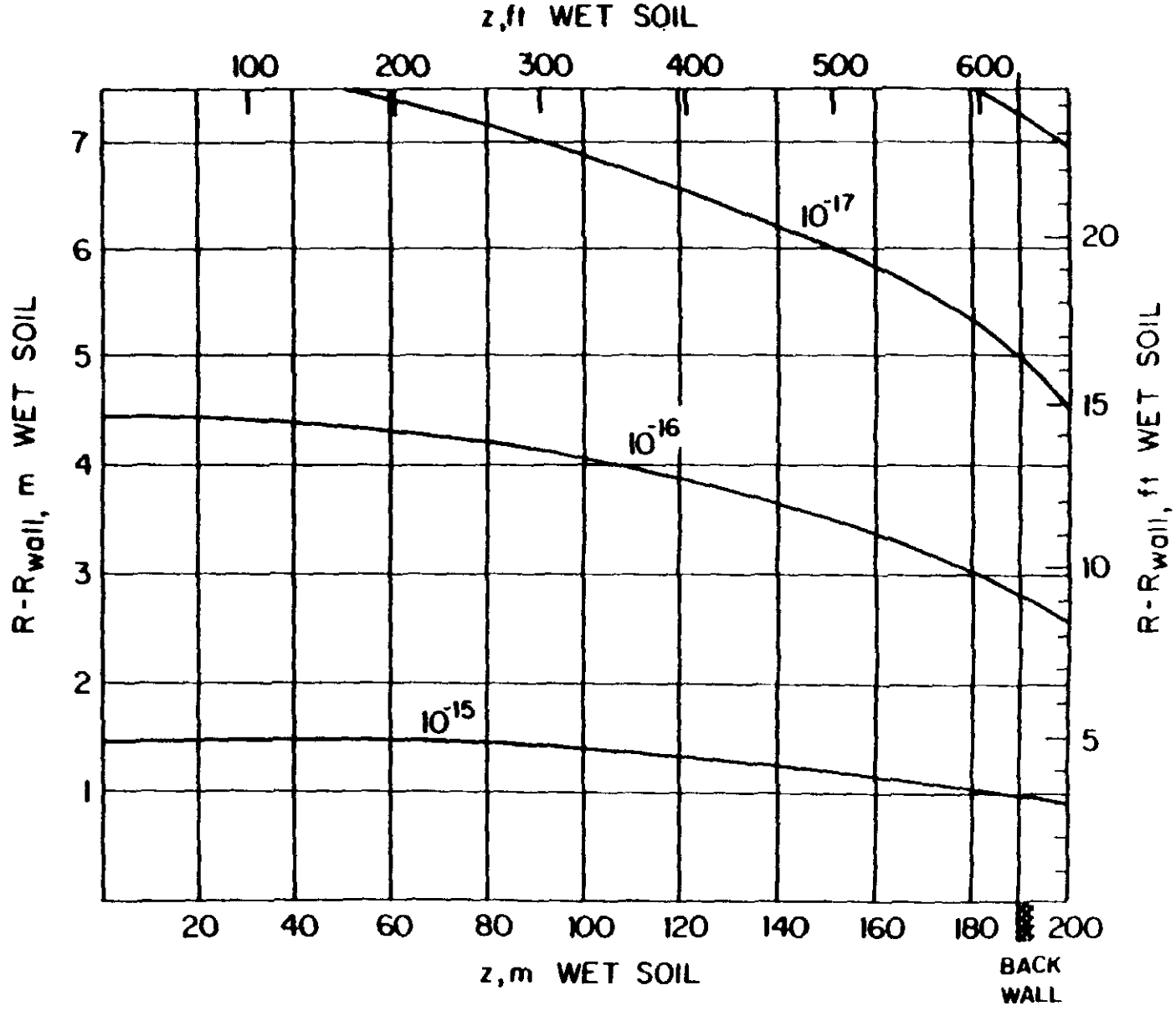

Fig 177 Contours of equal dose equivalent (in rem/inelastic collision) in soil side wall of collision hall due to muons for colliding beams of 20 TeV each. A 1m thick beampipe is present. Some contours may be omitted for clarity or due to statistical uncertainty

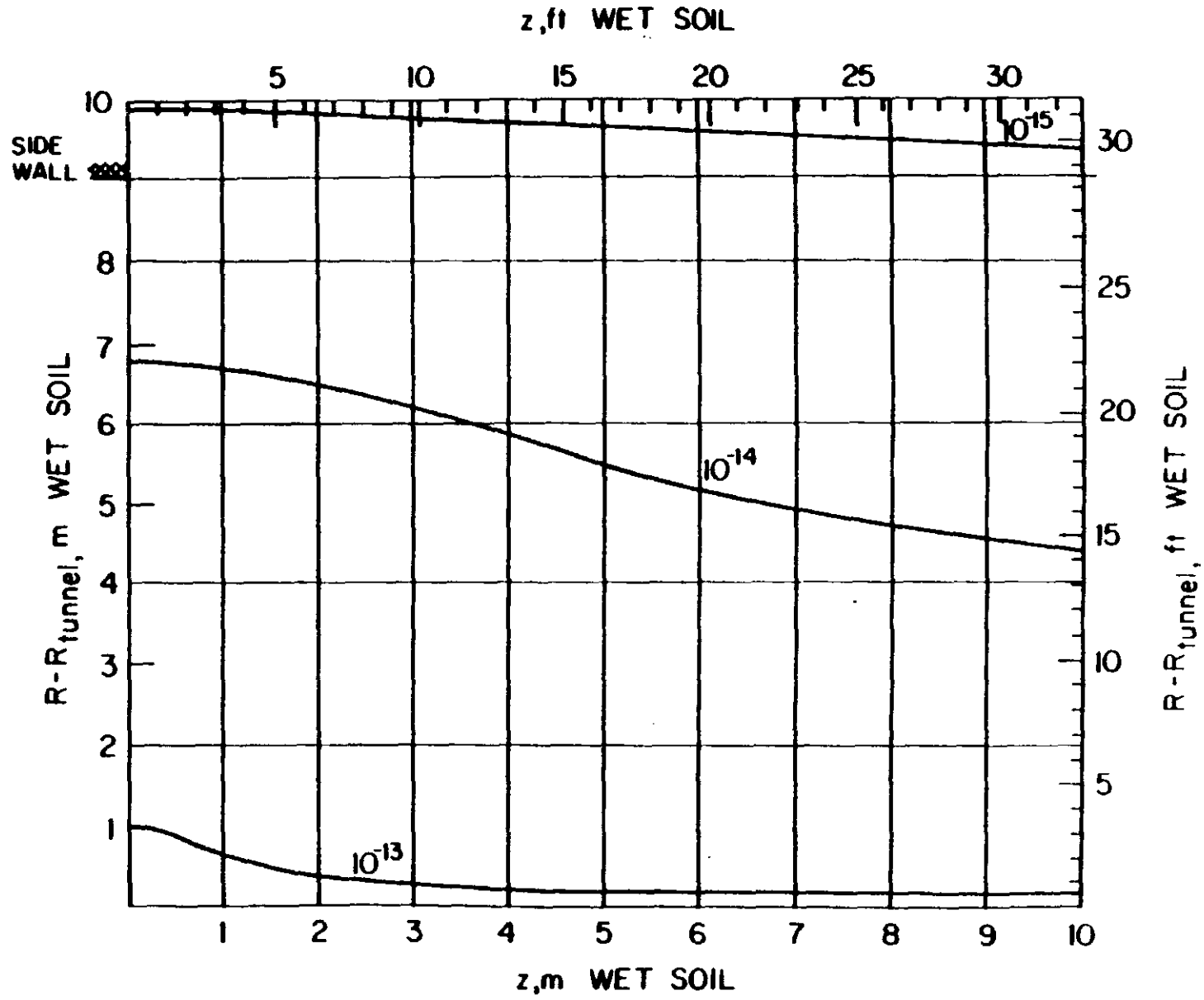

Fig. 178. Contours of equal dose equivalent (in rem/inelastic collision) in soil back wall of collision hall due to muons for colliding beams of 20 TeV each. A 1mm thick beampipe is present. Some contours may be omitted for clarity or due to statistical uncertainty.